Design and Development of ZnO Morphologies for Enhanced Photovoltaic Characteristics: Synthesis, Characterization and Fabrication of Photoanodes for Semiconductor Quantum Dot/Dye Sensitized Solar Cells

A Dissertation Submitted to the
Indian Institute of Technology Guwahati
as Partial Fulfillment for the Degree of

DOCTOR of PHILOSOPHY

by

Tridip Ranjan Chetia
Roll No: 10612238

Department of Chemistry
Indian Institute of Technology Guwahati
Guwahati – 781039, Assam, India
March 2016

STATEMENT

I hereby declare that this thesis entitled, "**Design and Development of ZnO Morphologies for Enhanced Photovoltaic Characteristics: Synthesis, Characterization and Fabrication of Photoanodes for Semiconductor Quantum Dot/Dye Sensitized Solar Cells"** is the outcome of research work carried out by me under the supervision of Dr. Mohammad Qureshi, at the Department of Chemistry, Indian Institute of Technology Guwahati, Guwahati, Assam, India.

In keeping with the general practice of reporting scientific observations, due acknowledgement has been made whenever work described here has been based on the findings of other investigators.

IIT Guwahati — Tridip Ranjan Chetia

March 2016 — Candidate

Dr. Mohammad Qureshi
Associate Professor
Department of Chemistry
Indian Institute of Technology Guwahati
Guwahati – 781036, India
Tel: +91 – 361 – 2582320; Fax: +91 – 361 – 2582349
Email: mq@iitg.ernet.in

Certificate

Certified that the work described in this thesis entitled "**Design and Development of ZnO Morphologies for Enhanced Photovoltaic Characteristics: Synthesis, Characterization and Fabrication of Photoanodes for Semiconductor Quantum Dot/Dye Sensitized Solar Cells**" by Mr. Tridip Ranjan Chetia, Department of Chemistry, Indian Institute of Technology Guwahati has been carried out under my supervision and has not been submitted elsewhere for a degree.

Guwahati
March 2016

Mohammad Qureshi
Thesis supervisor
Department of Chemistry
Indian Institute of Technology Guwahati
Guwahati – 781039, Assam, India

ACKNOWLEDGEMENT

The successful outcome of my thesis works has many supporting hands without which it was not possible to make it a reality. At the very onset, with a deepest sense of gratitude, I wish to express my sincere thanks to my supervisor, Dr. Mohammad Qureshi for his proficient guidance, inspiration, creative and scientific ideas which helped me to explore the domain of my work assembled in this thesis.

Besides my supervisor, I would also like to extend my heartiest thanks to the doctoral committee members, Dr. Chivukula V. Sastri, Dr. Bhubaneswar Mandal, Dr. A. S. Achalkumar and Dr. Akshai Kumar A. S. for their periodic evaluation of my work and valuable suggestions. I would like to thank all faculty members and staff members of Chemistry department. My sincere thanks to the staffs of Central Instruments Facility, for their help and in hand guidance to several analytical instruments, required during my research work.

I wish to express my sincere gratitude to IIT Guwahati for all the facilities that were made available to me and the Ministry of Human Resource Development (MHRD), India for the financial support.

I would like to thank my all my past and present group members Zia da, Dipankar, Momina, Anindya, Shaad, Avishek, Gaurangi and Tushar for their timely help, support and for creating a pleasant atmosphere in the lab.

I extend my sincere thanks to my friends Romen, Amlan, Anupal, Abhijit, Ashim Malakar, Satyabrat, Ashim Paul, Arindam, Ganesh, Murugavel, Sengoden, Satavisha, Anamika, Subbarao, Ashish, Dipjyoti and other close friends for their constant unfailing support, their encouragement and all the help they extended whenever required. I also wish to thank my junior friends, Hiranya, Nilotpal, Saurav, Jugal, Shyam, Monuj, Suman, Suranjan, Afsana for the joyful moments shared with me at IITG and their support.

No words would suffice to express my feelings for my teachers to whom I owe my obligations for all their great teachings and philosophy to be a good human; Nandita Ma'am, PKG Sir, Diganta Bora Sir, Pradip Goswami Sir, Manju Ma'am, RD Ma'am, Hazarika Sir, Gitika Ma'am, Pankaj Das Sir and the entire fraternity from my School, College and University who gave me the direction and insightful information to march forward in this field.

Finally, my Ph. D. endeavor could not have been completed without the endless love, unending support, tolerance and blessings from my family. I would like to express my deepest gratitude to my parents for all the unconditional love and sacrifices they have made for the sake of my upbringing. I am also grateful to my sister, and cousin brother and sisters for their affection and deep concern for my career.

Still many names are missing whose contribution and help is worth mentioning.

Tridip

Dedicated

To

My Parents

TABLE OF CONTENTS

SYNOPSIS i

CHAPTER 1: INTRODUCTION

1.1 AN OVERVIEW OF PHOTOVOLTAIC TECHNOLOGY DEVELOPMENT 1
1.2 WORKING PRINCIPLE OF DSSC/QDSSC DEVICES 4
1.3 DEVELOPMENT OF PHOTOANODIC MATERIALS AND ARCHITECTURES 8
1.4 CONCLUSIONS AND OUTLOOK 13
1.5 MOTIVATION AND OBJECTIVES OF THE PRESENT WORK 14
1.6 REFERENCES 15

CHAPTER 2: EXPERIMENTAL SECTION

2.1 INTRODUCTION 23
2.2 EXPERIMENTAL METODS 23
2.2.1 MATERIALS AND CHEMICALS USED 23
2.2.2 CHARACTERIZATION OF MATERIALS AND DEVICES 24
2.2.3 GENERAL FABRICATION PROCESSES OF DSSC AND QDSSC DEVICES 25
2.2.3 (i) Photoanode Preparation 25
2.2.3 (ii) Sensitization of Photoanodes 26
2.2.3 (iii) Counter Electrode Preparation 27
2.2.3 (iv) Assembling of Devices 27
2.2.4 EVALUATION OF SOLAR CELL PERFORMANCE 28
2.2.5 SOLAR CELL PERFORMANCE PARAMETERS 28
2.2.6 ELECTROCHEMICAL IMPEDENCE SPECTROSCOPY (EIS) MEASUREMENT 30
2.3 REFERENCES 32

CHAPTER 3: Hexagon Shaped ZnO Nanodisks with Exposed ±{0001} Polar Facets for Enhanced Photovoltaic Performance in Quantum Dot Sensitized Solar Cells

3.1 INTRODUCTION 33
3.2 EXPERIMENTAL METODS 35
3.2.1 SYNTHESIS OF ZnO NANODISKS 35
3.2.2 SYNTHESIS OF ZnO NANOPARTICLES 36
3.2.3 FABRICATION OF PHOTOANODES AND DEVICES 36
3.3 RESULTS AND DISCUSSIONS 38
3.3.1 POWDER X-RAY DIFFRACTION ANALYSIS 38
3.3.2 MATERIAL MORPHOLOGY 42
3.3.3 UV-VISIBLE ABSORPTION AND PHOTOLUMINESCENCE ANALYSIS 47
3.3.4 BET SURFACE AREA ANALYSIS 49

3.3.5	UV–VISIBLE ABSORPTION AND DIFFUSE REFLECTANCE ANALYSIS OF THE PHOTOANODES	50
3.3.6	PHOTOVOLTAIC CHARACTERISTICS OF THE SOLAR CELLS	52
3.4	CONCLUSIONS	60
3.5	REFERENCES	61

CHAPTER 4: Cage-Like ZnO Superstructures With Compacted 1-D Building Blocks For Enhanced Photovoltaic Performance

4.1	INTRODUCTION	64
4.2	EXPERIMENTAL METODS	65
4.2.1	SYNTHESIS OF ZnO CAGES	65
4.2.2	FABRICATION OF PHOTOANODES AND DEVICES	67
4.3	RESULTS AND DISCUSSIONS	68
4.3.1	POWDER X-RAY DIFFRACTION ANALYSIS	68
4.3.2	MATERIAL MORPHOLOGY	71
4.3.2 (i)	Effect of ammonium hydroxide (NH_4OH)	75
4.3.2 (ii)	Effect of sodium alginate (ALG) addition.	77
4.3.2 (iii)	Effect of reaction time	78
4.3.3	MECHANISM OF ZnO SUPERSTRUCTURE FORMATION	81
4.3.4	UV-VISIBLE ABSORPTION AND PHOTOLUMINESCENCE ANALYSIS	83
4.3.5	BET SURFACE AREA ANALYSIS	86
4.3.6	UV–VISIBLE ABSORPTION AND DIFFUSE REFLECTANCE ANALYSIS OF THE PHOTOANODES	88
4.3.7	PHOTOVOLTAIC CHARACTERISTICS OF THE SOLAR CELLS	89
4.4	CONCLUSIONS	96
4.5	REFERENCES	97

CHAPTER 5: Fabrication of Bilayer ZnO Based Hybrid Photoanode for Enhanced Photovoltaic Performance in CdS Quantum dot Sensitized Solar Cells

5.1	INTRODUCTION	100
5.2	EXPERIMENTAL METODS	101
5.2.1	SYNTHESIS OF HOLLOW MESOPOROUS ZnO MICROSPHERES (ZnO HMSP)	101
5.2.2	SYNTHESIS OF CdS NANOPARTICLES	102
5.2.3	GROWTH OF 1D ZnO NWs ON FTO SUBSTRATES	102
5.2.4	FABRICATION OF (ZnO NW–ZnO HMSP–CdS) HYBRID PHOTOANODE	103
5.2.5	DEVICE FABRICATION AND CHARACTERIZATION	104

5.3	RESULTS AND DISCUSSIONS	104
5.3.1	POWDER X-RAY DIFFRACTION ANALYSIS	104
5.3.2	MATERIAL MORPHOLOGY	105
5.3.3	BET SURFACE AREA ANALYSIS	109
5.3.4	DIFFUSE REFLECTANCE UV–VISIBLE ABSORPTION SPECTRA	109
5.3.5	PHOTOLUMINESCENCE ANALYSES OF THE MATERIALS	112
5.3.6	PHOTOVOLTAIC CHARACTERISTICS OF THE SOLAR CELLS	117
5.4	CONCLUSIONS	120
5.5	REFERENCES	121
CHAPTER 6:	**Binary Hybrid Composite of g-C_3N_4 and ZnO as a Photoanodic Material: A Synergistic Approach for Enhanced Charge Separation and Injection**	
6.1	INTRODUCTION	124
6.2	EXPERIMENTAL METODS	126
6.2.1	SYNTHESIS OF g-C_3N_4	126
6.2.2	SYNTHESIS OF ZnO NANORODS	126
6.2.3	SYNTHESIS OF ZnO NANOPARTICLES	126
6.2.4	PREPARATION OF (g-C_3N_4–ZnO NR) AND (g-C_3N_4–ZnO NP) COMPOSITES	127
6.2.5	FABRICATION OF PHOTOANODES AND DEVICES	127
6.3	RESULTS AND DISCUSSIONS	129
6.3.1	POWDER X-RAY DIFFRACTION ANALYSIS	129
6.3.2	MATERIAL MORPHOLOGY	130
6.3.3	DIFFUSE REFLECTANCE UV-VISIBLE ABSORPTION SPECTRA ANALYSES	136
6.3.4	STEADY STATE AND TIME RESOLVED PHOTOLUMINESCENCE ANALYSES	138
6.3.5	FOURIER TRANSFORM-INFRARED (FT–IR) ANALYSES	143
6.3.6	DIFFUSE REFLECTANCE UV–VISIBLE ABSORPTION SPECTRA OF THE PHOTOANODES	144
6.3.7	PHOTOVOLTAIC CHARACTERISTICS OF THE SOLAR CELLS	145
6.3.8	MORPHOLOGY DEPENDENT PHOTOVOLTAIC CHARACTERISTICS	152
6.4	CONCLUSIONS	157
6.5	REFERENCES	158
APPENDIX	**Boosting Photovoltaic Performance of SnO_2 based Dye Sensitized Solar Cells by Utilizing 2D MgO Nanosheets**	
7.1	INTRODUCTION	161
7.2	EXPERIMENTAL METODS	163

7.2.1	SYNTHESIS OF SK1 DYE	163
7.2.2	SYNTHESIS OF 3D HIERARCHICAL SnO_2 MICROSPHERES	165
7.2.3	SYNTHESIS OF POROUS 3D HIERARCHICAL MgO	165
7.2.4	FABRICATION OF PHOTOANODES AND DEVICES	166
7.3	RESULTS AND DISCUSSIONS	167
7.3.1	POWDER X-RAY DIFFRACTION ANALYSIS	167
7.3.2	MATERIAL MORPHOLOGY	168
7.3.3	BET SURFACE AREA ANALYSIS	171
7.3.4	DIFFUSE REFLECTANCE UV–VISIBLE ABSORPTION AND REFLECTANCE SPECTRA	172
7.3.5	DENSITY FUNCTIONAL THEORY (DFT) STUDY OF SK1 DYE	174
7.3.6	ELECTROCHEMICAL ANALYSIS OF SK1 DYE	175
7.3.7	PHOTOVOLTAIC CHARACTERISTICS OF THE SOLAR CELLS	176
7.4	CONCLUSIONS	181
7.5	REFERENCES	182

THESIS OVERVIEW 184

LIST OF PUBLICATIONS AND CONFERENCES ATTENDED 185

Thesis Title:	**Design and Development of ZnO Morphologies for Enhanced Photovoltaic Characteristics: Synthesis, Characterization and Fabrication of Photoanodes for Semiconductor Quantum Dot/Dye Sensitized Solar Cells**
Name of the Candidate:	Mr. Tridip Ranjan Chetia
Registration Number:	10612238
Thesis Supervisor:	Dr. Mohammad Qureshi
Department:	Chemistry
Institute:	Indian Institute of Technology Guwahati, Assam – 781039, India.

Thesis Overview:

Chapter 1 addresses the recent advancements in rational design and synthesis of various wide bandgap semiconductors based on their morphologies, which enhances the charge transport phenomenon as well the light harvesting ability. A brief discussion on the development of photovoltaic technology, basic concepts and working principle of dye/-semiconductor quantum dot (QD) sensitized solar cells are included. Promising role of ZnO heterostructures in light harvesting over the traditionally used similar TiO_2 heterostructures have been discussed. The chapter is concluded with a brief literature survey of current state-of-the art scenario and challenges related to the synthesis of ZnO based photoanodic architectures utilizing environmentally benign and easily available chemicals as the structure directing agents.

Chapter 2 describes the general protocols for the synthesis of materials, basic instrumentation techniques and methodologies used for material characterization, fabrication of dye-/ semiconductor QD-sensitized solar cells emphasizing the ZnO based photoanode preparation, and characterization of the devices using the basic and specific instrumental techniques/methods. Characterization technique of the devices using basic and specific instrumental techniques/methods such as solar simulator (Newport Sol3A), incident photon-to-current analyzer (IQE 200) and electrochemical impedance spectroscopy (EIS) measurements are also discussed.

Chapter 3 presents chemistry behind the formation of hexagonal ZnO nanodisks (NDs) with exposed ±(0001) polar facets and its application in quantum dot sensitized solar cell (QDSSC)

devices. The wet chemical synthetic approach utilizes ethyl cellulose (EC) and cetrimonium bromide (CTAB) as the capping and structure directing agents in 1-butanol: water (3:1) solvent system. Use of this particular strategy dramatically improves the photovoltaic properties of the material compared to its counterparts such as ZnO nanoparticles (NPs), nanorods (NRs) and porous nanoparticles (PNPs); the conventionally and frequently used ZnO morphologies in solar cells. A plausible mechanism of formation of ZnO ND is proposed based on the control reactions performed by varying the additive sequences of EC and CTAB and pervious works available in the literature. In the present reaction conditions, CTAB molecules are believed to be act as a carrier for negative zincate [i.e., $Zn(OH)_4^{2-}$] and organizer of ZnO crystal growth process while EC fibers impede classical crystal growth along *c*-axis by preferentially adhering onto the Zn^{2+} populated (0001) crystal surface leading to the formation of ZnO NDs. Photovoltaic properties of ZnO NDs as compared to ZnO NPs are investigated by co-sensitizing with CdS/CdSe quantum dots (QDs). A substantial increase in power conversion efficiency (PCE, η) is observed in ZnO NDs compared to ZnO nanoparticles. Enhanced performance of the proposed solar cell can be ascribed to following key factors – (i) efficient charge separation and collection, boosted by the exposed ±(0001) polar facets and their single crystalline nature (ii) better light-scattering effects and (iii) high BET surface area for sensitizer particle adsorption. Figure **1** represents FESEM features of as synthesized ZnO NDs which revealing the morphological characteristics of the material.

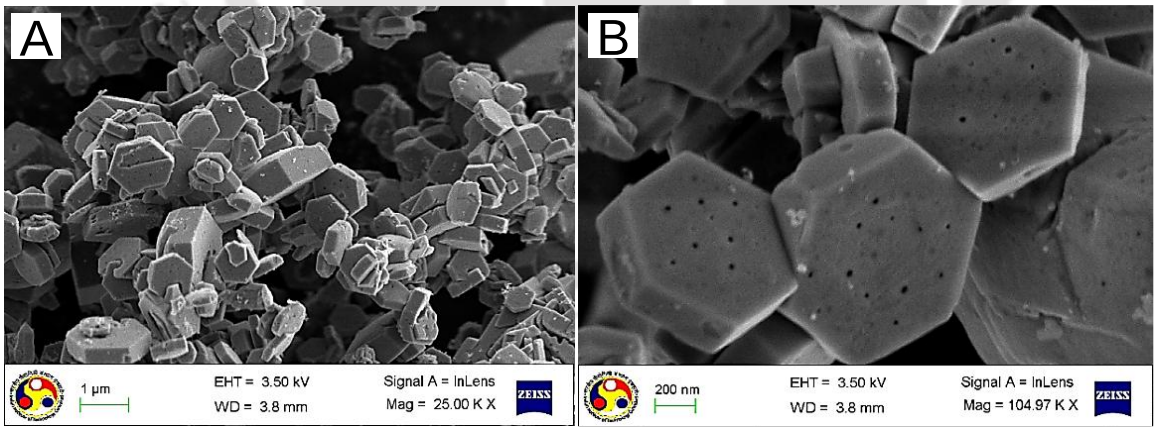

Figure 1. (A) FESEM images of as synthesized hexagonal ZnO Nano disks (NDs) at low magnification. (B) High magnification image of ZnO NDs showing pore formation on the surfaces. (*ACS Appl. Mater. Interfaces*, **2015**, *7*, 13266**)**

Chapter 4 presents a simple, green hydrothermal synthetic protocol for exotic 3D ZnO superstructures (ZnO Cages) assembled with compact 1D ZnO nano-rods which can provide faster photogenerated charge transfer pathways utilizing a naturally abundant bio-template "alginic

acid". Technological importance of the material is established by evaluating its photovoltaic properties in a dye sensitized approach. The synthetic protocol is investigated in detail by varying the reaction conditions in order to understand the interactions between the organic template and inorganic material. It is found that the optimum concentration of negatively charged alginate ions and NH_4OH in the reaction system are the key factors for formation of these exotic cage like, mesoporous superstructures. Experimental analyses reveal that the alginate ions, under hydrothermal reaction conditions, act as a structure directing agent and assemble 1D ZnO NRs hierarchically while NH_4OH assists formation of ZnO growth units. A plausible growth mechanism is proposed for the 1-D ZnO NR assembled ZnO superstructures and evaluated their photovoltaic properties. A comparative study on photovoltaic performance parameters of the fabricated dye sensitized solar cells (DSSCs), i.e. based on ZnO Cage, ZnO PNP and ZnO NR are carried out. An appreciated value of PCE (η) is furnished by the ZnO Cage based devices which is ~60 % and ~35 % improvement over the ZnO NR and ZnO PNP based devices. Enhanced photovoltaic performance of ZnO Cage based device is concluded mainly due to higher flux of photoinduced electrons, enhanced light scattering, probability of facile diffusion of electrolyte and efficient charge separation through nano sized 1-D ZnO NR conduits. Morphological characterizations of as synthesized ZnO cages along with the fabricated photoanode are performed and depicted in the figure **2**.

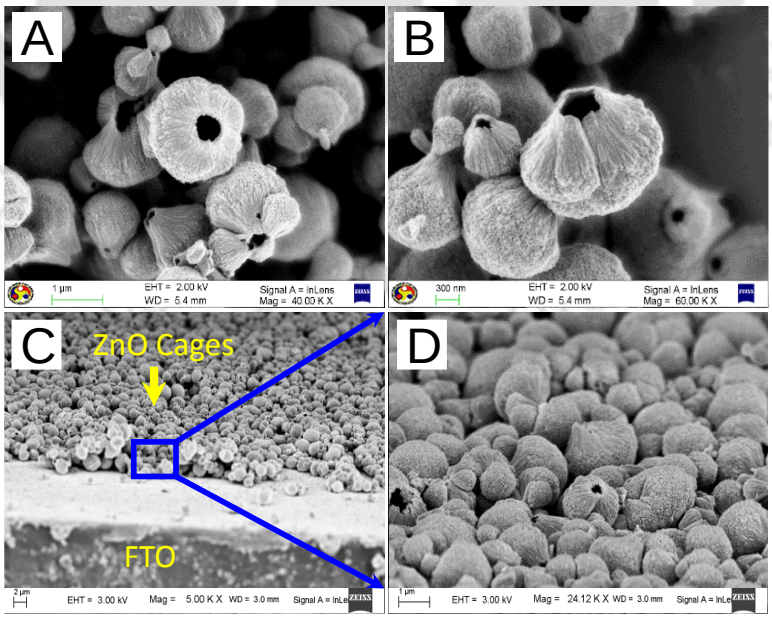

Figure 2. FESEM images (A) and (B) represents as synthesized cage like ZnO superstructures at different magnifications. Cross-sectional FESEM images (C & D) of as fabricated ZnO Cage based photoanode at lower and higher magnifications. (*Phys. Chem. Chem. Phys.*, **2016**, *18*, 5344).

Chapter 5 demonstrates fabrication of a bi-layered ZnO based photoanode and its utilization in QDSSCs. A combination of 3-dimensional (3D) hollow mesoporous ZnO microspheres (ZnO HMSP) and vertically grown one-dimensional ZnO nanowires (1D ZnO NWs) on fluorine doped tin oxide (FTO) coated glass substrate has been investigated as a potential hybrid photoanode for CdS QD-sensitized solar cell. Comparative study on photovoltaic performance of the solar cell with the devices fabricated with pristine ZnO HMSPs and ZnO NWs have been carried out. The proposed photovoltaic device exhibits an enhancement in PCE (η) upto ~74% and ~35%, as compared to the 1D ZnO NW and ZnO HMSP based solar cells. Incident photon-to-current conversion efficiency (IPCE) for the solar cell is observed to be ~40 %, whereas for the devices fabricated with bare ZnO HMSP and ZnO NW are only ~32% and ~19% respectively. Enhanced photovoltaic performance of the solar cell is attributed to high Brunauer–Emmett–Teller (BET) surface area, efficient light-scattering effects and facilitated diffusion of electrolyte for better functioning of the redox couple (S^{2-}/S_n^{2-}) in the hybrid photoanode. Moreover, a faster electron transport through 1D ZnO NWs provides better charge collection from the photoactive layer, which leads to increase in short circuit current density of the device. This maverick approach highlights the design and development of a new hybrid photoanode for solar harvesting. Morphological characterizations of the synthesized materials and the fabricated photoanode are depicted in the figure **3**.

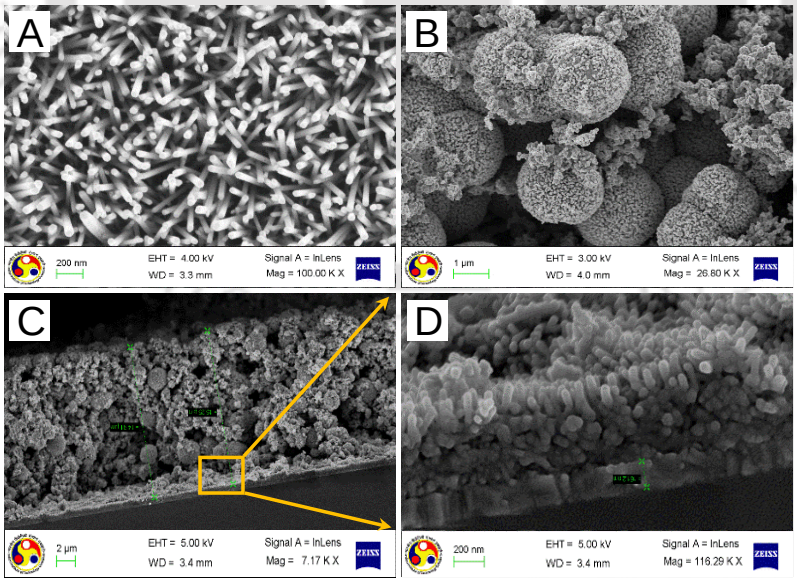

Figure 3. FESEM images of (A) Vertically grown 1D ZnO Nanowires (NW) on the FTO substrates, (B) 3D ZnO Microspheres (ZnO HMSP), (C) Cross-sectional view of the bi-layered hybrid photoanode (D) High-Resolution FESEM image of the photoanode showing 1D- ZnO NWs remain intact even after the deposition of 3D-ZnO HMSP. (*Phys. Chem. Chem. Phys.*, **2014**, *16*, 9625).

Chapter 6 demonstrates a practical strategy to boost light harnessing ability of QDSSCs by introducing a low cost and environmentally benign organic semiconductor, graphitic carbon nitride (g-C_3N_4) in the photoanodic segment.

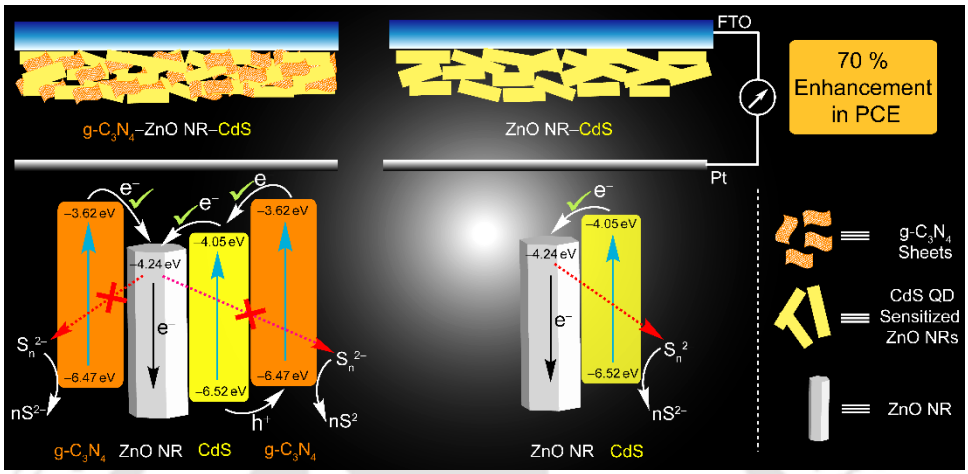

J. Mater. Chem. A., **2016** *(Just Accepted, DOI: 10.1039/C6TA00761A)*

A ~70% improvement in PCE (η) is observed for the devices fabricated with a binary hybrid composite of graphitic carbon nitride and zinc oxide nanorod, i.e., (g-C_3N_4–ZnO NR) [for an optimized weight ratio (0.5:1)] as compared to the pristine ZnO NR device. Systematic investigations reveal that g-C_3N_4 boosts light harvesting ability of the photovoltaic devices primarily by impeding photo-induced electron interception to the redox couple and injecting population to the conduction band of semiconductor. Electrochemical impedance spectroscopy (EIS) analysis shows a reduced tunneling of photo-induced electrons to the sulfide-polysulfide (S^{2-}/S_n^{2-}) redox shuttle in case of (g-C_3N_4–ZnO NR) composite devices. Higher recombination resistance (R_k) indicates that the g-C_3N_4 sheet act as a barrier for photoinduced electron interception at the working electrode/electrolyte interface. Preliminary investigation using steady state and dynamic photoluminescence analyses suggests a similar fact about the photo-induced electron injection from g-C_3N_4 sheets to ZnO, contributing to the enhanced light harvesting ability of (g-C_3N_4–ZnO NR) composite devices.

APPENDIX:

In this work, we have presented the idea to enhance the PCE (η) of **SnO_2 based DSSCs,** introducing an electron barrier layer in the form of 3D porous hierarchical MgO composed of 2D nanosheets by a simple ultra-sonication route followed by mixing process. A metal free carbazole derivative, namely 2-cyano-3-(4-(2-(9-*p*-tolyl-9*H*-fluoren-6-yl)vinyl)phenyl) acrylic acid (i.e. SK1 dye) is used as the sensitizer dye.

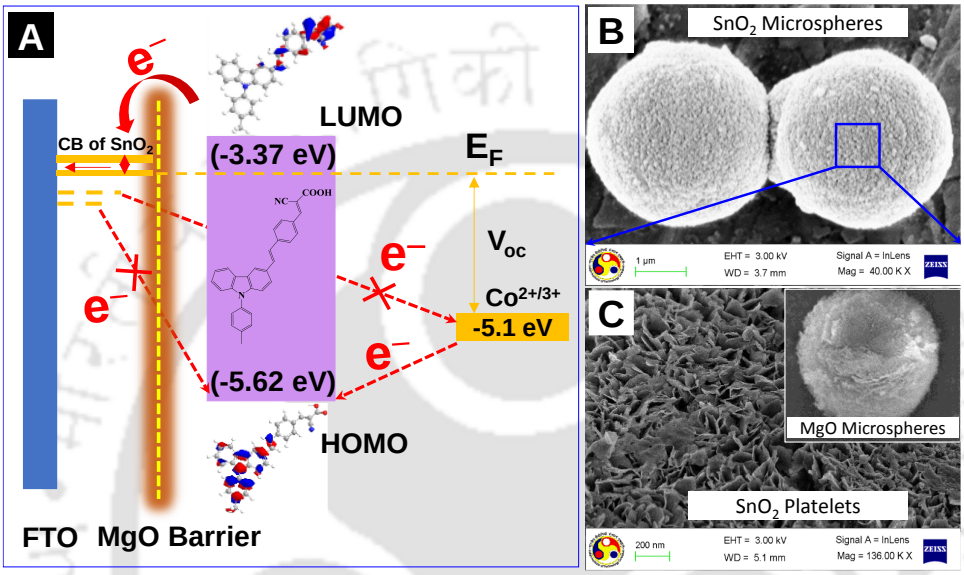

Figure 4.(A) Schematic representation of the energy levels of SnO_2–MgO device and inhibited electron interception at the SnO_2/electrolyte interface in presence of 2D MgO nanosheets. (B) FESEM image of as synthesized SnO_2 microspheres and (C) shows the high resolution image confirming SnO_2 Nanoplates on the surface of it. Inset to it shows FESEM image of as prepared MgO microspheres. (*J. Mater. Chem A*, **2015**, *3*, 4291)

Optimized PCE as high as ~3.71 % is achieved by introducing 15 wt % MgO and utilizing the redox mediator $[Co(bpy)_3]^{2+/3+}$. Moreover, we have observed a significant improvement in V_{oc} (**from 357 mV to 619 mV**) and *FF* (from **~38 % to ~57 %**) for the SnO_2-MgO based dye sensitized solar cell (DSSC) over the pristine SnO_2 device; translating to a **~74 % enhancement in PCE value**. The remarkable performance of the constructed cell can be ascribed to following key factors – (i) 2D MgO nanosheets are minimizing the electron interception at the SnO_2/electrolyte interfaces (ii) higher loading of SK1 dye molecules in the SnO_2-MgO photoanode for efficient light absorption (iii) noncorrosive cobalt$^{III/II}$ tris(2,2′-bipyridyl) redox mediator having higher redox potential than the traditional (I_3^-/I^-) redox shuttle thereby minimizing the mismatch between the redox potential and the sensitizer HOMO level and (iv) superior light scattering by the SnO_2-MgO photoanode compared to pristine SnO_2 photoanode.

CHAPTER 1

Introduction and Literature Review

This chapter presents a brief discussion on the development of photovoltaic technology, basic concepts and working principle of dye/-semiconductor quantum dot (QD) sensitized solar cells. Promising role of ZnO heterostructures in light harvesting over the traditionally used TiO_2 heterostructures have been discussed. The chapter is concluded with a brief literature survey of current state-of-the art scenario and challenges related to the synthesis of ZnO based photoanodic architectures utilizing environmentally benign and easily available chemicals as the structure directing agents.

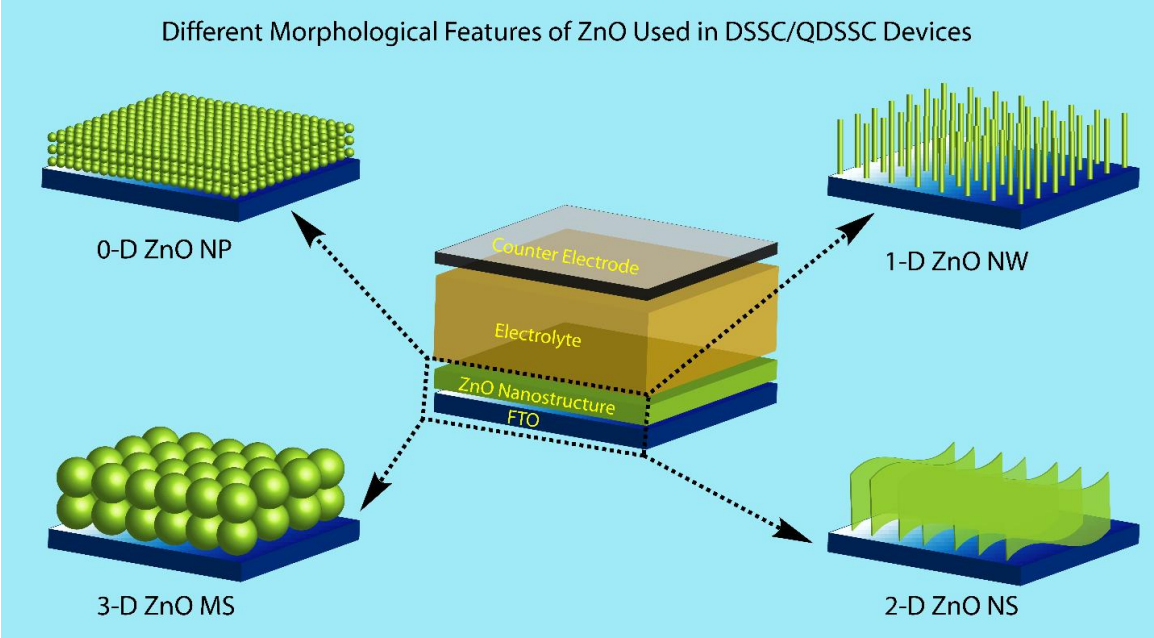

1.1 AN OVERVIEW OF PHOTOVOLTAIC TECHNOLOGY DEVELOPMENT

Challenges in solving the energy and environmental issues at the global level are leading to the development of new technologies which can harvest clean renewable energy resources and minimize the rising environmental pollution. Concurrently, by increasing the use of renewable energy resources, the global society is finding a way to reduce the consumption of fossil fuel, thereby reducing the greenhouse effect in protecting environment.[1–4] Amongst the renewable energy resources such as sunlight, wind, rain, tides, waves, biomass *etc.*, solar energy is the most abundant in earth and has the potential to satisfy future global need of energy.[5,6] Each year earth's surface receives about 12×10^5 TW of energy from the sun, which is about 6000 times the present rate of world's energy consumption. However, development of low cost, earth abundant and highly efficient light harvesting materials and devices remain a big challenge in order to convert the solar energy to electrical energy or chemical fuels, such as hydrogen in large scale.[7,8] "Photovoltaics" is one area of great promise for harvesting solar irradiation in which sunlight is converted into electrical energy by utilizing solar cell devices. Great efforts toward design and development of highly efficient solar cells and their commercial manufacturing have been made by the scientific community.[9] However, most of the solar cells are having disadvantages such as high cost, lack of long-term stability, toxic substances involved in materials or during processing etc, which limits their real world applications.[10] Figure **1.1.1** (A) is showing the solar energy distribution curve with the major components, i.e., visible and infrared radiation in solar spectrum and (B) distribution of global energy potential (renewable and non-renewable) *vs* world consumption of energy.

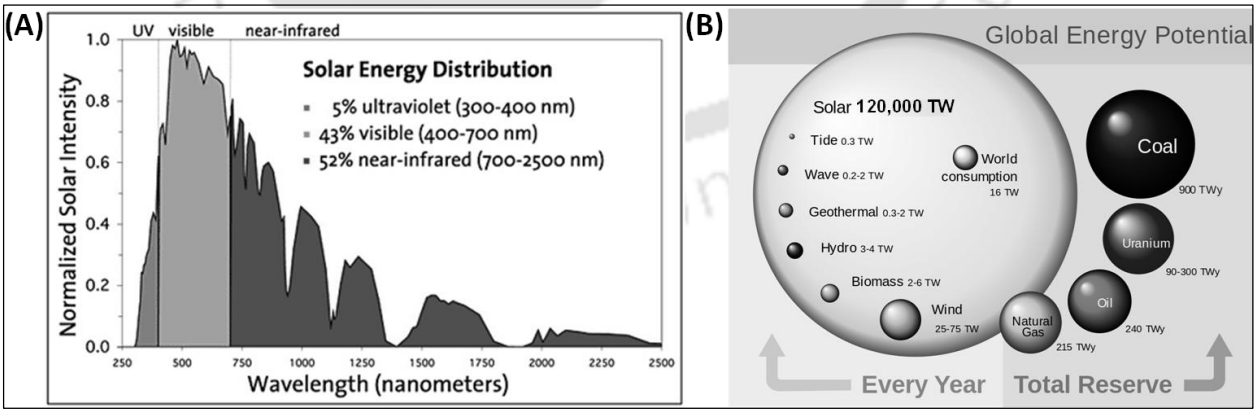

Figure **1.1.1** (A) Solar energy distribution graph illustrating visible and infrared radiation are the prime components of solar spectrum (Source: Lawrence Berkeley National Laboratory). (B) Energy potential of renewable energy sources per year and the total estimated energy potential of fossil and nuclear fuels *vs* world consumption of energy (Source: http://www.renewablegreenenergypower.com).

Solar cells can be classified according to the generation of technologies.[11] First generation solar cells are made from single crystalline Si (c-Si) wafers and are the dominant technology in the commercial solar panel market. A record power conversion efficiency (PCE) as high as ~25% has been reported for the *state-of-the-art* c-Si solar cells by Martin Green's group in 1998.[12,13] However, complicated manufacturing processes, high production cost, and long energy payback time have slowed down their implementation worldwide. Mainly motivated by simplification of manufacturing procedure and reduction of production cost, the second generation solar cell or thin-film solar cell have been introduced.[14,15] This kind of solar cells utilize amorphous silicon (a-Si), copper indium gallium selenide (CIGS), CdTe etc. as light harvesting materials. Although, second generation solar cells are economical, they are less efficient as compared to the first generation solar cells. Third generation solar cells are based on nanostructured photoactive materials.[16] The objectives of third generation solar cells are: (i) fabrication of high-efficiency, low-cost and lightweight solar cells from inexpensive, earth abundant, and environment-friendly materials, (ii) simple manufacturing processes and (iii) large-area fabrication. In addition, third generation solar cells could be able to overcome the Shockley and Queisser theoretical upper limit of single junction solar cells.[17,18] This type of photovoltaic devices include dye-sensitized solar cells (DSSCs), quantum dot sensitized solar cell (QDSSCs), polymer solar cells, Perovskite solar cells etc. Among these, DSSCs are most attractive and promising for future applications since they are made of earth abundant materials and fabricated with inexpensive equipments. Basically, DSSCs are electrochemical cells which was introduced by O'Regan and M. Grätzel in 1991.[19] They have used a mesoscopic TiO_2 electrode, anchored with electron-injecting organic sensitizer molecules, acts as a photoanode for light absorption and a platinized fluorine-doped tin oxide (FTO) glass as a passive cathode for catalysis of the electrolyte with a redox couple I^-/I_3^-, sandwiched between the two electrodes. They obtained overall efficiency of the cell ~7.1 % in simulated solar light. This maverick approach by Grätzel *et al.* have prompted the future research in exploration of novel light harvesting materials to design and develop photovoltaic devices with higher power conversion efficiency (PCE, η). Since the discovery of DSSC, enormous efforts are being made and a power conversion efficiency (PCE) up to ~13% has been achieved.[20] QDSSCs are the derivative form of dye sensitized solar cells which is based on the same photoelectrochemical working principle.[21,22] QDSSC utilizes narrow band gap semiconductor QDs as sensitizer particles instead of organic dye molecules and are deposited on the surface of mesoporous wide band gap semiconductor film.

Recently, an impressive PCE value of ~8.5 % for a CdSeTe/CdSe QD co-sensitized QDSSC is reported which have shown a promise towards its further development and practical application.[23]

DSSCs and QDSSCs are endowed with numerous advantages in contrast to first and second generation solar cell devices such as c-Si, a-Si, CdTe, and CIGS. They can be manufactured without inert atmosphere and high temperatures which results in low-cost as well as minimum energy payback time.[24] Lightweight and flexible DSSC/QDSSC modules can also be fabricated by employing *roll-to-roll* processing technology and utilizing conductive plastic substrates or metal foils.[24–26] Moreover, DSSC and QDSSC are constructed with environmentally benign, earth-abundant materials, and exhibit good performance in diverse lighting conditions. It has been established that, DSSCs can withstand for more than 20,000 h of continuous illumination, and stability tests infer potential outdoor lifetime beyond 20 years.[27–29] Due to these advantages of DSSC devices, a number of companies such as G24 Innovations (G24i), Dyesol, Solaronix, 3GSolar, Aisin Seiki, Toyota, Sharp, Sony etc. are involving in development, manufacturing and commercialization of this technology.[24,30] Figure **1.1.2** is depicting some examples of commercialized DSSC modules by G24i [Images (A) & (B)], and 3GSolar [Image (C)] and Dyesol [Image (D)].

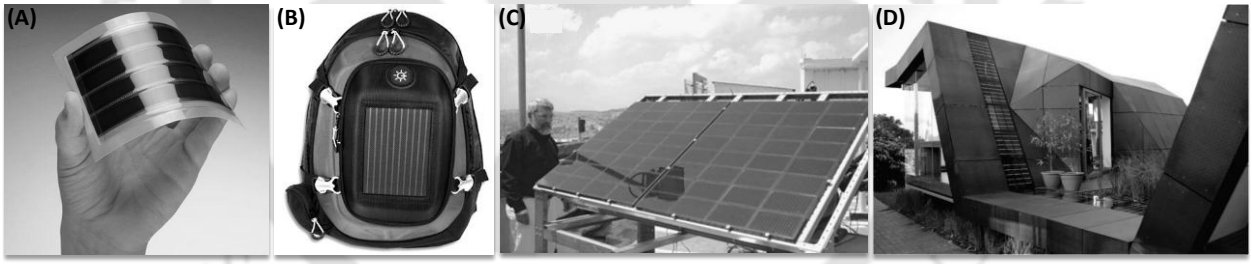

Figure **1.1.2.** (A) Flexible DSSC device fabricated by G24i Ltd., UK and (B) its integration to backpacks. (C) Large area DSSC module demonstration from 3GSolar Ltd., Israel. (D) Building-integrated DSSC module demonstration by Dyesol Ltd. Australia.

G24i is the first company to commercialize a DSSC product in 2009.[30] They have also integrated high efficiency flexible DSSC modules into the items like bags, [figure **1.1.2** (A) & (B)] luggage, backpacks, computer peripherals such as keyboards and mouse etc, for portable recharging of consumer electronics.[31] 3GSolar, Israel, is exclusively focusing on development of DSSC technology and extended the application of DSSC modules in lightening rural areas as well as to power up irrigation pumps [figure **1.1.2** (C)].[24,29] Dyesol, Australia, develops DSSC materials, components, and equipments for fabrication of large area modules and small area DSSC

devices for laboratory testing.[32] In order to address the building-integrated photovoltaics (BIPV) market, they have fabricated the largest DSSC module, over 1 m^2, on steel strips for use as roofing panels in collaboration with Tata Steel [figure **1.1.2** (D)].[33] Many more DSSC demonstration modules are now available in commercial market which proves the efficient harvesting of solar light by DSSC technology and its potential for use in everyday life.[34,35]

Since the first report of ~7 % efficient DSSC device in 1991, appreciated values of PCE as high as ~13 % for laboratory tested devices, ~10 % for modules and commercial products are achieved in past 24 years accredited to the intense research and great efforts by the scientific community across the globe.[36] Many challenges lie ahead to improve the DSSC technology with innovative ideas for widespread practical applications. Use of less expensive components, alternative metal oxide materials, redox couples and sensitizers is showing a way for rapid advancement of DSSC technology. Specially, narrow band gap semiconductor quantum dots (QDs) as the sensitizer have advantages over the organic dye molecules in terms of spectral response, generation of multiple excitons per photon and stability. However, utilization of semiconductor QDs as sensitizer in the QDSSC devices still demand enormous advancements to meet the threshold for mass production and commercial applications.

1.2 WORKING PRINCIPLE OF DSSC/QDSSC DEVICES

DSSCs and QDSSCs are the electrochemical devices comprises of two sandwiched electrodes, i.e., one photoanode and a passive cathode which act as a counter electrode. A suitable redox couple in the form of electrolyte is introduced in between the two electrodes to complete the device. Figure **1.2.1** (A) is depicting a pictorial presentation of all the segments in a conventional DSSC or a QDSSC device, while (B) is representing the cross-sectional schematic of the device with an external circuit.

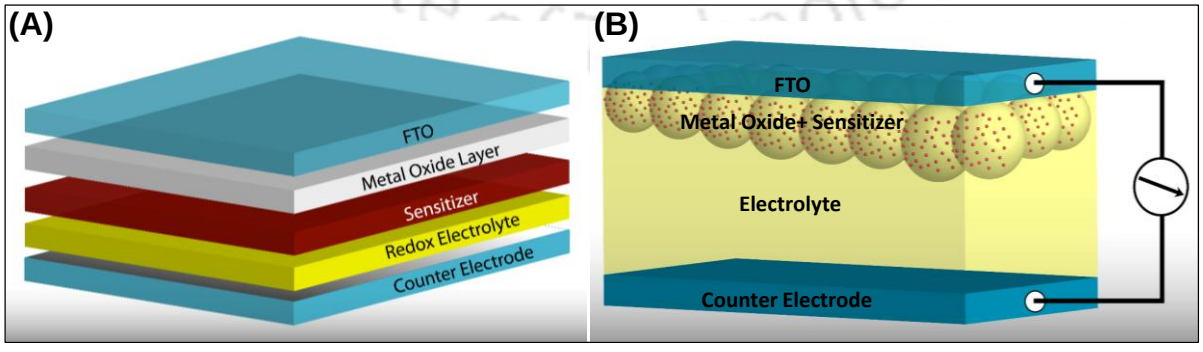

Figure 1.2.1 Schematic **(A)** is showing all the segments of a typical DSSC/QDSSC and **(B)** is depicting the graphical representation of cross-sectional schematic of the device.

There are four primary components of a DSSC or a QDSSC device. The construction of the components are discussed as follows:

- The anode is constructed with a wide band gap nanostructured metal oxide (e.g., TiO_2, ZnO, SnO_2, $SrTiO_3$ etc.) film which is deposited over a Fluorine doped Tin Oxide (FTO) or Indium Tin Oxide (ITO) coated glass substrate. In general, optimum thickness of the layer is in the range of 10–15 μm.
- A photosensitizer such as, metal complexes or organic molecules which absorb visible radiation of solar spectrum. In case of QDSSC devices, narrow band gap semiconductor quantum dots are utilized as sensitizers instead of dye molecules. The sensitizer molecules or particles are anchored to the metal oxide scaffolds and inject photoexcited electrons.
- A suitable redox electrolyte to regenerate the oxidized dye molecules or QDs. Some examples of conventionally used redox electrolytes are: iodide/tri-iodide (I^-/I_3^-), $Cobalt^{(II/III)}$ metal complex based redox shuttles in (acetonitrile: Valeronitrile) solvent mixture for DSSC devices, aqueous sulfide/polysulfide (S^{2-}/S_n^{2-}) redox electrolyte for QDSSC devices.
- A counter electrode which is most commonly fabricated by depositing a very thin layer of Pt on FTO substrate. Carbon based materials, metal sulfide–graphene composites etc are also employed as an alternative of Pt.

The basic working principle and electron transfer processes involved in a typical DSSC device is illustrated schematically in Figure **1.2.2**, showing a metal oxide (MO) layer deposited in a conductive FTO substrate. The sensitizer molecules are anchored to the surface of MO which are in contact with a suitable redox electrolyte. Excitation of the sensitizer upon solar light irradiation is followed by injection of photoexcited electrons into the conduction band (CB) of the MO (reactions **1** and **2**). The injected electrons are diffused through the mesoporous oxide film and extracted by the FTO substrate to the external circuit (reaction **3**). Meanwhile, a suitable redox couple regenerates the oxidized dye to regulate the process and catalyze at the counter electrode (reactions **4** and **5)**. For an effective regeneration of the oxidized dye molecules, the redox chemical potential of the electrolyte must be more positive than the highest occupied molecular orbital (HOMO) energy level of the dye molecules.[37] In case of QDSSC devices, holes are created in the valance band of semiconductor QDs and neutralized by a suitable redox couple to prevent photocorrosion.[38] Redox couple is reduced in turn at the counter electrode, while electron

migration from the anode to the counter electrode closes the circuit. The maximum output of photovoltage (V_{oc}) expected from a dye or QD sensitized electrochemical device is given by the difference between the semiconductor conduction band edge, i.e. the fermi level (E_F) of the MO and the electrolyte redox potential as shown in the figure **1.2.2**.[24]

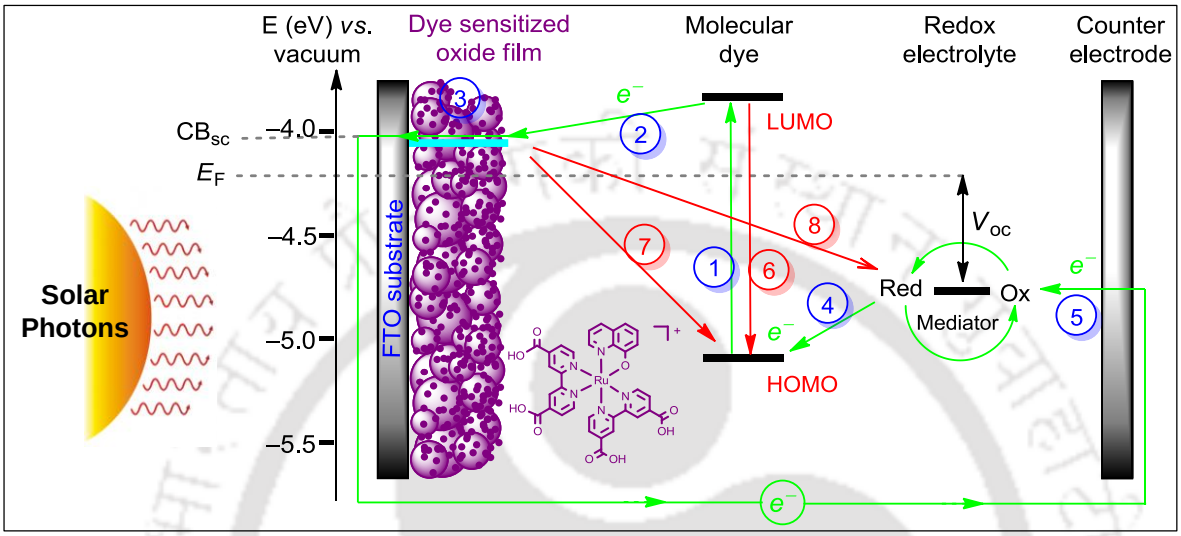

Figure 1.2.2 Schematic of the interior and basic working principle of dye-or semiconductor-sensitized solar cells with favorable energy levels of all the cell components. Green and red colored arrows are representing favorable energy transfer and non-favorable recombination processes respectively. (Source: www.renewablegreenenergypower.com).

For an efficient photoinduced electron injection, the excited state energy level of the dye has to be more positive to that of the metal oxide CB edge and they should firmly attached to the surface of the semiconductor by virtue of suitable anchoring groups such as, –COOH, –PO_3H_2, –OH *etc*. Moreover, the electron injection process (reaction **2**) should be faster than the relaxation or the deactivation process (reaction **6**) of the sensitizers.[39–41] In general, the relaxation process of a photoexcited dye molecule in a DSSC device is in the order of magnitude 10^{-7} s, while ultrafast electron injection from the dye molecules in femtosecond (10^{-15} s) range is observed.[42] As a result, the electron injection efficiency (ϕ_{inj}) close to unity is already achieved in case of optimized DSSC devices. However, the time scale of electron injection in case of semiconductor QD sensitizers is in the range of picosecond (10^{-12} s) regime which is slower in contrast to the dye molecules.[43–45] Also, from experimental observations it is demonstrated that intra-band recombination process (direct band-to-band recombination and trap mediated recombination) of photoexcited electrons in semiconductor QD sensitizers vary over orders of magnitude (10^{-11} to 10^{-6} s) and depends largely on the specific semiconductor as well as the nature of the semiconductor surface.[43]

Frequently used (II-VI) semiconductor QDs such as, CdS, CdSe, CdTe etc. exhibits recombination lifetimes in the range of (10^{-11}–10^{-9} s).[43] In some instances the recombination processes in semiconductor QDs seriously competes or even predominates the photoinduced electron injection and the sensitizer regeneration processes. This is primarily due to trap mediated recombination or electron interception from the photoexcited semiconductor QDs to the redox shuttle in the electrolyte.[46,47] A number of research works are devoted towards the minimization of recombination processes in the semiconductor QDs as well as to enhance the driving force of charge transfer process at the MO/sensitizer interfaces.[48] Utilization of surface passivated semiconductor QDs as sensitizer in QDSSC devices is observed to be beneficial for reduction of trap mediated recombination kinetics whilst by controlling the size of QDs and making use of elevated CB offset due to the size quantization effects, the electron injection kinetics can be improved.[49–53] After the photoexcited electron injection, diffusion of electrons through the semiconductor film ensues in a time scale of millisecond (10^{-3} s) regime.[54,55] In the course of moving through the semiconductor film, the injected electrons encounter with the oxidized sensitizer (i.e., dye molecules or semiconductor QDs) and the oxidized redox species (e.g., I_3^-) in the electrolyte which are adsorbed on the semiconductor surface.[56] Thus, some of the photo-injected electrons tend to undergo recombination with the oxidized sensitizer (reaction **7**) or with the oxidized redox species (reaction **8**) in the electrolyte before they are extracted to the external circuit. Both of these back transfer processes of electrons from the MO layer compete with the sensitizer regeneration process, i.e., reaction **4**. Fortunately, the sensitizer regeneration processes (10^{-8} s for dye and 10^{-11} for QD) are much faster than the recombination kinetics which occurs in micro to millisecond regime in the devices.[43,47] However, due to the slower transport of photoinduced electrons (in millisecond range) through the mesoscopic MO films, the recombination processes become feasible in real time devices. To suppress back electron transfer processes from the MO film, a compact blocking layer of the metal oxide onto the FTO substrate is deposited by using different techniques such as chemical bath deposition, spray pyrolysis, or sputtering which prevent contact between the redox mediator in the electrolyte and the TCO.[57–59] Surface passivation of the nanocrystalline MO film is also performed by depositing an ultrathin buffer layer of a suitable material (e.g., Al_2O_3, SiO_2, MgO, TiO_2 etc.) to reduce trap state mediated electron interception from the MO to the redox couple.[60,61] Again, by utilizing different

morphologies of MO in the photoanode, charge transport properties can be improved for a minimum electron interception and recombination.[62,63]

1.3 DEVELOPMENT OF PHOTOANODIC MATERIALS AND ARCHITECTURES

From previous discussions it is clear that recombination reactions which limit the light harvesting ability of a DSSC/QDSSC device, occur primarily due to the back transfer processes and trapping of electrons in crystal defect sites of the metal oxide layer in the photoanodic segment. In order to design and develop photovoltaic device with high efficiency, it is important to minimize the recombination processes by exploration and utilization of functional materials with superior physical, optical and electronic properties. Since the discovery of DSSC by Grätzel *et al.* in 1991, a number of wide band gap metal oxides such as ZnO,[64,65] SnO_2,[66,67] Nb_2O_5,[68,69] $SrTiO_3$[70] *etc.* are explored to as an alternative of TiO_2; the commonly used semiconductor metal oxide in DSSC devices. Amongst them, ZnO is the most propitious material to contribute with something new due to its unique intrinsic properties such as, (i) similar band gap and band edge alignment as that of TiO_2, (ii) superiority in electron mobility, (iii) anisotropic growth behavior of crystal planes.[71] Table **1.3.1** summarizes a comparative study of basic electronic and optical properties of ZnO, TiO_2, and SnO_2.

Table 1.3.1 Structural and electronic properties of semiconducting metal oxides used in photovoltaic devices.

Parameters	**ZnO**	**TiO_2**	**SnO_2**	**Reference**
Crystal Structure	Wurtzite	Anatase, Rutile	Rutile	72–75
Bandgap [eV]	3.2–3.4	3.0–3.2	3.6–3.8	72–76
Conduction Band Minimum [eV]	−4.36	−4.41	−4.88	77
Electron Effective Mass	0.26	9	0.275	78–80
Electron Mobility [$cm^2\ V^{-1}s^{-1}$]	130–200	0.1–4	200–250	72,80,81
Effective Electron Diffusion Coefficient [$cm^2.s^{-1}$]	1.1×10 −4	4.3×10 −4	7.3×10−5	82
Static Dielectric Constant ($\varepsilon_{\perp,//}$)	9.26, 8.2	86, 170	14, 9	83

As we have seen from table **1.3.1**, electron mobility in bulk and conduction band edge of ZnO are reported to be highest amongst its counterparts. Higher electron mobility of ZnO is beneficial for faster transport of photoinduced electrons in the photoanode whilst higher conduction band edge enable the possibility for a larger open circuit voltage (V_{oc}). In addition, n-type conductivity of ZnO can be further tuned by substituting Zn with suitable metal atoms such as Al, Ga, and In.[84–86] More importantly, the ease of crystallization and anisotropic growth of crystal planes allows the

preparation of ZnO nanostructures with diverse morphologies. A large variety of ZnO nanostructures with different morphological features, spanning from randomly arranged nanoparticles to highly ordered nanotube arrays or single crystalline nanorods are obtained by varying the synthetic routes.[87,88] Based on the morphologies of ZnO, nanostructured materials can be classified as: zero-dimensional (0-D) nanoparticles (NPs), one-dimensional (1-D) nanorods (NR)/nanowires (NW), two-dimensional (2-D) nanosheets (NS), and three-dimensional (3-D) nanomaterial [e.g microspheres (MS)]. All these morphological features of ZnO are endowed with unique physical, optical and electrical properties such as, specific surface area, scattering of light, charge transport *etc.* as shown in figure **1.3.1**.

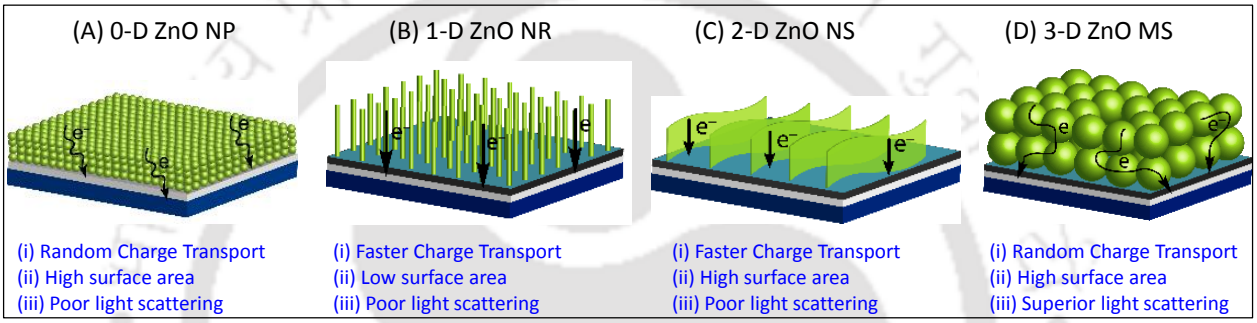

Figure 1.3.1 Schematic representation of different photoanodic architectures of ZnO made with (A) zero dimensional (0-D) nanoparticles, (B) 1-D nanorod (NR) networks, (C) 2-D nanosheets (NS) and 3-D microspheres (MS). A comparative study of intrinsic properties of the photoanodes such as charge transport, specific surface area, and internal scattering of light is also shown.

For utilization as a photoanodic material in DSSC/QDSSC devices, 0-D and 3-D structures of ZnO provide larger surface area for sensitizer adsorption, while 1-D and 2-D nanostructures offer direct and faster transport pathways for photo-induced electrons.[89–91] However, specific surface area and light scattering ability of vertically grown 1-D ZnO nanostructures is minimum. Limiting factor of 0-D and 3-D structures is the charge collection, wherein the photo-generated electrons undertake a random movement through the film and interact repeatedly with the trap sites.[92] Application of these morphological features or rational design and synthesis of novel superstructures of ZnO are showing possibilities to integrate all the expected key features i.e., (i) Faster charge transport, (ii) Higher specific surface area, and (iv) Superior light scattering ability, in a single photoanode for design and development of highly efficient DSSC and QDSSC devices.

Recent advances in the rational design and synthesis of exotic ZnO nanostructures with excellent charge transport and optical properties have open up their potential applicability in DSSC/QDSSC devices. A large variety of ZnO morphologies such as nanoparticles,[93] nanowires,[94]

nanotubes,[95] tetrapods,[96] nanosheets,[97] hierarchical aggregates,[98] nanoflowers,[99] microspheres,[100] *etc.* are employed as an electron transporting material in DSSC devices to improve the *solar-to-current* conversion efficiency as shown in table **1.3.2**.

Table 1.3.2 Photovoltaic performance of different morphologies of ZnO and its composites with other semiconductor materials reported for DSSC devices. (NWs: nanowires, NPs: nanoparticles, NTs: nanotubes).

ZnO Structures	Sensitizer	J_{sc} (mA.cm^{-2})	V_{oc} (mV)	FF (%)	η (%)	Ref.
Hierarchical aggregates	N719	19.8	640	59	7.5	101
Commercial nanopowders	N719	18.1	621	58	6.6	102
ZnO tetrapods/SnO_2 NPs	N719	16.3	656	59	6.3	103
ZnO aggregates/TiO_2 shell	N3	15.8	709	56	6.3	104
Hierarchical aggregates	N3	21	660	44	6.1	105
ZnO nanosheet	D149	18.0	530	63	6.1	97
Oriented porous films	D149	12.2	690	65	5.6	106
Nanoparticles/Hollow cavities	N719	15.7	563	62	5.5	107
Nanoparticles	D102	17.4	630	48	5.4	108
Hierarchical aggregates	N3	18.7	635	45	5.4	98
Hierarchical aggregates	D205	12.2	653	67	5.3	109
ZnO/Nb_2O_5 shell	N719	12.4	712	59	5.2	110
Tetrapod-like ZnO nanopowders	D149	12.4	607	65	4.9	111
Nanosheet/NWs	N719	10.9	680	65	4.8	112
Self-assembled nanostructures	N719	10.7	710	62	4.7	113
ZnO NWs/NPs	N3	15.2	610	46	4.2	114
Hierarchical NWs/nanoporous layer	D419	12.3	570	58	4.1	115
Mesoporous film	N719	11.8	650	52	4.0	116
Hierarchical NWs	N719	8.8	680	53	2.6	117
NWs	D102	14.1	550	34	2.6	118
Nanorods	Z907	6.4	720	49	2.3	119
NWs	N719	9.3	670	34	2.1	120
NTs	N719	3.3	739	64	1.6	121

Synthetic processes of different morphologies of ZnO involve utilization of a range of structure directing agents and additives such as oleic acid,[122] citrate ions,[123] sodium bis(2-ethylhexyl) sulfosuccinate or AOT,[124] starch,[125] polyvinylpyrrolidone,[126] pectin,[127] gelatin[128] sodium carboxymethyl cellulose,[129] *etc.* These chemicals can alter the classical arrangement of crystal growth units of ZnO in optimum reaction conditions and leads to the formation of novel morphologies with structural speciality and intricacy. Although, the use of ZnO in DSSC devices has increased dramatically in recent years due to the availability of nanostructures, it is still the runner up to TiO_2 counterparts in terms of efficiency. The highest PCE (η) reported for ZnO based DSSC devices up to now is ~7.5 % (table **1.3.2**), which is far less than the TiO_2 based device (~13%).[20] The origin of lower performance of ZnO based DSSC devices is attributed to following

two factors – (i) hindrance in photoinduced electron injection due to the formation of electrically bound (electron–dye cation) pairs after dye excitation and (ii) formation of (Zn^{2+}–dye) complexes due to the chemical instability of ZnO in acidic environment of dye sensitization process.[71,130] (Zn^{2+}–dye) complexes are inactive of visible light irradiation and incapable of injection of photoinduced electron to ZnO. Careful control of the concentration of the dye solution and sensitization time minimizes the probability of formation of (Zn^{2+}–dye) complex.[131] Another strategy to enhance the light harvesting ability of ZnO based DSSC is surface passivation of the photoanode with more stable semiconductors such as TiO_2, SnO_2, Nb_2O_5 *etc.*, which minimizes the reactivity of ZnO towards acidic dye molecules during sensitization.[103,104,110]

The benefits of superior electron transport property and tunable morphologies of ZnO has also been implemented in advancement of QDSSC devices in past few years. In QDSSC devices inorganic semiconductor QDs are employed as the sensitizer particles to harvest solar photons. Semiconductor QDs have number of advantages over the dye molecules such as, size controlled band gap tunability,[132] higher extinction coefficients,[133] multiple exciton generation per photon,[134] higher stability *etc*. However, traditional mesoscopic photoanodes with nanoparticle matrices are not observed to be suitable for utilization in QDSSC devices as they furnish low PCE values. It is due to the clogging of mesopores during the QDs sensitization processes which impedes smooth diffusion of electrolyte throughout the photoanode for efficient regeneration of the oxidized QDs.[135] For facilitated diffusion of electrolyte and adequate loading of QDs, open-type photoanodic architectures such as, 1-D ZnO nanorod/nanowire networks, tetrapods, nanotubes, nanosheets *etc.* are utilized and achieved a PCE upto ~6.2 %.[136,137] However, due to the deficit in specific surface area in these photoanodes, sensitizer uptake is observed to be lower and further exploration is needed. In view of this, hybrid photoanodic architectures such as, double-layer ZnO nanorod–nano-tetrapod,[138] combination of ZnO nanoparticles–porous microspheres,[139] *etc.* are also investigated to enhance the specific surface area for sufficient loading of sensitizer QDs. More than 5% PCE values are observed in these instances. The hybrid photoanodic architectures provides an opportunity to utilize beneficial effects of different morphological features in a single photoanode and shown a possibility for further improvement in light harvesting ability of the devices. Recent advancements in design and fabrication of ZnO based photoanodic architectures for enhanced photovoltaic performance of QDSSC devices are summarized in Table **1.3.3**.

Table **1.3.3** Photovoltaic performance of different morphologies of ZnO and their combinations reported for QDSSC devices. (NWs: nanowires, NPs: nanoparticles, NTs: nanotubes, NR: nanorod, NS: nanosheet).

ZnO Structures	Sensitizer	J_{sc} (mA.cm^{-2})	V_{oc} (mV)	FF (%)	η (%)	Ref.
Nano-tetrapods	ZnSe/CdSe/ZnSe	17.3	760	47	6.2	136
Nanorods/Tetrapods	CdS/CdSe	16.5	700	45	5.2	138
NP film/Microsphere	CdS/CdSe	17.1	560	53	5.1	139
NW array	$Zn_xCd_{1-x}Se$	18.0	650	40	4.7	140
NPs passivated with TiO_2	CdS/CdSe	15.4	620	49	4.6	141
NW array	ZnSe/CdSe	11.9	836	45	4.5	142
NPs	CdS/CdSe	10.4	683	62	4.4	93
Nano-tetrapods	CdS/CdSe	13.8	722	42	4.2	96
NW array	CdS/CdSe	17.3	627	38	4.1	94
NW array	ZnSe/CdSe	11.4	810	43	4.0	143
NW array	ZnSe/CdSe	11.0	822	41	3.7	144
NW array	CdS/CdSe	12.6	685	42	3.6	135
NW array	CdS/CdSe	9.3	663	56	3.4	145
Hierarchical NR/NS	CdS/CdSe	10.7	610	50	3.2	137
NRs passivated with TiO_2	CdS/CdSe	9.9	610	52	3.1	146
NSs	CdS/CdSe	19.3	490	28	2.6	147
Hierarchical NWs array	CdS	7.3	700	31	1.6	148

Figure **1.3.2** shows some examples of different photoanodic architectures of ZnO utilized in DSSC [traces (A), (B), & (C)] and QDSSC devices [traces (D), (E) & (F)] with their power conversion efficiency values.

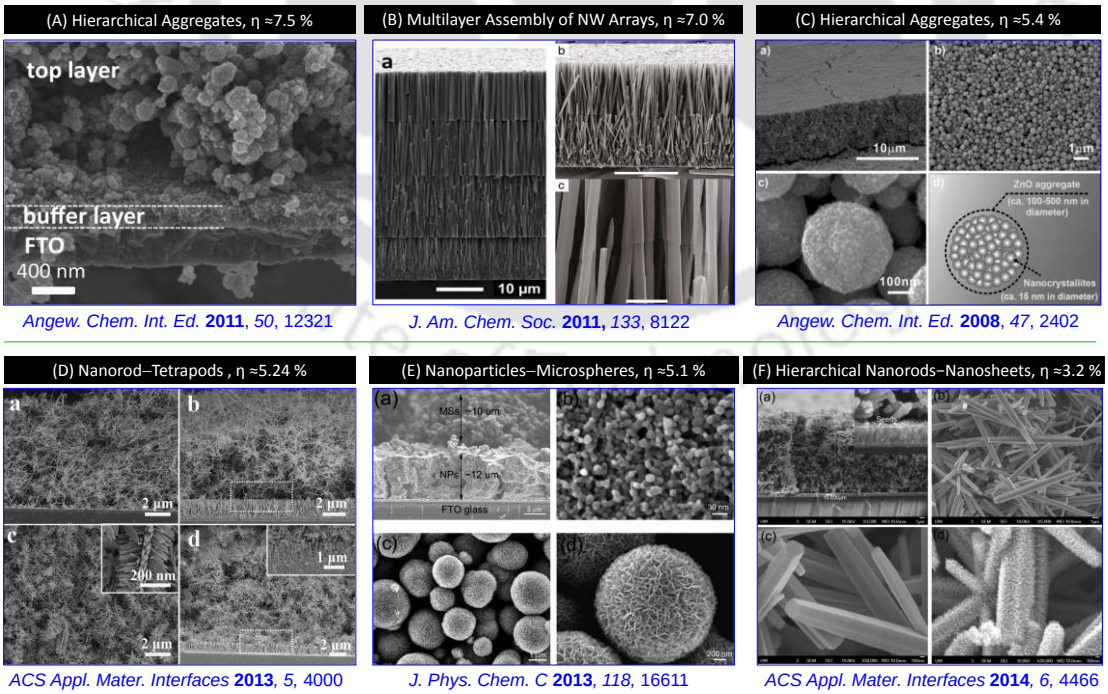

Figure 1.3.2 Some examples of morphological features of ZnO photoanodic architectures utilized in DSSC [traces (A), (B), & (C)] and QDSSC devices [traces (D), (E) & (F)]. Reprinted with permission.

1.4 CONCLUSIONS AND OUTLOOK

With the great efforts in rational design and synthesis of different morphologies of ZnO, optimization of the photoanodic architectures and surface passivation of ZnO nanostructures, power conversion efficiency (PCE, η) upto ~7.5 % for ZnO based DSSC device and 6.2 % for QDSSC device has been achieved. However, further development ZnO based photovoltaic devices is necessary to meet the requirements for their practical applications. In this context, different strategies can be integrated to improve the photovoltaic performance of ZnO based photoanodes. Coupling of ZnO with excellent light harvesting materials is a practical approach to enhance charge separation and minimize the electron loss in devices. Inhibition of recombination processes and electron interception can be achieved by utilization of core-shell structures and blocking layers. Besides, band engineering of ZnO by doping its crystal structure with suitable atoms can improve the photoinduced charge injection from dye molecules or QDs. All these strategies allow the creation of highly efficient multifunctional photoanodic materials for better light harvesting. Despite it is still challenging to optimize the all the expected key features in single photoanode for greater improvement in light harvesting ability. Implementation of maverick approaches for generation of new class of photoanodic architecture is highly desirable to bring a new hope for this field of research.

1.5 MOTIVATION AND OBJECTIVES OF THE PRESENT WORK

ZnO provides excellent bulk electron mobility as well as the richest family of nanostructures which has established it as the most promising photoanodic material to be used in DSSC and QDSSC devices. Ease of crystallization in wet chemical synthetic processes enable the use of easily available chemicals as structure directing agents for generation of novel morphologies with fascinating properties. Moreover, suitable band positions of ZnO allow to couple with most of other semiconductor materials enhanced light harvesting. Based on these intrinsic properties, we have intended to further improve the light harvesting ability of the ZnO based dye as well as semiconductor quantum dot sensitized solar cell devices. The objectives of the present work are as follows:

- Rational design and synthesis of ZnO morphologies using easily available and environmentally benign chemicals as the structure directing agents.
- Understanding the interactions between the ZnO growth units and the structure directing agents in respective reaction conditions for evaluation of mechanism of formation.
- Optimization of the reaction conditions for achieving anticipated size and shape of the ZnO morphologies.
- Design and fabrication of hybrid photoanodic architectures utilizing beneficial effects of different morphologies of ZnO.
- Coupling of ZnO with suitable photoactive materials based on band alignments for enhanced charge separation.
- Evaluation of photovoltaic properties of as synthesized materials or the photoanodic architectures in dye/quantum dot sensitized approaches.
- Understanding the photovoltaic performances of the materials for further improvements.

1.6 REFERENCES

(1) Kerr, R. A.; Service, R. F. *Science*, **2005**, *309*, 101.

(2) Potočnik, J. *Science*, **2007**, *315*, 810

(3) Ringpfeil, M. *Nature Biotechnol*, **2004**, *22*, 1077.

(4) Goldemberg, J. *Science*, **2007**, *315*, 808.

(5) Gross, R.; Leach, M.; Bauen, A. *Environ. Int.*, **2003**, *29*, 105.

(6) Hedberg, D.; Kullander, S.; Frank, H. *Ambio.*, **2010**, *39*, 1.

(7) Butler, D. *Nature*, **2008**, *454*, 558.

(8) Schiermeier, Q.; Tollefson, J.; Scully, T.; Witze, A.; Morton, O. *Nature*, **2008**, *454*, 816.

(9) Tyagi, V.V.; Rahim, N. A. A.; Rahim, N.A.; Selvaraj, J. A./L. *Renew. Sust. Energ. Rev.*, **2013**, *20*, 443.

(10) Chaar, L. El.; Lamonta, L.A.; Zein, N. El *Renew. Sust. Energ. Rev.*, **2011**, *15*, 2165.

(11) Bagnall, D. M.; Boreland, M. *Energy Policy*, **2008**, *36*, 4390.

(12) Zhao, J.; Wang, A.; Green, M.A.; Ferrazza, F. *Appl. Phys. Lett.*, **1998**, *73*, 1991.

(13) Green, M. A.; Emery, K.; Hishikawa, Y.; Warta, W.; Dunlop, E. D. *Prog. Photovolt: Res. Appl.*, **2012**, *20*, 12.

(14) Shah, A.; Torres, P.; Tscharner, R.; Wyrsch, N.; Keppner, H. *Science*, **1999**, *285*, 692.

(15) Bloss, W. H.; Pfisterer, F.; Schubert, M.; Walter, T. *Prog. Photovoltaics*, **1995**, *3*, 3.

(16) Kim, M. R.; Ma, D. *J. Phys. Chem. Lett.*, **2015**, *6*, 85.

(17) Shockley, W.; Queisser, H J. *J. Appl. Phys.*, **1961**, *32*, 510.

(18) Green, M. A. *Third Generation Photovoltaics: Advanced Solar Energy Conversion*; Springer-Verlag: Berlin, Heidelberg, **2003**.

(19) O'Regan, B.; Grätzel, M. *Nature*, **1991**, *353*, 737.

(20) Mathew, S.; Yella, A.; Gao, P.; Humphry-Baker, R.; Curchod, B. F. E.; Ashari-Astani, N.; Tavernelli, I.; Rothlisberger, U.; Nazeeruddin, M. K.; Grätzel, M. *Nat. Chem.*, **2014**, *6*, 242.

(21) Kamat, P. V. *J. Phys. Chem. Lett.*, **2013**, *4*, 908.

(22) Kamat, P. V.; Tvrdy, K.; Baker, D. R.; Radich, J. G. *Chem. Rev.*, **2010**, *110*, 6664.

(23) Zhao, K.; Pan, Z,; Mora-Seró I.; Cánovas, E.; Wang, H.; Song, Y.; Gong, X.; Wang, J.; Bonn, M.; Bisquert, J.; Zhong, X. *J. Am. Chem. Soc.*, **2015**, *137*, 5602.

(24) Hagfeldt, A.; Boschloo, G.; Sun, L.; Kloo L.; Pettersson, H. *Chem. Rev.*, **2010**, *110*, 6595.

(25) Toyoda, T.; Sano, T.; Nakajima, J.; Doi, S.; Fukumoto, S.; Ito, A.; Tohyama, T.; Yoshida, M.; Kanagawa, T.; Motohiro, T.; Shiga, T.; Higuchi, K.; Tanaka, K.; Takeda, Y.; Fukano, T.; Katoh, N.; Takeichi, A.; Takechi, K.; Shiozawa, M. *J. Photochem. Photobiol. A*, **2004**, *164*, 203.

(26) Kato, N.; Higuchi, K.; Tanaka, H.; Nakajima, J.; Sano, T.; Toyoda, T. *Sol. Energy Mater. Sol. Cells*, **2011**, *95*, 301.

(27) Harikisun, R.; Desilvestro, H. *Sol. Energy*, **2011**, *85*, 1179.

(28) Gratzel, M. *Nature*, **2001**, *414*, 338.

(29) Goldstein, J.; Yakupov, I.; Breen, B. *Sol. Energy Mater. Sol. Cells*, **2010**, *94*, 638.

(30) Baxter, J. B. *J. Vac. Sci. Technol., A*, **2012**, *30*, 020801.

(31) http://gcell.com/

(32) https://www.dyesol.com/

(33) http://www.interpv.net/market/market_view.asp?idx=634&part_code=05

(34) Desilvestro, H.; Bertoz, M.; Tulloch, S.; Tulloch, G. E. "*Packaging, Scale-up, and Commercialization of Dye Solar Cells*," edited by K. Kalyanasundaram (CRC Press, Lausanne, **2010**)

(35) Kalyanasundaram, K.; Ito, S.; Yanagida, S.; Uchida, S. "*Scale-up and Product-Development Studies of Dye-Sensitized Solar Cells in Asia and Europe*," edited by K. Kalyanasundaram (CRC Press, Lausanne, **2010**)

(36) Green, M. A.; Emery, K.; Hishikawa, Y.; Warta, W. *Prog. Photovoltaics*, **2011**, *19*, 84.

(37) Kashif, M. K.; Nippe, M.; Duffy, N. W.; Forsyth, C. M.; Chang, C. J.; Long, J. R.; Spiccia, L.; Bach, U. *Angew. Chem. Int. Ed.* **2013**, *52*, 5527.

(38) Mora-Seró, I.; Giménez, S.; Fabregat-Santiago, F.; Gómez, R.; Shen, Q.; Toyoda, T.; Bisquert, J. *Acc. Chem. Res*, **2009**, *42*, 1848.

(39) Ramakrishna, G.; Jose, D. A.; Kumar, D. K.; Das, A.; Palit, D. K.; Ghosh, H. N. *J. Phys. Chem. B*, **2005**, *109*, 15445.

(40) Kuang, D.; Ito, S.; Wenger, B.; Klein, C.; Moser, J.-E.; Humphry-Baker, R.; Zakeeruddin, S. M.; Grätzel, M. *J. Am. Chem. Soc.*, **2006**, *128*, 4146.

(41) Benko, G.; Kallioinen, J.; Korppi-Tommola, J. E. I.; Yartsev, A. P.;Sundstrom, V. *J. Am. Chem. Soc.*, **2002**, *124*, 489.

(42) Haque, S. A.; Palomares, E.; Cho, B. M.; Green, A. N. M.; Hirata, N.; Klug, D. R.; Durrant, J. R. *J. Am. Chem. Soc.*, **2005**, *127*, 3456.

(43) Hodes, G. *J. Phys. Chem. C*, **2008**, *112*, 17778.

(44) Kietzmann, R.; Willig, F.; Weller, H.; Vogel, R.; Nath, D. N.; Eichberger, R.; Liska, P.; Lehnert, J. *Mol. Cryst. Liq. Cryst.*, **1991**, *194*, 169.

(45) Evans, J. E.; Springer, K. W.; Zhang, J. Z. *J. Chem. Phys.*, **1994**, *101*, 6222.

(46) Shalom, M.; Dor, S.; Rühle, S.; Grinis, L.; Zaban, A. *J. Phys. Chem. C*, **2009**, *113*, 3895.

(47) Hod, I.; González-Pedro, V.; Tachan, Z.; Fabregat-Santiago, F.; Mora-Seró, I.; Bisquert, J.; Zaban, A. *J. Phys. Chem. Lett.*, **2011**, *2*, 3032.

(48) Zhao, K.; Pan, Z.; Zhong, X. *J. Phys. Chem. Lett.*, **2016**, *7*, 406.

(49) Kamat, P. V. *Acc. Chem. Res.*, **2012**, *45*, 1906.

(50) Robel, I.; Subramanian, V.; Kuno, M.; Kamat, P. V. *J. Am. Chem. Soc.*, **2006**, *128*, 2385.

(51) Santra, P.; Kamat, P. V. *J. Am. Chem. Soc.*, **2013**, *135*, 877.

(52) Barea, E.; Shalom, M.; Giménez, S.; Hod, I.; Mora-Seró, I.; Zaban, A.; Bisquert, J. *J. Am. Chem. Soc.*, **2010**, *132*, 6834.

(53) de la Fuente, M.; Sanchez, R.; González-Pedro, V.; Boix, P.; Mhaisalkar, S.; Rincón, M.; Bisquert, J.; Mora-Seró, I. *J. Phys. Chem. Lett.*, **2013**, *4*, 1519.

(54) O'Regan, B.; Moser, J.; Anderson, M.; Grätzel, M. *J. Phys. Chem.*, **1990**, *94*, 8720.

(55) Solbrand, A.; Lindström, H.; Rensmo, H.; Hagfeldt, A.; Lindquist, S. E.; Södergren, S. *J. Phys. Chem. B*, **1997**, *101*, 2514.

(56) J. Bisquert, D. Cahen, G. Hodes, S. Ruhle, and A. Zaban, *J. Phys. Chem. B*, **2004**, *108*, 8106.

(57) Kavan, L.; Grätzel, M. *Electrochim. Acta*, **1995**, *40*, 643.

(58) Cameron, P. J.; Peter, L. M. *J. Phys. Chem. B*, **2003**, *107*, 14394.

(59) Ito, S.; Liska, P.; Comte, P.; Charvet, R. L.; Pechy, P.; Bach, U.; Schmidt-Mende, L.; Zakeeruddin, S. M.; Kay, A.; Nazeeruddin, M. K.; Grätzel, M. *Chem. Commun.*, **2005**, 4351.

(60) Chappel, S.; Chen, S.-G.; Zaban, A. *Langmuir*, **2002**, *18*, 3336.

(61) Kay, A.; Grätzel, M. *Chem. Mater.*, **2002**, *14*, 2930.

(62) Concina, I.; Vomiero, A. *Small*, **2015**, *11*, 1744.

(63) Tian, J.; Cao, G. *J. Phys. Chem. Lett.*, **2015**, *6*, 1859.

(64) Rensmo, H.; Keis, K.; Lindström, H.; Södergren, S.; Solbrand, A.; Hagfeldt, A.; Lindquist, S.-E.; Wang, L. N.; Muhammed, M. *J. Phys. Chem. B*, **1997**, *101*, 2598.

(65) Leschkies, K. S.; Divakar, R.; Basu, J.; Enache-Pommer, E.; Boercker, J. E.; Carter, C. B.; Kortshagen, U. R.; Norris, D. J.; Aydil, E. S. *Nano Lett.*, **2007**, *7*, 1793.

(66) Snaith, H. J.; Ducati, C. *Nano Lett.*, **2010**, *10*, 1259.

(67) Hossain, Md. A.; Jennings, J. R.; Koh, Z. Y.; Wang, Q. *ACS Nano*, **2011**, *5*, 3172.

(68) Sayama, K.; Sugihara, H.; Arakawa, H. *Chem. Mater.*, **1998**, *10*, 3825.

(69) Kang, J. H.; Myung, Y.; Choi, J. W.; Jang, D. M.; Lee, C. W; Park, J.; Cha, E. H. *J. Mater. Chem.*, **2012**, *22*, 8413.

(70) Burnside, S.; Moser, J.-E.; Brooks, K.; Gratzel, M.; Cahen, D. *J. Phys. Chem. B*, **1999**, *103*, 9328.

(71) Anta, J. A.; Guillén, E.; Tena-Zaera, R *J. Phys. Chem. C*, **2012**, *116*, 11413.

(72) Özgür, Ü.; Alivov, Ya. I.; Liu, C.; Teke, A.; Reshchikov, M. A.; Doğan, S.; Avrutin, V.; Cho, S.-J.; Morkoç, H. *J. Appl. Phys.*, **2005**, *98*, 041301.

(73) Diebold, U. *Surf. Sci. Rep.*, **2003**, *48*, 53.

(74) Scanlon, D. O.; Dunnill, C. W.; Buckeridge, J.; Shevlin, S. A.; Logsdail, A. J.; Woodley, S. M.; Catlow, C. R. A.; Powell, M. J.; Palgrave, R. G.; Parkin, I. P.; Watson, G. W.; Keal, T. W.; Walsh, P. S. A.; Sokol, A. A. *Nat. Mater.*, **2013**, *12*, 798.

(75) Batzill, M.; Diebold, U. *Prog. Surf. Sci.*, **2005**, *79*, 47.

(76) Matar, S. F.; Campet, G.; Subramanian, M. A. *Prog. Solid State Chem.*, **2011**, 39, 70.

(77) Tvrdy, K.; Frantsuzov, P. A.; Kamat, P. V. *Proc. Natl. Acad. Sci. USA.*, **2011**, *108*, 29.

(78) Oskam, G.; Hu, Z.; Penn, R. L.; Pesika, N.; Searson, P. C. *Phys. Rev. E*, **2002**, *66*, 011403.

(79) Button, K. J.; Fonstad, C. G.; Dreybrodt, W. *Phys. Rev. B*, **1971**, *4*, 4539.

(80) Jarzebski, Z. M.; Marton, J. P. *J. Electrochem. Soc.*, **1976**, *123*, 299C.

(81) Tang, H.; Prasad, K.; Sanjinès, R.; Schmid, P. E.; Lévy, F. *J. Appl. Phys.* **1994**, *75*, 2042.

(82) Tiwana, P.; Docampo, P.; Johnston, M. B.; Snaith, H. J.; Herz, L. M. *ACS Nano*, **2011**, *5*, 5158.

(83) Young, K. F.; Frederikse, H. P. R. *J. Phys. Chem. Ref. Data*, **1973**, *2*, 313.

(84) Yuan, G.-D.; Zhang, W.-J.; Jie, J.-S.; Fan, X.; Tang, J.-X.; Shafiq, I.; Ye, Z.-Z.; Lee, C.-S.; Lee, S.-T. *Adv. Mater.* **2008**, *20*, 168.

(85) Xu, C. X.; Sun, X. W.; Chen, B. J. *Appl. Phys. Lett.* **2004**, *84*, 1540.

(86) Wang, R.-C.; Liu, C.-P.; Huang, J.-L.; Chen, S.-J. *Appl. Phys. Lett.* **2006**, *88*, 023111.

(87) Wang, Z. L. *Mater. Today*, **2004**, *7*, 26.

(88) Klingshirn, C. *ChemPhysChem*, **2007**, *8*, 782.

(89) Chen, H.-Y.; Kuang, D.-B.; Su, C.-Y. *J. Mater. Chem.*, **2012**, *22*, 15475.

(90) Zhang, Q.; Cao, G. *Nano Today*, **2011**, *6*, 91.

(91) Zhang, Q.; Dandeneau, C. S.; Zhou, X.; Cao, G. *Adv. Mater.*, **2009**, *21*, 4087.

(92) Law, M.; Greene, L. E.; Johnson, J. C.; Saykally, R.; Yang, P. *Nat. Mater.*, **2005**, *4*, 455.

(93) Li, C.; Yang, L.; Xiao, J.; Wu, Y.-C.; Søndergaard, M.; Luo, Y.; Li, D.; Meng, Q.; Iversen, B. B. *Phys. Chem. Chem. Phys.*, **2013**, *15*, 8710.

(94) Seol, M.; Kim, H.; Taka, Y.; Yong, K. *Chem. Commun.*, **2010**, *46*, 5521.

(95) Luo, L.; Lv, G.; Li, B.; Hu, X.; Jin, L.; Wang, J.; Tang, Y. *Thin Solid Films*, **2010**, *518*, 5146.

(96) Cheng, H. M.; Huang, K. Y.; Lee, K. M.; Yu, P.; Lin, S. C.; Huang, J. H.; Wu, C. G.; Tang, J. *Phys. Chem. Chem. Phys.* **2012**, *14*, 13539.

(97) Lin, C. Y.; Lai, Y. H.; Chen, H. W.; Chen, J. G.; Kung, C. W.; Vittal, R.; Ho, K. C. *Energy Environ. Sci.*, **2011**, *4*, 3448.

(98) Zhang, Q. F.; Chou, T. R.; Russo, B.; Jenekhe, S. A.; Cao, G. Z. *Angew. Chem., Int. Ed.*, **2008**, *47*, 2402.

(99) Jiang, C. Y.; Sun, X. W.; Lo, G. Q.; Kwong, D. L. *Appl. Phys. Lett.*, **2007**, *90*, 263501.

(100) Dong, Z.; Lai, X.; Halpert, J. E.; Yang, N.; Yi, L.; Zhai, J.; Wang, D.; Tang, Z.; Jiang, L. *Adv. Mater.*, **2012**, *24*, 1046.

(101) Memarian, N.; Concina, I.; Braga, A.; Rozati, S. M.; Vomiero, A.; Sberveglieri, G. *Angew. Chem., Int. Ed.*, **2011**, *50*, 12321.

(102) Saito, M.; Fujihara, S. *Energy Environ. Sci.*, **2008**, *1*, 280.

(103) Chen, W.; Qiu, Y.; Zhong, Y.; Wong, K. S.; Yang, S. *J. Phys. Chem. A*, **2010**, *114*, 3127.

(104) Park, K.; Zhang, Q.; Garcia, B. B.; Zhou, X.; Jeong, Y.-H.; Cao, G. *Adv. Mater.*, **2010**, *22*, 2329.

(105) Zhang, Q.; Dandeneau, C. S.; Candelaria, S.; Liu, D.; Garcia, B. B.; Zhou, X.; Jeong, Y.-H.; Cao, G. *Chem. Mater.*, **2010**, *22*, 2427.

(106) Yoshida, T.; Zhang, J. B.; Komatsu, D.; Sawatani, S.; Minoura, H.; Pauporte, T.; Lincot, D.; Oekermann, T.; Schlettwein, D.; Tada, H.; Wohrle, D.; Funabiki, K.; Matsui, M.; Miura, H.; Yanagi, H. *Adv. Funct. Mater.*, **2009**, *19*, 17.

(107) Sheng, X.; Zhao, Y.; Zhai, J.; Jiang, L.; Zhu, D. *Appl. Phys. A: Mater. Sci. Process.*, **2007**, *87*, 715.

(108) Ambade, S. B.; Mane, R. S.; Han, S.-H.; Lee, S.-H.; Sung, M.-M.; Joo, O.-S. *J. Photochem. Photobiol., A*, **2011**, *222*, 366.

(109) Cheng, H.-M.; Hsieh, W.-F. *Energy Environ. Sci.*, **2010**, *3*, 442.

(110) Ueno, S.; Fujihara, S. *Electrochim. Acta*, **2011**, *56*, 2906.

(111) Chiu, W. H.; Lee, C. H.; Cheng, H. M.; Lin, H. F.; Liao, S. C.; Wu, J. M.; Hsieh, W. F. *Energy Environ. Sci.*, **2009**, *2*, 694.

(112) Xu, F.; Dai, M.; Lu, Y. N.; Sun, L. T. *J. Phys. Chem. C*, **2010**, *114*, 2776.

(113) Ranga Rao, A.; Dutta, V. *Nanotechnology*, **2008**, *19*, 445712.

(114) Yodyingyong, S.; Zhang, Q. F.; Park, K.; Dandeneau, C. S.; Zhou, X. Y.; Triampo, D.; Cao, G. Z. *Appl. Phys. Lett.* **2010**, *96*, 073115.

(115) Guérin, V.-M.; Pauporté, T. *Energy Environ. Sci.*, **2011**, *4*, 2971.

(116) Pérez-Hernández, G.; Vega-Poot, A.; Pérez-Juárez, I.; Camacho, J. M.; Arés, O.; Rejón, V.; Peña, J. L.; Oskam, G. *Sol. Energy Mater. Sol. Cells.*, **2012**, *100*, 21.

(117) Ko, S. H.; Lee, D.; Kang, H. W.; Nam, K. H.; Yeo, J. Y.; Hong, S. J.; Grigoropoulos, C. P.; Sung, H. J. *Nano Lett.*, **2011**, *11*, 666.

(118) Chen, G.; Zheng, K.; Mo, X.; Sun, D.; Meng, Q.; Chen, G. *Mater. Lett.*, **2010**, *64*, 1336.

(119) Xie, Y.; Joshi, P.; Darling, S. B.; Chen, Q.; Zhang, T.; Galipeau, D.; Qiao, Q. *J. Phys. Chem. C*, **2010**, *114*, 17880.

(120) Xu, C. K.; Shin, P.; Cao, L. L.; Gao, D. *J. Phys. Chem. C*, **2010**, *114*, 125.

(121) Martinson, A. B. F.; Elam, J. W.; Hupp, J. T.; Pellin, M. J. *Nano Lett.*, **2007**, *7*, 2183.

(122) Mclaren, A.; Valdes-Solis, T.; Li, G.; Tsang, S. C. *J. Am. Chem. Soc.*, **2009**, *131*, 12540.

(123) Meagley, K. L.; Garcia, S. P. *Cryst. Growth Des.*, **2011**, *12*, 707.

(124) Li, F.; Ding, Y.; Gao, P.; Xin, X.; Wang, L. Z. *Angew. Chem.*, **2004**, *116*, 5350.

(125) Changb, P. R.; Yua, J.; Ma, X. *Carbohydr. Polym.*, **2011**, *83*, 1016.

(126) Kavitha, M. K.; John, H.; Gopinath, P. *Mater. Res. Bull.*, **2014**, *49*, 132.

(127) Wang, A. J.; Liao, Q. C.; Feng, J. J.; Zhang, P. P.; Li, A. Q.; Wang, J. J. *CrystEngComm* **2012**, *14*, 256.

(128) Tseng, Y. H.; Lin, H. Y.; Liu, M. H.; Chen, Y. F.; Mou, C. Y. *J. Phys. Chem. C*, **2009**, *113*, 18053.

(129) Yin, J.; Lu, Q.; Yu, Z; Wang, J.; Pang, H.; Gao, F. *Cryst. Growth Des.*, **2010**, *10*, 40.

(130) Horiuchi, T.; Miura, H.; Sumioka, K.; Uchida, S. *J. Am. Chem. Soc.*, **2004**, *126*, 12218.

(131) Keis, K.; Lindgren, J.; Lindquist, S. E.; Hagfeldt, A. *Langmuir*, **2000**, *16*, 4688.

(132) Leatherdale, C. A.; Woo, W. K.; Mikulec, F. V.; Bawendi, M. G. *J. Phys. Chem. B*, **2002**, *106*, 7619.

(133) Yu, W. W.; Qu, L.; Guo, W.; Peng, X. *Chem. Mater.*, **2003**, *15*, 2854.

(134) Trinh, M. T.; Houtepen, A. J.; Schins, J. M.; Hanrath, T.; Piris, J.; Knulst, W.; Goossens, A. P. L. M.; Siebbeles, L. D. A. *Nano Lett.*, **2008**, *8*, 1713.

(135) Seol, M; Ramasamy, E.; Lee, J; Yong, K, *J. Phys. Chem. C*, **2011**, *115*, 22018.

(136) Yan, K.; Zhang, L.; Qiu, J.; Qiu, Y.; Zhu, Z.; Wang, J.; Yang, S. *J. Am. Chem. Soc.*, **2013**, *135*, 9531.

(137) Tian, J; Uchaker, E.; Zhang, Q.; Cao. G. *ACS Appl. Mater. Interfaces*, **2014**, *6*, 4466.

(138) Zhu, Z.; Qiu, J.; Yan, K.; Yang, S. *ACS Appl. Mater. Interfaces*, **2013**, *5*, 4000.

(139) Tian, J.; Lv, L.; Wang, X.; Fei, C.; Liu, X. Zhao, Z.; Wang, Y.; Cao, G. *J. Phys. Chem. C*, **2014**, *118*, 16611.

(140) Xu, J.; Yang, X.; Wang, H.; Chen, X.; Luan, C.; Xu, Z.; Lu, Z.; Roy, V. A. L.; Zhang, W.; Lee, C.-S. *Nano Lett.*, **2011**, *11*, 4138.

(141) Tian, J.; Zhang, Q.; Uchaker, E.; Gao, R.; Qu, X.; Zhang, S.; Cao, G. *Energy Environ. Sci.*, **2013**, *6*, 3542.

(142) Xu, J.; Yang, X.; Yang, Q.-D.; Wong, T.-L.; Lee, S.-T.; Zhang, W.-J.; Lee, C.-S. *J. Mater. Chem.* **2012**, *22*, 13374.

(143) Xu, J.; Yang, X.; Wong, T.-L.; Lee, C.-S. *Nanoscale*, **2012**, *4*, 6537.

(144) Xu, J.; Yang, X.; Yang, Q.-D.; Wong, T.-L.; Lee. C.-S. *J. Phys. Chem. C*, **2012**, *116*, 19718.

(145) Zhang, R.; Luo, Q.-P.; Chen, H.-Y.; Yu, X.-Y.; Kuang, D.-B.; Su, C.-Y. *ChemPhysChem*, **2012**, *13*, 1435.

(146) Tian, J.; Zhang, Q.; Uchaker, E.; Liang, Z.; Gao, R.; Qu, X.; Zhang, S.; Cao, G. *J. Mater. Chem. A*, **2013**, *1*, 6770.

(147) Hou, Q.; Zhu, L.; Chen, H.; Liu, H.; Li, W. *Electrochim. Acta*, **2013**, *94*, 72.

(148) Chen, X.-Y.; Ling, T.; Du, X.-W. *Nanoscale*, **2012**, *4*, 5602.

CHAPTER 2

Experimental

This chapter describes basic instrumentation techniques and methodologies used for material characterization, fabrication of dye-/ semiconductor QD-sensitized solar cells emphasizing the ZnO based photoanode preparation. Characterization technique of the devices using basic and specific instrumental techniques/methods such as solar simulator (Newport Sol3A) and incident photon-to-current analyzer (IQE 200) are included. A short introduction to photovoltaic performance parameters and electrochemical impedance spectroscopy (EIS) measurement is also given.

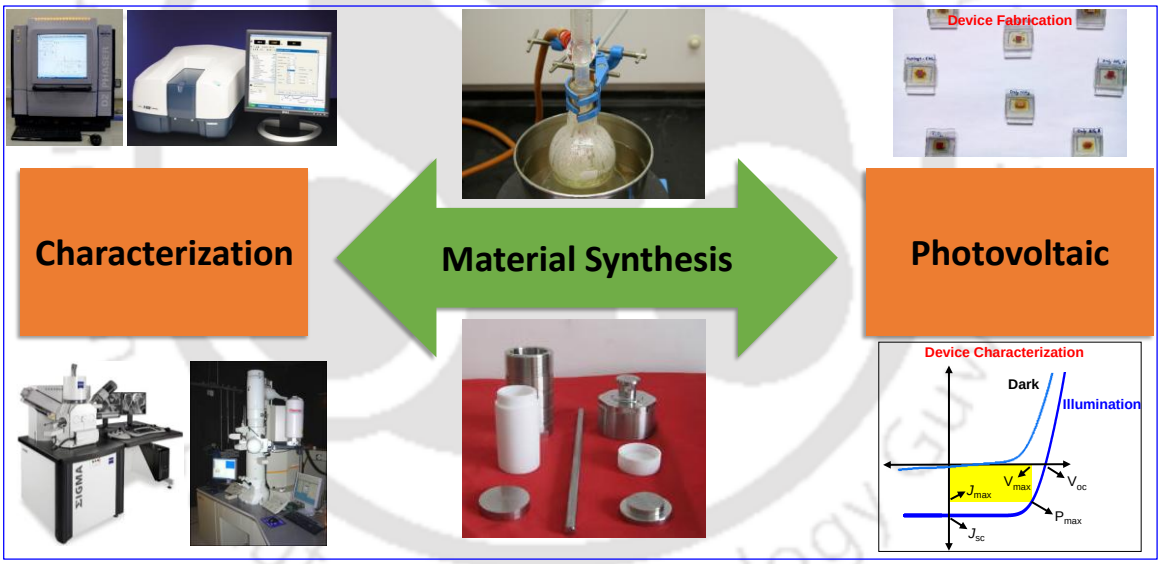

2.1 INTRODUCTION

ZnO is endowed with excellent bulk electron mobility and anisotropic growth of the crystal planes which enable rational design of diverse nanostructured morphologies having unique physical, electrical and optical properties.[1–3] Rational design and synthesis of different morphological features of ZnO involve utilization of a range of chemicals as structure directing agents and additives in different reaction conditions. In this Chapter, a list of all the materials employed at different stages of the investigation and basic characterization techniques for the as synthesized materials are given. General fabrication procedures of dye sensitized solar cell (DSSC) and quantum dot sensitized solar cell (QDSSC) devices are also included. Characterization techniques of the fabricated photovoltaic devices and solar cell performance parameters are discussed in detail.

2.2 EXPERIMENTAL METODS

2.2.1 MATERIALS AND CHEMICALS USED

Zinc nitrate hexahydrate (Merck), polyethylene glycol (PEG) 200 (Merck), zinc acetate dihydrate (Merck), 2-methoxyethanol (Merck), ethanolamine (Merck), cadmium nitrate tetrahydrate (Merck), hexamethylenetetramine (Merck), sodium sulphide (Merck), chloroplatinic acid (Sigma Aldrich), a triblock copolymer poly(ethylene glycol)-block-poly(propylene glycol)-block-poly(ethyleneglycol) or PEG-PPG-PEG (Sigma Aldrich), ethyl cellulose (Himedia; ethoxy content, 48%), cetyltrimethylammonium bromide (Rankem), zinc chloride (Merck), sodium hydroxide (Himedia), sodium sulfide (Merck), cadmium acetate (Merck), selenium powder (Merck), sodium sulfite (Merck), ammonium hydroxide (Merck), terpineol (Himedia), chloroplatinic acid (Sigma-Aldrich), 1-butanol (Merck), methanol (Merck), and ethanol (TMEDA), urea (from Loba Chemie), sulfur powder (Merck), potassium chloride, hydrochloric acid (Merck), 2-propanol (Merck), acetone (Merck), sodium alginate (Himedia), ammonium hydroxide (Merck), lithium iodide (Sigma Aldrich), iodine (Merck), 4-tert-butylpyridine (Himedia), acetonitrile (HPLC grade, Merck), valeronitrile (Sigma Aldrich), 1-butyl 3-methyl imidazolium iodide (Sigma Aldrich), sealant material (Dyesol), tin dichloride dihydrate (Rankem), oxalic acid (Merck), hydrazine monohydrate (Loba chemie), magnesium dichloride hexahydrate (Merck), guanidium thiocyanate (Aldrich), cobalt chloride hexahydrate (Merck), 2,2′- bipyridyl

(bpy, Aldrich), tetrabutyl ammonium hexafluoro phosphate (SigmaAldrich), potassium hexafluoro-phosphate (Aldrich), FTO (sheet resistance 8-12 Ω cm^{-2} ,Aldrich, USA) are purchased and used without further purification.

2.2.2 CHARACTERIZATION OF MATERIALS AND DEVICES

The synthesized compounds (photoanode materials, sensitizers etc.) and fabricated solar cells are characterized using a number of techniques. The instrumental methods/tools used in the present investigation include:

(1) Powder X-ray diffraction (PXRD) using Bruker D2 PHASER X-ray diffractometer with Cu–Kα X-ray generator (λ = 1.54 Å) and operating voltage of 30 kV and current 30kA.

(2) Diffuse reflectance UV-visible spectra (DRS) using a JASCO Model V-650 spectrophotometer equipped with a 150 mm integrating sphere and $BaSO_4$ as an internal standard.

(3) Steady state photoluminescence (PL) measurements are carried out using a Horiba−Jobin Yvon Fluoromax 4C spectrophotometer

(4) Time-resolved photoluminescence (TRPL) measurements are performed using a LifeSpec II Edinburgh instrument having a lamp with frequency 5MHz and Nd:YAG lasers of different excitation wavelengths.

(5) Brunauer–Emmett–Teller (BET) surface area analysis using Beckman-Coulter SA 3100 N_2 adsorption apparatus.

(6) Field emission scanning electron microscope (FESEM) images using a Zeiss (Gemini) instrument operated at the voltage of 3 kV−10kV.

(7) Energy-dispersive X-ray spectroscopy (EDS) analysis using INCA, Oxford instruments.

(8) The transmission electron microscopy (TEM) measurements using a JEOL JEM 2100 microscope with an operating voltage of 200 kV.

(9) Fourier transformed infrared spectroscopy (FT-IR) using a Perkin Elmer FT-IR instrument.

(10) Cyclic Voltammetry (CV) using CH instruments, Model CH 1600E.

(11) Spin Coating using SPIN-150 spin coater.

(12) Film/Layer thickness measurements using a Veeco Dektak 150 surface profilometer.

(13) For solar light illumination of the fabricated photovoltaic devices, Newport ORIEL Sol3A solar simulator having AM 1.5G artificial solar simulator of power 100 mW/cm^2 and of the intensity of 450 W is used. Before illumination it is calibrated with a standard Si photovoltaic cell.

(14) Keithley 2400 sourcemeter is used to probe the current density (J_{sc}) and voltage (V_{oc}) output from the fabricated devices.

(15) Incident photon to current conversion efficiency (IPCE) plots of the devices are recorded using a Newport ORIEL IQE-200 instrument fitted with a 250 W quartz tungsten halogen lamp calibrated by standard Si and Ge diodes.

(16) Electrochemical impedance spectroscopic (EIS) analyses of the devices are performed using an electrochemical work station provided by CH instruments, Model CH1600E.

2.2.3 GENERAL FABRICATION PROCESSES OF DSSC AND QDSSC

(i) Photoanode Preparation

(1) A homogeneous paste of the semiconductor oxide (e.g., ZnO, SnO_2) is prepared using binder material, i.e., PEG–PPG–PEG and terpineol. Prior to the addition of binder materials, the semiconductor powder is ultra-sonicated in ethanol for 1 h to minimize the agglomerations. The steps are shown pictorially in figure **2.2.1**, [digital pictures (1), (2), and (3)].

(2) Fluorine doped Tin Oxide (FTO) coated glass substrate is cut into specific dimension [(2×2) cm^2, 2 slides for 1 cell)]. Device area is fixed by using scotch tape mask as shown in image (4), figure **2.2.1**.

(3) Scotch tape is then removed and the semiconductor oxide films are dried at 120 ºC in a hot air oven followed by calcination at 520 ºC temperatures in a muffle furnace to remove the binder materials. Metal oxide coated FTO substrates are thus obtained as shown in image (5), figure **2.2.1**.

(4) As prepared films are sensitized with sensitizer materials such as dye molecules or semiconductor quantum dot (QD) particles. For example, CdS/CdSe QDs co-sensitized photoanode is shown in image (6) in figure **2.2.1**.

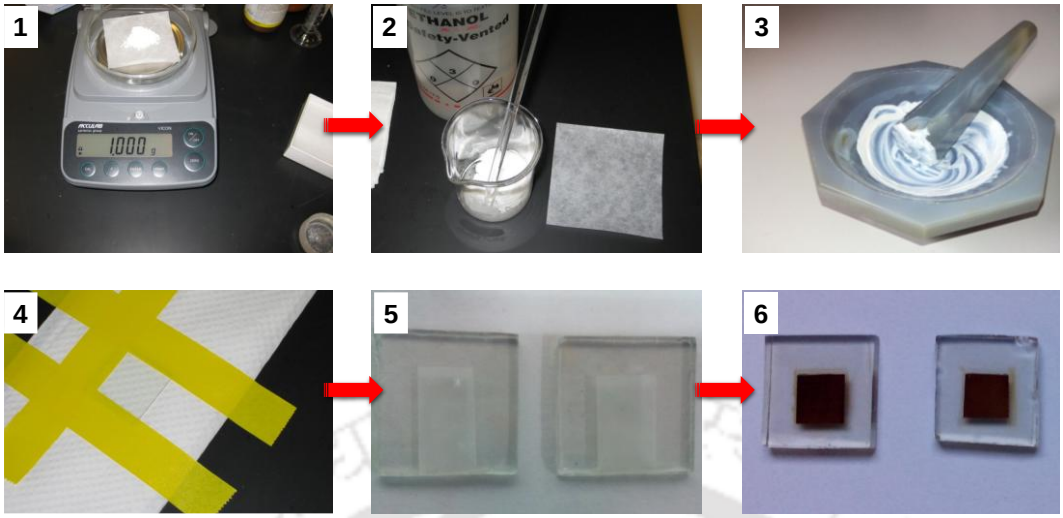

Figure 2.2.1 Pictorial presentation of *step-by-step* fabrication process of photoanodes.

(ii) Sensitization of Photoanodes

(1) To sensitize with dye molecules, as prepared photoanodes are immersed in the dye solution of particular concentration from 6 h to 12 h depending on the sensitizer scaffolds.

(2) In this thesis work, CdS and CdSe QDs are used as the sensitizer for fabrication of QDSSC. For sensitization of CdS QDs successive ionic layer adsorption and reaction (SILAR) method is employed while chemical bath deposition (CBD) method is used to sensitize with CdSe QDs as shown in figure **2.2.2**.

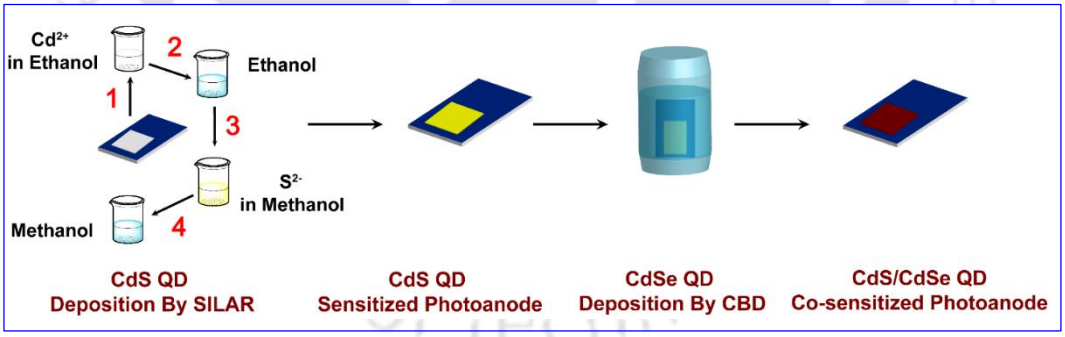

Figure 2.2.2 Schematic of sensitization processes of the photoanodes with CdS QDs and CdSe QDs.

In SILAR method, first the electrodes are dipped into an ethanolic solution of $Cd(NO_3)_2$. $4H_2O$ (0.5 M) for 5 min, rinsed with ethanol, and dried under hot air blow. Again they are dipped into a Na_2S (0.5 M) solution in methanol for 5 min, rinsed with methanol and dried. The amount of CdS grown onto the ZnO system is controlled by the number of repeated SILAR cycles. In CBD method, the metal oxide coated substrate or CdS QD sensitized

substrate is dipped into a solution containing both the cationic (Cd^{2+}) and anionic precursors (Se^{2-}) ions, in presence of a base, i.e., NH_4OH of particular concentration. The solution in the chemical bath is heated at 95 °C for 3 h and allowed to cool normally to room temperature. The CdSe QD sensitized photoanodes are taken out from the chemical bath and washed thoroughly with ethanol several times. Then the films are dried under hot air blow to obtain final photoanode.

(iii) Counter Electrode Preparation

(1) The Pt counter electrodes are prepared by spin coating a solution of chloroplatinic acid on a pre-cleaned FTO substrate followed by the calcination at 450 °C for (heating ramp of 5 °C /min) 30 min in a muffle furnace and cooled down to room temperature naturally. Figure **2.2.3** represents *step-by-step* preparation processes of counter electrode depicting digital pictures of H_2PtCl_6 solution, spin coater and as prepared Pt coated FTO substrates.

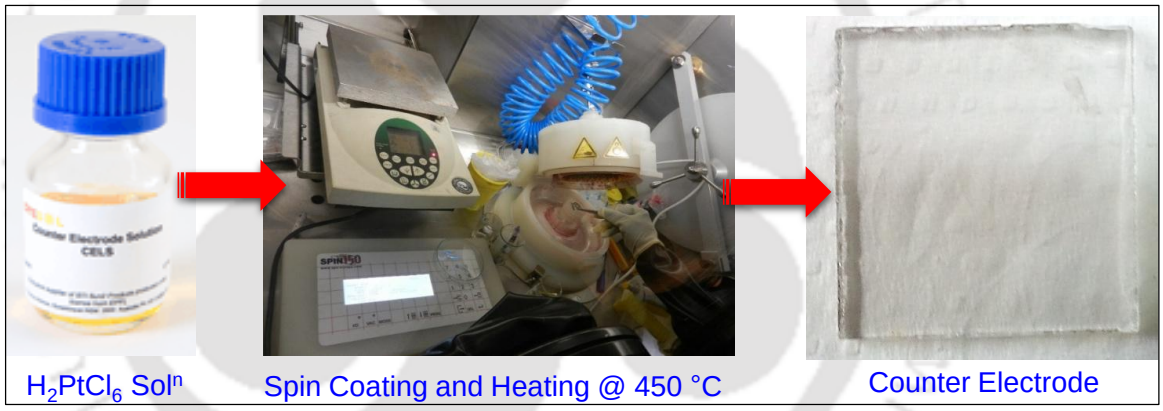

Figure 2.2.3 Pictorial presentation of step-by-step counter electrode preparation process.

(2) After that, two holes are made in the counter electrode for electrolyte filling using a glass driller.

(iv) Assembling of Devices

Finally, photovoltaic devices are fabricated by sandwiching the as prepared photoanode and counter electrode. Low-temperature thermoplastic sealant (thickness ~50 µm) is employed in between the two electrodes and heated to 90 °C to seal the device. Devices are allowed cool down to room temperature naturally and electrolyte solution (20 µL) is added through the two holes in the counter electrode to complete the device. The devices are now ready for measurement as shown in figure **2.2.4**.

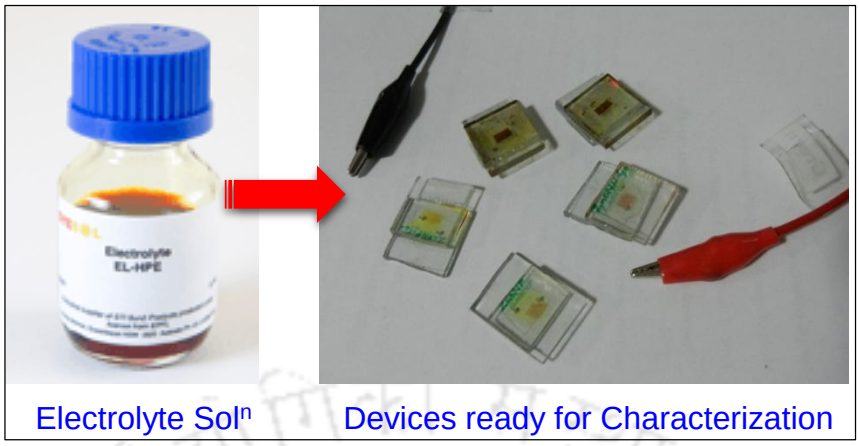

Figure 2.2.4 Digital pictures of the (I^-/I_3^-) electrolyte solution and as fabricated devices in our laboratory.

2.2.4 EVALUATION OF SOLAR CELL PERFORMANCE

(1) The devices are connected to Keithley 2400 SourceMeter using connecting cables.

(2) In dark condition, dark current values were measured by sweeping the voltage in the range of –1 V to +1 V across the photovoltaic devices.

(3) Simulated solar light is then shined on the fabricated devices and step 2 has been repeated. This step has been repeated for 5 times to check the consistency.

(4) Current *vs.* Voltage (*I*–*V*) graphs of the devices are plotted by taking current values as abscissa and voltage as ordinate.

(5) Values of photovoltaic parameters such as current density (J_{sc}), open circuit voltage (V_{oc}), Fill Factor (FF), maximum power output (P_{max}) and Power Conversion Efficiency (PCE, η) are obtained and calculated from the (*I*–*V*) plot. Please note that, short-circuit current density (J_{sc}) is typically reported instead of short circuit current (I_{sc}) for all the fabricated devices in order to allow comparison between devices whose dimensions may vary.

$$J_{sc} = \frac{I_{sc}}{Active\ area}$$

2.2.5 SOLAR CELL PERFORMANCE PARAMETERS

Photovoltaic performance of any solar cell can be defined by the following physical parameters; (1) short-circuit current (J_{sc}), (2) open-circuit voltage (V_{oc}), (3) fill factor (FF), (4) power conversion efficiency (PCE, η) and (5) incident photon to current conversion efficiency (IPCE). The performance parameters of a solar cell are evaluated from its corresponding photocurrent-voltage (*I*–*V*) curve. A schematic representation of the (*I*–*V*) curve of a solar cell is

shown in figure **2.2.5 (A)**. (*I–V*) curve of a solar cell gives the information regarding how a photovoltaic device is behaving with the irradiation of light.

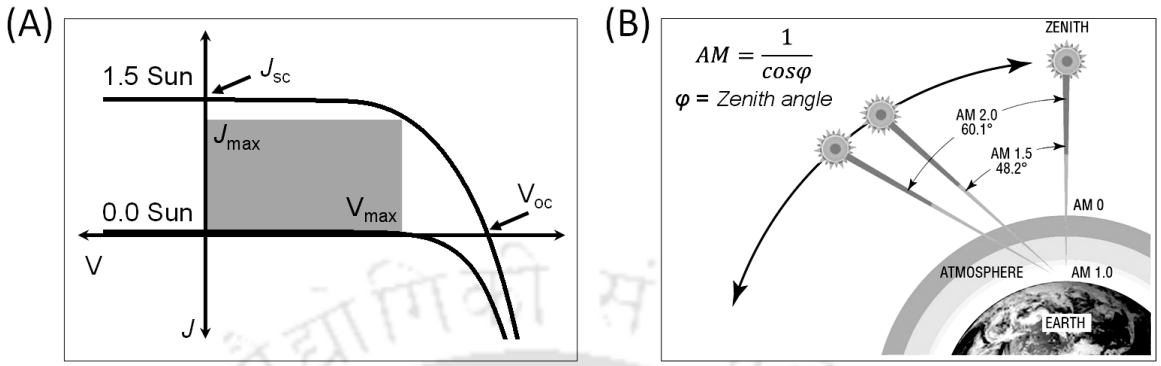

Figure 2.2.5 (A) Schematic of typical current–voltage (*J–V*) curve of a solar cell in dark condition and under AM 1.5 G simulated solar irradiation. **(B)** Path length of solar irradiation in air mass (AM) unit showing the zenith angle (φ); (source: https://teknologisurya.wordpress.com).

To compare the characteristics of solar cells characterized at different laboratories all over the world, a simulated solar spectrum of air mass 1.5 G (AM 1.5 G) corresponding to a Zenith angle (φ) 42° is used as the standard to test their efficiency. The path length of the solar irradiation to reach the earth surface is known as the air mass and is expressed as: $(AM = 1/cos\varphi)$. Zenith angle (φ) is the angle of elevation of the sun and is shown schematically in figure **2.2.5 (B)**.

Short-circuit current is the current flowing through the solar cell when the voltage across the solar cell is zero, which is obtained due to the collection of light-generated charge carriers. Short-circuit current increases with light intensity because higher intensity releases higher number of photons and so more number of photoinduced electrons are generated. In order to eliminate the area dependence of solar cells, short-circuit current is expressed in terms of short-circuit current density (J_{sc}, in mA/cm^2).

The open-circuit voltage (V_{oc}) is the maximum voltage generated in a solar cell and is obtained at zero current. Since V_{oc} corresponds to the amount of forward bias on the solar cell, it measures the amount of recombination in the device. The fill factor (FF), ratio of the maximum power from the solar cell to the product of V_{oc} and J_{sc}, determines the maximum power from a solar cell. Graphically, FF is obtained from the area of the largest rectangle which will fit in the (*I*–V) curve as shown in Figure 2.2.5 (A). The FF can be expressed as:

$$FF = \frac{P_{max}}{J_{sc} \times V_{oc}}$$

Where, P_{max} is the maximum power output of the solar cell obtained from the product of maximum photocurrent and photovoltage output. The overall *solar-to-electrical energy* conversion efficiency or power conversion efficiency (η) of a solar cell is given by the relation;

$$\eta = \frac{J_{sc} \times V_{oc} \times FF}{P_{in}}$$

Another fundamental measurement of the performance of a solar cell is the incident photon-to-current conversion efficiency (IPCE). IPCE corresponds to the photocurrent density produced in the external circuit under monochromatic illumination of the cell divided by the photon flux that strikes the cell. It can be expressed as;

$$\text{IPCE} = 1240 \times \frac{J_{sc}}{\lambda \times P_{in}(\lambda)}$$

IPCE is measured from 350 nm onwards as the percentage of photons of wavelengths range lower than 350 nm is low in the spectra of AM 1.5 G solar light irradiation.

2.2.6 ELECTROCHEMICAL IMPEDENCE SPECTROSCOPY (EIS) MEASUREMENT

To monitor electron transport and recombination kinetics at the solid/liquid heterojunctions in photovoltaic devices, electrochemical impedance spectroscopy (EIS) analyses are performed. Figure **2.2.6** (A) shows the schematic of the cross-section of a DSSC/QDSSC device which is depicting solid/liquid heterojunctions, i.e., ZnO/sensitizer(S)/electrolyte and counter electrode (CE)/electrolyte interfaces. Figure **2.2.6** (B) and (C) is showing typical Nyquist and Bode phase plots recorded under dark condition in a frequency range from 0.1 Hz to 100 kHz for typical electrochemical devices. In general, Nyquist plot is comprises of two main semicircles, one in the medium frequency region while another one in the higher frequency region. The semicircle in the medium frequency region encompasses the charge-transfer process at the working electrode/electrolyte interface, while the smaller semicircle in the higher frequency region is attributed to the counter electrode/electrolyte interfacial redox reactions.[4] The diameter of the right semicircle (R_k) primarily contributed from electron recombination resistance and is partly due to the transport resistance.[5] Higher value of R_k signifies greater recombination resistance at the working electrode/ electrolyte interfaces.

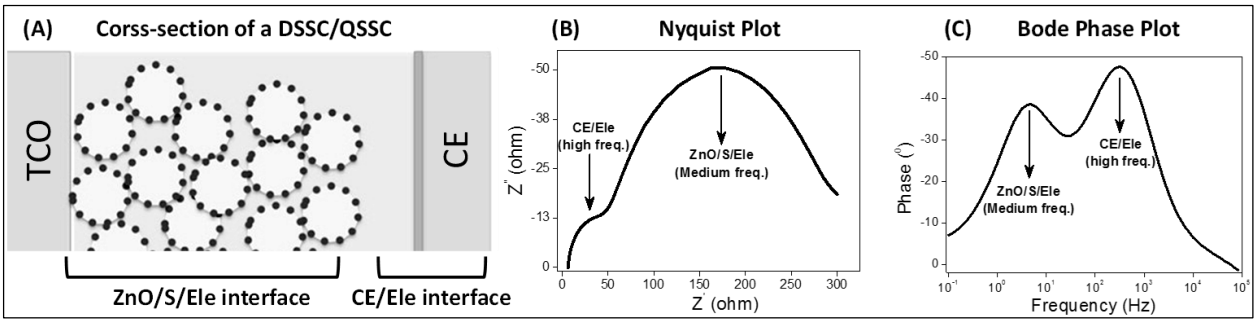

Figure 2.2.6 (A) Schematic of cross-sectional view of a DSSC/QDSSC device showing solid/liquid heterojunctions such as ZnO/sensitizer(S)/electrolyte and counter electrode (CE)/electrolyte interfaces. **(B)** Typical Nyquist plot for a DSSC/QDSSC device and **(C)** represents corresponding Bode Phase plot.

It should be mentioned that, Nyquist plot can also give information about the impedance of the Nernst diffusion of redox couple (R_D) in the electrolyte throughout the photoanode. However the semicircle associated with the Nernst diffusion process appears at low-frequency (10^{-1} to 10^{-2} Hz) and requires a longer time for analysis. In order to eliminate the unenviable effects of slow evaporation of volatile solvent of the electrolyte, EIS data recording time for the fabricated devices was limited to a couple of minutes per cell and frequency range of 10^5 to 10^{-1} Hz was selected for acquisition of data. Related to the theme of the present work, we have emphasized the charge transfer processes occurring at working electrode/electrolyte interfaces and counter electrode/electrolyte interfaces. Figure **2.2.7** shows a Nyquist plot with all the three semicircles for better understanding. The value of R_s represents sheet resistance of the FTO substrate in the device while R_k and R_D represent diameter of the respective semicircles. The maximum peak frequency of the second semicircle (f_{max}) is correlated to the rate of recombination of electrons (k_{eff}) at the Working electrode/Electrolyte interfaces.

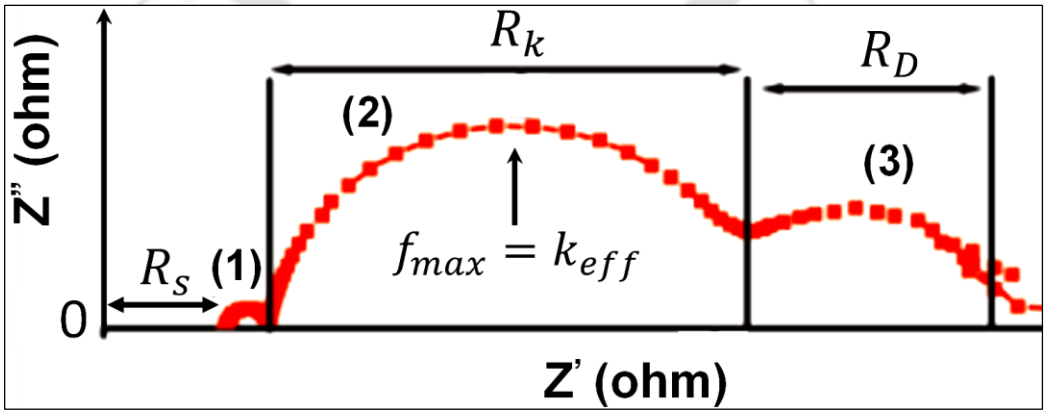

Figure **2.2.7** Schematic of a Nyquist plot with all the three semicircles, i.e., **(1)** charge transfer process at CE/Electrolyte interface **(2)** charge transfer process at working electrode/Electrolyte interface and **(3)** Nernst diffusion of the electrolyte in the photoanode. (Figure taken from reference No. 4)

Bode phase plots also furnishes the characteristic peak frequency in the medium frequency region (f_{max}) which is used in the calculation of photoinduced electron lifetime (τ_e) in the photovoltaic devices. We have estimated the values of τ_e by using the following equation.[6]

$$\tau_e = \frac{1}{2\pi f_{max}}$$

Higher τ_e value infers maximum photoinduced electron density availability in the photovoltaic devices for extraction to the external circuit.

2.3 REFERENCES

(1) Anta, Juan A.; Guillén, E.; Tena-Zaera, R. *J. Phys. Chem. C*, **2012**, *116*, 11413.

(2) Klingshirn, C. *ChemPhysChem*, **2007**, *8*, 782.

(3) Wang, Z. L. *Mater. Today*, **2004**, *7*, 26.

(4) Phadke, S.; Pasquier, A. D.; Birnie, D. P. *J. Phys. Chem. C*, **2011**, *115*, 18342.

(5) Tian, J.; Uchaker, E.; Zhang, Q.; Cao, G. *ACS Appl. Mater. Interfaces*, **2014**, *6*, 4466.

(6) Kern, R.; Sastrawan, R.; Ferber, J.; Stangl, R.; Luther, J. *J. Electrochim. Acta*, **2002**, *47*, 4213.

CHAPTER 3

Hexagon Shaped ZnO Nanodisks with Exposed ± {0001} Polar Facets for Enhanced Photovoltaic Performance in Quantum Dot Sensitized Solar Cells

This chapter describes chemistry behind the formation of hexagon shaped ZnO nanodisks (NDs) with exposed ±(0001) polar facets and its application in quantum dot sensitized solar cell (QDSSC) devices. The wet chemical synthetic approach utilizes ethyl cellulose (EC) and cetrimonium bromide (CTAB) as the capping and structure directing agents in 1-butanol: water (3:1) solvent system. Enhanced light harvesting ability of ZnO ND based devices can be ascribed to following key factors – (i) efficient charge separation boosted by the exposed ±(0001) polar facets and their single crystalline nature (ii) better light-scattering effects and (iii) high BET surface area for sensitizer particle adsorption.

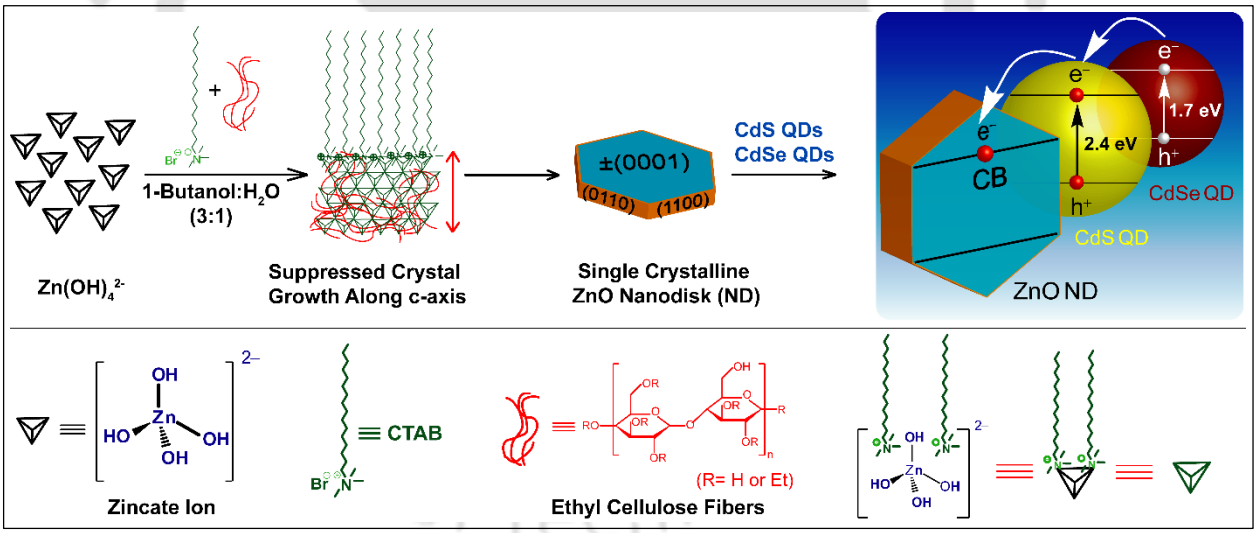

ACS APPLIED MATERIALS & INTERFACES

T. R. Chetia, M. S. Ansari, M. Qureshi **2015**, *7*, 13266.

3.1 INTRODUCTION

Zinc oxide (ZnO) can be tailored into various architectures such as zero (0-D), one (1-D) and two dimensional (2-D) nanostructures as well as three dimensional (3-D) microstructures due to its ease of crystallization and anisotropic growth behavior, which allow to control the electrical transport and optical (sensitizer particle loading and light scattering) properties of the photoanodes for an enhanced solar cell performance.[1–3] 0-D and 3-D structures of ZnO provide larger surface area for sensitizer adsorption, while 1-D and 2-D nanostructures offer direct and faster transport pathways for photo-generated electrons.[4] However, insufficient internal active surface area of vertically grown 1-D ZnO nanostructures always limit their energy conversion performance. Limiting factor of 0-D and 3-D structures is charge collection, wherein the photo-generated electrons undertake a random movement through the film and interact repeatedly with the trap sites in grain boundaries.[5] Although a number of size and shape-dependent morphologies of ZnO such as, nanoparticles,[6] nanowires,[7–10] nanotubes,[11] hierarchical tetrapod-like structures,[12] nanosheets,[13] nanoflower,[14] micro-sphere,[15] hollow-microsphere,[4,16] etc. are explored as the candidates for photoanodes to fabricate efficient QDSSCs as well as dye sensitized solar cells (DSSCs), there are fewer reports about the possibility of exploring the exposed polar facets in enhancing the efficiency of the devices[17,18] as compared to the photocatalytic activity.[19–23] It is observed that, hexagon shaped ZnO nanodisks (NDs) with exposed polar ±(0001) facets facilitate the photoinduced charge separation process and enhances light harvesting ability. However, in most of the synthetic methods, 1-D ZnO nanowires or nanorods with exposed nonpolar ±(10$\bar{1}$0), ±(1$\bar{1}$00) and ±(01$\bar{1}$0) facets are generally produced due to the intrinsic faster growth along [0001] direction instead of hexagon shaped ZnO nanodisks (NDs)[24] as shown in scheme **3.1.1**.

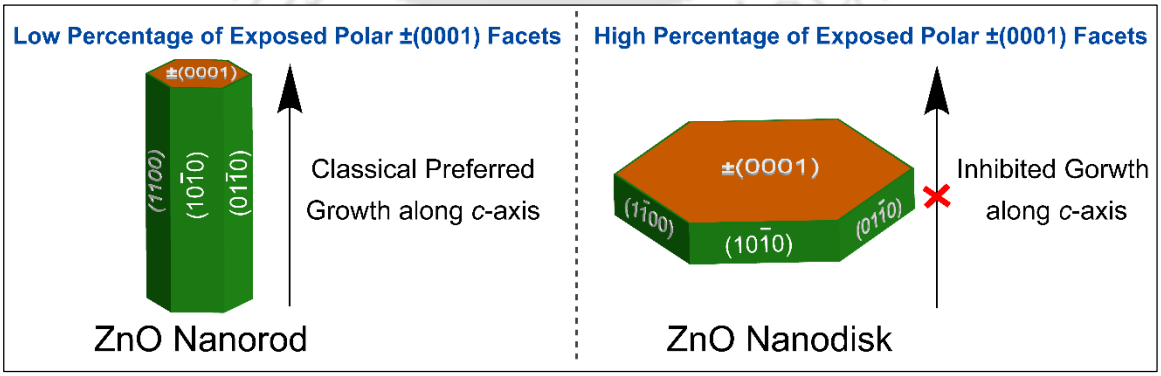

Scheme 3.1.1 Schematic presentation of favorable growth of ZnO nanorods (NRs) in general reaction conditions as well as template assisted inhibited growth of ZnO nanodisks (NDs).

In order to control the exposure of ZnO crystal facets, it is necessary to minimize surface energy of the polar high energy crystal facets during crystal growth. Selective adsorption of appropriate capping agents or additives on these polar facets can compensate the surface charges and alter the crystal growth habits of ZnO. Capping agents, such as oleic acid,[25] citrate ions,[26] sodium bis(2-ethylhexyl) sulfosuccinate or AOT,[27] starch,[28] polyvinyl pyrrolidone,[29] poly(ethyleneglycol),[30] pectin,[31] gelatin[32] etc. are utilized in the synthetic processes of ZnO to control growth kinetics of high energy facets and to obtain anticipated size and shape. There are a few reports on the synthesis of hexagon shaped ZnO nanodisks by wet chemical route, however, rarely studied for the quantum dot (QD) loading so far,[33,34] although they have got great potential as photoanodic material for efficient QDSSCs. QDs have several advantages over the organic dye molecules such as higher stability and higher extinction coefficient,[35] tunable absorption edge controlled by the particle size,[36,37] generation of multiple electron–hole pairs per photon[38] and low cost. Due to these distinctive features of semiconductor QDs as light harvesters, QDSSCs are gaining considerable attention as a next generation photovoltaics.[39,40] Among various QDs that are used in QDSSCs, for example, CdS,[41,42] CdSe,[43] PbS,[44] $CuInS_2$,[45] Sb_2S_3,[46] InP[47] etc.; co-sensitization of metal oxide by CdS/CdSe is attractive owing to their high potential of light absorption in the visible light region, efficient transfer of photo-generated charge-carrier and ease of deposition techniques.[48,49] It was found that CdS grown on ZnO acts as a good interfacial layer between CdSe QDs and ZnO for effective charge carrier transport as well as facilitation of smooth deposition of CdSe QDs on to the photoanode.[50,51]

This chapter presents synthesis and chemistry behind the formation of hexagon shaped ZnO nanodisks (NDs) with exposed ±(0001) polar facets and its application in QDSSC devices. Porous hexagon shaped ZnO NDs are synthesized by utilizing ethyl cellulose (EC) as a capping agent and a cationic surfactant, Cetyl-trimethyl ammonium bromide (CTAB) as a structure directing agent. Controlled reactions are performed to understand the mechanism of formation of ZnO NDs and evaluated their photovoltaic properties in CdS/CdSe sensitized solar cells. An optimized power conversion efficiency (PCE, η) as high as ~4.86 % is achieved which is about 35 % increment over the conventionally used morphology of ZnO, i.e., nanoparticles (NPs). Enhanced efficiency of the porous ZnO ND based photovoltaic device is due to efficient photo-excited charge separation and collection, better light scattering and high surface area for sensitizer adsorption.

3.2 EXPERIMENTAL METHODS

3.2.1 SYNTHESIS OF ZnO NANODISKS

In a typical procedure, 1 g of EC is dissolved in 75 mL of 1-Butanol (solvent) to get a clear solution (solution 1). 25 ml of water (anti-solvent) is then added to the solution 1 with constant stirring. A turbid colloidal dispersion of EC is obtained (solution 2). 5 mmol (1.82 g) of cationic surfactant (i.e. CTAB) is then added to the solution and stirred for 5 min. Subsequently, zinc nitrate hexahydrate (5 mmol; 1.48 g) is added into the solution 2, followed by dropwise addition of aqueous sodium hydroxide solution (10 mmol; 0.4 g) with continuous stirring and pH of the solution is found to be around 9–9.5. The resulting solution is then transferred into a 250 mL round bottom flask, gradually heated upto 100 °C and refluxed for 10 h. After cooling down to the room temperature, the resultant precipitate is centrifuged, washed with distilled water and absolute ethanol several times. As obtained product is dried in a hot air oven at 70 °C for 10 h. A pale white powder is formed which is calcined at 500 °C for 2 h in a muffle furnace to get the hexagon shaped mesoporous ZnO nanodisks. Graphical representation of the synthetic methodology is depicted in the scheme **3.2.1.**

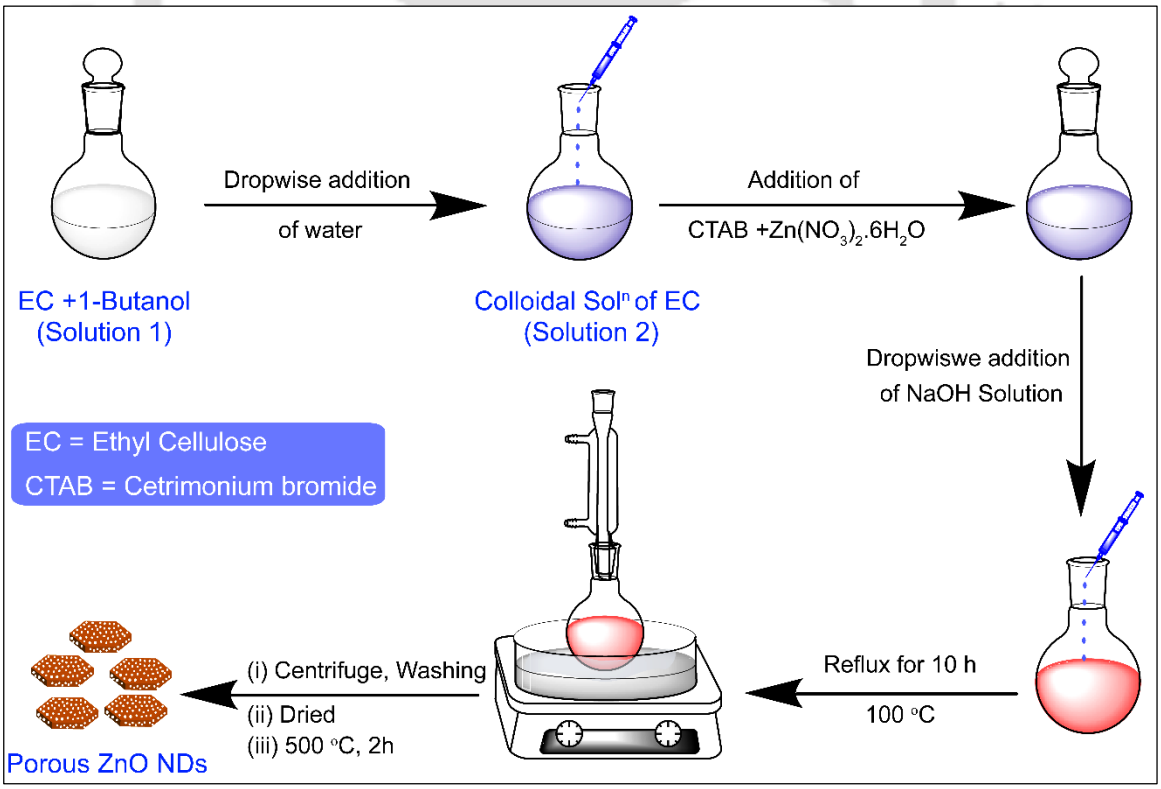

Scheme 3.2.1 Step-by-step synthetic protocol for hexagon shaped ZnO NDs with exposed ±(0001) polar facets.

Control reactions in presence of only EC and only CTAB are also carried out separately keeping the same reaction conditions in order to compare the influence of both the additives.

3.2.2 SYNTHESIS OF ZnO NANOPARTICLES

ZnO nanoparticles (NPs) are synthesized by following a previously reported procedure.[52] To prepare ZnO nanoparticles, $ZnCl_2$ (1.1 g, 40 mmol) is dissolved in Milli-Q water (40.0 mL) and the solution is heated at 90 °C with constant stirring. Then 16 mL of 5 M aqueous NaOH solution is added slowly into the reaction mixture with stirring at same temperature for another 30 min. The reaction mixture is allowed to cool down to room temperature and the precipitate is separated out by discarding the supernatant liquid. The precipitate is washed with distilled water several times for complete removal of NaCl, which is confirmed by $AgNO_3$ titration method. Further, purified particles are dispersed in iso-propanol under an ultrasonic bath for 10 min at room temperature. The obtained product is centrifuged and dried in a hot air oven at 80 °C for 4 h. Finally the ZnO nanoparticles are obtained via calcination at 450 °C for 5 h in a muffle furnace.

3.2.3 FABRICATION OF PHOTOANODES AND DEVICES

ZnO NDs-based photoanodes are fabricated by preparing a homogeneous paste of as synthesized ZnO ND powder (0.5 g) with a mixture of 2 mL of terpineol and 0.2 g of PEG-PPG-PEG (Triblock co-polymer) in an agate mortar. This homogenous paste is deposited on pre-cleaned conductive glass substrate i.e. FTO via doctor blade technique and the films are dried in air. After that these films are calcined at 525 °C for 30 min to remove the polymer. Thickness of the ZnO ND layer is measured by surface profilometer and it is found to be in the range of 12−15 μm. The ZnO ND electrodes are co-sensitized with the CdS and CdSe. CdS QDs are deposited on ZnO via successive ionic layer adsorption and reaction (SILAR) process. In SILAR method, first the electrodes are dipped into an ethanolic solution of $Cd(NO_3)_2.6H_2O$ (0.5 M) for 1 min, rinsed with ethanol, and dried on a hot plate at 70 °C. Again they are dipped into a Na_2S (0.5 M) solution in methanol for 1 min, rinsed with methanol and dried at 70 °C. The amount of CdS grown onto the ZnO system is controlled by the number of repeated SILAR cycles. Chemical bath deposition (CBD) method is used for CdSe sensitization. For the CBD, various solutions having different precursor concentration ratios are prepared. At a fixed concentration of 5 mM $Cd(CH_3COO)_2.2H_2O$, the Na_2SeSO_3 concentrations are set at 2.0, 1.5, 1 and 0.5 mM in four different chemical baths from which four different CdSe deposited photoanodes are prepared and designated as Se [2.0], Se [1.5],

Se [1.0] and Se [0.5] respectively. For deposition of CdSe QDs, the CdS sensitized ZnO ND photoanodes are immersed in aforementioned solutions with an added 75 µL of ammonium hydroxide for 3h at 95 °C and this procedure is repeated three times. Hereafter, the fabricated photoanode is represented as ZnO ND-CdS-CdSe. Graphical representation of step-by-step photoanode preparation process is shown in the scheme **3.2.2**.

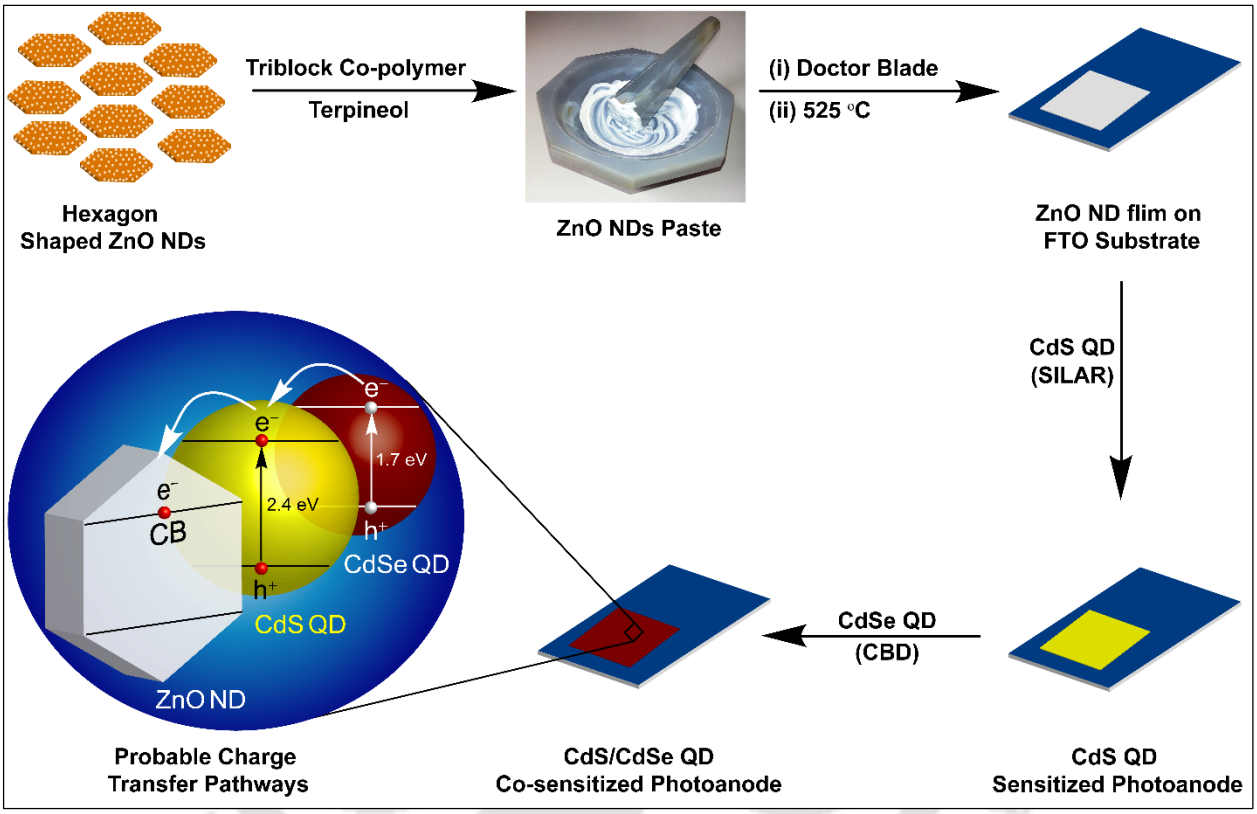

Scheme 3.2.2 Step-by-Step photoanode fabrication process showing probable charge transfer pathways.

ZnO NPs-based photoanodes are fabricated by following the same procedure used for ZnO NDs based photoanodes. In brief, a ZnO NPs paste is prepared by simple mixing and grinding of ZnO NPs (0.5 g), terpineol (2 mL), and triblock PEG−PPG−PEG copolymer (0.2 g) in an agate mortar. The ZnO NPs paste is coated by using doctor blade technique over pre-cleaned FTO substrates. These substrates are dried in air and then calcined at 525 °C for 30 min to get ZnO NPs films with thickness ~12−15 µm, confirmed by the surface profilometer. For co-sensitization of CdS/CdSe, same methods i.e. SILAR (CdS) and CBD (CdSe) are employed. The photovoltaic devices are fabricated by sandwiching the photoanodes and counter electrodes. Electrolyte solution of sulfide/polysulfide (S^{2-}/S_n^{2-}) is added after sealing the device by using low-temperature thermoplastic sealant, (thickness ~50 µm). The Pt counter electrodes are prepared by spin coating

a solution of chloroplatinic acid (5 mM in isopropanol) on a pre-cleaned FTO substrate followed by the calcination at 450 °C for (heating ramp of 5 °C /min) 30 min in a muffle furnace and cooled down to room temperature naturally. Sulfide/polysulfide (S^{2-}/S_n^{2-}) electrolyte is prepared by dissolving 1 M Sulfur powder, 1 M Na_2S and 0.2 M KCl in a solvent mixture of methanol–water (7:3, v/v). The active area for all fabricated devices are same and it is found to be ~0.25 cm^2. Before the photovoltaic measurements, the fabricated devices are kept under dark condition for 24 h.

3.3 RESULTS AND DISCUSSIONS

3.3.1 POWDER X-RAY DIFFRACTION ANALYSIS

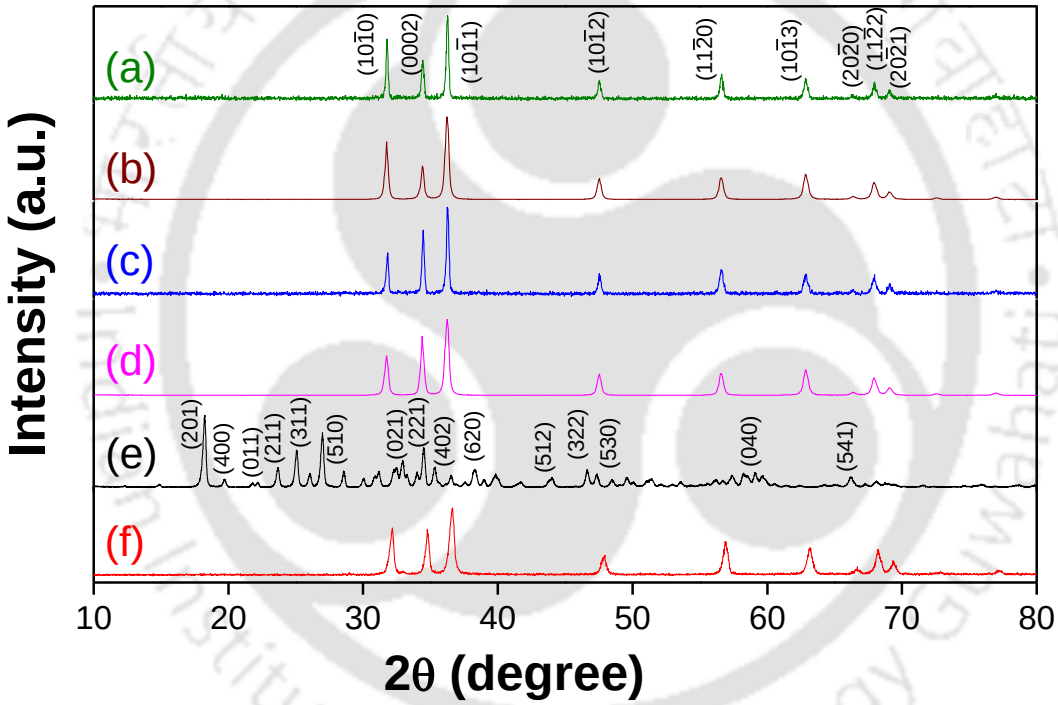

Figure 3.3.1 Powder X-ray diffraction (PXRD) patterns for as-synthesized ZnO before and after calcination in presence of EC and CTAB (a & b), ZnO before and after calcination in presence of only CTAB (c & d), the precursor complex $Zn_5(OH)_8(NO_3)_2.2H_2O$ before calcination (e) and ZnO after calcination in presence of only EC (f).

Figure **3.3.1** shows powder X-ray diffraction (PXRD) pattern for all the synthesized products, i.e., ZnO before and after calcination, in presence of both EC and CTAB (traces a & b), ZnO before and after calcination in presence of only CTAB (traces c & d), the precursor complex $Zn_5(OH)_8(NO_3)_2.2H_2O$ before calcination (trace e) and for ZnO obtained after calcination, synthesized in presence of only EC (trace f). Crystal phase for all the ZnO is concluded as hexagonal wurtzite phase with (10$\bar{1}$0), (0002), (10$\bar{1}$1), (10$\bar{1}$2), (11$\bar{2}$0), and (10$\bar{1}$3) planes and a

*P*6$_3$*mc* space group symmetry according to the JCPDS Card No. 36-1451. No peaks due to impurities are detected in the PXRD patterns of ZnO and characteristic diffraction peaks become sharp and intense after calcination, indicating their improved crystalline nature. A precursor complex is formed when the reaction is carried out in presence of only EC. The PXRD pattern of ZnO precursor complex is well matched with the diffraction pattern of $Zn_5(OH)_8(NO_3)_2.2H_2O$ (JCPDS Card No. 25-1028). After calcination the precursor complex is converted into pure ZnO as confirmed from the PXRD pattern, trace (f).

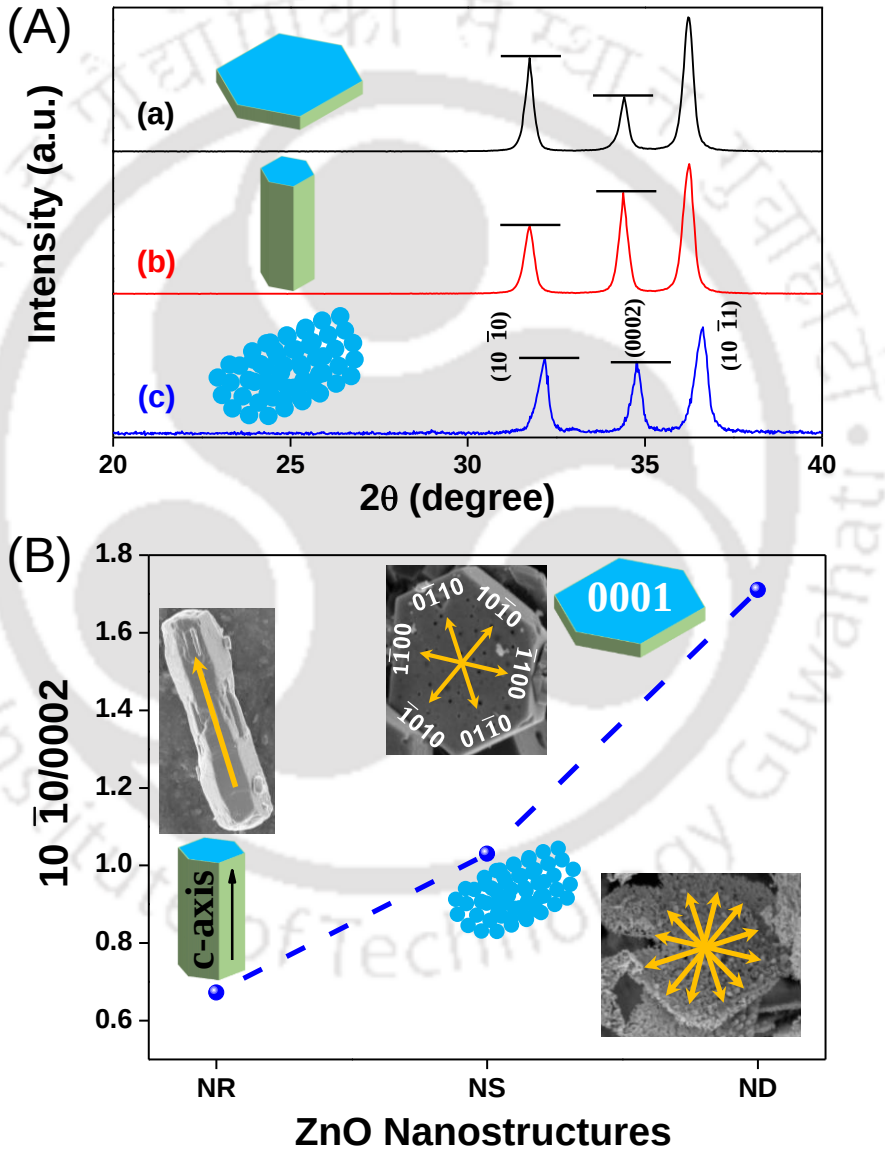

Figure 3.3.2 (A) Intensity variation of powder X-ray diffraction peaks for (10$\bar{1}$0), (0002) and (10$\bar{1}$1) planes of ZnO prepared in presence of (a) CTAB and EC, (b) only CTAB and (c) only EC **(B)** Plot of the (10$\bar{1}$0)/(0002) intensity ratio vs all the ZnO nanostructures obtained under different reaction conditions along with schematic illustration of the morphology models for nanorods (NR), nanosheets (NS) and nanodisks (ND) respectively. Inset shows FESEM images of a ZnO ND, ZnO NR and ZnO NS.

Figure **3.3.2** (A) represents intensity variation of PXRD peaks for $(10\bar{1}0)$, (0002) and $(10\bar{1}1)$ planes of ZnO synthesized in presence of (a) both CTAB and EC, (b) only CTAB and (c) only EC. All the products are observed to be crystallized in hexagonal wurtzite phase with a $P6_3mc$ space group symmetry. Note that the ratio of intensities from $(10\bar{1}0)$ and (0002) planes varied significantly, indicating a differential growth behavior of ZnO crystals in all the three reaction conditions. A smaller value of $(10\bar{1}0)/(0002)$ ratio indicates the formation of ZnO rods showing a preferential (oriented) growth along the c-axis, whereas a larger value of $(10\bar{1}0)/(0002)$ ratio specifies inhibited growth along the *c*-axis, leads to the formation of disks as represented in figure (B).[23,25]

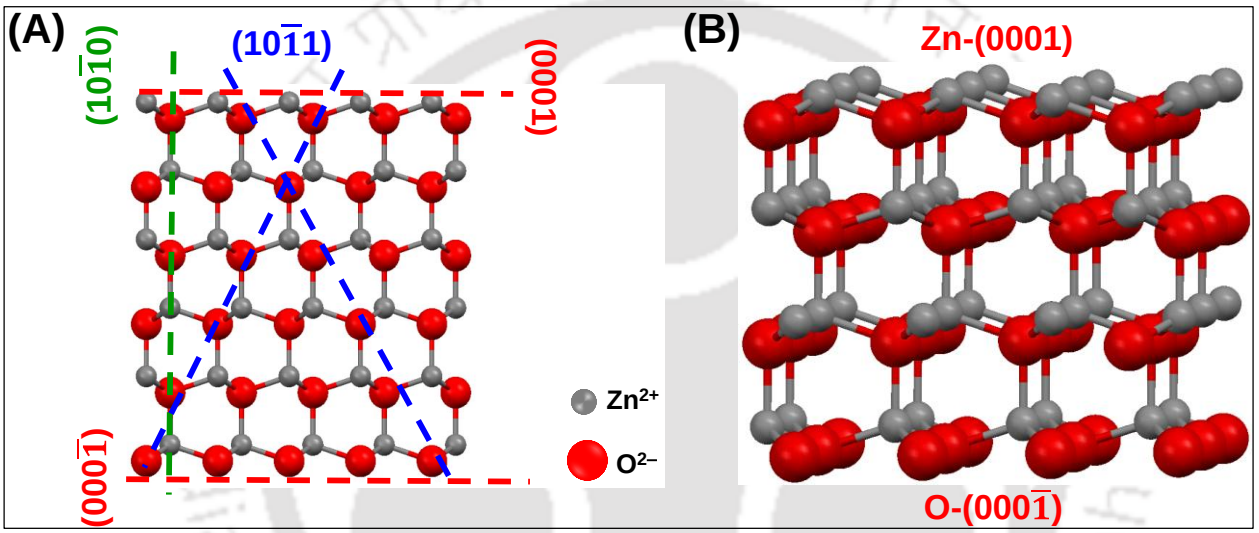

Figure 3.3.3 (A) 2D Atomic stacking model of wurtzite ZnO showing {±(0001), ±(10$\bar{1}$0), ±(10$\bar{1}$1)} planes **(B)** 3D Atomic stacking model of wurtzite ZnO showing Zn-terminated (0001) plane and O-terminated (000$\bar{1}$) plane.

Figure **3.3.3** (A) is a model representing atomic stacking of wurtzite ZnO polar crystal in which O^{2-} and Zn^{2+} ions stack alternatively along the *c*-axis, resulting in Zn terminated (0001) and the O-terminated (000$\bar{1}$) planes with higher surface energy. Another group of semi-polar planes (10$\bar{1}$1) and nonpolar planes are (10$\bar{1}$0), (0$\bar{1}$10) and (1$\bar{1}$00) in wurtzite ZnO crystal. The non-polar planes are composed of equivalent O^{2-} and Zn^{2+} ions and have the lowest surface energy.[24] It is well known that in general reaction conditions, ZnO prefers to grow along *c*-axis with high energy polar ±(0001) facets, to minimize the high surface energy. Therefore, the polar (0001) and (000$\bar{1}$) planes are less exposed or disappear from these ZnO nanorod structures. But in case of hexagon shaped ZnO crystals, high percentage of polar surfaces are exposed due to the inhibited growth along the *c*-axis and favored growth along six symmetric directions of ±(0$\bar{1}$10), ±(10$\bar{1}$0) and

±(1$\bar{1}$00). Figure (B) represents 3-D atomic stacking model of wurtzite ZnO showing Zn-terminated (0001) and O-terminated (000$\bar{1}$) polar planes in either side of the crystal.

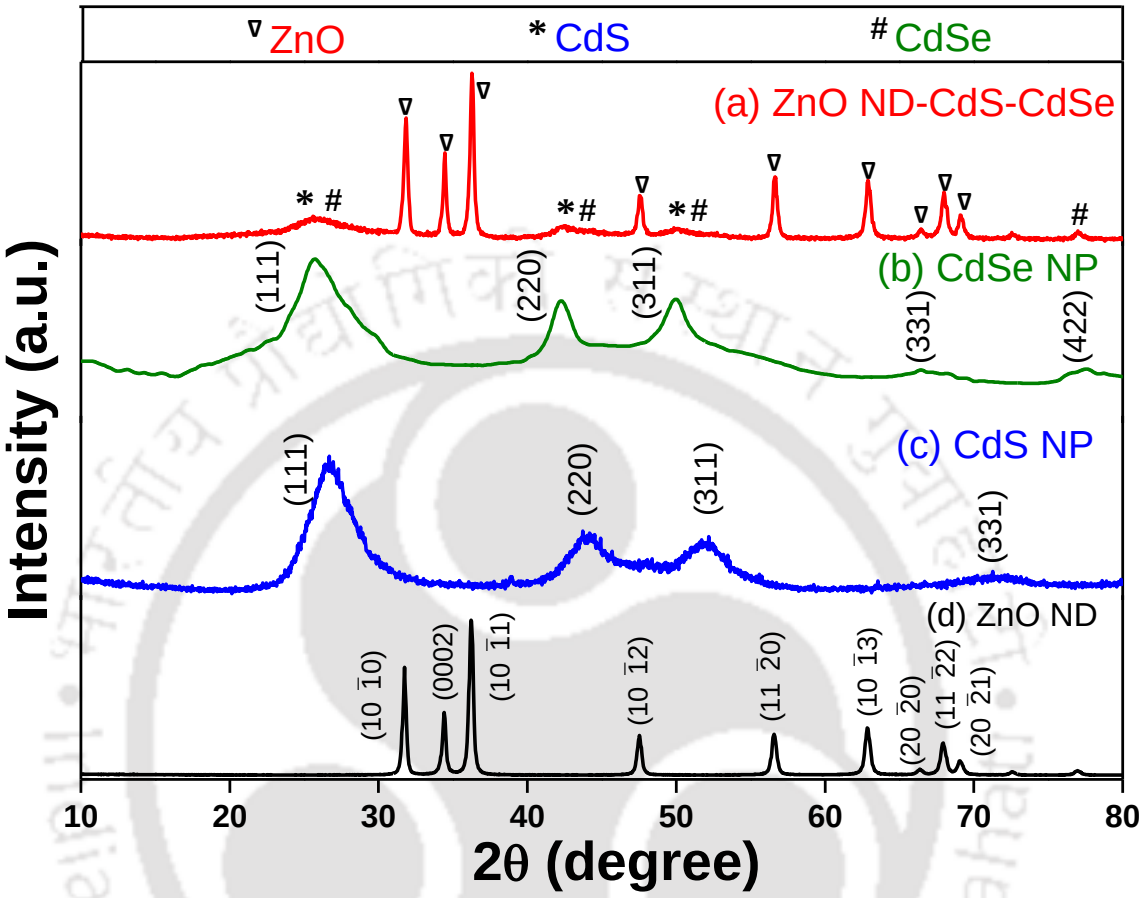

Figure. 3.3.4 PXRD patterns for (a) CdS and CdSe co-sensitized ZnO NDs, (b) CdSe NPs, (c) CdS NPs and (d) pristine ZnO NDs.

Figure **3.3.4** represents PXRD patterns for CdS and CdSe co-sensitized ZnO NDs (trace a), CdSe NPs (trace b), CdS NPs (trace c) and pristine ZnO NDs (trace d). All the resolved diffraction peaks of CdS and CdSe in the diffraction pattern of CdS/CdSe co-sensitized ZnO ND photoanode (trace a) reveal successful deposition of cubic zinc blende CdSe (JCPDS no. 19-0191, trace b) and CdS (JCPDS no. 10-0454, trace c) QDs without any indication of crystalline impurities such as SeO_2, CdO etc. Average crystallite size of the CdS and CdSe QDs deposited on the photoanodes are estimated from Debye-Scherrer equation and are found to be around ~5.0–5.5 nm. In addition, the diffraction peaks for pristine ZnO NDs can also be seen in the diffractogram for CdS/CdSe sensitized photoanodes, which is a symptomatic of the retention of crystal structure of ZnO ND even after sensitization processes.

3.3.2 MATERIAL MORPHOLOGY

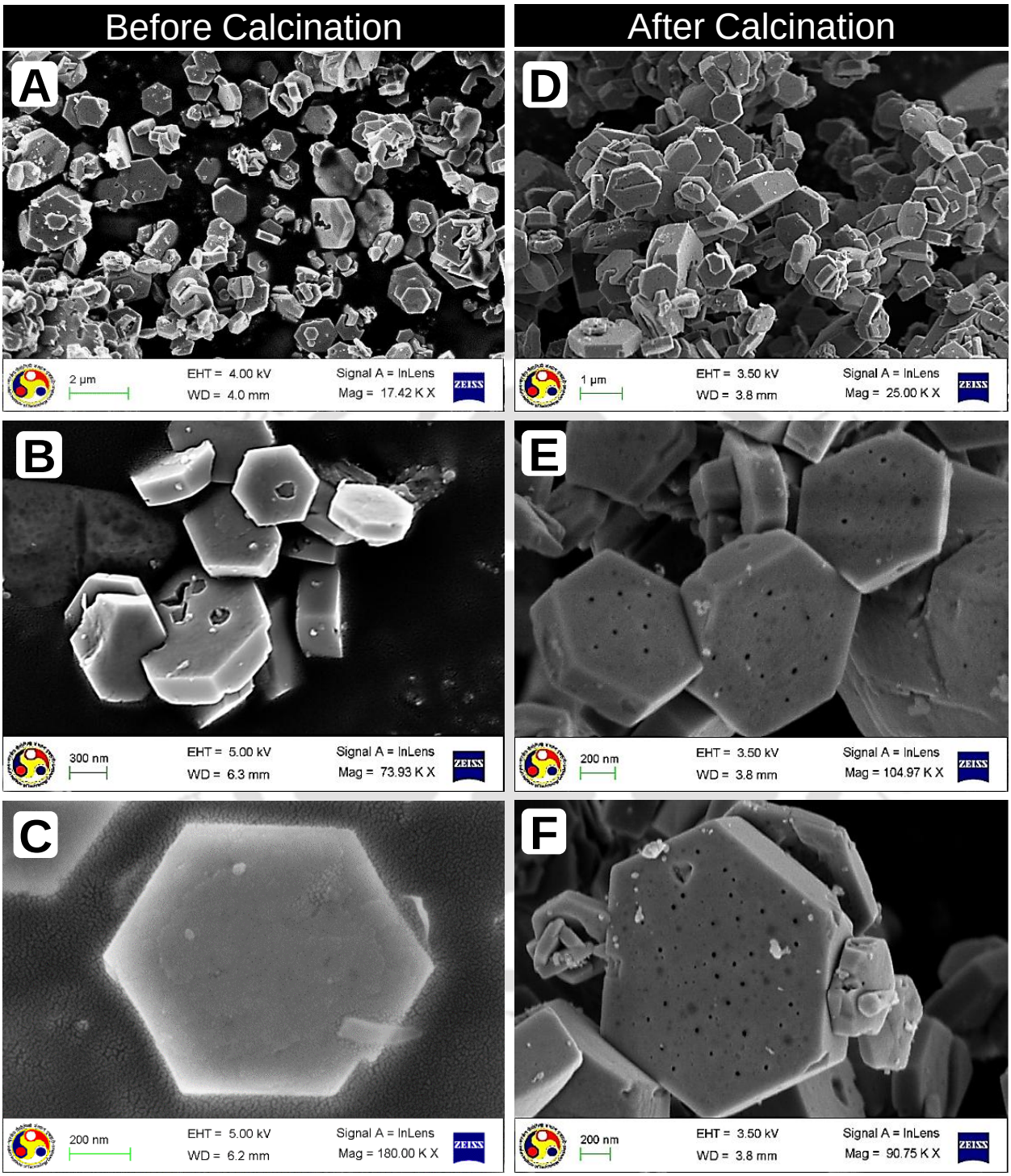

Figure 3.3.5 FESEM images of the ZnO NDs before calcination, (A, B, and C) and porous hexagonal ZnO NDs (D, E and F) after calcination at different magnifications.

Figure **3.3.5** shows the FESEM features of as synthesized hexagon shaped ZnO NDs before calcination (A, B and C) and after calcination (D, E and F) at different magnifications. Average

dimension of the ZnO hexagons are in the range of 1–4 μm and thickness are in the range of 70–100 nm. Before calcination the surface morphology of the ZnO NDs is observed to be smooth and nonporous while after the calcination pores are formed on the surface of ZnO NDs. Distinct porous structure of ZnO NDs has been observed from the FESEM images (E) and (F).

Furthermore, to confirm morphological characteristics of the ZnO NDs, TEM analysis is performed and shown in the Figure **3.3.6**. Formation of pores in the hexagon shaped ZnO NDs after the calcination process is also evident from the TEM image (A). It can be seen from Inverse Fast Fourier Transform (IFFT) of atomic planes (trace B) of ZnO NDs that the arrangement of atoms is regular and form a six-fold symmetric projected structure. Interplanar distance of the lattice pattern is found to be ~0.28 nm which corresponds to the $(10\bar{1}0)$ lattice planes. This is an indicative of favorable growth mainly along the six symmetric directions of $\pm(10\bar{1}0)$, $\pm(1\bar{1}00)$, and $\pm(01\bar{1}0)$ lattice planes and suppression of typical growth along [0001] direction.[51] Inset to trace B represents Fast Fourier transform (FFT), obtained from the HRTEM image, accords with the diffraction pattern of the [0001] zone axis of ZnO. Figure C depicts selected area electron diffraction (SAED) pattern of ZnO ND, when the electron beam was perpendicular to the ZnO ND top facet which is recognized as the [0001] growth direction of ZnO. The ZnO ND is diffracting as a wurtzite single crystal and exhibits a hexagonally symmetrical pattern with [0001] zone axis, confirming dominant exposed facets are the polar ±[0001] planes which are top/bottom surfaces.[24]

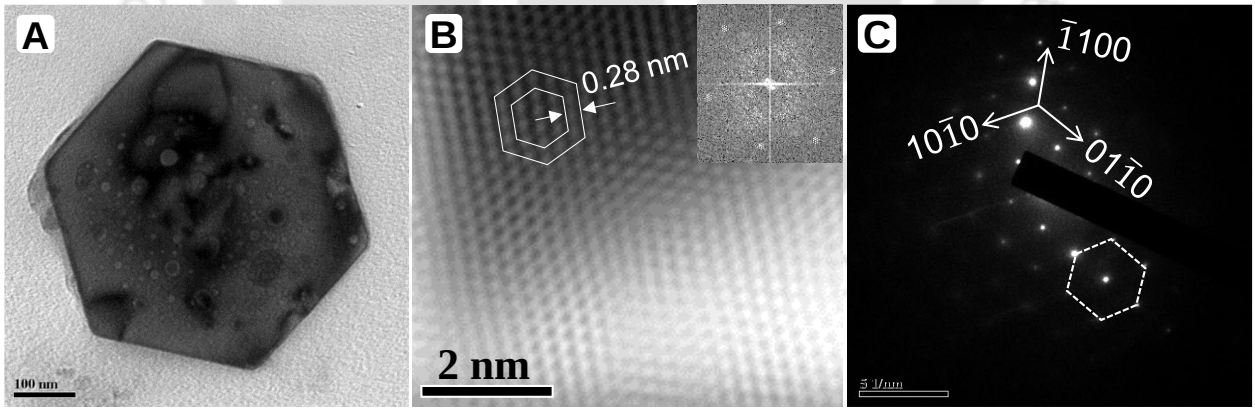

Figure 3.3.6 Trace (A) represents TEM image of a single ZnO ND. HRTEM image of the ZnO ND (figure B), showing inter-planar spacing, viewed along [0001] direction with FFT in the inset. SAED pattern of the ZnO ND (figure C) confirms its single crystalline nature.

In order to understand the role of CTAB and EC in the reaction mixture we have performed controlled reactions by varying the additive sequences of both the additives. In presence of only CTAB and keeping other reaction conditions unchanged, formation of hexagon shaped ZnO

nanorods (NRs) are observed as we have shown in figure **3.3.7** (A, B and C). This observation is in accordance with the PXRD analysis of the as synthesized products. Interestingly, formation of pores is not observed in this case even after the calcination process at 500 ^{o}C for 2h. This observation divulges that growth of hexagon shaped ZnO is encouraged by the CTAB molecules and are not responsible for the formation of pores in the ZnO NDs.

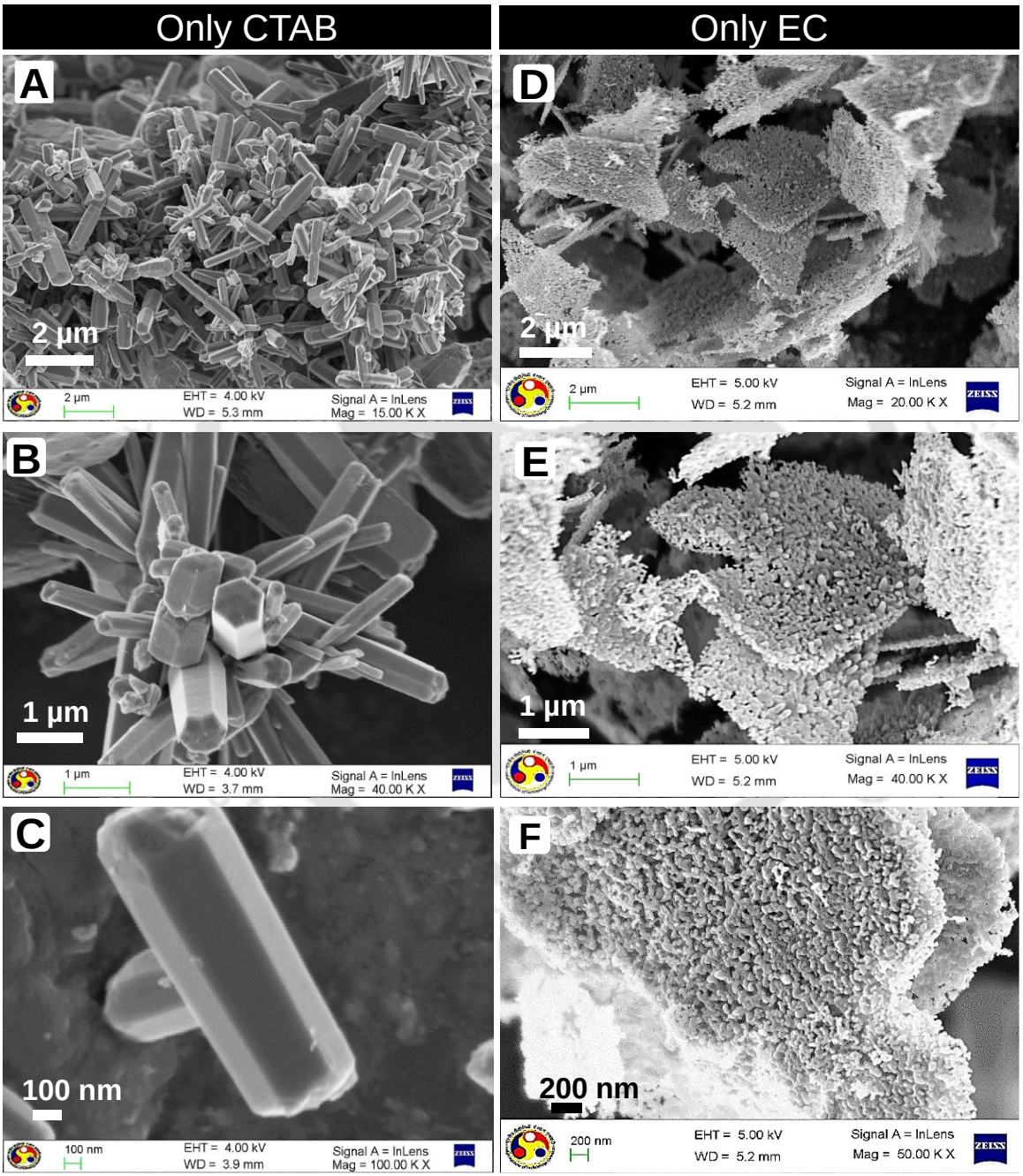

Figure 3.3.7 FESEM images of the ZnO NRs (A, B, and C) and porous ZnO NSs (D, E and F) after calcination at different magnifications prepared in presence of only CTAB and only EC respectively.

Figure **3.3.7** (D, E and F) represents FESEM images of ZnO synthesized in presence of only EC and the formation of ZnO nanosheets composed of numerous nanoparticles is noted in this instance. This may be due to random arrangement and adsorption of the growth units [i.e., zincate or $Zn(OH)_4^{2-}$] onto the EC fibers. This confirms that EC molecules are not only responsible for pore formation but also inhibiting growth of ZnO along the direction of *c*-axis leading to high percentage exposure of active ± (0001) polar facets. Formation of all the ZnO heterostructures obtained under different reaction conditions are schematically represented in scheme **3.3.1**.

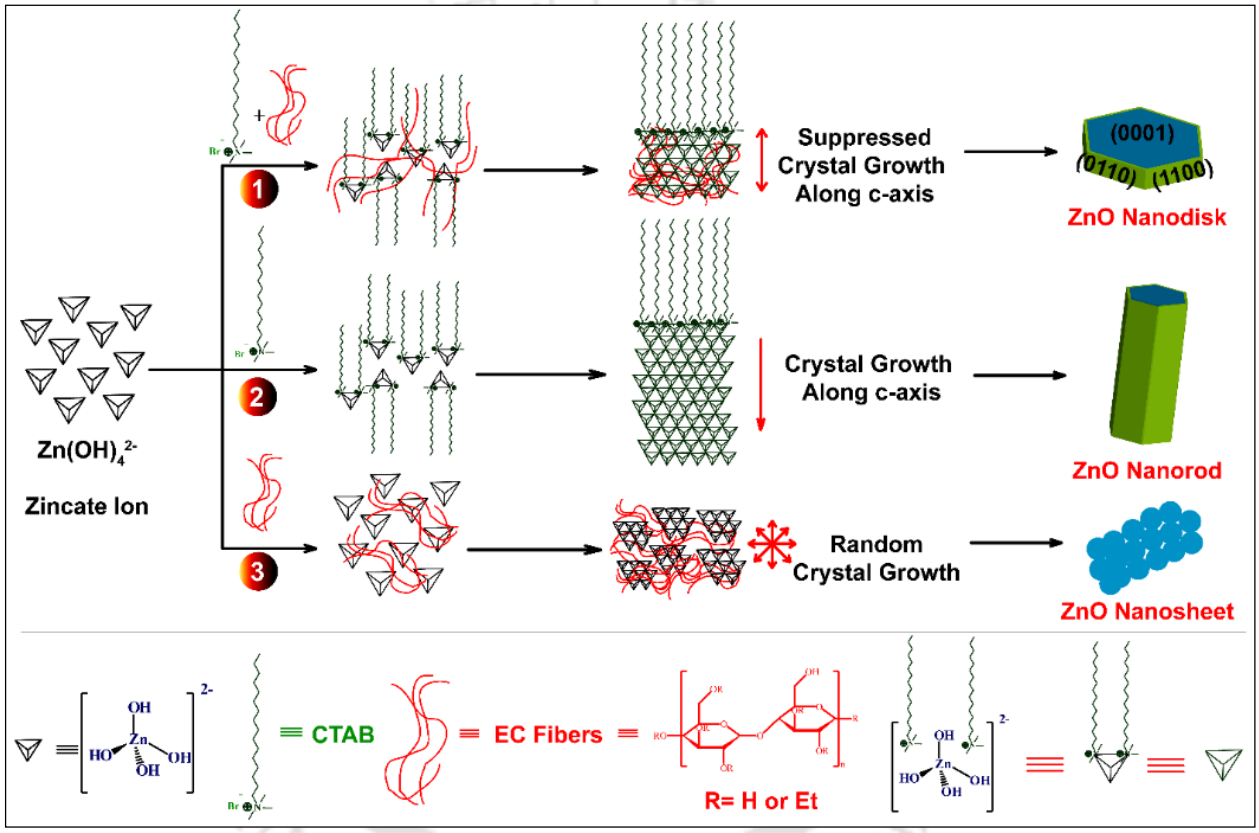

Scheme 3.3.1 Schematic representation of synthetic routes of ZnO nanodisks (NDs) (reaction 1), nanorods (NRs) (reaction 2), and nanosheets (NSs) (reaction 3) under three different reaction conditions.

Hence, the CTAB molecules are acting as structure directing agent while the EC molecules are playing the role of capping agent in the reaction system. On the basis of all the above experimental observations and discussions a plausible formation mechanism of ZnO NDs can be explained from the scheme **3.3.2**.

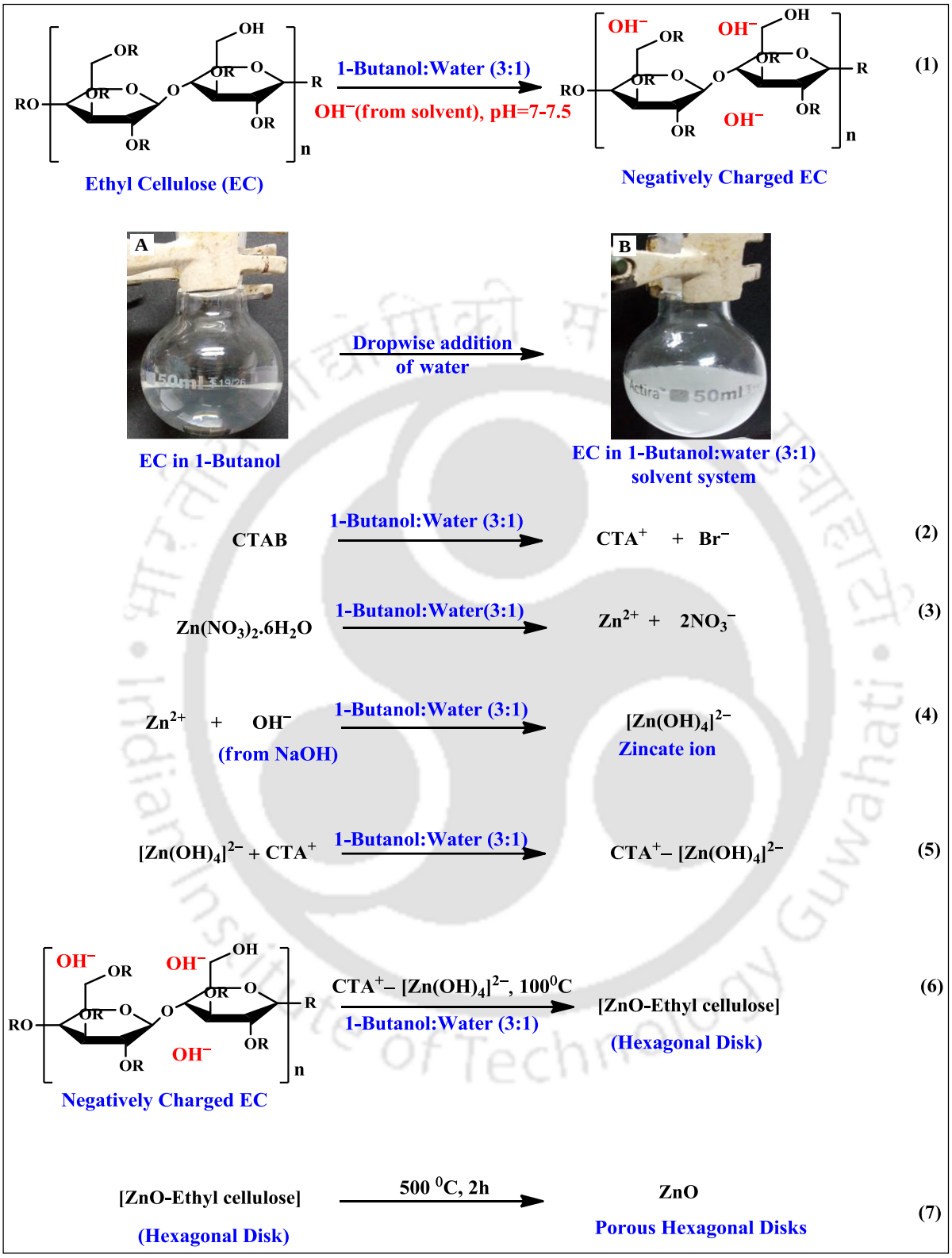

Scheme 3.3.2 Chemical reactions involved in formation of porous hexagonal ZnO NDs and digital images [(A) and (B)] of EC solutions in 1-butanol and 1-butanol: water (3:1) solvent system.

EC is a derivative of cellulose, comprising of an anhydroglucose (cellulose) repeating backbone in which high degree of hydroxy-groups on the anhydroglucose are converted into ethyl ether groups. It is insoluble in water, hydrophobic in nature and having no native charge. Jin *et al.* reported that EC molecules in a solvent and anti-solvent system (e.g., acetone: water) forms a turbid colloidal dispersion having apparent charge due to hydroxyl ion adsorption induced by the solvent.[54] In the present study, we have also observed formation of a stable colloidal dispersion of EC molecules in 1-butanol: water (3:1) solvent system [see images (A) and (B), scheme **3.3.2**]. Zeta potential (ζ) of the colloidal dispersion is found to be around −32 mV (reaction 1) while the net charge of the EC solution in 1-butanol is found to be almost zero. These negatively charged EC molecules are believed to electrostatically interact with the positively charged Zn^{2+} populated (0001) facets of polar ZnO during crystal growth and alter the crystal growth habits. CTAB is a cationic surfactant and completely ionizes in water as shown in reaction 2. It is well known that zinc nitrate ionizes in aqueous solutions and zinc cations readily react with hydroxide anions in basic reaction conditions to form stable tetrahedral $Zn(OH)_4^{2-}$ complexes which act as the growth units for various ZnO structures (reaction 3 and 4). In presence of CTA^+ ions, negatively charged zincate ions form CTA^+–$Zn(OH)_4^{2-}$ ion pairs due to their electrostatic interactions (reaction 5). Previously, Sun *et al.* had reported that CTA^+ ions can serve as a carrier for negative zincate [i.e., $Zn(OH)_4^{2-}$] and organizes the growth process of ZnO nanorod.[55] Additionally, CTAB molecules decreases the surface tension of the solution which decreases the energy needed to form a new phase. In the present reaction conditions, it is believed that the nucleation of ZnO from zincate ions are organized by CTA^+ ions, while the negatively charged EC molecules provide adsorption sites for the ZnO growth units, i.e., CTA^+-$Zn(OH)_4^{2-}$ ion pairs and adhere preferentially on the Zn^{2+} populated (0001) crystal surface to impede the CTAB assisted favorable *c*-axis growth of ZnO crystal and leads to the formation of hexagonal disk shaped ZnO (reaction 6). After calcination in air at 500 °C the EC molecules decomposes and escapes as CO_2 and H_2O from the ZnO hexagonal disks to develop pores (reaction 7).

3.3.3 UV-VISIBLE ABSORPTION AND PHOTOLUMINESCENCE ANALYSIS

Figure **3.3.8** (A) represents UV-vis absorption spectra for all the ZnO heterostructures, i.e., ZnO NS (black line), ZnO NR (red line) and ZnO ND (blue line). A moderate blue shift of absorption onset in case of ZnO NS (~ 25 nm) and ZnO NR (~ 20 nm) as compared to the ZnO ND is observed.

This may be due to smaller size of ZnO nanoparticles in ZnO NS and smaller size distribution of ZnO NR as compared to ZnO NDs. Inset to figure (A) depicts corresponding Tauc's plots to estimate the band gap values of all the samples, where $(\alpha h\nu)^2$ is plotted against the photon energy ($h\nu$) and α is the absorption coefficient. The band gap values of ZnO hetero-structures are estimated as 3.21 eV for ZnO NS, 3.18 eV for ZnO NR and 3.15 for ZnO ND. The observed lowering of band gap values for ZnO NR and ZnO ND in contrast to ZnO NS is in accordance with the blue shift of absorption profiles.

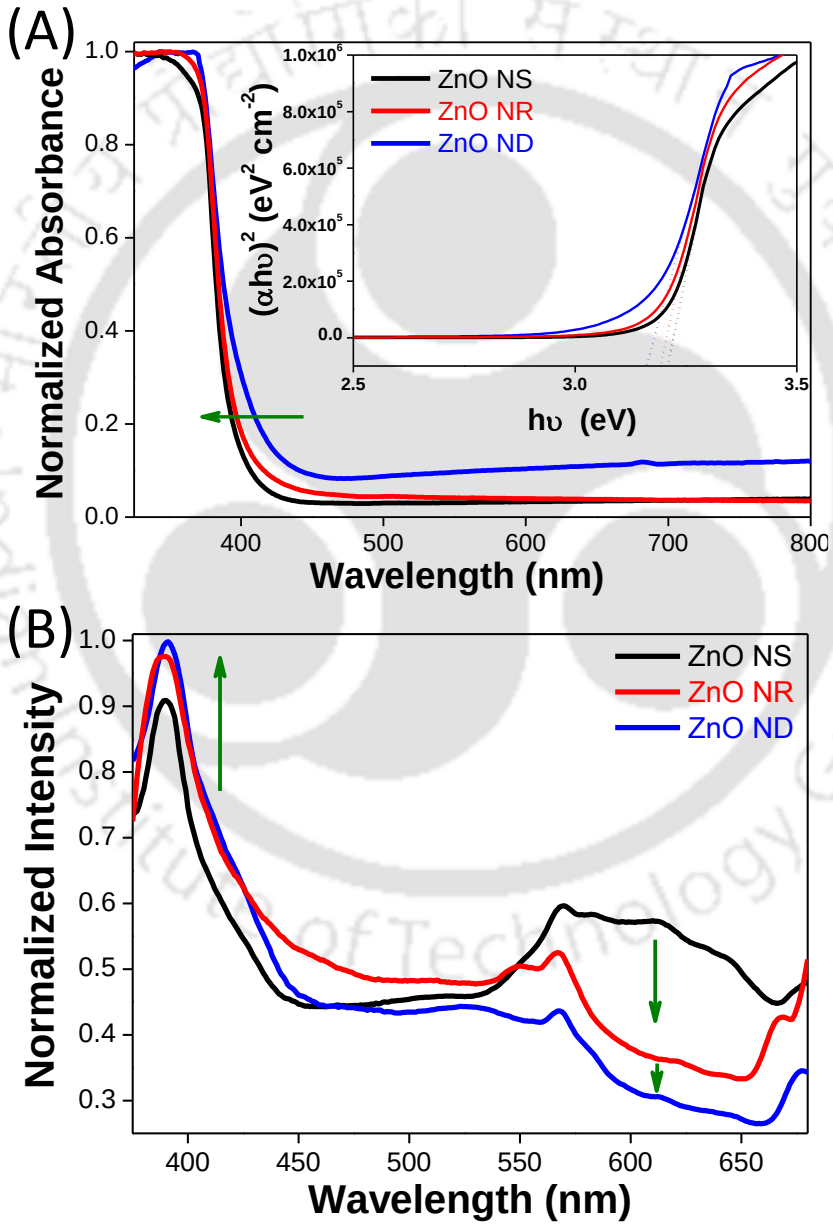

Figure 3.3.8 (A) UV-Visible absorption profile for all the ZnO heterostructures (ZnO NS, ZnO NR and ZnO ND). Inset shows corresponding Tauc's plots to estimate optical band gap values. **(B)** Steady state photoluminescence spectra for all the ZnO heterostructures.

Room-temperature steady state PL spectra of ZnO with different morphologies are carried out in order to analyze their emission characteristics, defect states and crystal quality as shown in Figure **3.3.8** (B). For all the samples sharp emissions in the UV range (~380 nm) and broad emission bands in the visible region (~580–680 nm) are observed. The sharp emission in the UV range is the near-band-edge emission and arises due to radiative exciton recombination while the emission peaks observed in the visible region is attributed to defect states in the ZnO crystal structure in which oxygen vacancies are the most probable source.[56,57] From figure (B), it is clear that the intensity of near-band-edge emission increases in the order ZnO NS< ZnO NR< ZnO ND while the intensity of broad emission band in the visible region is maximum for ZnO NS and gradually decreases from ZnO NR to ZnO ND. This is a clear reflection of minimum defect sites in ZnO ND and ZnO NR than ZnO NS which is beneficial for efficient photo-induced charge migration followed by collection in photovoltaic devices. It should be noted that ZnO NS are composed of numerous interconnected ZnO NP, for which probability of population of grain boundary induced defect sites will be maximum and is consistent with the PL analysis.

3.3.4 BET SURFACE AREA ANALYSIS

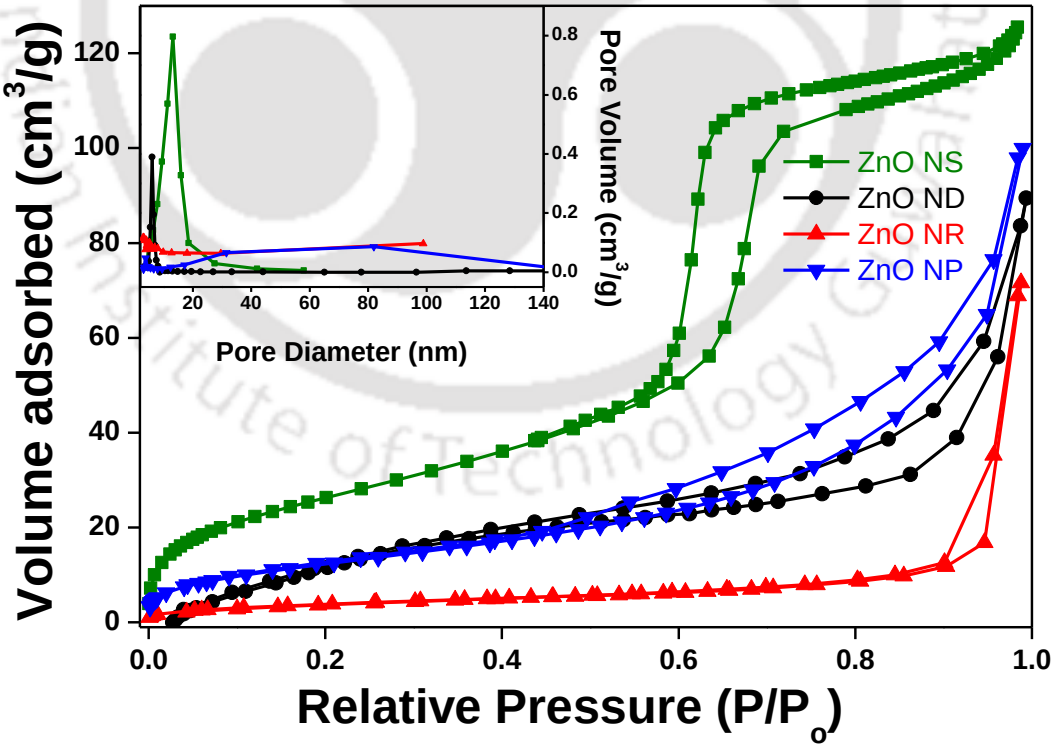

Figure 3.3.9. Nitrogen adsorption–desorption isotherms and Barrett–Joyner–Halenda (BJH) pore size distribution plots (inset) for as synthesized ZnO nanosheets, hexagon shaped ZnO nanodisks ZnO nanorods and ZnO nanoparticles.

Specific surface area of as synthesized ZnO heterostructures namely, ZnO NDs, ZnO NRs, ZnO NSs, and ZnO NPs are estimated from N_2 adsorption and desorption isotherms as shown in the figure **3.3.9**. For determination of pore size distribution in the samples, Barrett–Joyner–Halenda (BJH) curves are also recorded and displayed in the inset to figure **3.3.9**. Desired characteristics of a wide band gap semiconductor (i.e. Photoanodic materials) to be used in QDSSCs in order to achieve better photovoltaic performance is that it should have (i) high surface area and (ii) highly porous in nature. The observed BET surface area of the as-synthesized ZnO NS is found to be ~83 m^2g^{-1}, for ZnO NPs is 52 m^2g^{-1}, for ZnO ND is ~46 m^2g^{-1} and for ZnO NR is ~18 m^2g^{-1}. From the BJH pore size distribution curves (inset to figure 7), we have observed pore size distribution for ZnO NS is ~7–16 nm and for ZnO ND is ~5–8 nm, while there is no indication of pores in case of ZnO NR and ZnO NPs.

3.3.5 UV–VISIBLE ABSORPTION AND DIFFUSE REFLECTANCE ANALYSIS OF THE PHOTOANODES

Figure **3.3.10** (A) represents the normalized UV–vis diffuse reflectance spectra (DRS) of pristine ZnO ND film and CdS/CdSe co-sensitized ZnO NDs photoanodes with different Se precursor concentrations (0.0 mmol, 0.5 mmol, 1.0 mmol, 1.5 mmol and 2.0 mmol). Scan range is (200–800) nm for all the samples and recorded against a blank FTO as the reference. The characteristic absorption spectrum of ZnO NDs shows a steep absorption edge at ~380 nm. It is well known that, nanocrystalline CdS QDs absorb photon energy in the region (380–520 nm) while the CdSe QDs expand the absorption edge upto 750 nm. All the photoanodes absorbs UV as well as in the visible region, confirming the roles of all the components, i.e. ZnO, CdS and CdSe. With the increase in precursor concentration of Se in CBD process, the quantity of deposited CdSe QDs are increased in the photoanodes and absorption onsets are red shifted from 700 nm to 750 nm. The observed red shifting of the absorption onset is due to the subsequent growth of CdSe QDs[58]; thus absorbance of ZnO ND-CdS-CdSe photoanode prepared with 2 mM of Na_2SeSO_3 is higher than the other photoanodes due to the increased QD loading. Digital photograph of each sample (inset to Figure **3.3.10**) also indicates the gradual change in color from light brown to dark red with the increase in Se concentration demonstrating increased loading of CdSe QDs.

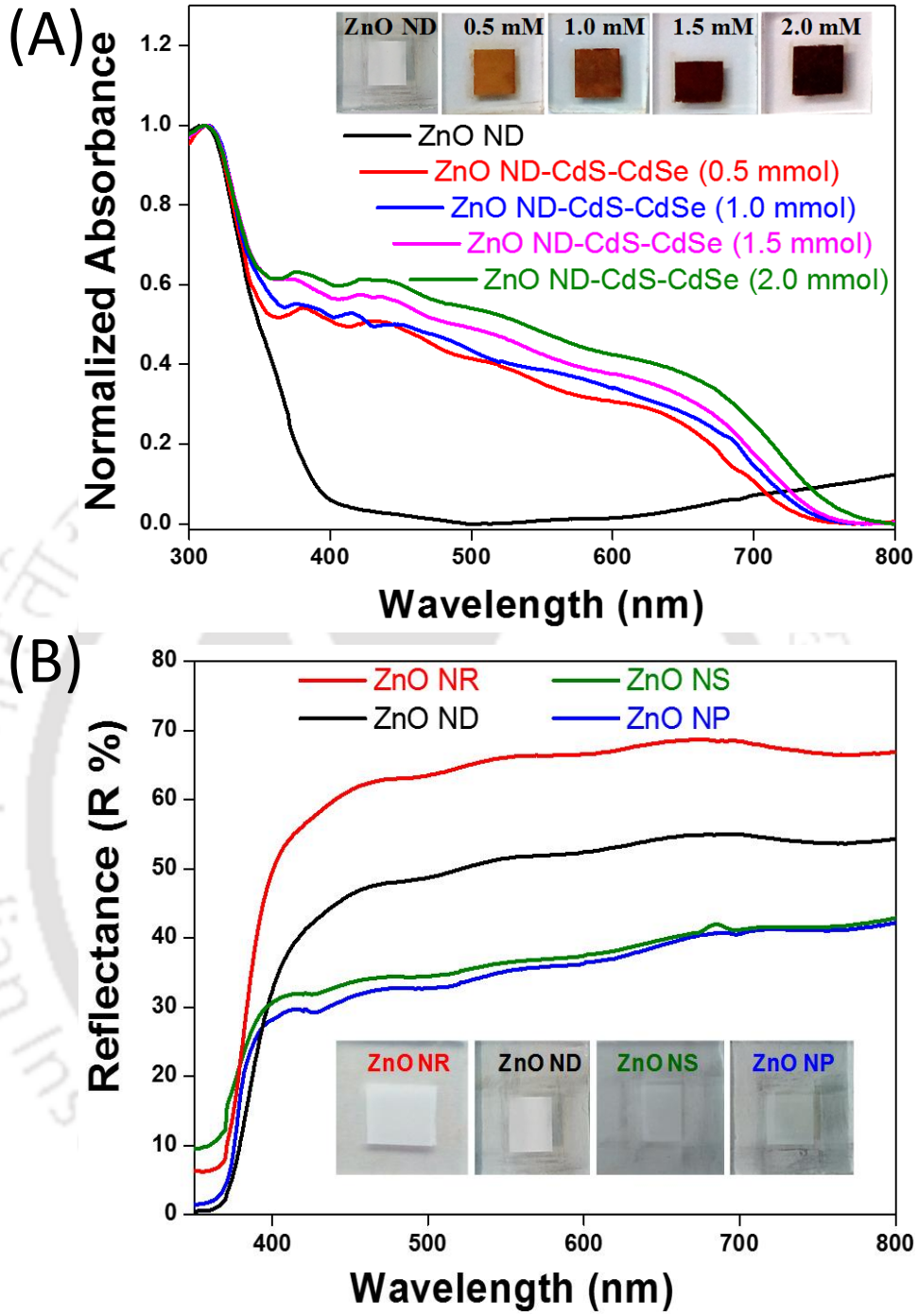

Figure 3.3.10 (A) UV-Vis diffused reflectance spectra of CdS/CdSe co-sensitized ZnO ND based photoanodes with different Se precursor concentrations during the chemical bath deposition (CBD) methods. Inset shows the digital photographs of all the photoanodes. **(B)** Diffuse reflectance spectra of the ZnO NR, ZnO ND, ZnO NS and ZnO NP based films of similar thickness on FTO substrates. Inset shows the digital photographs of both the films.

In order to investigate light scattering properties of all the photoanodic films of ZnO heterostructures, diffuse reflectance measurements are performed and analyzed. Figure **3.3.10** (B) represents diffuse reflectance spectra of ZnO NR, ZnO ND, ZnO NS and ZnO NP based films

deposited on FTO substrates. The ZnO NR film exhibits much higher reflectance in the wavelength range 420–800 nm in contrast to ZnO ND, ZnO NS and ZnO NP based films. This is an indication of higher light scattering ability of ZnO NR photoanode than the ZnO ND, ZnO NS and ZnO NP based photoanodes.[4,59]

3.3.6 PHOTOVOLTAIC CHARACTERISTICS OF THE SOLAR CELLS

Figure **3.3.11** (A) shows the current density–voltage (*J–V*) characteristics of the CdS/CdSe co-sensitized ZnO ND based solar cells for optimization of CdSe QD loading under AM 1.5G simulated sunlight with a light intensity of 100 mW cm^{-2}. The photovoltaic parameters such as short circuit current density (J_{sc}), open circuit voltage (V_{oc}), fill factor (*FF*) and the overall power conversion efficiency (PCE, η) of all devices are listed in the table **3.3.1**.

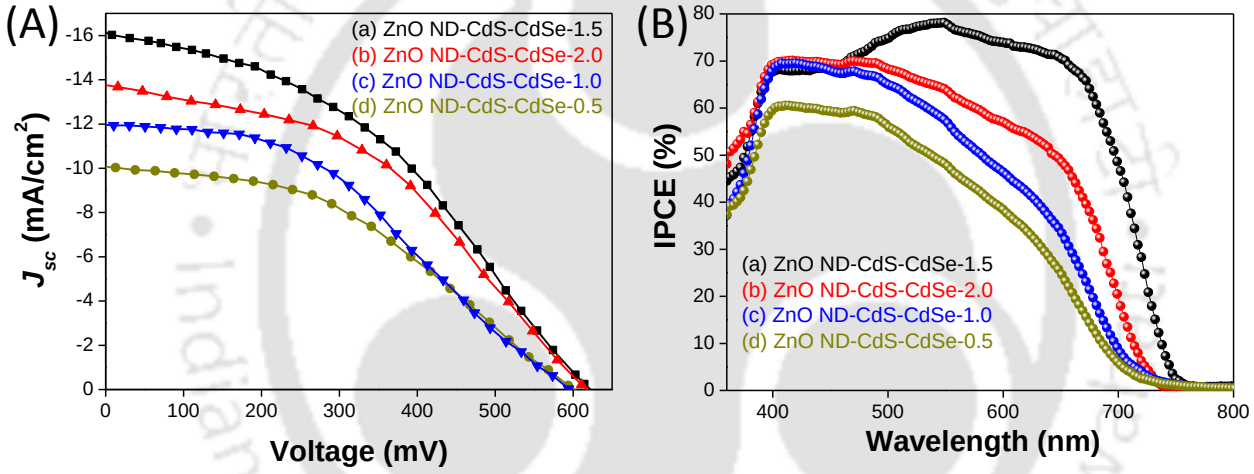

Figure 3.3.11 (A) Current density–voltage (*J–V*) curves for the photovoltaic devices (a) ZnO ND-CdS-CdSe (1.5), (b) ZnO ND-CdS-CdSe (2.0), (c) ZnO ND-CdS-CdSe (1.0) and (d) ZnO ND-CdS-CdSe (0.5) under AM 1.5 G solar illumination **(B)** IPCE plots for the respective devices employing S^{2-}/S_n^{2-} as the redox couple.

Table 3.3.1 Short-circuit current density (J_{sc}), open-circuit voltage (V_{oc}), fill factor (*FF*), and power conversion efficiency (η) for the fabricated solar cells incorporating different photoanodes.

Devices	J_{sc} (mA/cm^2)	V_{oc} (mV)	*FF* (%)	PCE (η %)	Redox couple
(a) ZnO ND-CdS-CdSe (1.5)	16.0 (± 0.6)	620 (± 26)	49 (± 2.5)	4.86 (±0.33)	S^{2-}/S_n^{2-}
(b) ZnO ND-CdS-CdSe (2.0)	13.7 (± 0.5)	619 (± 25)	48 (± 1.4)	4.15 (±0.27)	S^{2-}/S_n^{2-}
(c) ZnO ND-CdS-CdSe (1.0)	12.0 (± 0.4)	595 (± 25)	45 (± 1.3)	3.21 (±0.25)	S^{2-}/S_n^{2-}
(d) ZnO ND-CdS-CdSe (0.5)	10.1 (± 0.6)	602 (± 33)	47 (± 1.8)	2.83 (±0.24)	S^{2-}/S_n^{2-}

From table **3.3.1**, we have observed that the device (a) based on the photoanode with ZnO ND-CdS-CdSe (1.5), i.e., CdSe deposition with Se precursor solution of 1.5 mM concentration, exhibits maximum PCE(~4.86 %), whilst lowest PCE (~2.83 %) is observed for the device based on the photoanode, ZnO ND-CdS-CdSe (0.5) which is due to low CdSe QD loading. For the

devices (a), (c) and (d) with photoanodes ZnO ND-CdS-CdSe (1.5) [$J_{sc} \approx 16.0$ mA/cm^2], ZnO ND-CdS-CdSe (1.0) [$J_{sc} \approx 12.0$ mA/cm^2] and ZnO ND-CdS-CdSe (0.5) [$J_{sc} \approx 10.1$ mA/cm^2] respectively, as the amount of CdSe deposition increases, the J_{sc} values also increases consistently resulting in higher PCE values. But for the device (b), with ZnO ND-CdS-CdSe (2.0) photoanode, the J_{sc} value drops to ~13.7 mA/cm^2 and consequently decreasing the PCE value to ~4.15 %; possibly due to agglomeration of CdSe QDs with increase in QD loading which increases recombination of the photo-induced electron in the photoanode. Additionally, the formation of crystalline impurities such as SeO_2, CdO etc in the ZnO ND-CdS-CdSe (2.0) photoanode are being probed, which can quench the J_{sc} value, by powder X-ray diffraction (PXRD) analysis as shown in figure **3.3.12**.

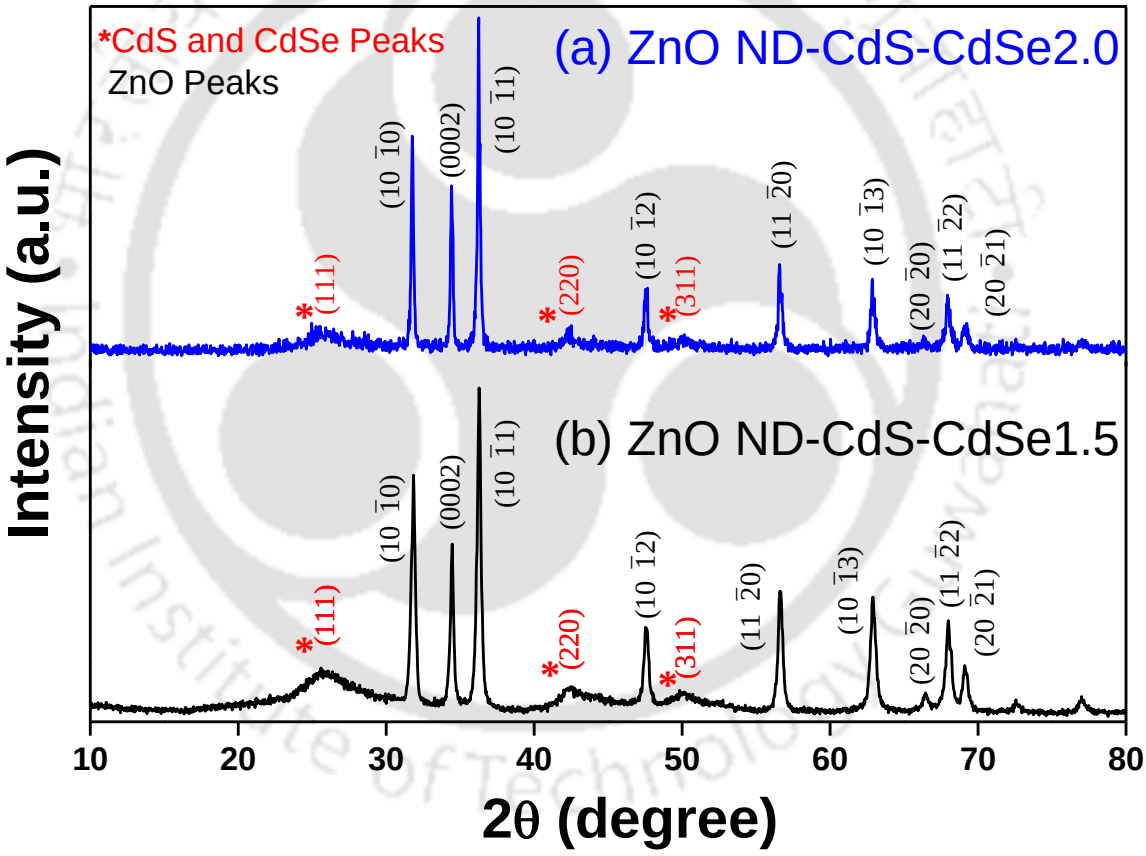

Figure 3.3.12 Powder X-ray Diffraction pattern for the photoanodes (a) ZnO ND-CdS-CdSe2.0 and (b) ZnO ND-CdS-CdSe1.5 respectively.

From figure **3.3.12** it is clear that, no detectable impurity peaks are observed in the PXRD pattern of ZnO ND-CdS-CdSe2.0. This result is in accordance with our claim of decrease in J_{sc} for the device (b) with (ZnO ND-CdS-CdSe2.0) photoanode which is mainly due to agglomeration of CdSe QDs. A schematic presentation of higher charge recombination in the ZnO ND-CdS-

CdSe2.0 photoanode as compared to the ZnO ND-CdS-CdSe1.5 photoanode is illustrated in scheme **3.3.3**.

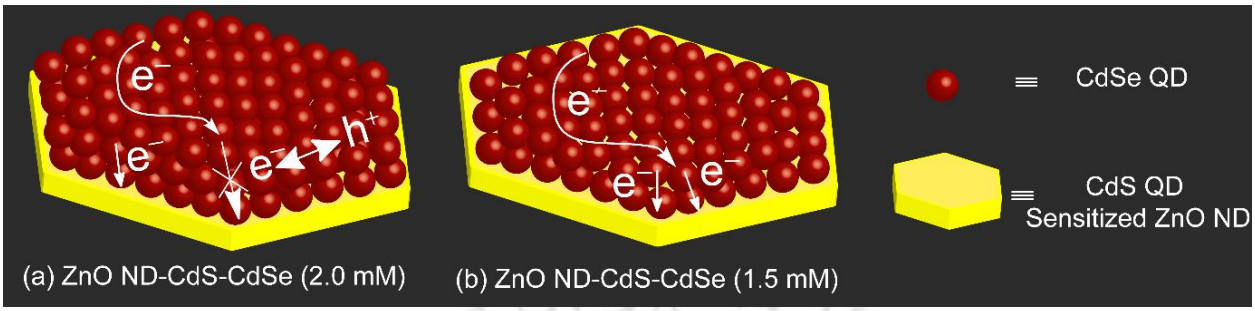

Scheme 3.3.3 Schematic presentation of charge recombination in (a) ZnO ND-CdS-CdSe (2.0 mM) photoanode compared to the (b) ZnO ND-CdS-CdSe (1.5 mM) due to agglomeration of CdSe QDs.

Figure **3.3.11** (B) illustrates the incident photon-to-current conversion efficiency (IPCE) as a function of wavelength for all the fabricated QDSSCs. Increasing trend of J_{sc} values for the devices, i.e., (d) < (c) < (b) < (a) is also explicit in the IPCE plot; device (a) is exhibiting the maximum IPCE value as high as ~80 % in the measured wavelength range (450-700 nm) while minimum for device (d). Maximum IPCE value obtained for the device (a) with photoanode ZnO ND-CdS-CdSe (1.5) is indicating minimum photo-induced electron recombination and better light harvesting ability than the other three devices, i.e. ZnO ND-CdS-CdSe (2.0) [device (b), ~70-60 %], ZnO ND-CdS-CdSe (1.0) [device (c), ~70-55 %] and ZnO ND-CdS-CdSe (0.5) [device (d), ~60-40 %]. Hence from all the above discussions it is concluded that for optimal loading of CdSe QDs in ZnO ND photoanode, concentration of Se precursor should be kept at 1.5 mmol in the CBD method of CdSe QD sensitization.

In order to ensure the superiority of ZnO NDs in light harnessing ability, we have compared the photovoltaic parameters of highest performed solar cell device, i.e. device (a) ZnO ND-CdS-CdSe (1.5) with similar type of device fabricated with conventional ZnO NPs, as synthesized ZnO NRs and ZnO NSs. Figure **3.3.13** (A) represents characteristic current density–voltage (*J*–*V*) curves for optimized CdS/CdSe co-sensitized ZnO ND, ZnO NP, ZnO NR and ZnO NS based devices. Figure **3.3.13** (B) shows IPCE plots for the respective devices. Photovoltaic parameters such as short circuit current density (J_{sc}), open circuit voltage (V_{oc}), fill factor (*FF*) and the overall power conversion efficiency (PCE, η) for all the fabricated devices are listed in table **3.3.2**.

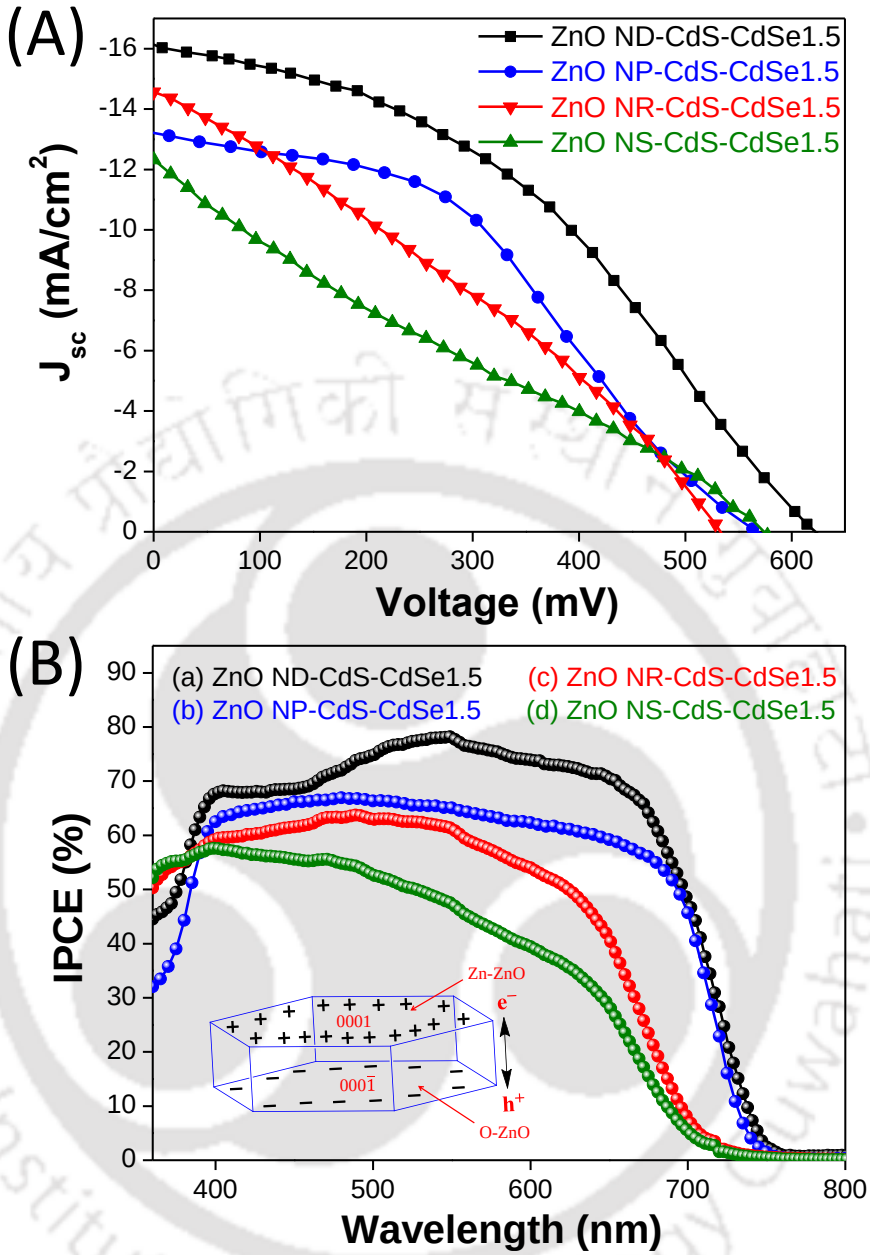

Figure 3.3.13 (A) Current density–voltage (*J–V*) curves for the photovoltaic devices (a) ZnO ND-CdS-CdSe (1.5) [black line], (b) ZnO NP-CdS-CdSe (1.5) [blue line], (c) ZnO NR-CdS-CdSe (1.5) [red line] and (d) ZnO NS-CdS-CdSe (1.5) [olive line] **(B)** IPCE plots for the respective devices employing S^{2-}/S_n^{2-} as the redox couple. Inset shows schematic illustration of charge separation model between polar Zn-populated (0001) [i.e., Zn-ZnO] and O-populated ($000\bar{1}$) [i.e., O-ZnO] surfaces.

Table 3.3.2 Short-circuit current density (J_{sc}), open-circuit voltage (V_{oc}), fill factor (*FF*), and power conversion efficiency (η) for the fabricated solar cells incorporating different photoanodes.

Devices	J_{sc}(mA/cm^2)	V_{oc}(mV)	*FF* (%)	PCE (η %)	Redox couple
(a) ZnO ND-CdS-CdSe (1.5)	16.0 (± 0.6)	620 (± 26)	49 (± 2.5)	4.86 (±0.33)	S^{2-}/S_n^{2-}
(b) ZnO NP-CdS-CdSe (1.5)	13.2 (± 0.5)	567 (± 20)	42 (±2.3)	3.14 (±0.15)	S^{2-}/S_n^{2-}
(c) ZnO NR-CdS-CdSe (1.5)	14.6 (± 0.8)	534 (±20)	32 (± 2.3)	2.52 (±0.15)	S^{2-}/S_n^{2-}
(d) ZnO NS-CdS-CdSe (1.5)	12.4 (± 1.0)	577 (± 28)	23 (± 2.4)	1.64 (± 0.2)	S^{2-}/S_n^{2-}

Form figure **3.3.13** (A) and (B), higher J_{sc} value and IPCE of ZnO ND based device in contrast to the ZnO NP, ZnO NR and ZnO NSs based devices indicates better absorption of solar irradiation by the ZnO ND based photoanode probably due to better photo-induced charge separation and collection. In principle the IPCE of a solar cell is dependent on (i) the light harvesting efficiency, (ii) the quantum yield of electron injection and (iii) the efficiency of collecting injected electrons.[60] Better light harvesting ability of the ZnO ND based device is attributed to the enhanced light confinement (over ZnO NP and ZnO NS based photoanodes) in the photoanode and efficient sensitization with CdS and CdSe QDs boosted by high surface area (~46 m^2g^{-1}), which upsurges the flux of photoinduced electron injection for an esteemed value of short circuit current density (J_{sc} ≈16 mA cm^{-2}). From table **3.3.2**, an appreciated value of J_{sc} for ZnO NR based device (~14.6 mA/cm^2) is observed relative to ZnO ND based device (~16.0 mA/cm^2). This is mainly due to high crystallinity and minimum intrinsic defect sites in the ZnO nanorods as evident from the powder X-ray diffraction (PXRD) pattern and photoluminescence (PL) analysis. Additionally, higher light scattering ability of ZnO NR based photoanode is noted than the ZnO ND based photoanode [see figure 3.3.10 (B)], which contributed towards an elevated value of short circuit density. Deprived V_{oc} and *FF* of the ZnO NP (~567 mV and ~42 % respectively), ZnO NR (~534 mV and ~32 % respectively) and ZnO NS based devices (~577 mV and ~23 % respectively) as compared to the ZnO ND based device (~620 mV and ~49 % respectively) are indicative of inferiority in efficient charge separation and regeneration of oxidized sensitizer particles. Enhanced charge separation in the ZnO ND based device can be well explained with the help of a charge separation model between reactive polar Zn-populated (0001) [i.e., Zn-ZnO] and O-populated ($000\bar{1}$) [i.e., O-ZnO] surfaces; proposed by Chen et al.[61] as depicted in the inset to figure (B) on the basis of periodic DFT calculations. Since ZnO ND is a polar single crystal with exposed Zn^{2+} populated (0001) and O^{2-} populated ($000\bar{1}$) surfaces, an internal electric field is expected to be generated between the two planes due to spontaneous polarization. When ZnO NDs are employed as a photoanodic material in the solar cell devices, the photo-injected electrons from the sensitizer particles, i.e. CdS and CdSe, will be migrated towards positive polar (0001)–Zn-ZnO surfaces under the internal electric field and diffuses through the photo-anode film to the external circuit. Additionally, single crystalline nature of the ZnO ND with less intrinsic defect sites, facilitate the photo-induced electron diffusion process in the photoanode and enhances the charge separation to increase V_{oc} and *FF* of the device. As a consequence, the ZnO ND based device is furnishing a PCE value of

~4.86 %, while ~3.14 % for ZnO NP and ~2.52 % for ZnO NR based devices. It is noteworthy that the surface area of ZnO NS (~83 m^2g^{-1}) is higher than ZnO NP (~52 m^2g^{-1}) and ZnO ND (~46 m^2g^{-1}) and ZnO NR (18 m^2g^{-1}) and hence the expected trend of sensitizer particle loading will be ZnO NS> ZnO NP > ZnO ND > ZnO NR. However, we have observed that the absorption intensity in the visible region is highest for ZnO NP and lowest for ZnO NS based photoanodes as shown in figure **3.3.14**, which implies the actual trend of sensitizer particle loading is ZnO NP> ZnO ND> ZnO NR> ZnO NS.

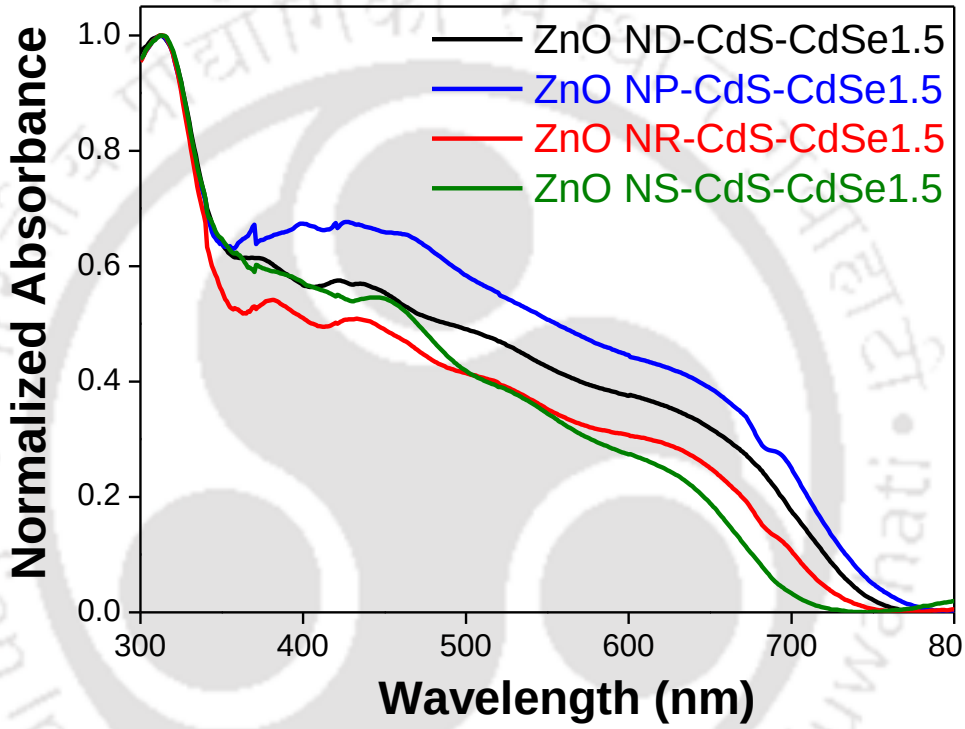

Figure 3.3.14 UV-visible diffused reflectance spectra of CdS/CdSe co-sensitized ZnO ND, ZnO NP, ZnO NR and ZnO NS based photoanodes with 1.5 mM Se precursor concentration used during the chemical bath deposition (CBD) methods.

Probable explanation for this observation is the layered structure of ZnO NSs, which causes minimum pore formation due to inter-particle stacking in the photoanode. Note that ZnO NS are composed of numerous interlinked ZnO nanoparticles with number of pores (i. e., intra-particle pores). After deposition of optimum CdS QDs, both the intra-particle and inter particle pores are clogged and inhibit the diffusion of CdSe QDs in the film during sensitization process. Consequently, minimum deposition of CdSe QDs in the ZnO NS based photoanode is observed. This claim is also supported by the poor value of FF observed for the ZnO NS (~23 %) based device than that of ZnO ND (~49 %), ZnO NP (~42 %) and ZnO NR (~32 %) based devices, which

reflects slower regeneration of sensitizer particles by the redox couple in the ZnO NS based device. This may be caused by minimum available pores in the ZnO NS based photoanode for electrolyte diffusion relative to the ZnO ND, ZnO NP and ZnO NR based photoanodes. It is well known that the values of FF reflect sensitizer particle regeneration kinetics by the redox couple and photoinduced charge separation in the devices.

To further gain insight into the electron transport and recombination kinetics in the photovoltaic devices namely, (a) ZnO ND-CdS-CdSe (1.5), (b) ZnO NP-CdS-CdSe (1.5), (c) ZnO NR-CdS-CdSe (1.5) and (d) ZnO NS-CdS-CdSe (1.5); electrochemical impedance spectroscopy (EIS) is employed as shown in figure **3.3.15** (A) and (B), recorded under dark condition in a frequency range from 0.1 Hz to 100 kHz at the applied bias equivalent to the open-circuit voltages. From the figure (A) it is observed that all Nyquist plots are composed of two semicircles: one in the medium-frequency region (right semicircle) is due to the charge-transfer process at the working electrode/electrolyte interface while another in the high-frequency region (left semicircle) is attributed to the redox reaction at the counter electrode/electrolyte interface.[62] As can be seen from figure **3.3.15** (A), diameter (R_k) of the right semicircle for the ZnO ND based device is larger relative to that of all other device and the increasing trend of R_k is ZnO NS < ZnO NP < ZnO NR < ZnO ND. It is well-known that R_k is mainly determined by the charge recombination resistance with partial contribution from transport resistance.[51] Large value of R_k for ZnO ND based device implies retarded backward reaction of QD injected electron at the ZnO ND/CdS-CdSe/electrolyte interface or lesser interfacial charge recombination with holes of the electrolyte in the device. This observation supports our claim of faster and efficient charge transport through the single crystalline ZnO NDs in the entire photoanode due to its single crystalline and exposed polar facets which is causing higher FF for the device (~49 %). Moreover, the photovoltaic devices behave like a diode on the applied bias voltage, R_k is considered as a part of shunt resistance (R_{sh}).[15] The relation between R_{sh} and *FF* can be expressed by the following equation:

$$FF = FF_o\left(1 - \frac{1}{R_{sh}}\right)$$

Where, FF_0 is the theoretical maximum *FF*. It can be expected that as a result of an increase in R_{sh} in the QDSSC assembled with the ZnO NDs, larger value of *FF* is perceived. On the other hand, the effect of charge separation boosted by exposed polar facets in ZnO NR based devices is minimum for which the observed charge recombination resistance is lesser than the ZnO ND based

devices. However, in case of ZnO NP and ZnO NS devices the photo-induced electrons interact repeatedly with the traps in the grain boundaries as they undertake a random movement throughout the film. As a consequence, recombination reactions in these two photoanodes (ZnO NP and ZnO NS) become more prominent than in the ZnO ND based photoanode which is reflected in the deprived values of *FF* and V_{oc} for the devices.

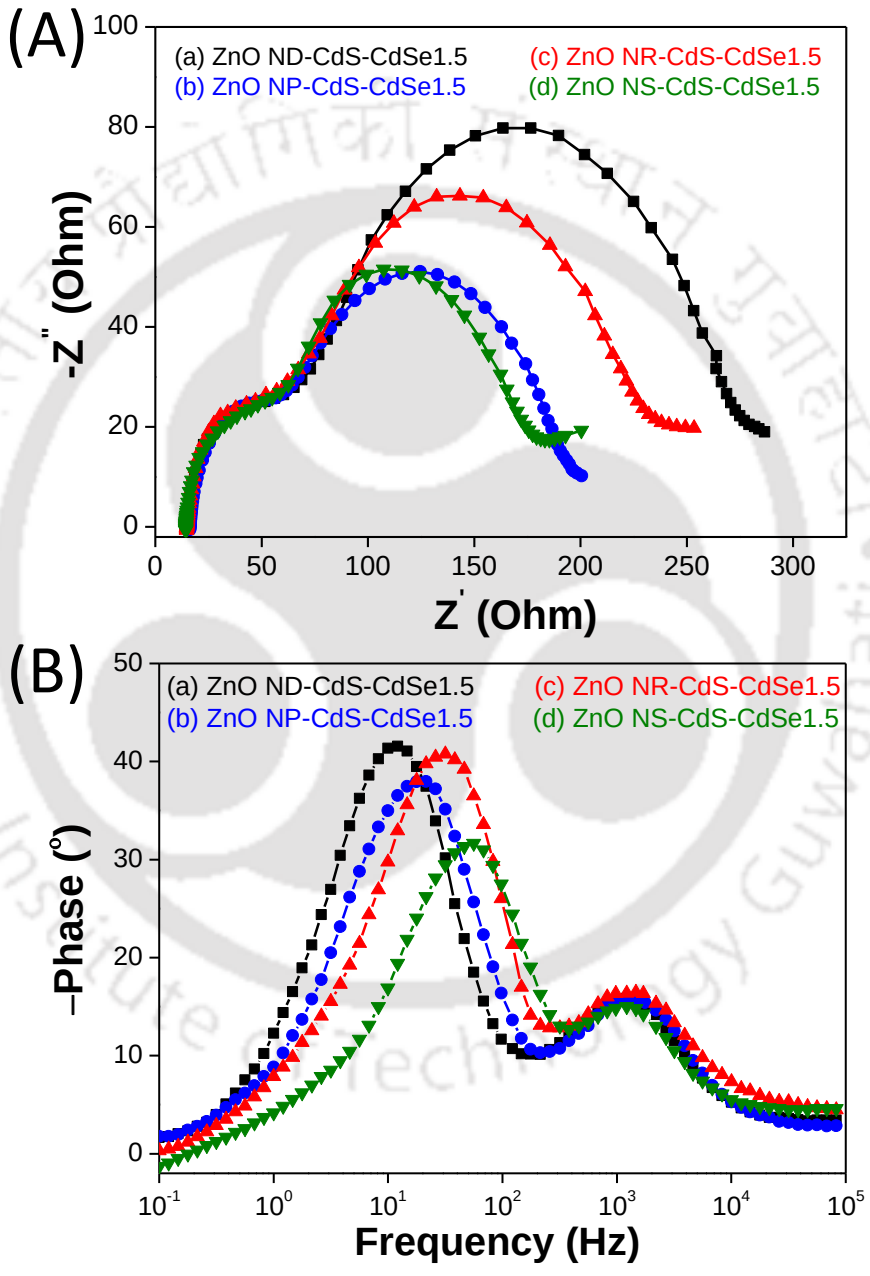

Figure 3.3.15 (A) Nyquist plots for photovoltaic devices (a) ZnO ND-CdS-CdSe (1.5) [black line], (b) ZnO NP-CdS-CdSe (1.5) [blue line], (c) ZnO NR-CdS-CdSe (1.5) [red line] and (d) ZnO NS-CdS-CdSe (1.5) [olive line] in dark at open-circuit voltage and in a frequency range from 0.1 Hz to 100 kHz. **(B)** Bode phase plots for the respective devices.

Bode phase plots for all the fabricated devices are presented in the figure **3.3.15** (B). Characteristic peak frequencies in the medium frequency region (f_{max}) for the ZnO NS, ZnO NR and ZnO NP based device is located at ~56.2 Hz, ~31.6 Hz and ~21.5 Hz while for the ZnO ND based device is found to be ~12.1 Hz. We have calculated the photo-induced electron life time (τ_e) in the CB of ZnO NS, ZnO NR, ZnO NP and ZnO ND by using the formula ($\tau_e = \frac{1}{2\pi f_{max}}$)[63] and are found to be ~2.8 ms, ~5.0 ms, ~7.4 ms, and ~13.1 ms respectively. The increase in electron life time further confirms minimized photo-induced electron interception to the S^{2-}/S_n^{2-} redox shuttle in the ZnO ND device than all other devices. As a result, photo-induced electron density in the CB level of ZnO ND increases, leading to a higher value of Short circuit current density (J_{sc}) which is contributed towards increased trend of power conversion efficiency (η) of the devices.

3.4 CONCLUSIONS

We have developed a synthetic protocol for mesoporous hexagonal ZnO NDs with exposed ±(0001) polar facets utilizing ethyl cellulose (EC) and Cetyl-trimethyl-ammonium bromide (CTAB) as capping and structure directing agents. A plausible mechanism of ZnO ND formation is proposed based on the controlled reaction conditions by varying the additive sequences of EC and CTAB and pervious works available in literature. In presence of only EC, ZnO NSs are obtained while in presence of only CTAB - ZnO NRs formation is observed due to CTAB assisted c-axis growth of ZnO crystal. Photovoltaic properties of the hexagon shaped ZnO NDs as a photoanodic material for CdS/CdSe co-sensitized solar cells shows a PCE upto ~4.86 %. Superiority of the ZnO ND based device is proved by comparing the cell performance with the similar device fabricated with conventional ZnO NPs (PCE ~3.14 %), ZnO NRs (PCE ~2.52 %) and ZnO NSs (PCE ~1.64 %). Higher PCE obtained for the ZnO ND based device is mainly due to efficient photo-induced charge separation boosted by the exposed polar ±(0001) facets. EIS analysis further explains higher V_{oc} and *FF* values for the ZnO NDs based photoanode attributed to slower electron-hole (e^-–h^+) recombination rate and faster charge migration. Larger value of photoinduced electron lifetime is observed in case of ZnO ND photovoltaic device relative to all other fabricated devices which confirms minimum leakage of trapped electrons in the conduction band level of ZnO NDs, resulting higher values of open circuit voltage (V_{oc}) and short circuit current density (J_{sc}).

3.5 REFERENCES

(1) Guillen, E.; Peter, L. M.; Anta, J. A. *J. Phys. Chem. C*, **2011**, *115*, 22622.

(2) Anta, J. A.; Guillen, E.; Tena-Zaera, R. *J. Phys. Chem. C*, **2012**, *116*, 11413.

(3) Ramgir, N. S.; Late, D. J.; Bhise, A. B.; More, M. A.; Mulla, I. S.; Joag, D. S.; Vijayamohanan, K. *J. Phys. Chem. B*, **2006**, *110*, 18236.

(4) Chetia, T. R.; Barpuzary, D.; Qureshi, M. *Phys. Chem. Chem. Phys.*, **2014**, *16*, 9625.

(5) Law, M.; Greene, L. E.; Johnson, J. C.; Saykally, R.; Yang, P. *Nat. Mater.*, **2005**, *4*, 455.

(6) Li, C.; Yang, L.; Xiao, J.; Wu, Y.-C.; Søndergaard, M.; Luo, Y.; Li, D.; Meng, Q.; Iversen, B. B. *Phys. Chem. Chem. Phys.*, **2013**, *15*, 8710.

(7) Seol, M.; Kim, H.; Taka, Y.; Yong, K. *Chem. Commun.*, **2010**, *46*, 5521.

(8) Seol, M.; Ramasamy, E.; Lee, J.; Yong, K. *J. Phys. Chem. C*, **2011**, *115*, 22018.

(9) Chen, J.; Wu, J.; Lei, W.; Song, J. L.; Deng, W. Q.; Sun, X. W. *Appl. Surf. Sci.*, **2010**, *256*, 7438.

(10) Barpuzary, D.; Patra, A. S.; Vaghasiya, J. V.; Solanki, B. G.; Soni, S. S.; Qureshi, M. *ACS Appl. Mater. Interfaces*, **2014**, *6*, 12629.

(11) Luo, L.; Lv, G.; Li, B.; Hu, X.; Jin, L.; Wang, J.; Tang, Y. *Thin Solid Films*, **2010**, *518*, 5146.

(12) Cheng, H. M.; Huang, K. Y.; Lee, K. M.; Yu, P.; Lin, S. C.; Huang, J. H.; Wu, C. G.; Tang, J. *Phys. Chem. Chem. Phys.*, **2012**, *14*, 13539.

(13) Lin, C. Y.; Lai, Y. H.; Chen, H. W.; Chen, J. G.; Kung, C. W.; Vittal, R.; Ho, K. C. *Energy Environ. Sci.*, **2011**, *4*, 3448.

(14) Jiang, C. Y.; Sun, X. W.; Lo, G. Q.; Kwong, D. L. *Appl. Phys. Lett.*, **2007**, *90*, 263501.

(15) Tian, J.; Lv, L.; Wang, X.; Fei, C.; Liu, X. Zhao, Z.; Wang, Y.; Cao, G. *J. Phys. Chem. C*, **2014**, *118*, 16611.

(16) Dong, Z.; Lai, X.; Halpert, J. E.; Yang, N.; Yi, L.; Zhai, J.; Wang, D.; Tang, Z.; Jiang, L. *Adv. Mater.*, **2012**, *24*, 1046.

(17) Navaneethan, M.; Archana, J.; Arivanandhan, M.; Hayakawa, Y. *Phys. Status Solidi RRL*, **2012**, *6*, 120.

(18) Wang, J. X.; Wu, C. M. L.; Cheung, W. S.; Luo, L. B.; He, Z. B.; Yuan, G. D.; Zhang, W. J.; Lee, C. S.; Lee, S. T. *J. Phys. Chem. C*, **2010**, *114*, 13157.

(19) Boppella, R.; Anjaneyulu, K.; Basak, P.; Manorama, S. V. *J. Phys. Chem. C*, **2013**, *117*, 4597.

(20) Jang, E. S.; Won, J. H.; Hwang, S. J.; Choy, J. H. *Adv. Mater.*, **2006**, *18*, 3309.

(21) Xu, L.; Hu, Y. L.; Pelligra, C.; Chen, C. H.; Jin, L.; Huang, H.; Sithambaram, S. K.; Aindow, M.; Joesten, R.; Suib, S. L. *Chem. Mater.*, **2009**, *21*, 2875.

(22) Huang, M.; Weng, S.; Wang, B.; Hu, J.; Fu, X.; Liu, P. *J. Phys. Chem. C*, **2014**, *118*, 25434.

(23) Huang, M.; Yan, Y.; Feng, W.; Weng, S.; Zheng, Z.; Fu, X.; Liu, P. *Cryst. Growth Des.*, **2014**, *14*, 2179.

(24) Han, X. G.; He, H. Z.; Kuang, Q.; Zhou, X.; Zhang, X. H.; Xu, T.; Xie, Z. X.; Zheng, L. S. *J. Phys. Chem. C*, **2009**, *113*, 584.

(25) Mclaren, A.; Valdes-Solis, T.; Li, G.; Tsang, S. C. *J. Am. Chem. Soc.*, **2009**, *131*, 12540.

(26) Meagley, K. L.; Garcia, S. P. *Cryst. Growth Des.*, **2011**, *12*, 707.

(27) Li, F.; Ding, Y.; Gao, P.; Xin, X.; Wang, L. Z. *Angew. Chem.*, **2004**, *116*, 5350.

(28) Changb, P. R.; Yua, J.; Ma, X. *Carbohydr. Polym.*, **2011**, *83*, 1016.

(29) Kavitha, M. K.; John, H.; Gopinath, P. *Mater. Res. Bull.*, **2014**, *49*, 132.

(30) Rao, J.; Yu, A.; Shao, C.; Zhou, X. *ACS Appl. Mater. Interfaces*, **2012**, *4*, 5346.

(31) Wang, A. J.; Liao, Q. C.; Feng, J. J.; Zhang, P. P.; Li, A. Q.; Wang, J. J. *CrystEngComm*, **2012**, *14*, 256.

(32) Tseng, Y. H.; Lin, H. Y.; Liu, M. H.; Chen, Y. F.; Mou, C. Y. *J. Phys. Chem. C*, **2009**, *113*, 18053.

(33) Ma, J.; Su, S.; Fu, W.; Yang, H.; Zhou, X.; Yao, H.; Chen, Y.; Yang, L.; Sun, M.; Mu, Y.; Lv, P. *CrystEngComm*, **2014**, *16*, 2910.

(34) Chen, H.; Li, W.; Liu, H.; Zhu, L. *Electrochem. commun.*, **2011**, *13*, 331.

(35) Yu, W. W.; Qu, L.; Guo, W.; Peng, X. *Chem. Mater.*, **2003**, *15*, 2854.

(36) Leatherdale, C. A.; Woo, W. K.; Mikulec, F. V.; Bawendi, M. G. *J. Phys. Chem. B*, **2002**, *106*, 7619.

(37) Kan, S.; Mokari, T.; Rothenberg, E.; Banin, U. *Nat. Mater.*, **2003**, *2*, 155.

(38) Trinh, M. T.; Houtepen, A. J.; Schins, J. M.; Hanrath, T.; Piris, J.; Knulst, W.; Goossens, A. P. L. M.; Siebbeles, L. D. A. *Nano Lett.*, **2008**, *8*, 1713.

(39) Kamat, P. V. *J. Phys. Chem. Lett.*, **2013**, *4*, 908.

(40) Mora-Sero, I.; Bisquert, J. J. *J. Phys. Chem. Lett.*, **2010**, *1*, 3046.

(41) Li, L.; Yang, X.; Gao, J.; Tian, H.; Zhao, J.; Hagfeldt, A.; Sun, L. *J. Am. Chem. Soc.*, **2011**, *133*, 8458.

(42) Ma, X.; Zhao, K.; Tang, H.; Chen, Y.; Lu, C.; Liu, W.; Gao, Y.; Zhao, H.; Tang, Z. *Small*, **2014**, *10*, 4664.

(43) Robel, I.; Subramanian, V.; Kuno, M.; Kamat, P. V. *J. Am. Chem. Soc.*, **2006**, *128*, 2385.

(44) Plass, R.; Pelet, S.; Krueger, J.; Gratzel, M. Bach, U. *J. Phys. Chem. B*, **2002**, *106*, 7578.

(45) Chang, J. Y.; Lin, J. M.; Su, L. F.; Chang, C.F. *ACS Appl. Mater. Interfaces*, **2013**, *5*, 8740.

(46) Choi, Y. C.; Lee, D. U.; Noh, J. H.; Kim, E. K.; Seok, S. I. *Adv. Funct. Mater.*, **2014**, *24*, 3587.

(47) Yin, X.; Battaglia, C.; Lin, Y.; Chen, K.; Hettick, M.; Zheng, M.; Chen, C. Y.; Kiriya, D.; Javey, A. *ACS Photonics*, **2014**, *1*, 1245.

(48) Zhu, G.; Pan, L.; Xu, T.; Sun, Z. *ACS Appl. Mater. Interfaces*, **2011**, *3*, 3146.

(49) Santra, P. K.; Kamat, P. V. *J. Am. Chem. Soc.*, **2012**, *134*, 2508.

(50) Chong, L. W.; Chien, H. T.; Lee, Y. L. *J. Power Sources*, **2010**, *195*, 5109.

(51) Tian, J.; Uchaker, E.; Zhang, Q.; Cao, G. *ACS Appl. Mater. Interfaces*, **2014**, *6*, 4466.

(52) Barpuzary, D.; Khan, Z.; Vinothkumar, N.; De, M.; Qureshi, M. *J. Phys. Chem. C*, **2012**, *116*, 150.

(53) Xu, C. X.; Sun, X. W.; Dong, Z. L.; Yu, M. B. *Appl. Phys. Lett.*, **2004**, *85*, 3878.

(54) Jin, H.; Zhou, W.; Cao, J.; Stoyanov, D. S.; Blijdenstein, T. B. J.; de Groot, P. W. N.; Arnaudov, L. N.; Pelan, E. G. *Soft Matter*, **2012**, *8*, 2194.

(55) Sun, X. M.; Chen, X.; Deng, Z.X.; Li, Y. D. *Mater. Chem. Phys.*, **2002**, *78*, 99.

(56) Wu, X. L.; Siu, G. G.; Fu, C. L.; Ong, H. C. *Appl. Phys. Lett.*, **2001**, *78*, 2285.

(57) Zeng, H.; Duan, G.; Li, Y.; Yang, S.; Xu, X.; Cai, W. *Adv. Funct. Mater.*, **2010**, *20*, 561.

(58) Choi, Y.; Seol, M.; Kim, W.; Yong, K. *J. Phys. Chem. C*, **2014**, *118*, 5664.

(59) Qureshi, M.; Chetia, T. R.; Ansari, M. S.; Soni, S. S. *J. Mater. Chem. A*, **2015**, *3*, 4291.

(60) Barpuzary, D.; Qureshi, M. *ACS Appl. Mater. Interfaces*, **2013**, *5*, 11673.

(61) Chen, Y.; Zhang, L.; Ning, L.; Zhang, C.; Zhao, H.; Liu, B.; Yang, H. *Chem. Eng. J.*, **2015**, *264*, 557.

(62) Phadke, S.; Pasquier, A. D.; Birnie, D. P. *J. Phys. Chem. C*, **2011**, *115*, 18342.

(63) Kern, R.; Sastrawan, R.; Ferber, J.; Stangl, R.; Luther, J. *J. Electrochim. Acta*, **2002**, *47*, 4213.

CHAPTER 4

Cage-like ZnO Superstructures with Compacted 1D Building Blocks for Enhanced Photovoltaic Performance

This Chapter presents a simple and green hydrothermal synthetic protocol for exotic 3D ZnO superstructures (ZnO Cages) assembled with compact 1D ZnO nano-rods which can provide faster photogenerated charge transfer pathways. A naturally abundant water soluble bio-template, "Sodium Alginate" is utilized as the structure directing agent in the wet chemical synthetic process. Based on systematic analyses of the reaction conditions a plausible mechanism of formation of ZnO cages is proposed. Technological importance of the material is established by evaluating its photovoltaic properties in a dye sensitized approach.

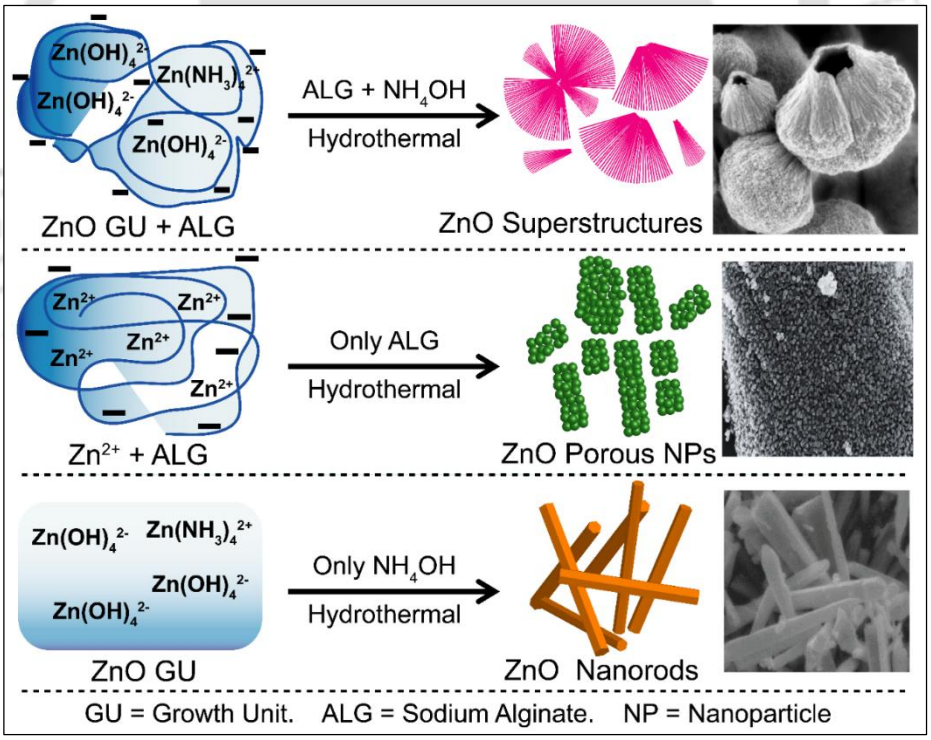

ROYAL SOCIETY OF CHEMISTRY PCCP **T. R. Chetia**, M. S. Ansari, M. Qureshi **2016**, *18*, 5344.

4.1 INTRODUCTION

Synthesis of 3-D superstructures assembled with 1-D nanostructures is a great challenge as they are enriched with superior optical and electrical properties for photovoltaic as well as photocatalytic applications.[1–5] 3-D superstructures have the potential to provide high surface area for sensitizer molecule adsorption, excellent light scattering ability along with direct and faster transport pathways for photo-generated electrons.[6] Additionally, porous and hollow characteristics of these materials are conducive to diffusion of electrolyte for better functioning of the redox couple in the photovoltaic devices. Very few synthetic protocols are developed to achieve anticipated superstructures of ZnO by various research groups.[7–11] Synthetic processes of these materials involve utilization of a range of structure directing agents and additives which can alter the classical arrangement of respective growth units. Among these synthetic methodologies, bio-inspired synthetic approaches utilize naturally abundant chemicals as structure directing agents and allow us to achieve control over morphology of materials to offer exotic structural speciality and intricacy.[12,13] Moreover, bio-templates are relatively economical and environmentally benign. The control over crystallization of inorganic materials achieved in biomimetic synthetic procedures have been a motivation for the development of new simple synthetic routes to materials of technological interest.[14] For instance, a number of naturally profuse bio-species such as peptides,[15] butterfly wings,[16] egg shell membrane,[17] cellulose fibers,[18] sodium carboxymethyl cellulose,[19] pollen grains,[20] gelatin,[21] hyaluronic acid and chondroitin-6-sulfate,[22] pectin,[23] etc. are employed as templates in the synthetic methods of inorganic functional materials as shown in the figure **4.1.1**.

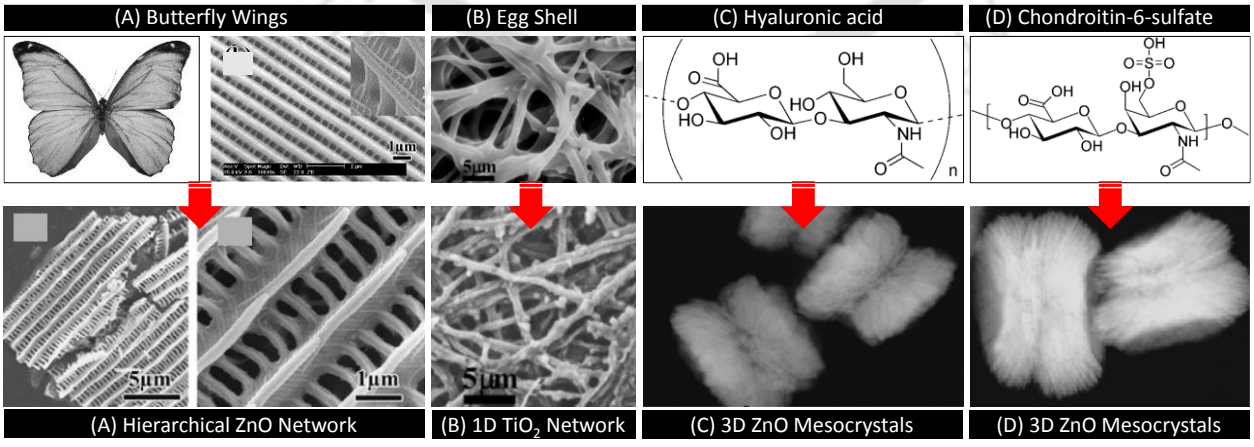

Figure 4.1.1 Evolution of morphologies of inorganic functional materials templated with (A) Butterfly wing, (B) Egg Shell membrane (C) Hyaluronic acid and (D) Chondroitin-6-sulfate.

In presence of these bio-templates, the crystal growth processes might in certain aspects resemble to mimic the bio-mineralization processes.[24] However, the formation mechanisms of aggregate morphologies are still scarce and need to be understood for better design of materials. It is believed that the formation of aggregates might be inspired by the templating effect of the bio-polymers along with electrostatic force driven, non-classical arrangement of the growth units.[14,25] In order to achieve novel structures of various materials, it is important to understand the interactions between the soft bio-materials and inorganic materials.

This chapter demonstrates controlled synthesis of mesoporous and hollow 3-D ZnO superstructures assembled with compact 1D nanorods which can provide faster photogenerated charge transfer pathways. In the synthetic process we have utilized a soft bio-template "sodium alginate" (ALG) as a structure directing agent and ammonium hydroxide (NH_4OH) as a precipitating base. We have optimized the reaction conditions by varying time and the additive sequences of ALG and NH_4OH. Based on the systematic experimental observations, a plausible formation and growth mechanism is proposed for the as-synthesized ZnO superstructures. Improved photovoltaic performance is observed for the devices based on ZnO superstructures over the conventionally used morphologies, i.e., ZnO nanorods (NRs) and porous ZnO nanoparticles (NPs). Figure **4.1.2** shows chemical structure of sodium alginate in water.

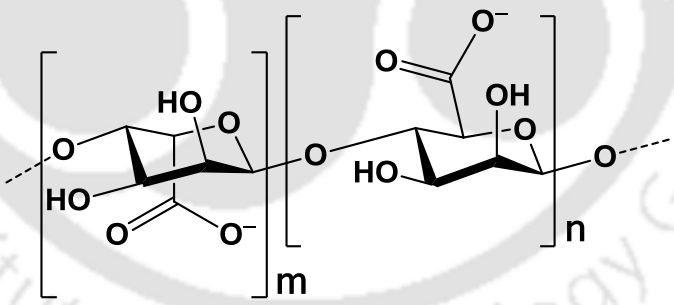

Figure 4.1.2 The chemical structure of sodium alginate in water.

4.2 EXPERIMENTAL METHODS

4.2.1 SYNTHESIS OF ZnO CAGES

The typical synthetic procedure of alginic acid assisted ZnO is as follows. A calculated amount of 0.1 wt % of sodium alginate (0.025 g) was dissolved in 25 mL of Milli-Q water with continuous stirring (**solution 1**) followed by the addition of zinc nitrate hexahydrate (1 mmol, 0.297 g). Instantly, a jelly like precipitate was observed in the solution and thereafter it was stirred

continuously for another 15 min. Subsequently, an optimized amount of 25 % NH_4OH (1.5 mL) was slowly added into the solution (**solution 2**). It was observed that, immediately after addition of NH_4OH, a white precipitate possibly of $Zn(OH)_2$ appear in the solution. Further addition of NH_4OH upto 0.8 mL to the reaction mixture, the white precipitate disappeared completely and became a clear solution. After complete addition of NH_4OH upto 1.5 mL, the pH of the solution was found to be ~10. The clear solution was transferred into a teflon lined stainless steel autoclave, sealed tightly and kept at 120 °C for 1.5 h. After cooling down to room temperature, the precipitate was centrifuged, washed with distilled water and absolute ethanol several times and dried in a hot air oven at 70 °C for 6 h. Graphical representation of the synthetic methodology is depicted in the scheme **4.2.1**.

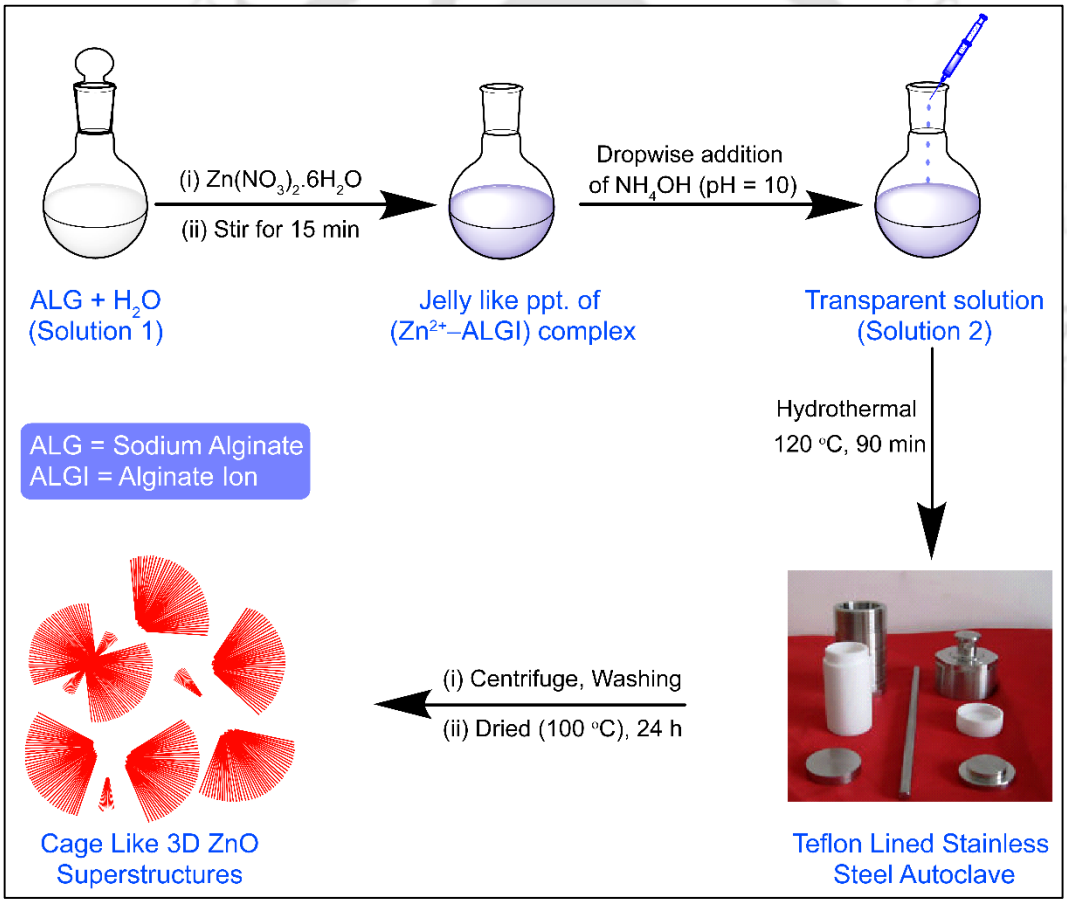

Scheme 4.2.1 Graphical representation of step-by-step synthetic process of cage-like 3D ZnO superstructures.

Control reactions in absence of NH_4OH and sodium alginate respectively were carried out. We had also investigated the reaction in detail by varying addition sequences of NH_4OH and ALG keeping other reaction conditions same in the order to gain insights into the effects of both the

additives. In addition, reactions were carried out at different interval of time, i.e., for 40 min, 60 min, 90 min and 120 min so as to follow and understand the growth process of the superstructures.

4.2.2 FABRICATION OF PHOTOANODES AND DEVICES

All ZnO based photoanodes were fabricated by making a homogenous paste of Zinc oxide and pasted it over the conductive glass substrates i.e. FTO. For the preparation of ZnO paste, ZnO powder (0.1 g) was ground with a mixture of terpineol and triblock copolymer (PEG-PPG-PEG) in an agate mortar until a homogenous paste was formed. This homogenous paste was coated on pre-cleaned conductive glass substrate i.e. FTO via doctor blade technique and the films were dried in air, followed by calcination at 525 °C for 60 min to remove the polymer. The thickness of the ZnO layer was measured by a surface profilometer (Veeco Dektak-150) and it was found to be in the range of 12−15 μm. These substrates were then immersed into N719 dye solution in ethanol (0.3 mM) for 2.5 h at 50 °C. Graphical representation of step-by-step photoanode preparation process is shown in the scheme **4.2.2**.

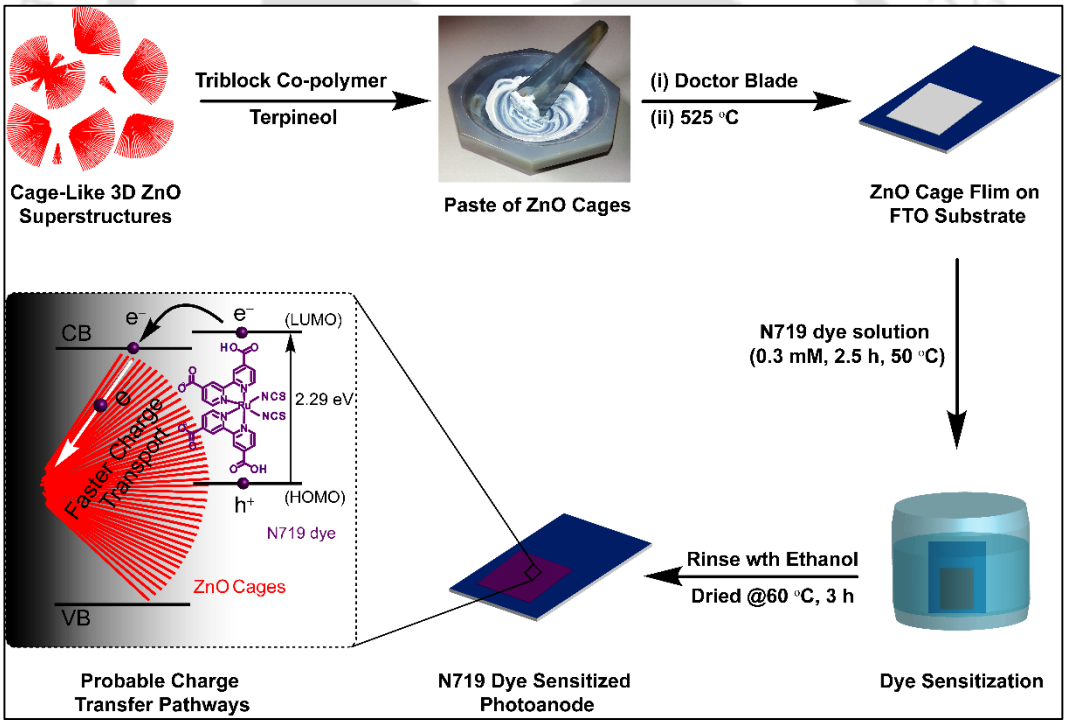

Scheme 4.2.2 Schematic representation of step-by-step fabrication process of the photoanodes and probable charge transfer pathways.

The sensitized photoanodes were taken out from dye solution, washed with absolute ethanol and dried at 60 °C for 3 h. Dye sensitized solar cell (DSSC) devices were fabricated by sandwiching the photoanodes and counter electrodes. To fabricate the counter electrode, a solution

of 5 mM chloroplatinic acid in isopropanol was spin coated on a cleaned, ozonized FTO substrate. The spin coated FTO substrate was then calcined at 450 °C for 30 min (heating ramp of 5 °C/min) in a muffle furnace. The furnace was cooled down to room temperature naturally and the as prepared platinum coated counter electrode was taken out. The electrolyte solution was introduced to the devices after sealing (using low-temperature thermoplastic sealant, thickness ~50 μm) through a hole in the counter electrode which was made by drilling using a glass driller. The I^-/I_3^- electrolyte solution was prepared by dissolving 0.5 M LiI, 0.05 M I_2, 0.1 M guanidium thiocyanate, and 0.5 M 4-tert-butylpyridine in a solvent mixture of acetonitrile: valeronitrile (9:1, v/v). The active area for all fabricated devices were fixed and it was found to be 0.25 cm^2. Before the photovoltaic measurements i.e. (*I*–*V*), IPCE and EIS measurements, the fabricated devices were kept under dark condition for 24h.

4.3 RESULTS AND DISCUSSIONS

4.3.1 POWDER X-RAY DIFFRACTION ANALYSIS

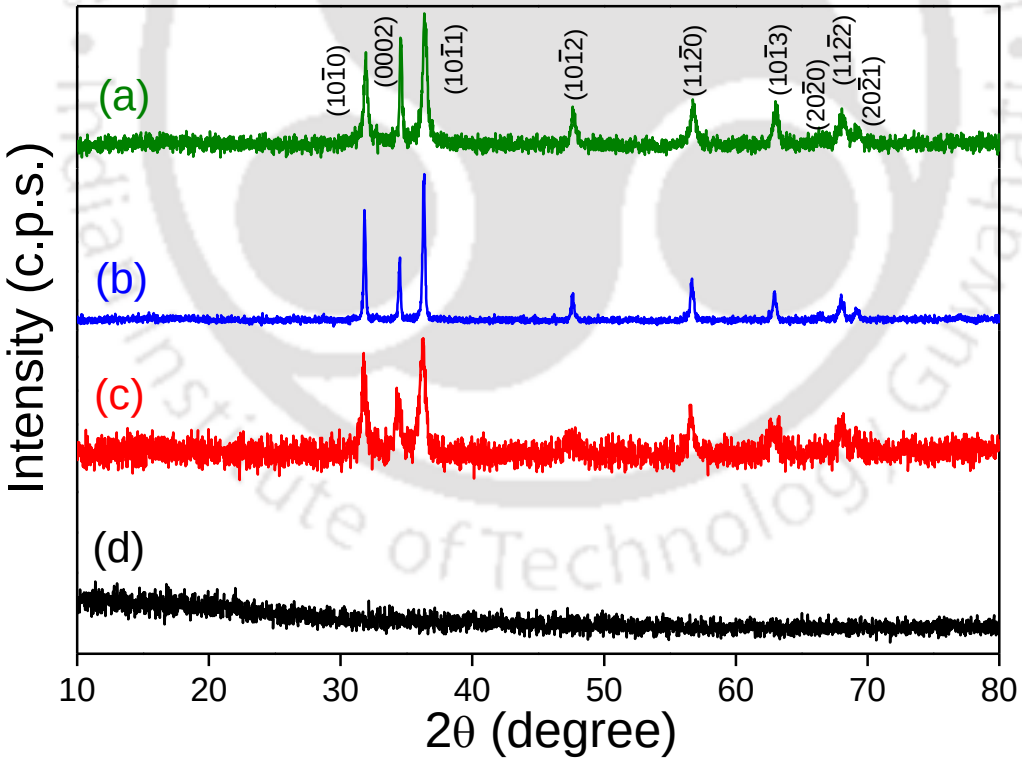

Figure 4.3.1 Powder X-ray diffraction (PXRD) patterns recorded for the products synthesized under different reaction conditions, i.e., in presence of (a) both ALG and NH_4OH (**reaction 1**), (b) only NH_4OH (**reaction 2**), (c) only ALG after calcination and (d) before calcination (**reaction 3**).

Figure **4.3.1** depicts powder X-ray diffraction (PXRD) patterns for all the as synthesized ZnO heterostructures. Trace (a) represents PXRD pattern of ZnO synthesized in presence of both ALG and NH_4OH (**reaction 1**). Traces (b) and (c) are for the ZnO synthesized in the control reactions; in presence of only NH_4OH (**reaction 2**) and in presence of only ALG (**reaction 3**). It is observed that an amorphous product is obtained, presumably an adduct of Zn^{2+} with alginate ions in the reaction 3 [trace (d)] which is converted into pure ZnO after calcination at 520 °C for 1 hour as evident from the PXRD patterns, traces (c) and (d). Crystal phase for all the three type of ZnO are defined to be hexagonal wurtzite phase with $(10\bar{1}0)$, (0002), $(10\bar{1}1)$, $(10\bar{1}2)$, $(11\bar{2}0)$, and $(10\bar{1}3)$ planes with a $P6_3mc$ space group symmetry and Zn atoms in tetrahedral sites according to the JCPDS Card No. 36-1451. No peaks due to impurity are detected in the PXRD patterns which infers that as-synthesized products are pure ZnO with good crystalline characteristics. It is noteworthy that the intensity ratio of $(10\bar{1}0)$ to (0002) crystal planes varied significantly for all the three type of ZnO which is indicative of differential tropism of the products in the three reaction conditions namely reaction 1, 2 and 3.[26]

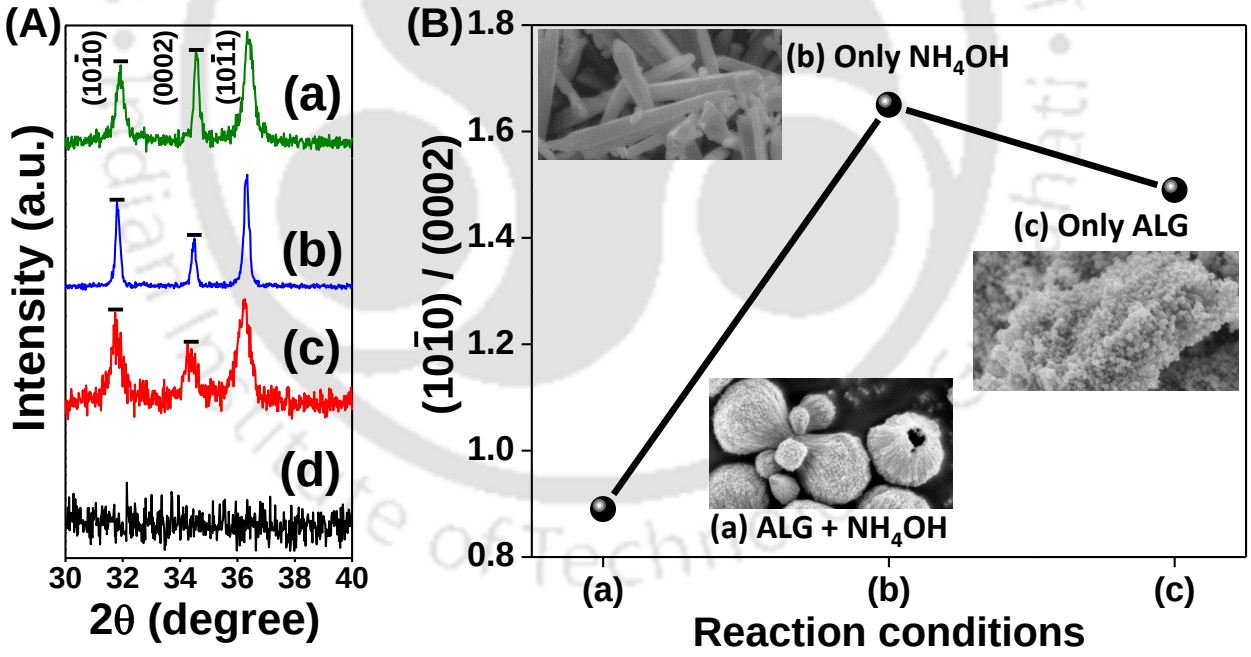

Figure 4.3.2 (A) PXRD patterns showing intensity variation of the peaks for $(10\bar{1}0)$, (0002) and $(10\bar{1}1)$ crystal planes of ZnO obtained from reaction 1 (a), reaction 2 (b), and reaction 3 (c) & (d); after and before calcination. **(B)** Plot of $(10\bar{1}0)$/(0002) intensity ratio obtained from the PXRD patterns (a), (b) and (c) of figure (A) *vs* all the ZnO nanostructures. Insets to it show FESEM images of (a) ZnO Cages, (b) ZnO Nanorods (NRs) and (c) ZnO Porous Nanoparticles (PNPs)

Figure **4.3.2** (A) depicts intensity variation of the X-ray diffraction peaks for the crystal planes $(10\bar{1}0)$ and (0002) of as synthesized ZnO heterostructures. A smaller value of the intensity

ratio $(10\bar{1}0)/(0002)$ indicates the formation of ZnO rods showing a preferential growth along the *c*-axis which also reflects the larger number of planes along the (0001) direction of the rod; whereas a larger value of $(10\bar{1}0)/(0002)$ ratio specifies inhibited growth along the c-axis.[27, 28] Figure **4.3.2** (B) represents a plot of $(10\bar{1}0)/(0002)$ intensity ratio obtained from the PXRD patterns (a), (b) and (c). From figure (B) it is pragmatic that the increasing order of $(10\bar{1}0)/(0002)$ intensity ratio for the ZnO obtained from the reactions (1), (2) and (3) is : (a) ALG + NH_4OH or reaction 1 <(c) Only ALG or reaction 3 <(b) Only NH_4OH or reaction 2. Lowest value of $(10\bar{1}0)/(0002)$ intensity ratio for ZnO obtained in the reaction 1 infers crystal growth anisotropy along longitudinal *c*-axis while higher values obtained from the products of reactions 2 and 3 suggests inhibited growth along *c*-axis. Topographies and dimensions of the products are further confirmed from FESEM analysis as we have displayed in the insets of figure **4.3.2** (B). In case of the reaction 1, ZnO superstructures assembled with tiny 1D ZnO nanorods are obtained while ZnO nanorods (NRs) and ZnO porous nanoparticles (PNPs) are formed in the reaction conditions (2) and (3) respectively. FESEM analyses of the products obtained from reactions 1 and 3 are in good agreement with the inferences carried out about crystal growth habit of ZnO from PXRD patterns on the basis of previous reported works, while it is not in the case of ZnO obtained from reaction 2. It is expected that the structure of ZnO in this case should be nanoparticles or nano-disks with less number of crystal planes along c-axis, i.e. (0001) direction, whereas it is observed to be the formation of ZnO nanorods. This observation might be due to the random arrangement of ZnO NRs in the horizontal plane of the substrate which causes less exposure of the crystal planes along (0001) direction. Please note that, if maximum number of ZnO NRs are aligned vertically on the substrate (i.e., normal to the substrate), strong appearance of (0002) diffraction peak at ($2\theta \approx 34.61°$) is observed whereas the intensity of the peak decreases if they are randomly arranged in the horizontal plane as shown in figure **4.3.3**; traces (a) and (b). However, in case of ZnO superstructures, numerous tiny ZnO NRs (diameter in the range ~8-10 nm) are hierarchically arranged which increases the percentage of vertically aligned ZnO NRs and consequently upsurges the intensity of the peak (0002) from the crystal planes along (0001) direction as we have seen in trace (c).

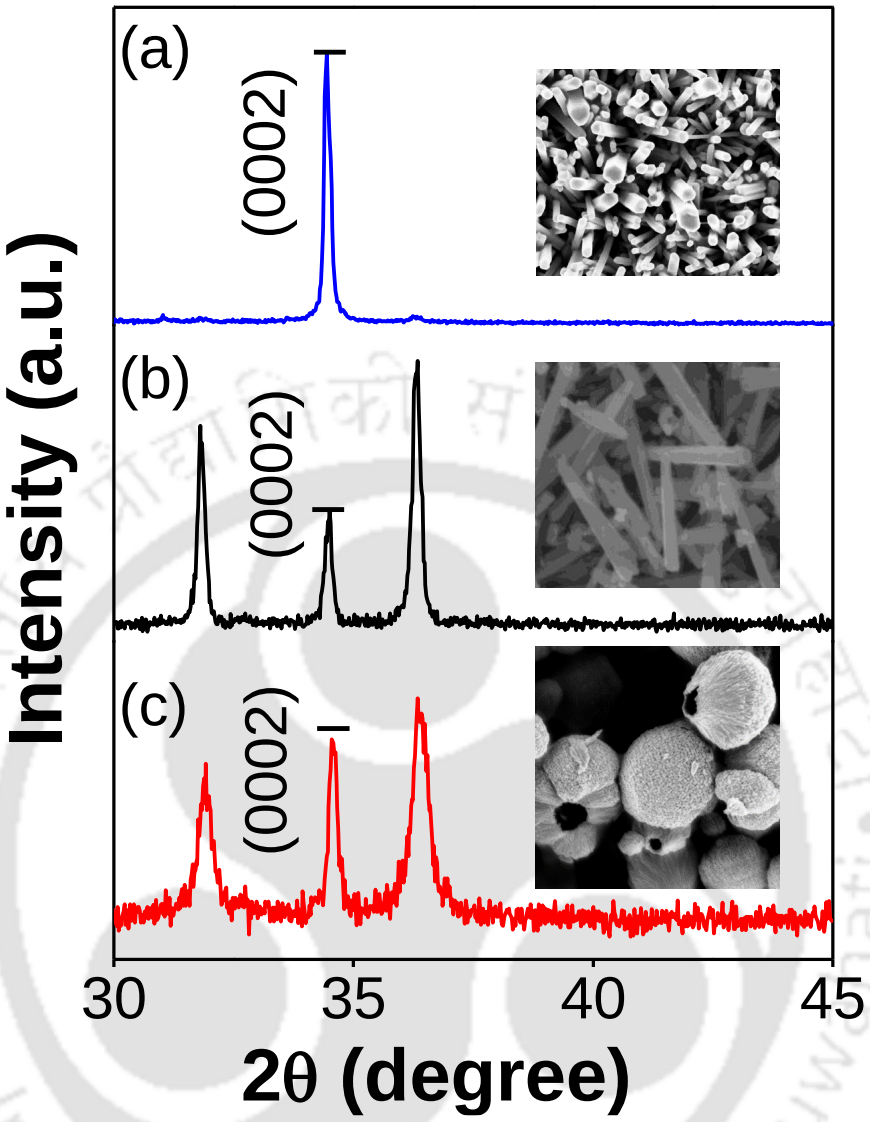

Figure 4.3.3 PXRD patterns showing variation of appearance for the peak (0002) obtained for (a) vertically grown ZnO NRs on the substrate (b) ZnO NRs laying horizontally on the substrate and (c) ZnO Cages.

4.3.2 MATERIAL MORPHOLOGY

Figure **4.3.4** (A, B, C, D and E) shows the FESEM features of as-synthesized cage like ZnO superstructures at different magnifications. From the FESEM images (A), (B) and (C) we have seen that as synthesized product comprises of both multi-cage and single cage 3D ZnO superstructures. The average longitudinal dimension of the ZnO multi-cage structures are in the range of 2–3 μm and ~1 μm for a single cage ZnO. Each multi-cage superstructure is composed of two main bigger cages adjoined opposite to each other, which are observed to be of similar size; while the branched cages growing from the adjoining point are smaller and have random size distribution. Consequently, there will be three types of ZnO cages in the sample namely: (a) multi-

cage ZnO, (b) bigger size single cage ZnO [indicated with red arrows in image (C)] and (c) smaller size single cage ZnO. It is obvious that the latter two type of cages [i.e., (b) and (c)] are originating due to fracture of multi-cage ZnO at the adjoining points.

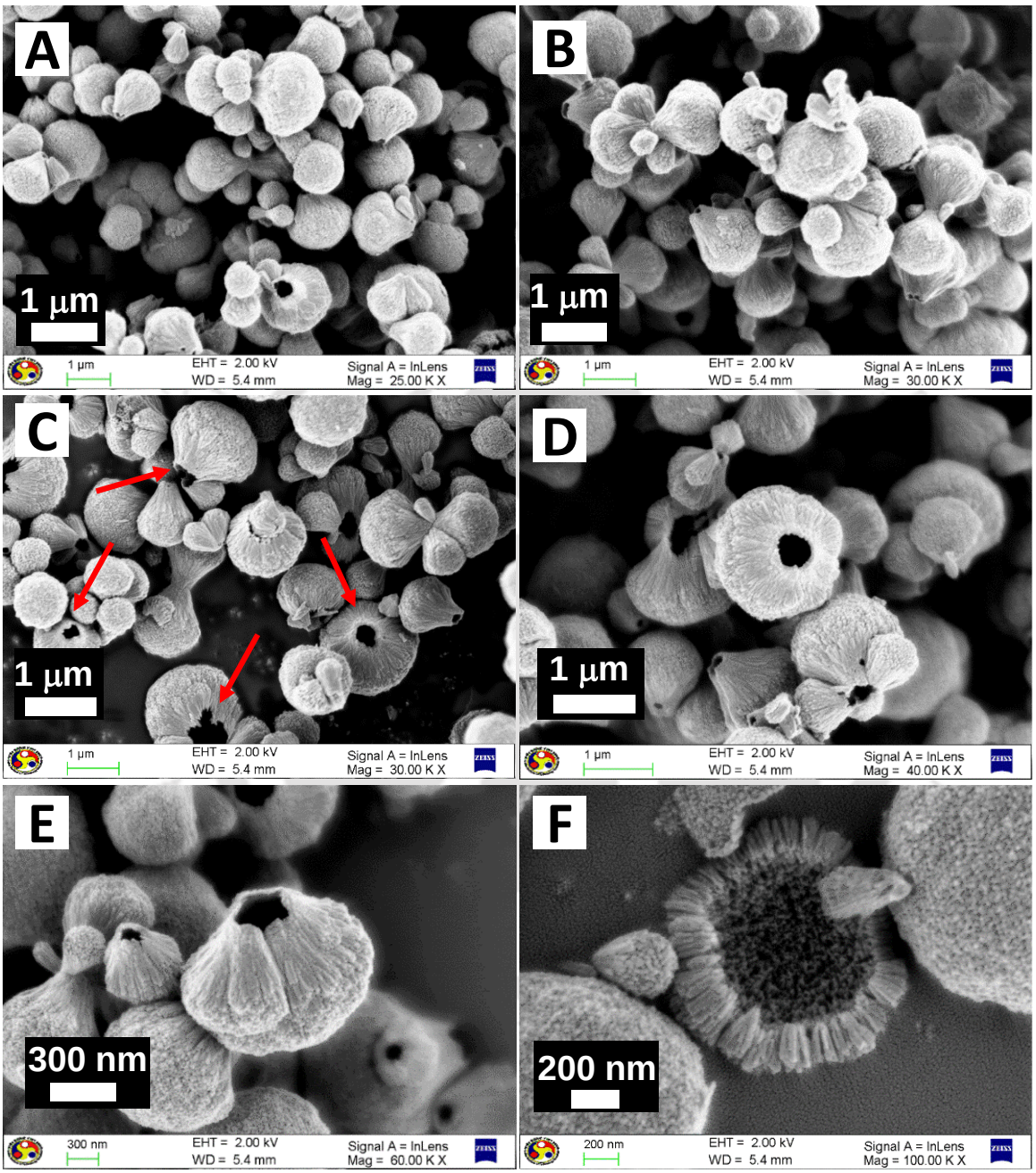

Figure 4.3.4 FESEM images (A, B, C, D and E) of as synthesized cage like ZnO superstructures at different magnifications. Image (F) shows a broken ZnO superstructure.

The presence of smaller cage ZnO is expected to be beneficial for the fabrication of photoanode with higher light harvesting ability. It can be ascribed to the high probability of smaller cage ZnO to occupy the voids produced in between the bigger size single cage ZnO and multi-

cage ZnO. This in turn will improve the inter-particle electrical connectivity to act as the photoinduced electron channels that leads to an increase in the current density (J_{sc}) value as well as light scattering. Figure (D) and (E) are FESEM images representing top and side view of ZnO cages at higher resolution. The width of as obtained ZnO cages is around 1-1.5 μm and are open with a macropore of diameter ~300 nm. The pore is representing the adjoining point of the cages in the multi-cage ZnO superstructures resulting from the detachment of the cages and is confirming the hollow characteristic of the material. It is observed that the ZnO cages are composed of numerous tiny ZnO NRs. Figure (F) shows a cracked ZnO cage at higher magnifications which confirms hierarchical arrangement of the nanorods to form ZnO superstructures. The attachment of the nanorods with different lengths is leading to formation of pores in-between them and thereby these superstructures may behave as mesoporous material. Furthermore, we have performed TEM and surface area analysis (BET measurements) to verify the morphological conclusions carried out from FESEM analysis.

TEM images (A) and (B) in figure **4.3.5** are representing a multi-cage and a single cage ZnO superstructures respectively. The high resolution TEM image [trace (C)] reveal that the ZnO cages are composed of a number of tiny ZnO NRs with diameter ~8-10 nm which is in accordance with the FESEM analysis. Density of ZnO NRs at the adjoining point of the ZnO cages is minimum which is divulged through the higher transparency towards electron beam at these points [Images (A) and (B)]. Accordingly, mechanical strength of the multi-cage ZnO superstructures at the adjoining point will be very less which is the most probable cause for detachment of the superstructures at this specific point. The selected area electron diffraction (SAED) pattern of ZnO cages is indexed as $(1\bar{1}00)$ zone axis and is shown in the inset to figure **4.3.5** (C). Red dotted lines in figure (C) indicates two adjacent ZnO NRs. The SAED pattern is unfolding the wurtzite single crystalline structure of each ZnO NRs and crystal growth anisotropy along (0002) crystal planes which is consistent with the PXRD results. Inverse Fast Fourier Transform (IFFT) of atomic planes is carried out for the indicated part of trace (C) and is as depicted in the figure (D). Interplanar distance of the crystal planes is found to be ~0.51 nm which is for (0001) crystal planes accrediting the preferable crystal growth along the *c*-axis or the (0001) direction. Inset to figure (D) is the related Fast Fourier Transform (FFT) pattern and verifies the single crystalline nature of the ZnO NRs.

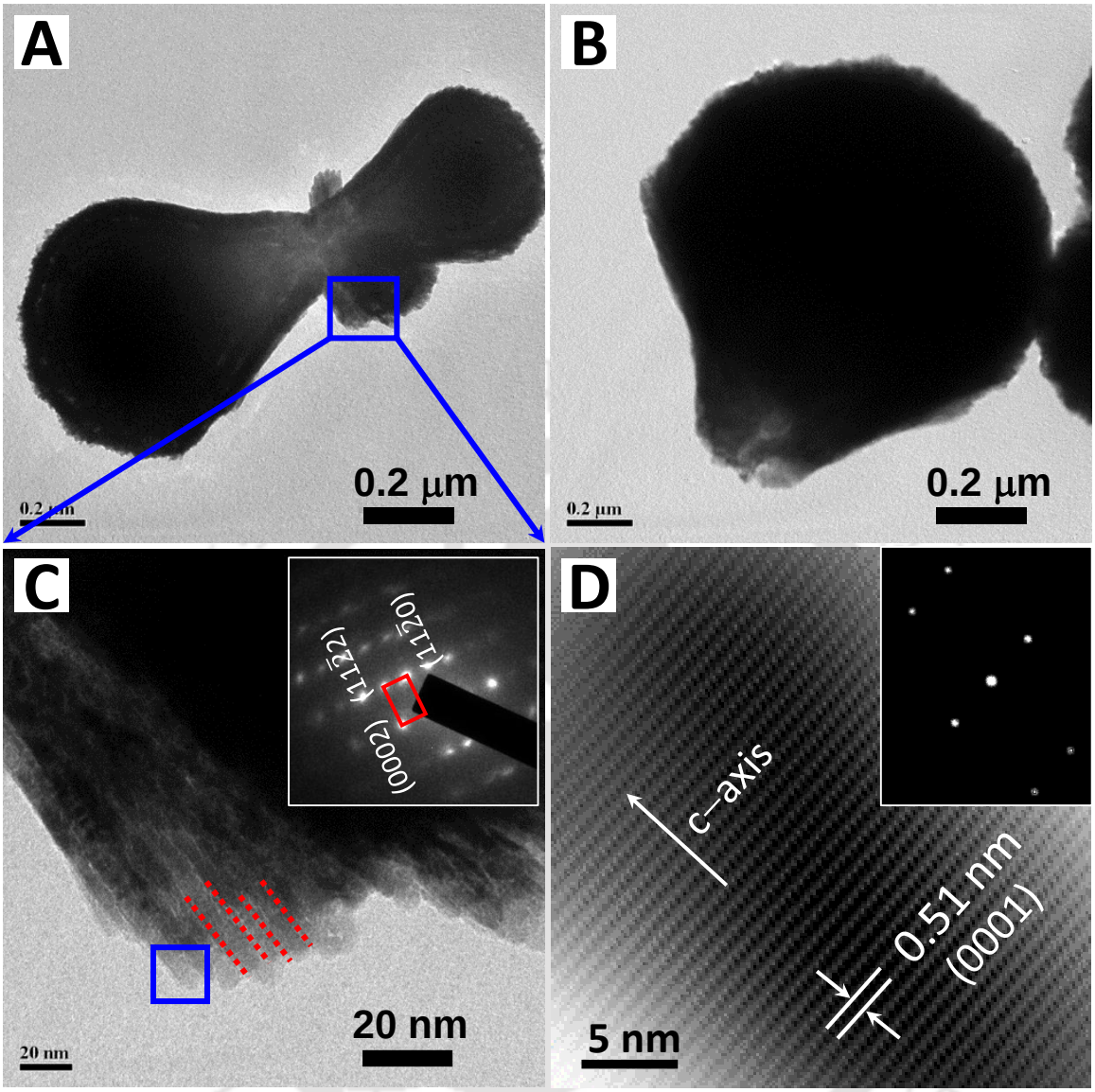

Figure 4.3.5 TEM images (A) and (B) are showing a multi-cage and a single cage ZnO superstructure respectively. High resolution transmission electron microscopy (HRTEM) image of the ZnO superstructure (trace C) and inset to it shows related SAED pattern. Trace (D) represents Inverse fast Fourier transform (IFFT) of atomic planes for the specified part of trace (C) with corresponding FFT in the inset.

In order to understand the growth mechanism and evolution of cage like morphology of ZnO superstructures we have investigated the reaction in detail by performing controlled reactions by varying the addition amount of NH_4OH, ALG and reaction times. Change in morphological characteristics and crystallinity of the products are monitored by performing FESEM and PXRD analysis respectively.

(i) Effect of ammonium hydroxide (NH_4OH)

In order to realize the role of NH_4OH in the growth process of cage like ZnO superstructures, we have carried out the reactions by sequentially varying the amount of NH_4OH per 25 mL of reaction mixture. It should be noted that the amount of ALG added and the time of the reaction kept constant at 0.1 wt % and 1.5 h.

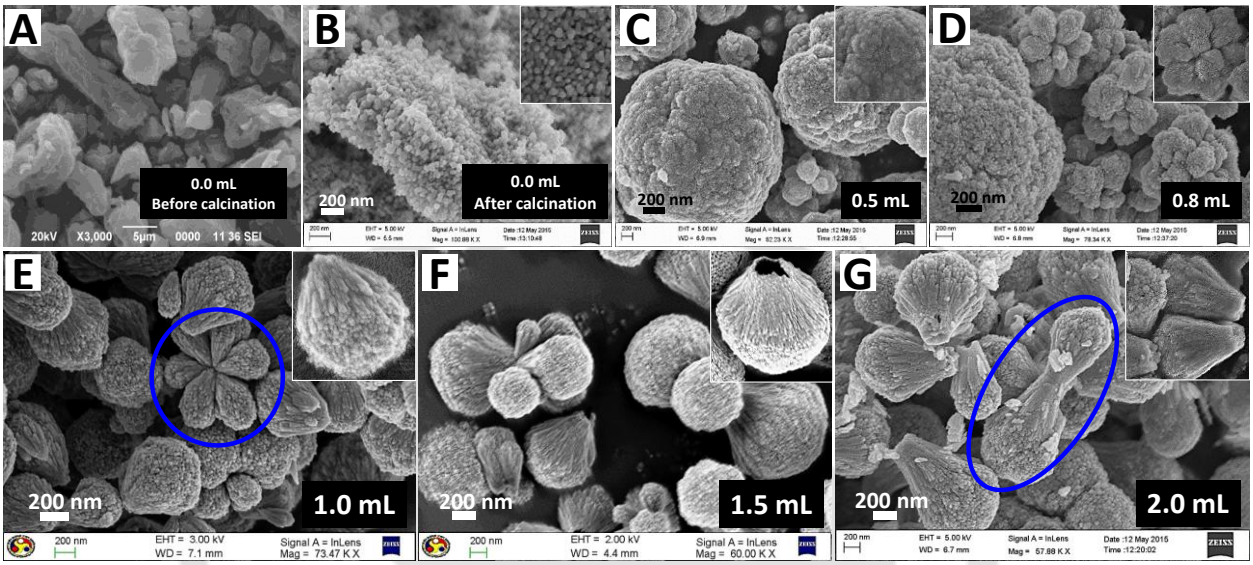

Figure 4.3.6 FESEM features of the as prepared products with different amount of NH_4OH: (A) 0.0 mL, (B) 0.5 mL, (C) 0.8 mL i.e., at the precipitate disappearing point, (D) 1 mL, (E) 1.5 mL and (F) 2 mL. Insets show corresponding higher magnification FESEM images for better clarity

Control reactions are performed by varying the amount of NH_4OH from 0.0 mL to 2.0 mL with an increment of 0.5 mL and topographies are presented in figure **4.3.6**. Additionally, a reaction at 0.8 mL of NH_4OH is also carried out, wherein we have observed a sudden disappearance of gelatinous precipitate. Observation of a gelatinous precipitate immediately after the addition of $Zn(NO_3)_2.6H_2O$ to the reaction mixture is due to the formation of an amorphous (ALGI–Zn^{2+}) complex as shown in the FESEM image (A). After calcination at 525 °C for 1 h in a muffle furnace, it translates into aggregates of ZnO nanoparticles with pores (abbreviated as ZnO PNPs) in the range of 10–20 nm respectively as we have observed from trace (B), figure 4.3.6. BET surface area analysis for the sample is conducted and discussed later. The size of the nanoparticles are in the range of 10–15 nm as confirmed from the high-resolution FESEM image shown in the inset to trace (B). On addition of 0.5 mL NH_4OH to the reaction mixture, two types of spherical ZnO aggregates, one with a size distribution of ~0.5–1 µm and another with ~1–3 µm are observed, trace (C). Further addition of NH_4OH (upto 0.8 mL), i.e., the precipitate disappearing

point, results in the formation of star shaped co-joined lobes of ZnO (size ~0.5–1 μm) along with the spherical aggregates (size range ~1–3 μm) as we have seen in image (D). Increase in the amount of NH_4OH to 1.0 mL, leads to the formation of cage like ZnO with smaller diameter (~500 nm) of uniform size distribution; see trace (E). Although, these cages are originating from the flower like superstructures as indicated in the image (E), the adjoining points of the single cages are not open. Image (F) manifests the anticipated ZnO cages with open hollow structures obtained on addition of 1.5 mL of NH_4OH. The crystallinity of this product is also observed to be superior relative to all others, including the structures acquired in case of 2.0 mL NH_4OH as displayed in the image (G). Hence, the optimum amount of NH_4OH to be added in the reaction is found to be 1.5 mL per 25 mL of the reaction mixture and is kept constant in further reactions. The size distribution of the ZnO cages perceived in the reaction of 2.0 mL of NH_4OH, is noted to be very similar to that obtained in the reaction with 1 mL. However, dumbbell shaped structures of ZnO appeared as indicated in the image (G), instead of flower like superstructures as in case of 1 mL NH_4OH. In scheme **4.3.1**, we have schematically represented all the controlled reaction condition pathways and variation of morphological characteristics ZnO superstructures in presence of alginate ion by varying the concentration of NH_4OH.

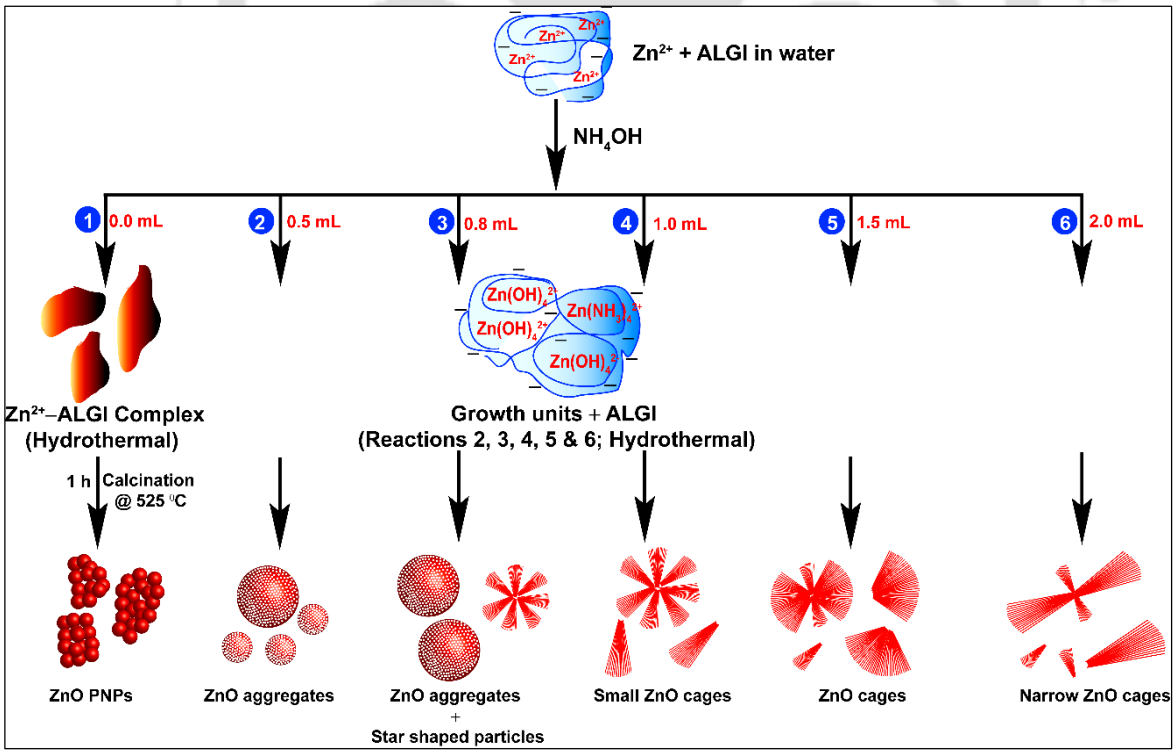

Scheme 4.3.1 Effect of ammonium hydroxide (NH_4OH) on variation of morphological characteristics of ZnO superstructures.

From all the above discussions it is clear that the addition of NH_4OH in the reaction have a profound effect on the material morphology as well as in the crystallinity of the superstructures. It is also clear that only the addition of NH_4OH facilitates the formation of ZnO in hydrothermal conditions, confirms that the growth units are $Zn(OH)_4^{2-}$ and $Zn(NH_3)_4^{2+}$. It is well known that, NH_4OH could provide both NH_3 and OH^- ions to the aqueous solution and they are good coordinating ligands of Zn^{2+}.[29] Moreover, cage-like ZnO superstructures are observed to be formed in the reaction which is carried out in presence of both ALG and NH_4OH. Therefore, it is important to understand the effects of the "bio-template" in the growth process of the superstructures.

(ii) Effect of sodium alginate (ALG) addition

To investigate the effect of the bio-template, reactions are carried out by varying the concentration of ALG from 0.0 wt % to 0.2 wt % and FESEM images are shown in the figure 4.3.7. The amount of NH_4OH and temperature of the reactions are kept constant at 1.5 mL and 120 °C respectively.

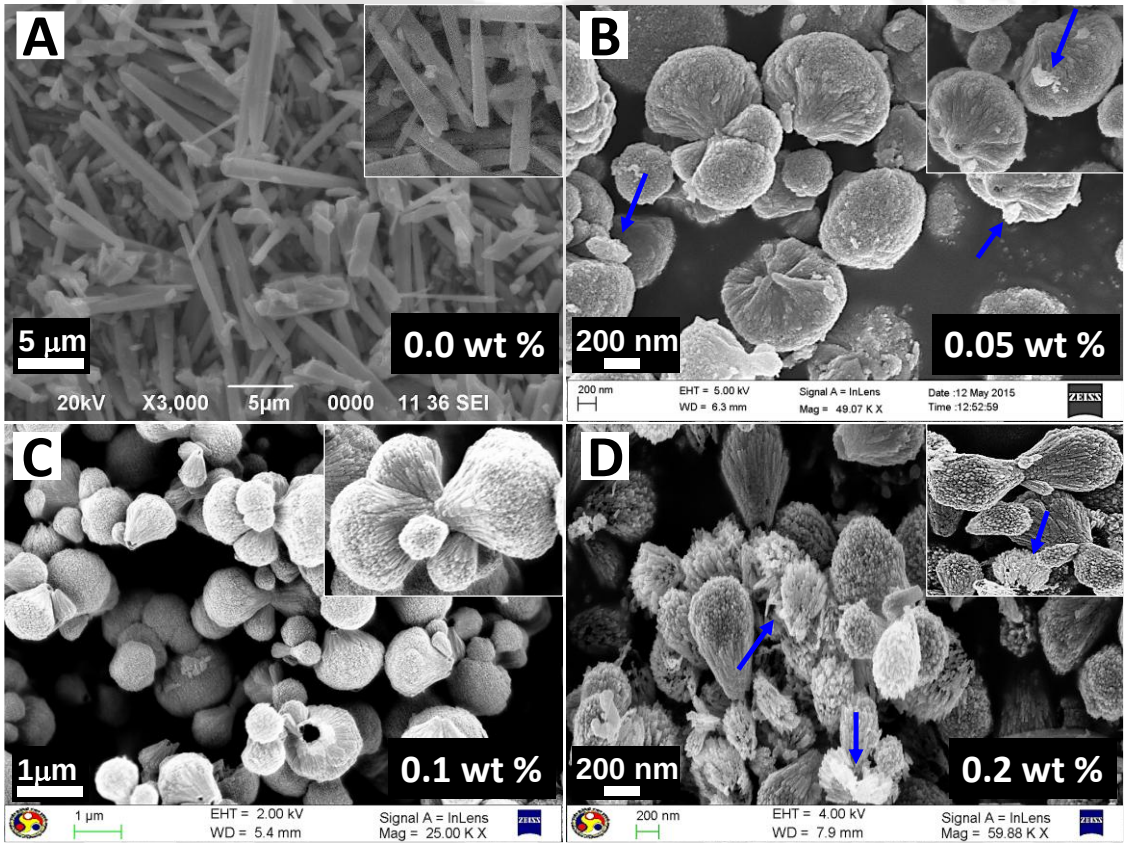

Fig. 4.3.7 FESEM images of the as synthesized products with different amount of ALG: (A) 0.0 wt %, (B) 0.05 wt %, (C) 0.1 wt % and (D) 0.2 wt %. Insets show corresponding higher magnification FESEM images for better clarity.

Formation of ZnO nanorods (NRs) with diameter in the range 300–400 nm are observed with only NH_4OH in the absence of ALG (0.0 wt %) as portrayed in the image **4.3.7** (A) and in its inset. These nanorods are single crystalline having hexagonal wurtzite crystal structure with a preferential crystal growth along (0001) direction. Reaction with an increase in the concentration of ALG to 0.05 wt % of ALG, bigger size ZnO cages (longitudinal diameter ~2 μm) along with some irregular multi-cages and tiny aggregates are noticed as indicated with blue arrows in the trace (B) and inset to it. Appearance of tiny ZnO aggregates may be due to the presence of excess NH_4OH compared to ALG which lead to higher number of growth units [i.e., $Zn(NH_3)_4^{2+}$ and $Zn(OH)_4^{2-}$] in the reaction mixture relative to the alginate ions (ALGI) and random crystal growth (note that the concentration of NH_4OH is fixed at 1.5 mL). In contrast, uniform multi-cages as well as single cages of ZnO appeared in case of the reaction with 0.1 wt % ALG; trace (C) and inset to it. Further increase in the amount of ALG upto 0.2 wt %, partially formed ZnO cages are observed [indicated with blue arrows in image (D) and inset to it], which is possibly due to inhibited crystal growth of ZnO in presence of excess ALGI. It is noteworthy that the carboxylate groups in the ALGI can preferentially bind to the Zn-populated (0001) crystal planes of the ZnO crystallites and adhere on the surface of them to impede the favorable longitudinal *c*-axis growth as well as the lateral growth of ZnO crystal in hydrothermal condition.[26] This claim is also in accordance with the formation of larger size ZnO NRs (length ~8–10 μm, diameter ~300–400 nm) in the controlled reaction carried out in absence ALG compared to the nanorods in the superstructures (length ~0.5–0.8 μm, diameter ~10–15 nm). The above discussions are establishing the optimum amount of ALG to be employed in the reaction is 0.1 wt % which results in uniform and highly crystalline ZnO superstructures compared to the products obtained in other two control reactions with 0.05 wt % and 0.2 wt %. However, crystallinity of the ZnO NRs obtained in the controlled experiment is highest among all the synthesized products and is unveiling the role of ALG as a crystal growth inhibitor and structure directing agent.

(iii) Effect of reaction time

For all the aforementioned reactions we have maintained the reaction time at 90 min. In order to optimize the time of the reaction and explore the growth behaviour of ZnO superstructures, morphological characterization of the material at different interval of time (i. e., from 40 min to 120 min) is carried out and are depicted in the figure **4.3.8**.

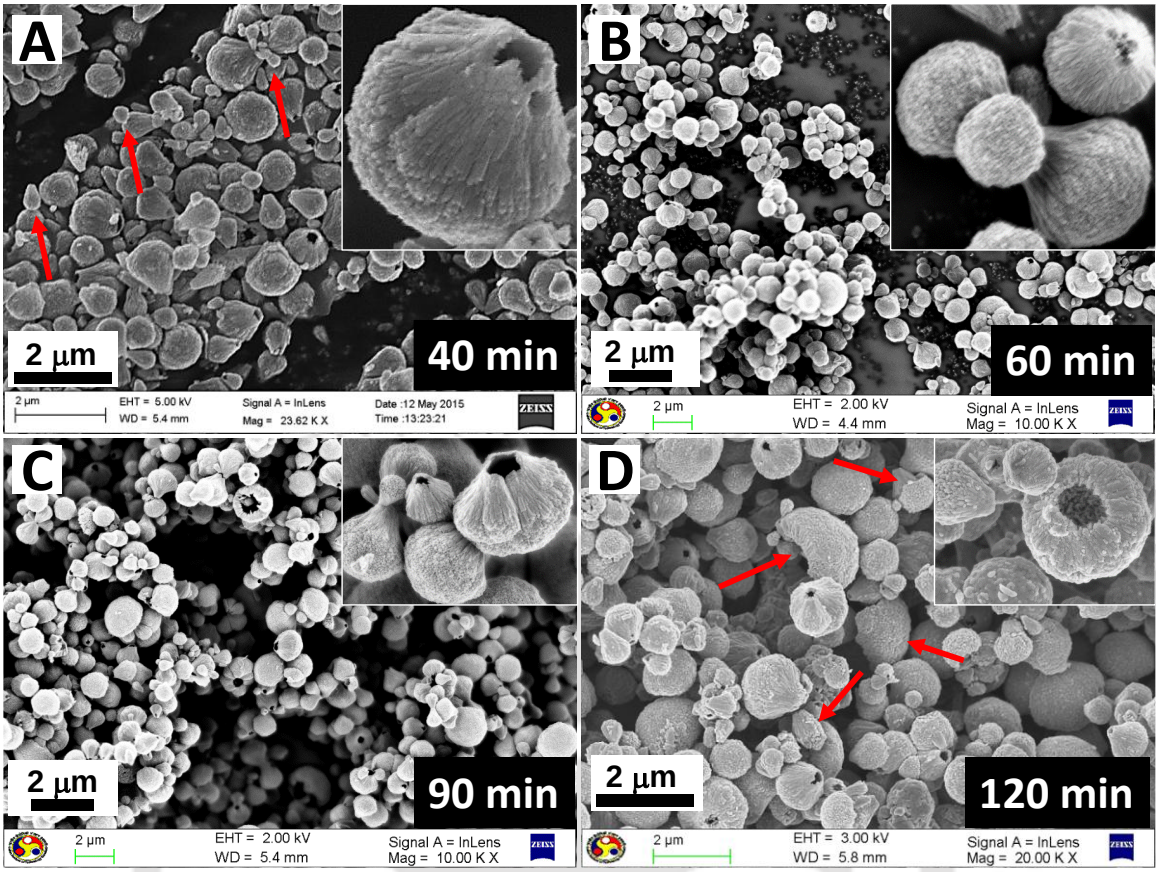

Figure 4.3.8 FESEM images of the products obtained from the control reactions performed by varying time i.e., after: (A) 40 minute, (B) 60 minute, (C) 90 minute and (D) 120 minute. Insets show corresponding higher magnification FESEM images for better clarity.

Morphology of the product at 40 min of reaction time is represented in the image (A) and inset to it, figure **4.3.8**. Cage like ZnO with hollow characteristics are observed in this case. However, partially developed narrower and smaller size cages are also observed [indicated with red arrows in image (A)]. This is an indicative of incompletion of reaction and is confirmed from the low crystallinity of the product compared to the other two cases, i.e., reactions with 60 min and 90 min. Please note that, variation of crystallinity is also probed for all the products from PXRD patterns and is depicted in figure **4.3.9**. We have tabulated the values of Full Width Half Maximum (FWHM), calculated crystallite size and intensity in counts per second (c.p.s) of the highest intense peak in the PXRD patterns in table **4.3.1**. Scherrer equation is used to calculate the crystallite size of the products. The Scherrer equation is represented as:

$$D = \frac{0.95 \times \lambda}{\Delta W \times cos\theta} \qquad (1)$$

Where, D is the crystallite domain diameter, λ is the wavelength of the incident X-ray beam (1.54 Å for the Cu Kα), θ is the Bragg's diffraction angle, ΔW the width of the X-ray pattern line at half peak-height in radians.

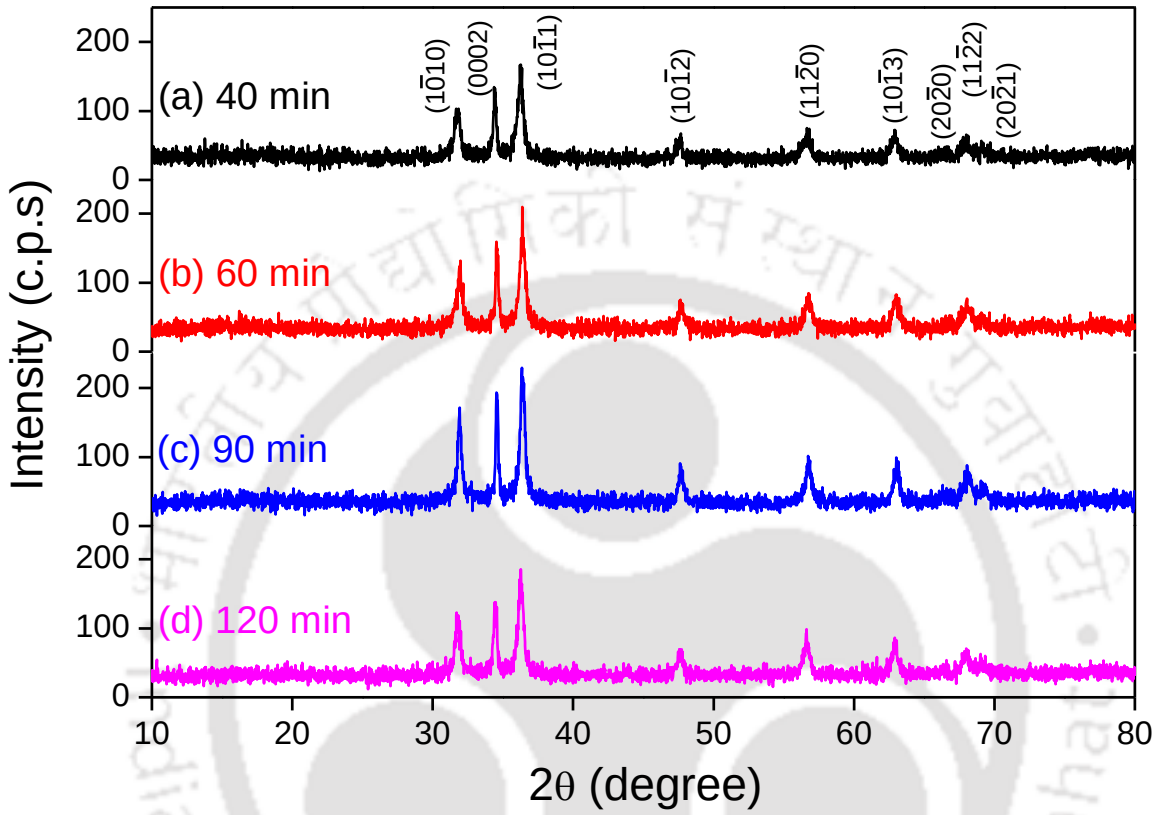

Figure 4.3.9 PXRD patterns obtained for the synthesized ZnO by varying reaction time, i.e. (a) 40 min, (b) 60 min, (c) 90 min and (d) 120 min

Table 4.3.1. Calculated crystallite size and intensity in counts per second (c.p.s) of the highest intense peak obtained from the PXRD patterns of figure 4.3.9.

Name of the compound	FWHM	Crystallite size D_p (nm)	Intensity maximum (c.p.s.)	2θ value (degree)	Crystal plane
(a) ZnO_40 min	0.57	20.0	165.6	36.2	(10$\bar{1}$1)
(b) ZnO_60 min	0.55	21.0	192.2	36.4	(10$\bar{1}$1)
(c) ZnO_90 min	0.46	25.7	215.4	36.4	(10$\bar{1}$1)
(d) ZnO_120 min	0.52	19.5	181.4	36.3	(10$\bar{1}$1)

It is observed from figure **4.3.9** that the PXRD peaks for the ZnO cages obtained after 90 min [trace (c)] are sharp (FWHM ~0.46) and intense (~215.4 c.p.s) as compared to the products recovered after 40 min [trace (a)] and 60 min [trace (b)] of reaction time. Moreover, the crystallite size (D_p) distribution (~26 nm; from table 4.3.1) is also found to be maximum for the product recovered after 90 min which is a clear reflection of higher crystallinity of the product as compared

to others. Although, the morphology of ZnO cages perceived in the reaction time at 60 min and 90 min are very similar as we have seen from the FESEM images **4.3.8** (B) and (C) respectively, the crystallinity of the later is superior to the former. This implies that an adequate time is achieved by the product, for aging in the reaction with time at 90 min which allows most possible regular arrangement of the ZnO crystal planes. Further, with an increase in the reaction time to 120 min, dissolution of the superstructures is noted, as evident from the high magnification FESEM image portrayed in the inset of the image (D), figure **4.3.8**. Dissolution of ZnO in wet chemical synthetic process is an inherent characteristic of the material, which leads to decrease in crystallinity.[29] The dissolution effect becomes more dominant in case of prolonged reaction time. Growth process reaches a certain equilibrium with the growth units; $Zn(OH)_4^{2-}$ and $Zn(NH_3)_4^{2+}$ after the formation of ZnO cages. As the reaction progresses, concentration of $Zn(OH)_4^{2-}$ and $Zn(NH_3)_4^{2+}$ is decreased. In order to maintain the equilibrium, dissolution process of ZnO cages in the reaction occurs and results in degraded ZnO cages with poor crystallinity. The PXRD analysis of the material is also in good agreement with the FESEM observations as shown in the figure **4.3.9** and table **4.3.1**. The increase in population of broken ZnO cages in this case, as indicated with red arrows in image (D), infers excess reaction time. Therefore, the optimum time for the completion of the reaction is established to be at 90 min.

Based on all the above discussions, the plausible formation mechanism of ZnO cages at optimized reaction conditions can be explained as follows.

4.3.3 MECHANISM OF ZnO SUPERSTRUCTURE FORMATION

Alginic acid is a linear copolymer of 1→4 covalently linked β-D-mannuronic acid and its C-5 epimer α-L-guluronic acid residues in different sequences to construct the backbone chain. Sodium salt of alginic acid, i.e., sodium alginate (ALG) is a naturally abundant polysaccharide or a "biopolymer" extracted from the cell walls of brown seaweed. It is soluble in water and ionizes to its anionic form, i.e., the alginate ion. 0.1 wt % solution of ALG in water is found to be negatively charged with zeta potential (ζ) ≈ –60 mV. These negatively charged alginate ions with carboxylate groups interact with the positively charged Zn^{2+} ions in the solution due to electrostatic forces and form a complex (1): [Zn^{2+}–ALGI] as shown in scheme **4.3.2**.[26] This complex appears in the reaction mixture as a gelatinous precipitate which is formed immediately after the addition of $Zn(NO_3)_2.6H_2O$ to the solution of ALG.

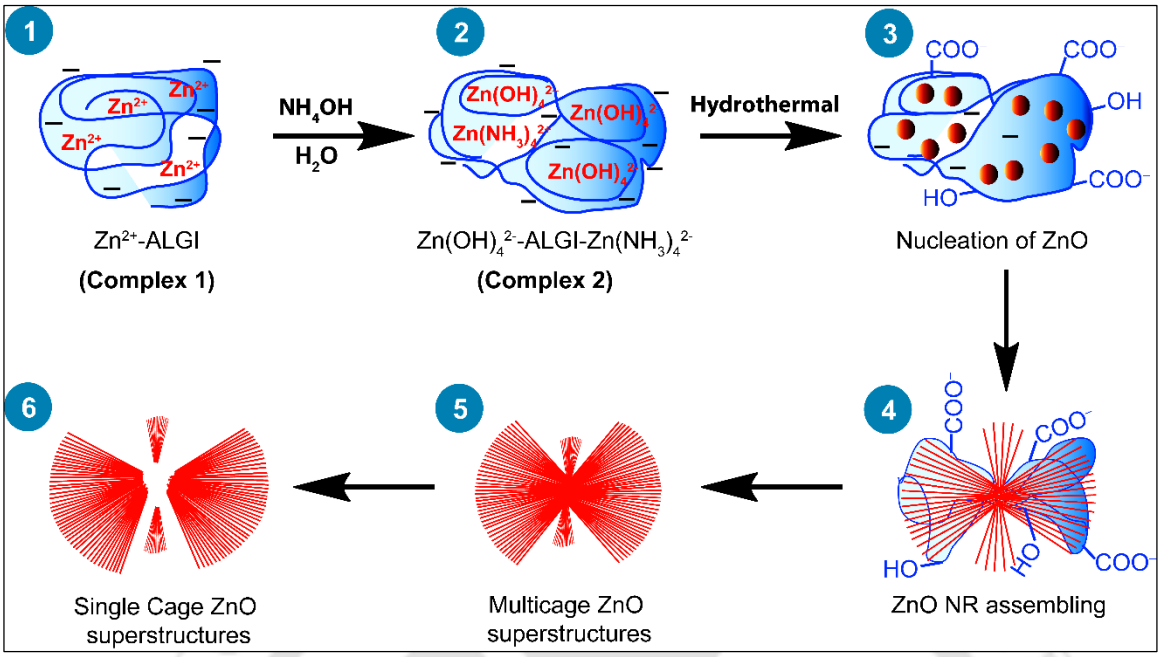

Scheme 4.3.2 Schematic representation of step by step evolution process of the ZnO cage formation in the reaction

On addition of NH_4OH, initially water insoluble white precipitate possibly of $Zn(OH)_2$ is observed. Further addition of NH_4OH upto the optimized amount, i.e., 1.5 mL per 25 mL, the aqueous solution becomes transparent and pH is found to be ~10 which infers the formation of water soluble $Zn(OH)_4^{2-}$ and $Zn(NH_3)_4^{2+}$ ions. It is well known that, $Zn(OH)_4^{2-}$ and $Zn(NH_3)_4^{2+}$ act as the growth units of ZnO crystal in the wet chemical reactions carried out in basic conditions.[30] Subsequently, due to Coulombic interactions, the $Zn(OH)_4^{2-}$ and $Zn(NH_3)_4^{2+}$ growth units are believed to be attached with the negatively charged alginate ions to form an adduct complex (2): $[Zn(OH)_4^{2-}–ALGI–Zn(NH_3)_4^{2+}]$. In hydrothermal reaction conditions, the growth units initiate the nucleation process and form numerous nuclei of ZnO. These ZnO nuclei tend to grow along (±) *c*-axes, i.e., along Zn^{2+} populated +(0001) and O^{2-} populated –(0001) high energy polar crystal facets promoted by $Zn(OH)_4^{2-}$ and the $Zn(NH_3)_4^{2+}$ growth units respectively which are leading to the formation of ZnO NRs.[31] Since, the ZnO crystal growth along (–) c-axis is the slowest growth direction, predominant growth units are $Zn(OH)_4^{2-}$ ions.[32] Simultaneously, the negatively charged alginate ions with ($–COO^-$) groups anchors to the positive Zn^{2+} populated +(0001) crystal facets of ZnO and adheres on the surface of ZnO NRs. Thus, the growth of ZnO NRs in presence of ALG is inhibited due to the minimized contact between the growth units and (0001) crystal surfaces. Additionally, the free (–OH) and ($–COO^-$) groups in the ALGI backbone

chain, triggers the assembling process of ZnO NRs and arrange hierarchically to form ZnO superstructures as shown in the step 4. At this step, the existence of optimum amount of NH_4OH and an equilibrium between gas–liquid in the autoclave are the crucial factors to acquire the anticipated size and shape of the product. As the reaction proceeds, some of the multi-cage super-structures fracture at the adjoining points and result in single cage superstructures.

4.3.4 UV-VISIBLE ABSORPTION AND PHOTOLUMINESCENCE ANALYSES

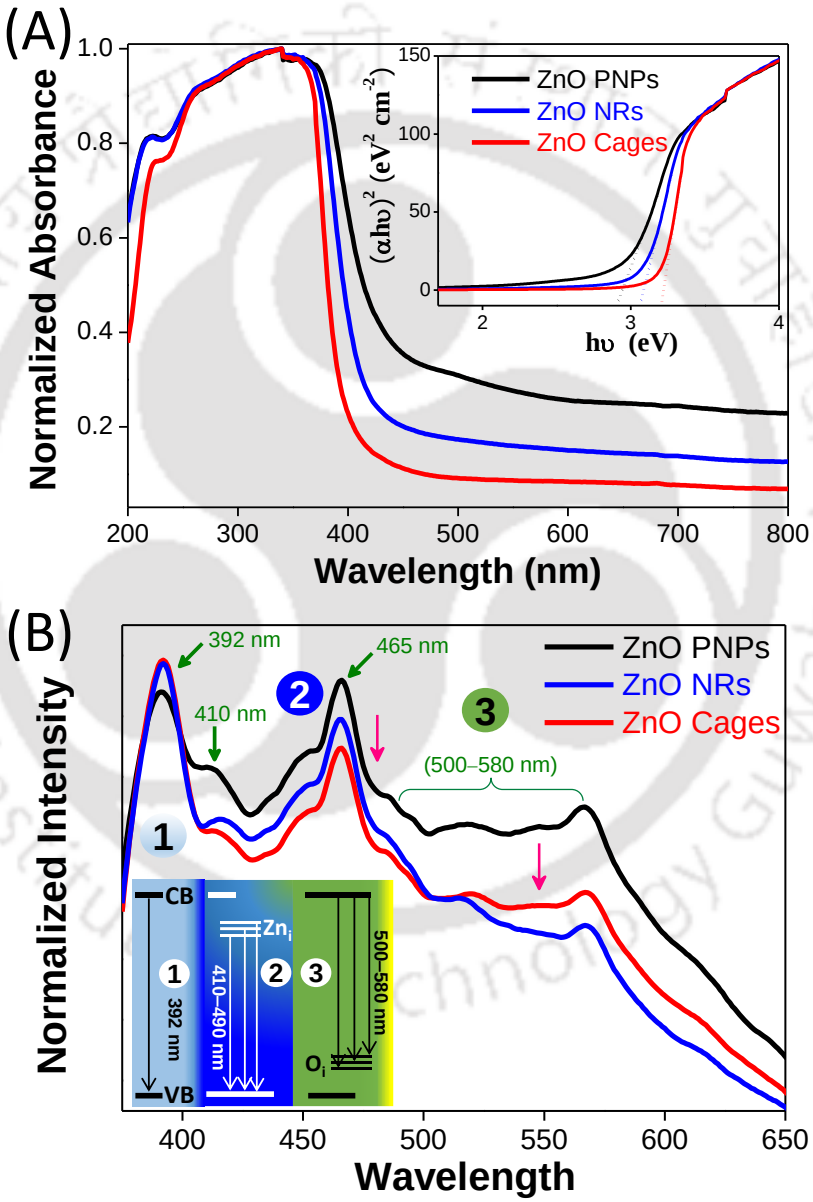

Figure 4.3.10 (A) UV-Visible absorption profiles for all the ZnO heterostructures (ZnO PNPs, ZnO NRs and ZnO Cages). Inset to it shows corresponding Tauc's plots. (B) Room temperature steady state photoluminescence (PL) spectra for all the ZnO heterostructures. Inset to it shows the corresponding electronic transitions of the peaks indicated in the spectra with green arrows.

Figure **4.3.10** (A) represents UV-Visible absorption spectra for all the synthesized ZnO heterostructures, i.e., ZnO cages (red line), ZnO NRs (blue line) and ZnO PNPs (black line). We have observed a moderate red shift of absorption onset in case of ZnO NRs (~25 nm) and ZnO PNPs (~30 nm) as compared to the ZnO cages. This may be due to smaller size distribution of ZnO NRs (~8-10 nm) in the superstructures relative to the particle size distribution in the other two samples (~1 µm and ~2 µm respectively). Optical band gap values for all the samples are estimated from corresponding Tauc's plots as depicted in the inset to figure **4.3.10** (A), considering ZnO as a direct bandgap material. In Tauc's plot, $(\alpha h\nu)^2$ is plotted against the photon energy ($h\nu$), where α is the absorption coefficient. The band gap values of ZnO hetero-structures are estimated as 3.2 eV for ZnO cages, 3.06 eV for ZnO NRs and 2.95 eV for ZnO PNPs. The observed lowering of band gap values for ZnO PNPs and ZnO NRs in contrast to ZnO cages is in accordance with the red shift of absorption profiles.

Emission characteristics and defect states of all three different morphologies of ZnO are analyzed by performing room temperature steady state photoluminescence (PL) spectroscopy at an excitation wavelength of 355 nm and illustrated in figure **4.3.10** (B). For all the samples, sharp emission in the UV range (~395 nm) followed by a shoulder around 410 nm and sharp peak at ~465 nm are noticed. A green broad emission band with satellite peaks at around ~500-580 nm are also observed. The sharp emission in the UV range signifies near-band-edge emission which is attributed to radiative exciton annihilation[33] as depicted in the inset (1). The shoulder peak around 410 nm and the sharp peak ~465 nm are originating from co-ordinatively unsaturated Zn^{2+} interstitial sites (Zn_i, shallow donor) in the ZnO nanostructures [see corresponding transitions in the inset (2)]. The emission peaks observed in the broad visible region (i.e., 500-580 nm) are accredited to the transitions from the conduction band to the deep trap levels of ZnO (created by oxygen vacancies in the ZnO crystal structure, O_i), as shown in the inset (3).[33,34] From figure **4.3.10** (B), it is clear that the intensity of near band-edge emission are comparable for ZnO NRs and ZnO cages while for ZnO PNPs the intensity is appreciably decreased. However, the intensity of the emission peaks due to zinc and oxygen defect sites are higher for ZnO PNPs as compared to ZnO NRs and ZnO cages. This is a clear reflection of higher population of defect sites in ZnO PNPs relative to the ZnO NRs and ZnO cages. This observation may be due to maximum population probability of grain boundary induced defect sites in ZnO PNPs, as they are composed of numerous inter-connected ZnO NP.

To gain insights into the variation of defect sites in the photoanodic films after the calcination, we have performed steady state and dynamic photoluminescence measurements as shown in figure **4.3.11**. Form the figure **4.3.11** (A), i.e., steady-state PL Spectra for the photoanodic films on FTO substrates, it is observed that calcination of photoanodes at 525 °C for 1h in a muffle furnace leads to the reduction in intensity of broad emission band in the visible region (~500-580 nm) which is attributed to the oxygen vacancies (or O_i) in the ZnO crystal structure. Among all the three samples, maximum reduction of oxygen vacancy distribution is observed in case of ZnO cages while it is at a minimum for ZnO PNPs. However, intensities of shoulder peak around 410 nm and the sharp peaks ~465 nm are slightly higher for ZnO cages which is an indicative of higher concentration of Zn_i defects sites in the photoanode than its counterparts, i.e., ZnO NR and ZnO PNP. Further, exciton lifetime in ZnO cages before and after the calcination is monitored by time resolved PL (TRPL) analysis to understand the charge transport kinetics in the photoanode as shown in figure **4.3.11** (B). Note that, the calcination temperatures were kept intentionally at 525 °C in order to have a match with the fabrication of photoanodes, where in a similar temperature regime was used to remove the binder and the other additives.

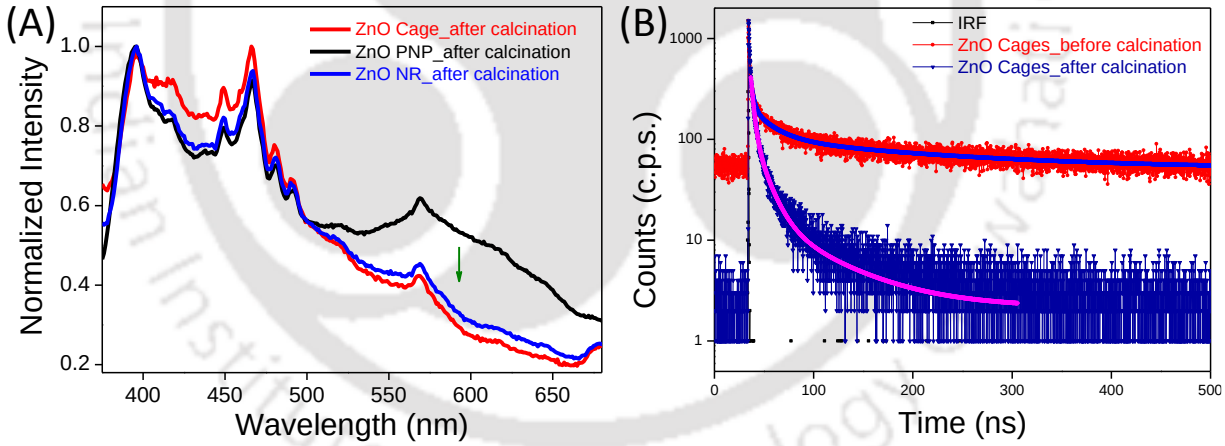

Figure 4.3.11 (A) Steady-State PL Spectra for the photoanodic films on FTO substrates namely ZnO cage (red line), ZnO PNP (black line), and ZnO NR (blue line) recorded at an excitation wavelength of 355 nm **(B)** Time resolved photoluminescence spectra for ZnO Cages recorded at an excitation wavelength of 355 nm before and after calcination, showing a sharp decline in the average lifetimes of the calcined samples.

The PL decay traces of all the samples were fitted with a tri-exponential function to calculate the exciton lifetime. Multi-exponential emission decay pattern is observed mainly due to influence of distribution in the recombination rate constants on the decay kinetics. The values of fitting parameter (χ^2), exciton lifetimes (τ_1, τ_2, τ_3), pre-exponential factors (α_1, α_2, α_3) and average exciton lifetimes $<\tau>$ are listed in the table **4.3.2**.

Table 4.3.2 The values of fitting parameter (χ^2), exciton lifetimes (τ_1, τ_2, τ_3), pre-exponential factors (α_1, α_2, α_3) and calculated values of average exciton lifetimes <τ>

Sample (ZnO Cage)	χ^2	τ_1 (ns)	τ_2 (ns)	τ_3 (ns)	α_1	α_2	α_3	<τ> (ns)
Before calcination	0.99	2.9	21.6	190.7	9.9	18.3	71.8	185.6
After calcination	1.05	2.8	12.5	61.9	44.7	33.9	21.4	46.8

The average lifetime values were calculated using equation (2)[35]

$$< \tau >= \frac{\alpha_1 \tau_1^2 + \alpha_1 \tau_2^2 + \alpha_1 \tau_3^2}{\alpha_1 \tau_1 + \alpha_1 \tau_2 + \alpha_1 \tau_3} \qquad (2)$$

From table **4.3.2**, we have seen that the value of average lifetime, <τ> is decreased about four times for the calcined ZnO cages as compared to the non-calcined sample. The faster exciton life time of calcined ZnO cages signifies improved charge separation and transport through the tiny 1D ZnO NR building blocks. This may be due to minimized oxygen vacancies in the ZnO cage based photoanode after calcination, also evident from the steady state PL analysis. It is well known that, the oxygen defect sites in the ZnO crystal structure can act as radiative recombination centers for photoexcited electrons and increases the exciton lifetime.[36]

4.3.5 BET SURFACE AREA ANALYSIS

Nitrogen adsorption and desorption isotherms of surface area analysis for all the as-synthesized ZnO with different morphologies are shown in the figure **4.3.12**. It is expected that if a wide band gap semiconductor material (i.e. Photoanodic materials) is to be used in dye sensitized solar cell devices (DSSCs), it should have (i) high surface area and (ii) high porosity; in order to achieve a better photovoltaic performance. Type IV isotherms and H3 hysteresis loops observed for ZnO PNPs and ZnO cages, confirm the characteristic mesoporous nature of both the materials. The observed BET surface area of the as-synthesized ZnO PNPs is found to be ~78 m^2g^{-1}, for ZnO cages is ~61 m^2g^{-1}, and for ZnO NR is ~10 m^2g^{-1}.

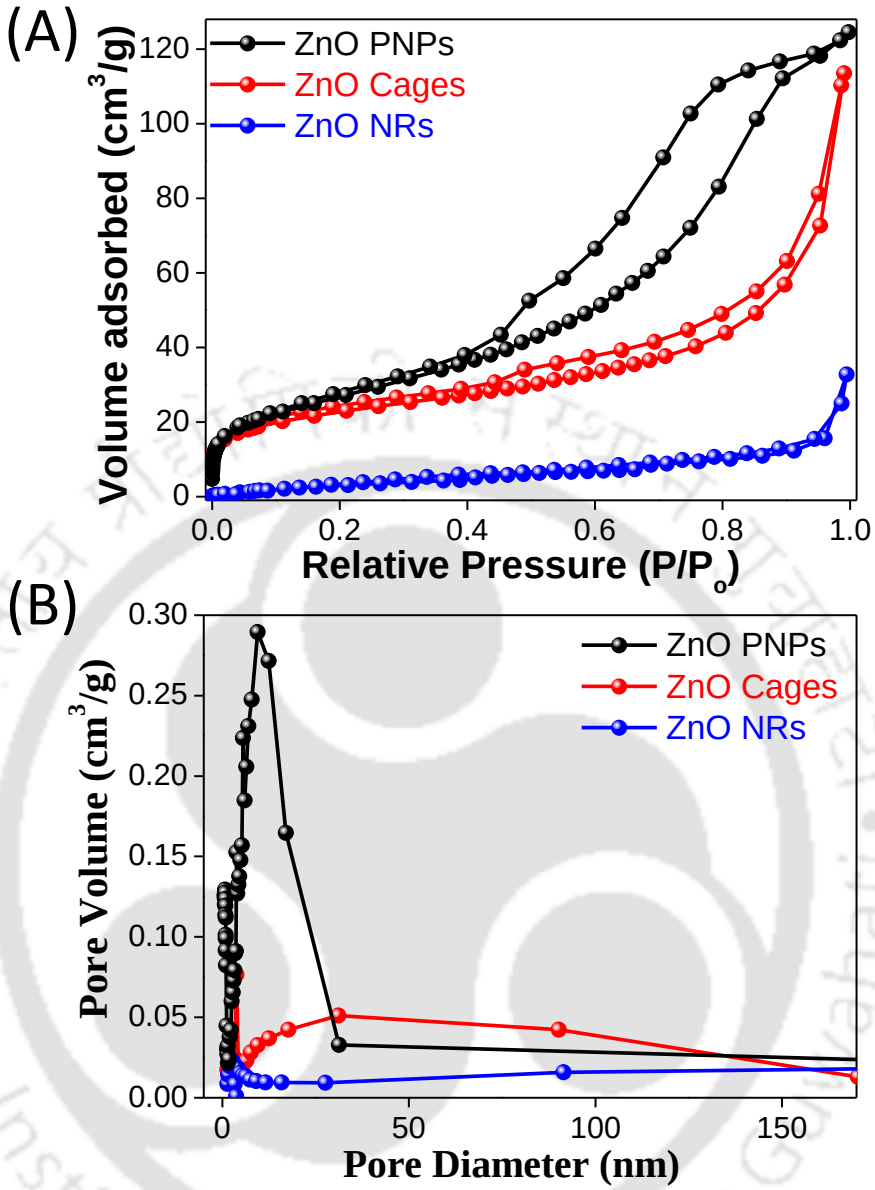

Figure 4.3.12 (A) Nitrogen adsorption–desorption isotherms and **(B)** Barrett–Joyner–Halenda (BJH) pore size distribution plots for as synthesized ZnO PNPs, ZnO cages and ZnO NRs.

Figure **4.3.12** (B) demonstrates corresponding Barrett–Joyner–Halenda (BJH) pore size distribution curves for the ZnO heterostructures namely ZnO PNPs (black line), ZnO Cages (red line) and ZnO NRs (blue line). We have observed that pore size distribution for ZnO PNPs is ~10–25 nm and for ZnO cages is in a broad range ~10–150 nm, while there is no indication of pores in case of ZnO NR. The broad range pore size distribution observed in case of ZnO cages is due to presence of two type of pores in them, i.e., (i) pores in between the tiny NRs and (ii) the macro-pores formed due to fracture of the multi cages at the adjoining points as we have discussed in the FESEM analysis section.

4.3.6 UV–VISIBLE ABSORPTION AND DIFFUSE REFLECTANCE ANALYSIS OF THE PHOTOANODES

Figure **4.3.13** (A) demonstrates the normalized UV–vis diffuse reflectance absorption profiles of N719 dye sensitized photoanodes fabricated with as synthesized ZnO heterostructures, i. e. ZnO PNPs, ZnO cages and ZnO NRs.

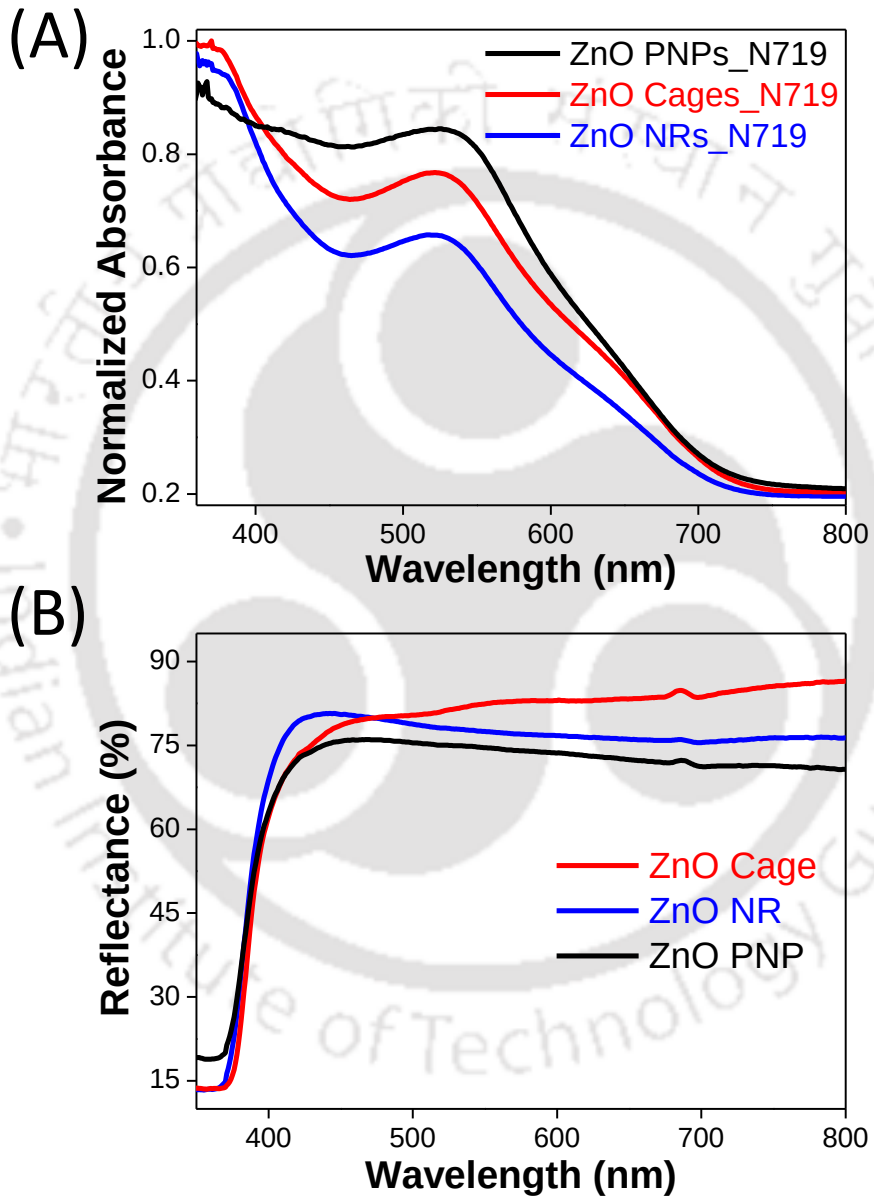

Figure 4.3.13 (A) UV-Vis diffuse reflectance absorption spectra of all fabricated photoanodes sensitized with N719 dye. **(B)** Diffuse reflectance spectra of ZnO cage, ZnO NR and ZnO PNP based films of comparable thickness deposited on the FTO substrates.

Increasing order of absorbance of the photoanodes in the visible region (~420–700 nm) is observed to be: ZnO NRs< ZnO cages< ZnO PNPs which suggests a higher dye adsorption in the

ZnO PNPs and ZnO cages as compared to the ZnO NRs scaffolds. It is well known that, the N719 dye absorb photon energy in the region (420–670 nm) starting the absorption onset from 710 nm. This observation validates the assumption of increase in dye loading capability of a material with increase in surface area. Accordingly, it is expected that the flux of photogenerated electron injection will be higher for ZnO PNP based photoanode relative to the other two photoanodes.

Reflectance measurements are carried out for all the photoanode films of comparable thickness based on ZnO cage (red line), ZnO NR (blue line) and ZnO PNP (black line) deposited on FTO substrates to investigate the light scattering effects as depicted in Figure **4.3.13** (B). The film based on ZnO cages is exhibiting a distinct higher reflectance in the wavelength range 500–800 nm than that of other two films based on ZnO NRs and ZnO PNPs. This confirms efficient light scattering by the ZnO cages in the photoanode to enhance the repeated excitation process of dye molecules over the ZnO NR and ZnO PNP based photoanodes. Hollow characteristic of ZnO cages is believed to be the most probable reason for superior light scattering which is not in case of ZnO PNP and ZnO NR based photoanodes. ZnO NR and ZnO PNP based films have shown similar reflectance ability.

4.3.7 PHOTOVOLTAIC CHARACTERISTICS OF THE SOLAR CELLS

In order to ensure the technological importance and superiority of ZnO cages over the ZnO PNPs, and ZnO NRs; DSSC devices are fabricated and compared their performance parameters. Figure **4.3.14** (A) represents characteristic current density–voltage (*J–V*) curves for the N719 sensitized ZnO cage, ZnO PNP and ZnO NR based devices. Figure **4.3.14** (B) shows IPCE plots for the respective devices. The photovoltaic performance parameters such as short circuit current density (J_{sc}), open circuit voltage (V_{oc}), fill factor (FF) and the overall power conversion efficiency (PCE, η) for all the fabricated devices namely, (a) ZnO Cage, (b) ZnO PNP, and (c) ZnO NR are listed in table **4.3.3**.

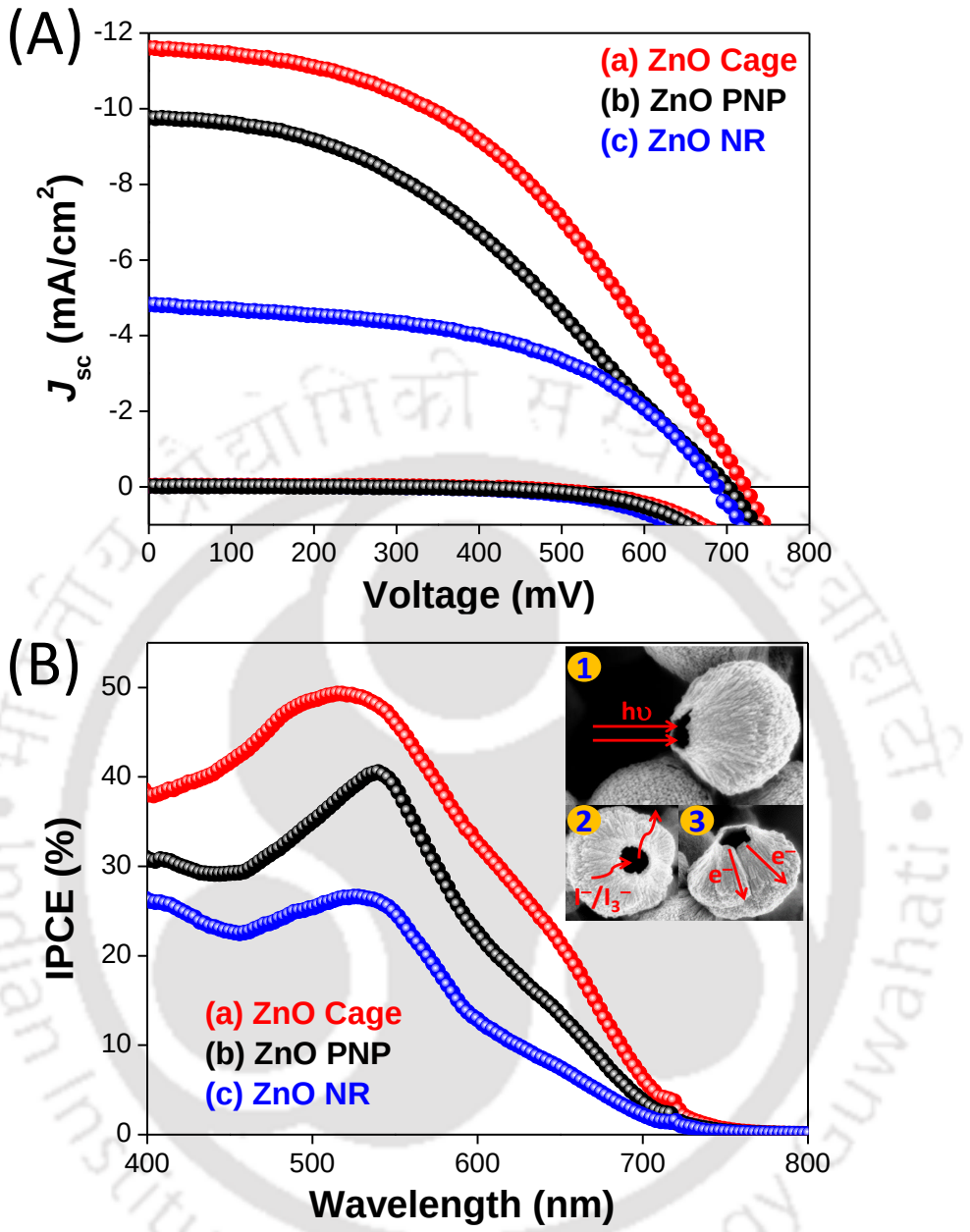

Figure 4.3.14 (A) Current density–Voltage (*J*–*V*) curves for the photovoltaic devices (a) ZnO Cage [red line], (b) ZnO PNP [black line] and (c) ZnO NR [blue line] **(B)** IPCE plots for the respective devices employing I^-/I_3^- as the redox couple. Inset shows advantages of ZnO cages in terms of (1) light scattering, (2) electrolyte diffusion and (3) electron transport in solar cell devices.

Table 4.3.3 Short-circuit current density (J_{sc}), open-circuit voltage (V_{oc}), fill factor (FF), and power conversion efficiency (η) for the fabricated solar cells incorporating different photoanodes

Devices	J_{sc} (mAcm^{-2})	V_{oc} (mV)	FF (%)	PCE (%)	Redox couple
(a) ZnO Cage	11.8 (11.2 ± 0.7)	720 (715 ± 7)	50 (50 ± 3)	4.26	I^-/I_3^-
(b) ZnO PNP	9.8 (9.5 ± 0.8)	702 (696 ± 8)	40 (38 ± 4)	2.75	
(c) ZnO NR	4.8 (4.5 ± 0.7)	690 (686 ± 6)	50 (47 ± 5)	1.67	

Form figure **4.3.14** (A) and (B), higher values of J_{sc} and IPCE of ZnO Cage based device (a) [11.8 mA/cm^2 and 50 %] in contrast to the ZnO PNP based device (b) [9.8 mA/cm^2 and 40 %] and ZnO NR based device (c) [4.8 mA/cm^2 and 27 %] are indicating a better absorption of solar irradiation by the device (a), probably due to a better light scattering ability and higher flux of photoinduced electron injection. As explicit from the IPCE plot, better light harvesting ability and red shift towards longer wavelength of about 50 nm of the device (a), is attributed to an efficient light confinement and repeated excitation of dye molecules in the ZnO cage based photoanode.[37,38] Efficient light confinement in the ZnO Cage based photoanode is expected due to hollow characteristic of ZnO cages and is shown in the inset (1), figure (B), which upsurges the value of J_{sc}.[39] Additionally, mesoporous characteristic of ZnO cages expedite the diffusion of electrolyte for better functioning of the redox mediator and the tiny 1-D ZnO NR building blocks act as the transport channels for faster migration of photo-induced electrons to boost the photovoltaic performances [depicted in the insets (2) and (3) to figure **4.3.14** (B)].[40,41] Lower values of J_{sc} (~9.8 mA/cm^2) and FF (40 %) for device (b) compared to device (a), even though it have higher dye loading, authenticates the presence of maximum population of crystal defect induced trap sites in ZnO PNPs as discussed in the PL analysis. Similarly, minimum dye loading in ZnO-NR based photoanode is reflected in its low values of J_{sc} (4.8 mA/cm^2) and V_{oc} (690 mV). However, an appreciated value of FF (~50 %) furnished by the device (c) is indicative of facilitated diffusion of electrolyte in the photoanode as compared to the ZnO PNP based photoanode. It is believed that, ZnO NRs in the photoanodic film are randomly arranged and fused to form bigger and higher number of inter-particle pores as compared to the ZnO PNP based photoanodes which expedite the electrolyte diffusion process for better functioning of redox shuttle. Note that, ZnO PNPs have an agglomerated structure of numerous interconnected ZnO NPs which decreases the probability of inter-particle pore formation and smooth diffusion of electrolyte in the photoanodic film. In summary, the enhanced photovoltaic performance parameters of the ZnO cage based device are leading to an appreciated value of PCE (~4.26 %) in current scenario which establishes the material to be of good technological importance.

We have investigated the morphological features of ZnO cages in the fabricated photoanodes by performing top view and cross-sectional FESEM analysis to establish the stability of the superstructures under rigorous device making conditions and shown in the figure **4.3.15**.

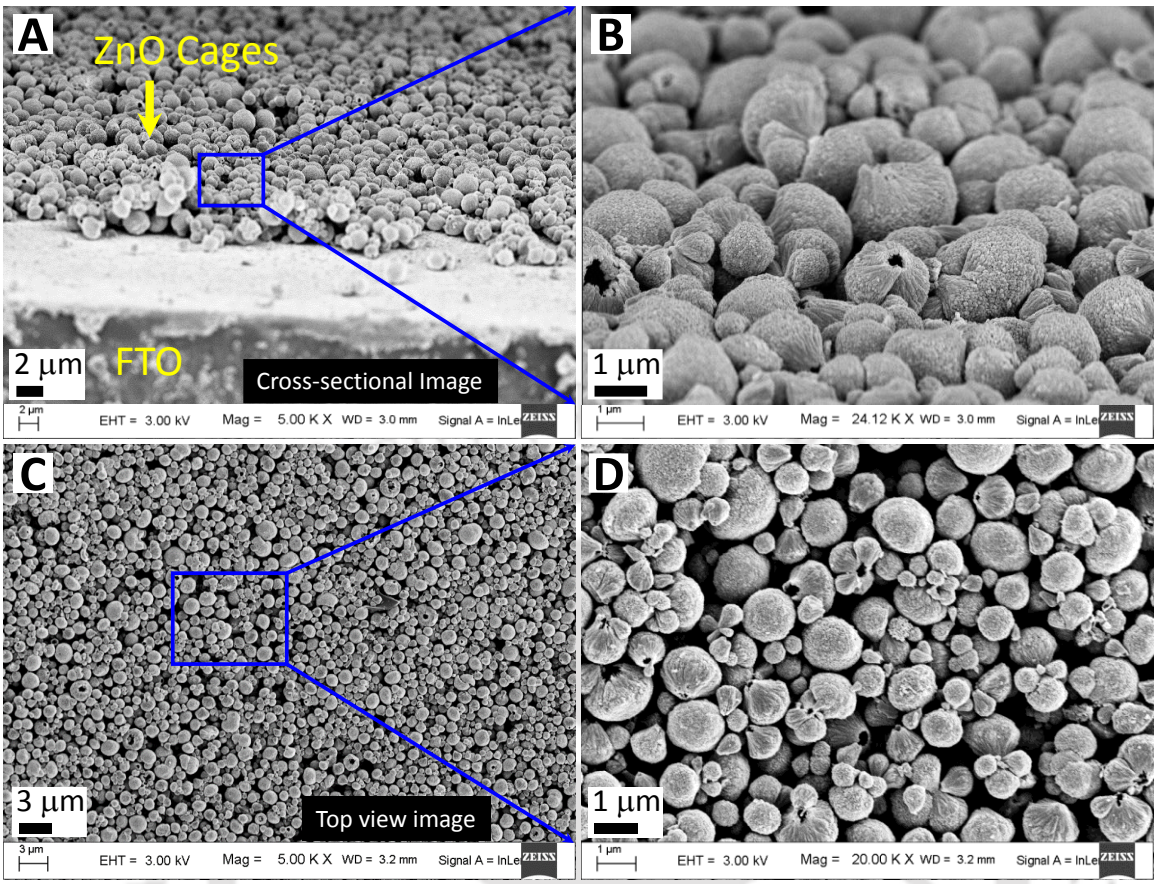

Figure 4.3.15 Cross-sectional (A & B) and top view (C & D) FESEM images of as fabricated ZnO cage based Photoanode.

Figure **4.3.15** (A) and (B) are representing cross-sectional FESEM images of ZnO cage based photoanode whereas the (C) and (D) are the top view images. From the FESEM images, it is clear that, cage-like ZnO superstructures remain intact even after the film deposition and calcination processes. This result confirms the beneficial role of hollow and mesoporous characteristics of ZnO cages in its enhanced photovoltaic properties.

Electron transport and recombination kinetics in the photovoltaic devices namely, device (a) ZnO Cage, device (b) ZnO PNP, and device (c) ZnO NR are monitored by employing electrochemical impedance spectroscopy (EIS). Nyquist and Bode phase plots under dark conditions in the frequency range from 0.1 Hz to 100 kHz at an applied bias equivalent to the open-circuit voltages as shown in figure **4.3.16** (A) and (B). From the Nyquist plots, i.e. figure (A), the bigger semicircles in the medium-frequency region (right semicircle) specifies the process of charge-transfer at the working electrode/electrolyte interface while the smaller semicircles in the

high frequency region (left semicircle) describes the counter electrode/electrolyte interfacial redox reactions.[42]

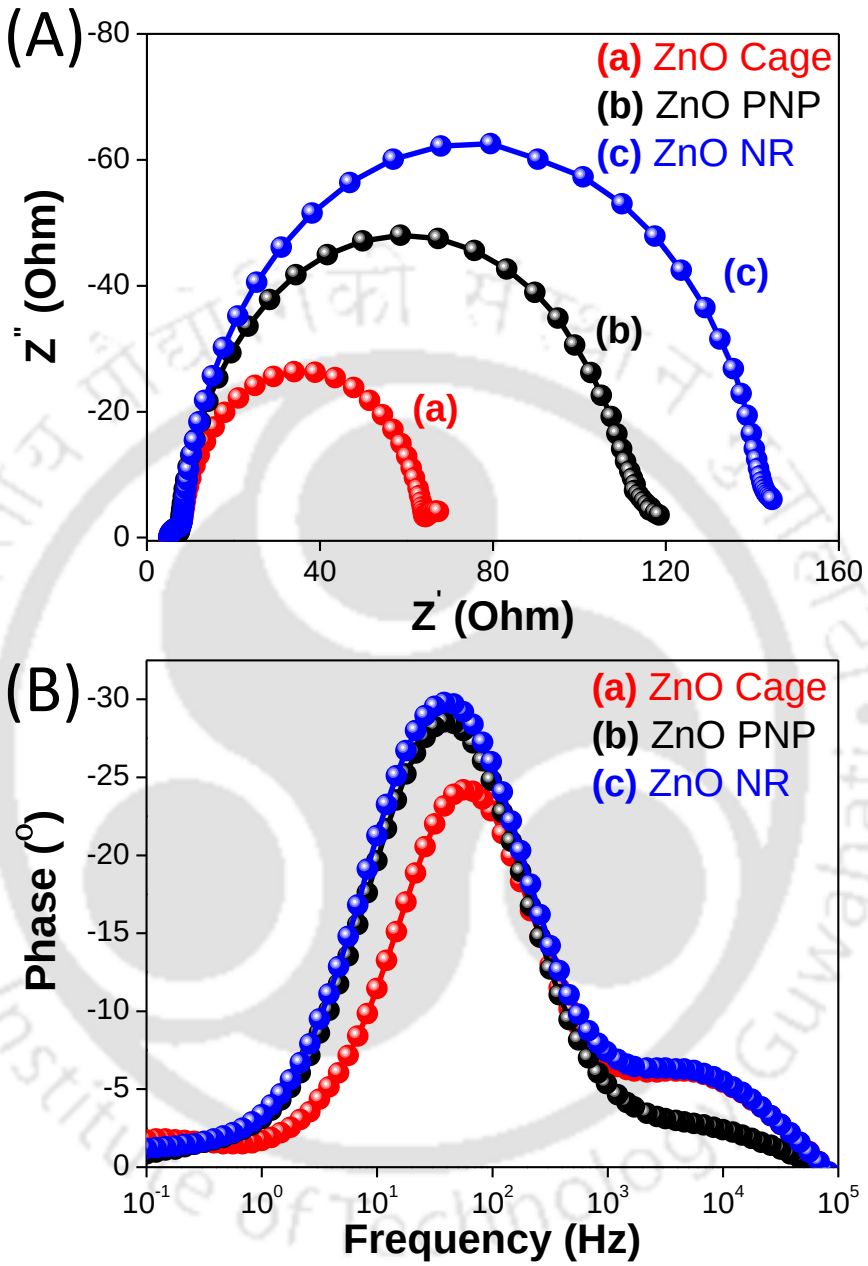

Figure 4.3.16 (A) Nyquist plots for the photovoltaic devices (a) ZnO Cage [red line], (b) ZnO PNP [black line] and (c) ZnO NR [blue line] in dark at open-circuit voltage and in a frequency range from 0.1 Hz to 100 kHz. **(B)** Bode phase plots for all the respective devices.

Corresponding Bode phase plots are portrayed in the figure **4.3.16** (B). The characteristic peak frequencies in the medium frequency region (f_{max}) for the ZnO Cage, ZnO PNP and ZnO NR based device is located at ~56.2 Hz, ~38.3 Hz and ~36.95 Hz respectively. We have calculated the

photo-induced electron life time (τ_e) in the conduction band (CB) of ZnO cage, ZnO PNP and ZnO NR by using the formula (3)[43]

$$\tau_e = \frac{1}{2\pi f_{max}} \qquad (3)$$

The τ_e values are found to be ~2.8 ms, ~4.15 ms, and ~4.3 ms for ZnO cage, ZnO PNP and ZnO NR respectively. It is observed from figure **4.3.16** (A) that the diameter (R_k) of the right semicircle for the ZnO NR based device is larger in contrast to all other devices. The increasing trend of R_k and life time (τ_e) of the photoinduced electrons in the CB of ZnO heterostructures is ZnO Cage< ZnO PNP< ZnO NR. It is well known that, R_k encompasses the charge recombination resistance and partial contribution from transport resistance.[44] Higher values of R_k and τ_e for ZnO NR based device confirms minimum photoinduced electron interception to the I^-/I_3^- redox shuttle at the ZnO NR/dye/electrolyte interface compared to the ZnO PNPs and ZnO cages respectively which is also reflected in the elevated value of FF (~50 %) for the device.[45,46] This may be due to single crystalline nature of ZnO NRs and minimum intrinsic defect sites as revealed from TEM and PL analysis respectively which eventually increases the diffusion length of photo-injected electrons. However, flux of photo-induced electrons is expected to be minimum in case of ZnO NR based photoanode due to a lesser amount of adsorption of dye molecules. It is observed that, despite the lower τ_e (~2.8 ms) and R_k values of ZnO Cage based device, the performance of the device is superior as compared to its counterparts. Injection of high flux of photo-induced electrons in ZnO cage as compared to the device with ZnO NRs overwhelms the efficiency parameters of the device. In order to understand the electronic interactions between N719 dye and as synthesized ZnO heterostructures (i.e., ZnO cage, ZnO PNP and ZnO NR), steady state photoluminescence (PL) analysis is performed for all the photoanodes and N719 dye drop-casted on glass substrate. Figure 4.3.17 is depicting normalized PL spectra for all the samples; namely, N719 dye (magenta line), ZnO PNP (black line), ZnO NR (blue line) and ZnO cage (red line).

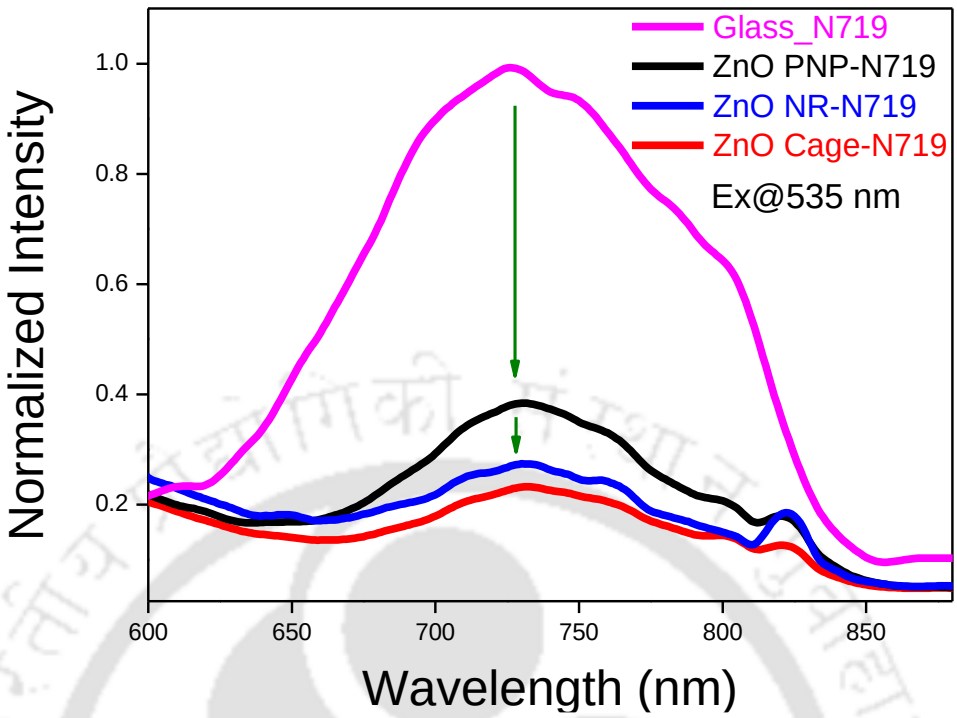

Figure 4.3.17 Steady-State Photoluminescence Spectra for N719 dye drop-casted on glass substrate (magenta line), ZnO PNP (black line), ZnO NR (blue line) and ZnO cage (red line), films sensitized with N719 dye on glass substrates. Excitation wavelength for all the samples is 535 nm.

From figure **4.3.17**, it is observed that significant quenching of PL emission intensity (indicated by olive arrow) originating from the N719 dye, when it is anchored to the ZnO. This observation infers excited state electronic interaction between N719 dye and ZnO which confirms the photoinduced charge injection from the dye molecules to the conduction band (CB) of ZnO.[45] Decreasing trend in emission intensity for the N719 dye sensitized photoanodes is ZnO PNP > ZnO NR > ZnO Cage. This is indicative of faster and efficient charge injection from the dye molecules to the ZnO cages as compared to the ZnO PNP and ZnO NRs; attributed to strong electronic interaction between ZnO cage and N719 dye molecules in the photoanode. Moreover, a faster migration of photoinduced electrons through the 1-D ZnO NR building blocks enriches efficient charge transfer to the external circuit. Similar explanation is validated for the ZnO PNP based device (b), in which adsorption of dye is observed to be the highest and probed to be lesser electron interception compared to device (a) with ZnO cages. However, due to a retarded diffusion of electrolyte and higher population of trap sites, the performance of the device is low as compared to the device (a). Lower diffusion of electrolyte in case of ZnO PNP based device is expected due to the agglomerated structure of ZnO PNPs. The agglomerated structure of ZnO PNPs decreases

the probability of inter-particle pore formation in the photoanode, which is also reflected in the lower value of FF (~40 %) for the device (b).

4.4 CONCLUSIONS

We have developed a simple, green hydrothermal synthetic protocol for high quality ZnO superstructures of extensive technological importance utilizing a naturally abundant bio-template "alginic acid". The reaction is investigated in detail by varying synthetic conditions in order to understand the interactions between the organic template and inorganic material. It is found that the optimum concentration of negatively charged alginate ions and NH_4OH in the reaction system are the key factors for formation of these exotic cage like, mesoporous superstructures. A plausible growth mechanism is proposed for the 1-D ZnO NR assembled ZnO superstructures and evaluated their photovoltaic properties. A comparative study on photovoltaic performance parameters of the fabricated dye sensitized solar cells, i.e. based on ZnO cage, ZnO PNP and ZnO NR are carried out. An appreciated value of power conversion efficiency (PCE, η) is furnished by the ZnO cage based devices (η ≈4.26 %) which is ~60 % and ~35 % improvement over the ZnO NR (η ≈1.67 %) and ZnO PNP (η ≈2.75 %) based devices. Enhanced photovoltaic performance of ZnO cage based devices are concluded mainly due to higher flux of photoinduced electrons, enhanced light scattering, probability of facile diffusion of electrolyte and efficient charge separation through nano sized 1-D ZnO NR conduits.

4.4 REFERENCES

(1) Liu, Y.; Goebl J.; Yin, Y. *Chem. Soc. Rev.*, **2013**, *42*, 2610.

(2) Zeng, H. C. *J. Mater. Chem.*, **2011**, *21*, 7511.

(3) Shi, W.; Song S.; Zhang, H. *Chem. Soc. Rev.*, **2013**, *42*, 5714.

(4) Nguyen, T.-D. *Nanoscale*, **2013**, *5*, 9455.

(5) Chen, Z.; Jiao, Z.; Pan, D.; Li, Z.; Wu, M.; Shek, C.-H.; Wu, C. M. L.; Lai, J. K. L. *Chem. Rev.* **2012**, *112*, 3833.

(6) Zhang, Q.; Uchaker, E.; Candelaria, S. L.; Cao, G. *Chem. Soc. Rev.*, **2013**, *42*, 3127.

(7) Liu, B.; Zeng, H. C. *J. Am. Chem. Soc.*, **2004**, *126*, 16744.

(8) Feng, J.-J.; Liao, Q.-C.; Wang, A.-J.; Chen, J.-R. *CrystEngComm*, **2011**, *13*, 4202.

(9) Hu, P.; Han, N.; Zhang, X.; Yao, M.; Cao, Y.; Zuo, A.; Yang, G.; Yuan, F. *J. Mater. Chem.*, **2011**, *21*, 14277.

(10) Liu, B.; Zeng, H. C. *Chem. Mater.*, **2007**, *19*, 5824.

(11) Mo, M.; Yu, J. C.; Zhang, L.; Li, S.-K. A. *Adv. Mater.*, **2005**, *17*, 756.

(12) Zhou, H.; Fan T.; Zhang, D. *ChemSusChem*, **2011**, *4*, 1344.

(13) Yao, H.-B.; Fang, H.-Y.; Wang X.-H.; Yu, S.-H. *Chem. Soc. Rev.*, **2011**, *40*, 3764.

(14) Sotiropoulou, S.; Sierra-Sastre, Y.; Mark S. S.; Batt, C. A. *Chem. Mater.*, **2008**, *20*, 821.

(15) McMillan, R. N.; Paavola, C. D.; Howard, J.; Chan, S. L; Zaluzec, N. J.; Trent, J. D. *Nat. Mater.*, **2002**, *1*, 247.

(16) Huang, J.; Wang X.; Wang, Z. L. *Nano Lett.*, **2006**, *6*, 2325.

(17) D. Yang, L. Qi and J. Ma, *Adv. Mater.*, **2002**, *14*, 1543.

(18) J. He, T. Kunitake and A. Nakao, *Chem. Mater.*, **2003**, *15*, 4401.

(19) Yin, J.; Lu, Q.; Yu, Z.; Wang, J.; Pang H.; Gao, F. *Cryst. Growth Des.*, **2010**, *10*, 40.

(20) Hall, S. R.; Bolger, H.; Mann, S., *Chem. Commun.*, **2003**, *22*, 2784.

(21) Tseng, Y.-H.; Lin, H.-Y.; Liu, M.-H.; Chen, Y.-F.; Mou, C.-Y. *J. Phys. Chem. C*, **2009**, *113*, 18053.

(22) Waltz, F.; Wißmann, G.; Lippke, J.; Schneider, A. M.; Schwarz, H.-C.; Feldhoff, A.; Eiden, S.; Behrens, P. *Cryst. Growth Des.*, **2012**, *12*, 3066.

(23) Wang, A.-J.; Liao, Q.-C.; Feng, J.-J.; Zhang, P.-P.; Li, A.-Q.; Wang, J.-J.; *CrystEngComm*, **2012**, *14*, 256.

(24) Xu, A.-W.; Ma, Y.; Cölfen, H. *J. Mater. Chem.*, **2007**, *17*, 415.

(25) Begum, G.; Manorama, S. V.; Singh, S.; Rana, R. K. *Chem.–Eur. J.*, **2008**, *14*, 6421.

(26) Chetia, T. R.; Ansari, M. S.; Qureshi, M. *ACS Appl. Mater. Interfaces*, **2015**, *7*, 13266.

(27) Huang, M.; Yan, Y.; Feng, W.; Weng, S.; Zheng, Z.; Fu, X.; Liu, P. *Cryst. Growth Des.*, **2014**, *14*, 2179.

(28) Mclaren, A.; Valdes-Solis, T.; Li, G.; Tsang, S. C. *J. Am. Chem. Soc.*, **2009**, *131*, 12540.

(29) Yu, Q.; Fu, W.; Yu, C.; Yang, H.; Wei, R.; Li, M.; Liu, S.; Sui, Y.; Liu, Z.; Yuan, M.; Zou, G. *J. Phys. Chem. C*, **2007**, *111*, 17521.

(30) Wang, Z.; Qian, X. F.; Yin, J.; Zhu, Z. K. *J. Solid State Chem.*, **2004**, *177*, 2144.

(31) Sun, X. M.; Chen, X.; Deng, Z. X.; Li, Y. D. *Mater. Chem. Phys.*, **2002**, *78*, 99.

(32) Govender, K.; Boyle, D. S.; Kenway, P. B.; O'Brien, P. *J. Mater. Chem.*, **2004**, *14*, 2575.

(33) Zeng, H.; Duan, G.; Li, Y.; Yang, S.; Xu, X.; Cai, W. *Adv. Funct. Mater.*, **2010**, *20*, 561.

(34) Wu, X. L.; Siu, G. G.; Fu, C. L.; Ong, H. C.; *Appl. Phys. Lett.*, **2001**, *78*, 2285.

(35) Kongkanand, A.; Tvrdy, K.; Takechi, K.; Kuno, M.; Kamat, P. V. *J. Am. Chem. Soc.*, **2008**, *130*, 4007.

(36) Cheng, H.-M.; Huang, K.-Y.; Lee, K.-M.; Yu, P.; Lin, S.-C.; Huang, J.-H.; Wu, C.-G.; Tang, J. *Phys. Chem. Chem. Phys.*, **2012**, *14*, 13539.

(37) Barpuzary, D.; Qureshi, M. *ACS Appl. Mater. Interfaces*, **2013**, *5*, 11673.

(38) Chetia, T. R.; Barpuzary, D.; Qureshi, M. *Phys. Chem. Chem. Phys.*, **2014**, *16*, 9625.

(39) Qureshi, M.; Chetia, T. R.; Ansari, M. S.; Soni, S. S. *J. Mater. Chem. A*, **2015**, *3*, 4291.

(40) Plass, R.; Pelet, S.; Krueger, J.; Grätzel, M.; Bach, U. *J. Phys. Chem. B*, **2002**, *106*, 7578.

(41) Barpuzary, D.; Banik, A.; Panda, A. N.; Qureshi, M.; *J. Phys. Chem. C*, **2015**, *119*, 3892.

(42) Phadke, S.; Pasquier, A. D.; Birnie, D. P. *J. Phys. Chem. C*, **2011**, *115*, 18342.

(43) Kern, R.; Sastrawan, R.; Ferber, J.; Stangl R.; Luther, J. *J. Electrochim. Acta*, **2002**, *47*, 4213.

(44) Tian, J.; Uchaker, E.; Zhang, Q.; Cao, G. *ACS Appl. Mater. Interfaces*, **2014**, *6*, 4466.

(45) Barpuzary, D.; Patra, A. S.; Vaghasiya, J. V.; Solanki, B. G.; Soni, S. S.; Qureshi, M. *ACS Appl. Mater. Interfaces*, **2014**, *6*, 12629.

(46) Peng, W.; Han, L.; Wang, Z. *Chem.–Eur. J.*, **2014**, *20*, 8483.

CHAPTER 5

Fabrication of Bilayer ZnO Based Hybrid Photoanode for Enhanced Photovoltaic Performance in CdS Quantum dot Sensitized Solar Cells

This chapter demonstrates fabrication of a multifunctional bi-layered ZnO based hybrid photoanode and its utilization in QDSSC devices. The key features of the proposed hybrid photoanode are – (i) faster charge transport through 1D ZnO NWs for an enhanced charge separation, (ii) excellent light scattering effects for repeated excitation of the sensitizer particles, (iii) better diffusion of electrolyte for smooth functioning of the redox couple and (iv) higher surface area provided by the 3D mesoporous ZnO microspheres for efficient loading of sensitizer particles.

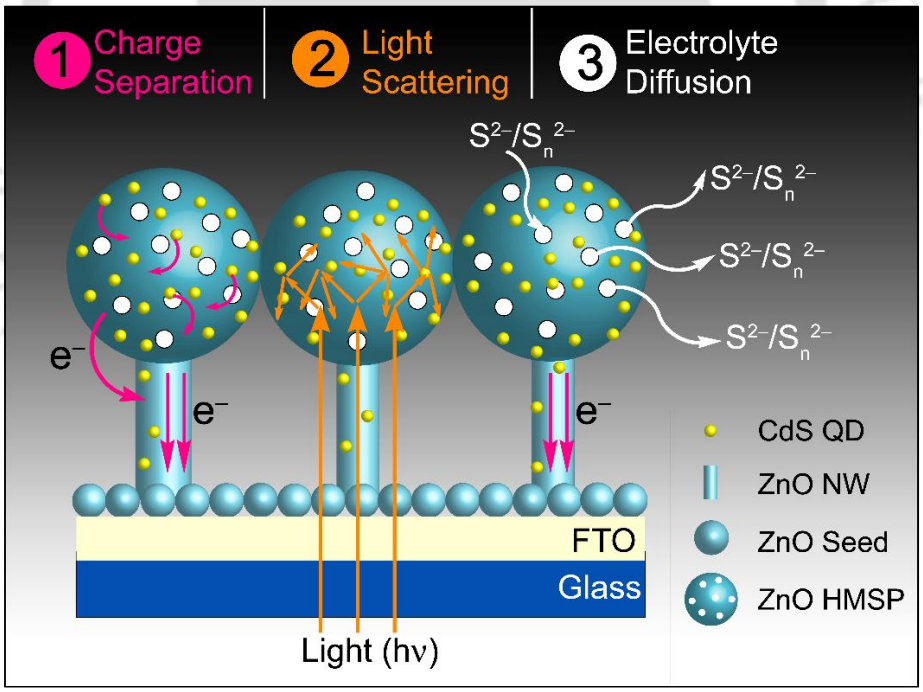

ROYAL SOCIETY OF CHEMISTRY PCCP **T. R. Chetia**, D. Barpuzary, M. Qureshi **2014**, *5*, 11673.

5.1 INTRODUCTION

Diverse morphologies of ZnO with distinct physical, electrical and optical properties are investigated as photoanodic materials to fabricate cost efficient solar cells such as quantum dot or dye sensitized solar cells (QDSSC/DSSC); out of which one dimensional (1D) architectures have shown intriguing effects in enhancing the efficiency.[1–3] One of the possible reason could be the availability of direct transport pathway for photogenerated electrons along the direction of nanowire (NW) axes and increased electron diffusion length by minimizing grain boundaries, reducing the charge trapping sites.[4] These 1D ZnO NW networks grown on conducting glass substrates provide insufficient exposed surface area for the adsorption of sensitizer particles; instead, the use of 3D hollow mesoporous microstructures provide higher exposed surface area along with better light scattering effects to harvest the solar energy.[5] The advantage of mesoporous hollow 3D microstructures is that they facilitate the electrolyte diffusion process governed by the available pores remaining after sensitization to regenerate the oxidized species, which is not the case for 1D NWs. However, the limiting factor for the 3D structures is the charge collection, wherein the photo-generated electrons makes the repeated interactions with the traps as they undertake a random movement through the film.[6] Expected key features of a photoanodic architecture to be used in DSSC or QDSSC device for efficient photoelectric conversion are – (i) Faster pathways for transportation of photo-injected electrons, (ii) Higher specific surface area for sensitizer particle adsorption, (iii) Availability of pores even after the sensitization process for smooth diffusion of electrolyte and (iv) Higher light scattering ability to extend the traveling distance of incident light for repeated excitation of sensitizer.[7–9] However, it is a very challenging task to integrate all the aforementioned features in a single photoanode as they are often incompatible with one another due to the unique properties of different morphologies of semiconductor oxide such as ZnO. An optimized hybrid photoanodic structure with different morphologies of ZnO have the possibility of utilizing beneficial effects of size-and shape-dependent properties of the semiconductor oxide material. Regrettably, only a few reports have focused in the design and development of hybrid photoanodes with multifunctional properties.[10,11]

Although, DSSCs are showing superior light harvesting ability in contrast to its counterpart QDSSCs, their usefulness is limited by the photo-degradation of the dye used under rigorous conditions.[12–14] Moreover, QDSSCs are considered as emerging technological candidates for the

next generation solar cells as they have the possibility of boosting the energy conversion efficiency beyond the traditional Shockley and Queisser limit of 32% for Si based solar cells.[15–17] Semiconductor quantum dots (QDs) such as CdS,[18–20], CdSe,[21,22] PbS,[23] $CuInS_2$,[24] Sb_2S_3,[25] InP,[26] are preferable (over dye molecules) because of their high stability and high absorption coefficients,[27] tunable absorption edge by controlling the particle size[28,29] and the possibility to generate multiple electron–hole pairs per photon. Among all the QDs, cadmium chalcogenide QDs (CdX, X=S, Se or Te) have gained a significant interest due to their higher potential of light absorption in the visible light region, efficient transfer of photogenerated charge carrier, and ease of deposition techniques. Ideally, QDSSC should have simplistic approach in terms of material synthesis and ease of electron interactions between the combinations of semiconductor for better performance.[30, 31]

In this chapter, we have introduced a strategy to integrate the 1D structures and 3D microstructures in a way that their combination provides an enhanced surface area to adsorb sufficient sensitizer particles, facilitated diffusion of electrolyte, efficient photogenerated charge collection and light scattering effects. In the present work, we have designed and successfully fabricated a novel ZnO based hybrid photoanode utilizing the advantages of both 1D ZnO NWs and 3D ZnO HMSP as shown in Scheme **5.1.1**.

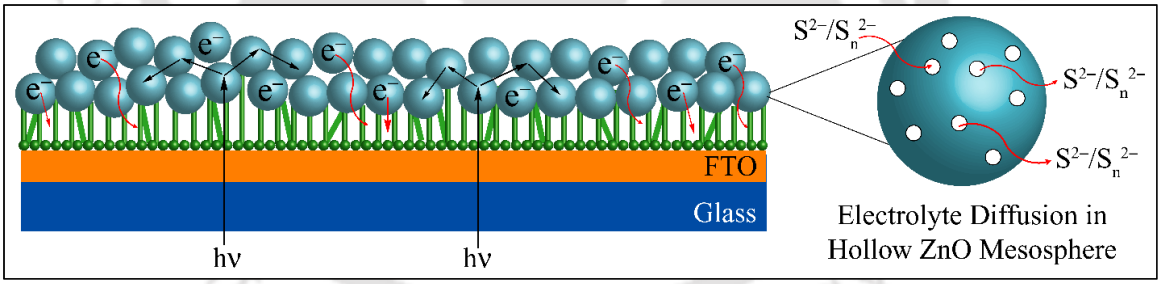

Scheme 5.1.1 Schematic cross-sectional contour of the bi-layered hybrid photoanode showing charge migration from 3D ZnO HMSP to 1D ZnO NWs injected by CdS QDs, light scattering and facilitate diffusion of electrolyte.

5.2 EXPERIMENTAL METHODS

5.2.1 SYNTHESIS OF HOLLOW MESOPOROUS ZnO MICROSPHERES (ZnO HMSP)

3D ZnO microspheres were synthesized by following a reported protocol and is presented schematically in scheme **5.2.1**.[32] In a typical procedure, zinc nitrate hexahydrate (10 mmol) was dissolved in 100 mL polyethylene glycol 200 (PEG 200). The solution was then transferred into a 250 mL round bottom flask, gradually heated to 160 °C and refluxed for 6 h. The solution was

then allowed to cool down to the room temperature. The precipitate was collected by centrifugation at 10,000 RPM, washed with ethanol and distilled water several times to remove the excess solvent and impurities. The precipitate was dried in a hot air oven at 90 °C for 24 h. The obtained brown powder was annealed at 500 °C for 4 h in a muffle box furnace and white powders of ZnO HMSP were finally obtained.

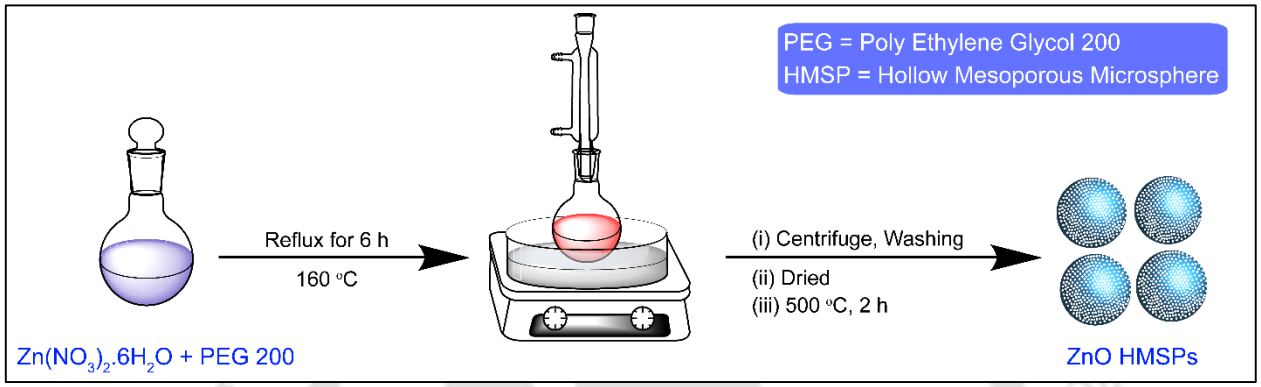

Scheme 5.2.1 Schematic presentation of step-by-step synthetic process of 3D ZnO microspheres (HMSPs).

5.2.2 SYNTHESIS OF CdS NANOPARTICLES

Synthesis of CdS nanoparticles (NPs) was carried out by a simple precipitation method in aqueous media. Briefly a 0.5 M Na_2S solution (25 mL) in deionized (DI) water was added drop wise to an equal volume of 0.5 M $Cd(NO_3)_2.4H_2O$ solution under vigorous stirring at room temperature. The reaction was continued upto 12 h for completion and then centrifuged, washed with ethanol, DI water and dried in hot air oven at 60 °C for 12 h.

5.2.3 GROWTH OF 1D ZnO NWs ON FTO SUBSTRATES

Growth of 1D ZnO NWs was carried out on precleaned FTO substrates coated with ZnO seed layer as reported by *Gradečak et.al.*[33] First, the fluorine doped tin oxide (FTO) substrates were washed with soap solution and plenty of distilled water, followed by ultrasonic treatment in ethanol and isopropanol and dried under Argon. ZnO seed layer was deposited on FTO substrates by spin coating a solution of 300 mM of zinc acetate dihydrate and ethanolamine in 2-methoxyethanol at 4000 rpm for 60 s under inert atmosphere. The substrates were then subjected to anneal at 175 ºC for 10 min under ambient conditions. The process was repeated twice to form a uniform ZnO seed layer, which offers a platform for the well aligned, uniform growth of ZnO nanowire arrays over a large area. The role of ZnO seed layer in growing ZnO NW is to initialize the uniform growth of one dimensionally oriented NWs. The seed layer also acts as a thin ZnO

blocking layer that resists the direct contact between the two electrodes through electrolyte solution in photovoltaic devices. The seeded substrates were then immersed in an aqueous solution containing 50 mM zinc nitrate hexahydrate and 50 mM hexamethylenetetramine for 4 h at 90 °C to grow ZnO NWs. After cooling down to room temperature, the substrates were taken out from the solution, thoroughly rinsed with DI water and finally annealed at 200 °C for 5 min. We have schematically presented step-by-step experimental processes for growth of 1D ZnO NWs on FTO substrates in scheme **5.2.2**.

5.2.4 FABRICATION OF (ZnO NW– ZnO HMSP–CdS) HYBRID PHOTOANODE

ZnO NW–ZnO HMSP–CdS hybrid photoanode was prepared as follows. As synthesized ZnO HMSPs (0.5 g) were added to a mixture of 1 mL of terpineol and 0.2 g of PEG-PPG-PEG and stirred well till a homogeneous slurry was obtained. The slurry was then coated over the ZnO NWs grown over FTO substrates by doctor blade technique. The films were then dried in air and calcined at 480 °C for 30 min to remove the polymer. The measured thickness of ZnO NW–ZnO HMSP layer using surface profilometer was found to be in the range of 12−15 μm, which was further confirmed by the cross-sectional field emission scanning electron microscopy (FESEM) analysis. The ZnO NW–ZnO HMSP electrodes were in-situ sensitized with CdS QDs using successive ionic layer adsorption and reaction (SILAR) process. The schematic of the fabrication procedure is represented in scheme **5.2.2**.

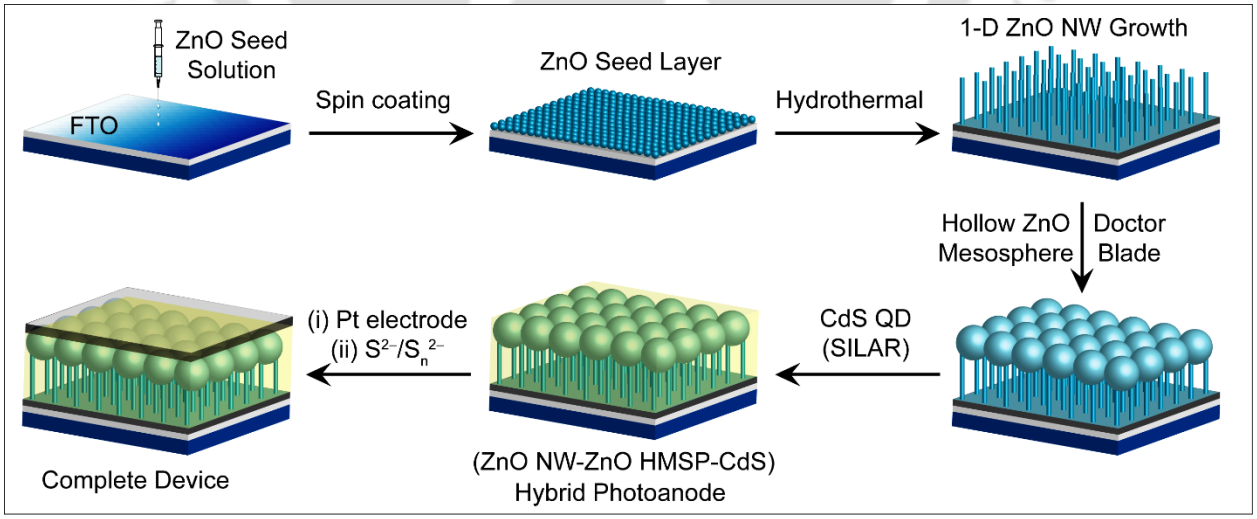

Scheme 5.2.2 Step-by-step device fabrication of photovoltaic cell based on all solution processable route.

Briefly, the electrodes were dipped into an ethanol solution containing $Cd(NO_3)_2.4H_2O$ (0.5 M) for 1 min, rinsed with ethanol, and dried on a hot plate at 70 °C. Again they were dipped into a

Na_2S (0.5 M) solution in methanol for 1 min, rinsed with methanol and dried at 70 °C. The amount of CdS grown onto the ZnO system was controlled by the number of repeated SILAR cycles, however, the exact concentration of CdS QDs might vary from batch to batch. This cycle was repeated for 5 times to adsorb the CdS QDs on the ZnO microspheres as well as ZnO NWs. Hereafter, the fabricated photoanode is represented as ZnO NW–ZnO HMSP–CdS. The FTO substrates having bare ZnO NWs (ZnO microsphere free) and ZnO HMSP (ZnO NW free) were sensitized by CdS QDs following the same procedure and named hereafter as ZnO NW–CdS and ZnO HMSP–CdS, respectively. In order to perform the powder X-ray diffraction (PXRD), UV–Vis diffused reflectance absorption (DRS) and FESEM analysis, identical films of ZnO NW–ZnO HMSP–CdS, ZnO NW–CdS and ZnO HMSP–CdS were made on glass substrates.

5.2.5 DEVICE FABRICATION AND CHARACTERIZATION

Devices were fabricated by sandwiching the as prepared photoanodes with platinized FTO counter electrodes. The Pt counter electrode preparation was performed by spin coating a solution of chloroplatinic acid (5 mM in isopropanol) on a pre-cleaned FTO substrate. The FTO substrates were then placed in a muffle furnace at 450 °C (heating ramp of 5 °C/min) for 15 min and cooled down to room temperature naturally. The photovoltaic cell construction was completed by injecting a drop of sulfide/polysulfide (S^{2-}/S_n^{2-}) electrolyte into the devices. Electrolyte solution was prepared by dissolving 2 M S and 2 M Na_2S in methanol–water (7:3, v/v). The active areas of the QD sensitized ZnO films were found to be ~1.0 cm^2. The cells were ready for photocurrent and incident photon-to-current conversion efficiency (IPCE) measurements.

5.3 RESULTS AND DISCUSSIONS

5.3.1 POWDER X-RAY DIFFRACTION ANALYSIS

Figure **5.3.1** depicts powder X-ray diffraction (PXRD) patterns recorded for ZnO NW–ZnO HMSP–CdS composite, CdS nanoparticles (NPs), 3D ZnO HMSPs and 1D ZnO NWs. From trace (a), it is observed that the characteristic diffraction peaks of CdS NPs are also present in the diffractogram which indicates successful deposition of CdS QDs in the photoanode, i.e., ZnO NW–ZnO HMSP. It is also concluded that the CdS QDs are crystallized in hexagonal phase according to JCPDS Card No. 06-0314 and the diffractogram for CdS NPs [trace (b)] synthesized by simple precipitation method. Broad and low intense peaks obtained from CdS infers deposition

of smaller size CdS QDs onto the ZnO scaffolds. Average crystallite size of CdS QDs (deposited on the photoanode) is estimated to be ~12.5 nm using the Debye-Scherrer equation.

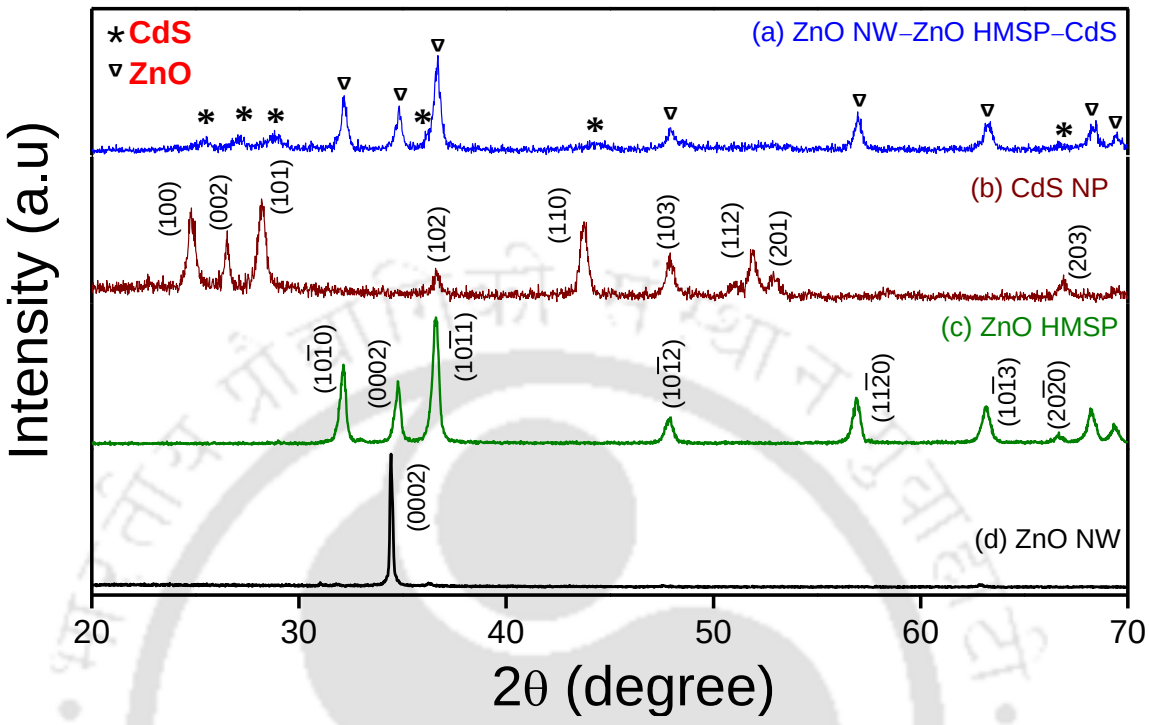

Figure 5.3.1 Powder X-ray diffraction patterns for (a) ZnO NW–ZnO HMSP–CdS, (b) CdS NPs, (c) ZnO HMSPs and (d) ZnO NWs grown on glass substrates.

The PXRD patterns recorded for ZnO HMSPs [trace (c)] and ZnO NWs [trace (d)] have evidenced their hexagonal wurtzite crystal phase with space group $P6_3mc$ according to JCPDS Card No. 036-1451 and 05-0664 respectively. Sharp and intense diffraction peaks obtained from ZnO HMSP are retained even after the deposition of CdS QDs by SILAR process as we have observed from traces (a) and (c); which indicates the crystalline nature of ZnO HMSP in the photoanode. Strong appearance of (0002) diffraction peak at 2θ ≈34.6° in trace (d) confirms well aligned 1D ZnO NWs grown along the *c*-axis normal to the substrate and verifies high degree of crystallinity.[34]

5.3.2 MATERIAL MORPHOLOGY

Morphological characteristics of as synthesized materials and the hybrid photoanode are investigated by FESEM analysis. Figure **5.3.2** shows the FESEM images of 3D ZnO microspheres or ZnO HMSPs, before and after sensitization with CdS QDs at different magnifications. Figure (A) represents the ZnO microspheres having average size dimension of 1–2 µm. Inset to it shows the hollow architecture of the material which favours efficient scattering of light in the photoanode. Image (B) depicts FESEM image of a single ZnO microsphere which confirms mesoporous nature

of it. A magnified FESEM image of a single ZnO microsphere [image (C)] further confirms high degree of uniformity of pores within the microspheres.

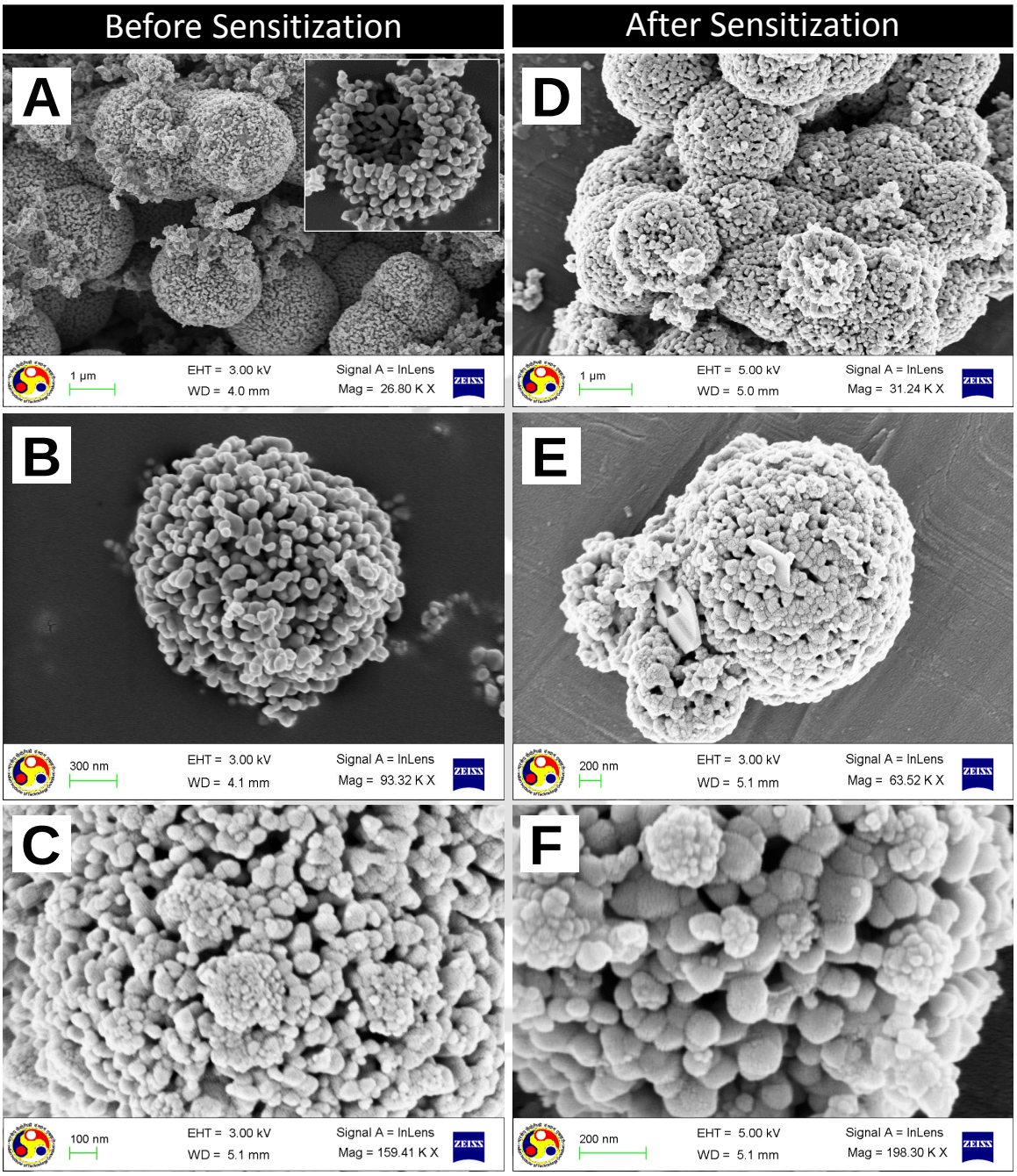

Figure 5.3.2 FESEM images of the ZnO HMSPs before sensitization, (A, B, and C) and after sensitization (D, E and F) with CdS QDs at different magnifications. Inset to image (A) shows the hollow architecture of ZnO microspheres.

From the FESEM images (D) and (E), we have seen that structural properties of ZnO HMSPs are remained intact even after sensitization with CdS QDs. Please note that, CdS sensitized ZnO HMSPs are scratched out from the photoanodes for FESEM analyses. The high magnification

FESEM image (F) of a CdS QD sensitized ZnO HMSP is showing available pores in it which are conducive of electrolyte diffusion for effective regeneration of the oxidized QDs.

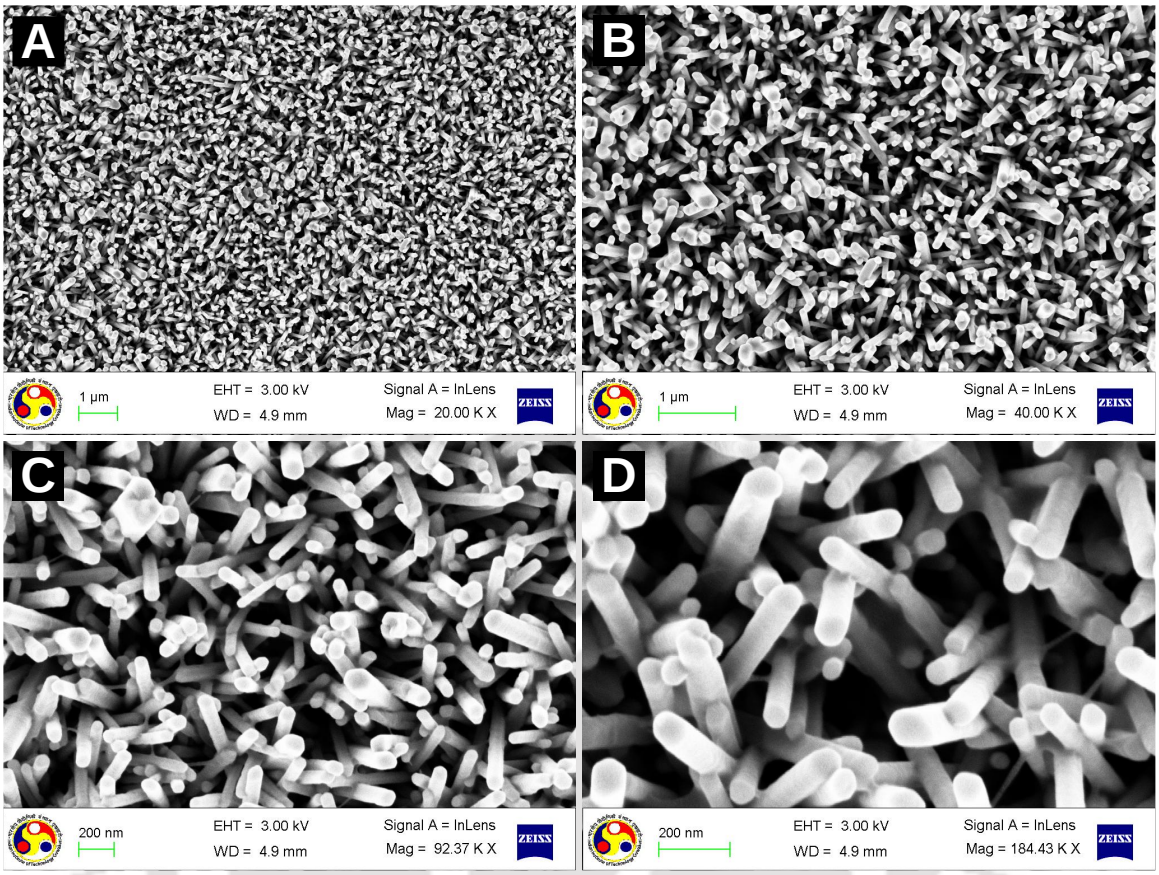

Figure 5.3.3 FESEM images (A, B, C & D) of 1D ZnO NWs grown hydrothermally on the FTO substrates at different magnifications.

Figure **5.3.3** (A, B, C &D) represents the FESEM images of 1D ZnO NWs grown on FTO substrates at different magnifications. From the lower magnification FESEM images (A) and (B) it is clear that the 1D ZnO NWs are grown homogeneously on the FTO substrates and they are normal to the substrate as we have inferred from the PXRD diffraction analyses. Higher energy of unsaturated ±(0001) crystal planes of ZnO favors preferential growth along the *c*-axis and resulted in the formation 1D ZnO NWs. Since the ZnO NWs are in direct contact with the FTO substrate and have single crystalline characteristics they can offer direct charge transfer routes to the photo-injected electrons. Higher magnification FESEM images (C) and (D) confirms formation of porous networks of NWs on the FTO substrates which facilitate the faster diffusion of electrolyte.

We have performed FESEM analyses of the hybrid photoanode with 1D ZnO NWs and 3D ZnO HMSPs to confirm structural characteristics and displayed in the figure **5.3.4**.

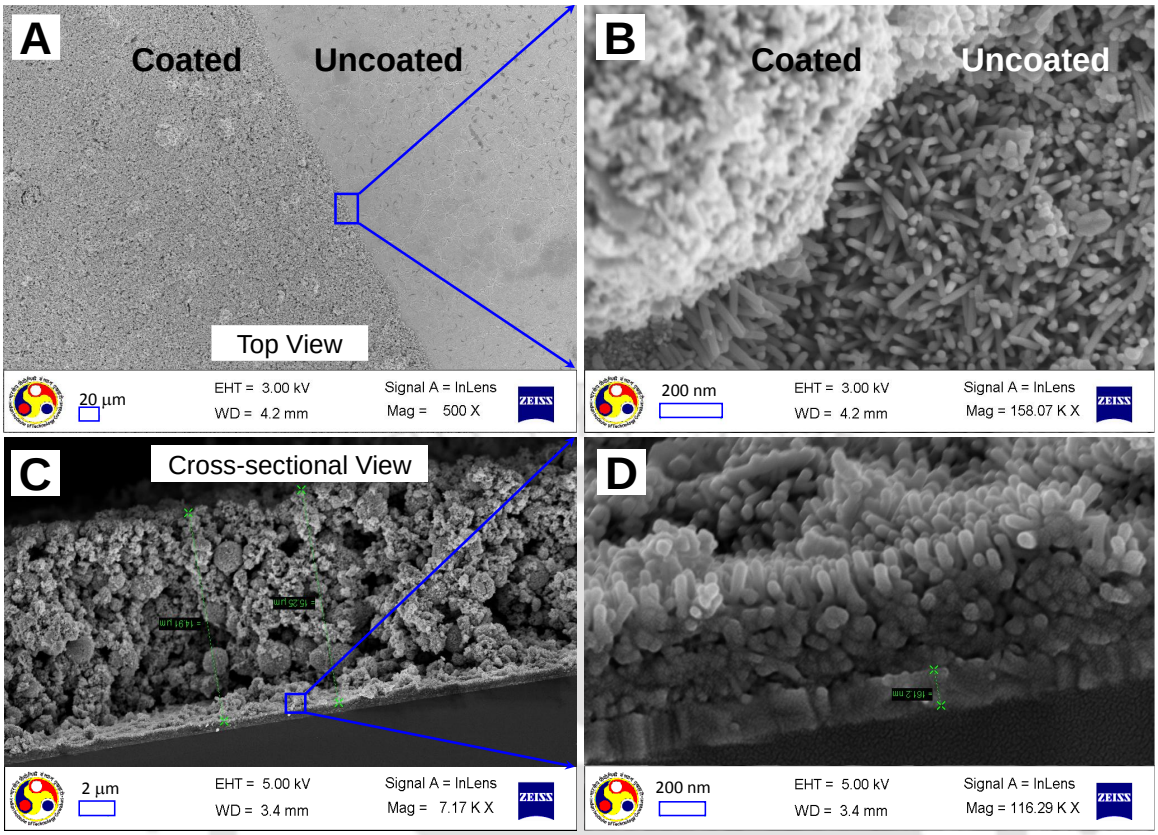

Figure 5.3.4 Top view (A & B) and cross-sectional (C & D) FESEM images of the photoanode. (A) Interface of the ZnO HMSP layer coated and uncoated portion over the ZnO NW network on FTO substrate. (B) Magnified view of the interface showing successful deposition of ZnO HMSP over the ZnO NWs. (C) Cross-sectional image of the photoanode. (D) Magnified image of the indicated portion of image (C).

Image (A) represents the top view of the photoanode, wherein the left half represents ZnO HMSP coated layer and the right half shows bare ZnO NWs (ZnO HMSP uncoated). A magnified FESEM image at the interface of the photoanode for better clarity is presented in image (B), which shows that the ZnO NWs have retained their 1D alignment even after depositing the ZnO HMSP layer. In order to confirm the structure of the fabricated photoanodes of the devices, a cross-sectional FESEM analysis of the photoanode has been carried out [images (C) and (D)]. The cross-sectional FESEM images of the photoanode shows that the thickness of ZnO HMSP layer over ZnO NWs is ~14 µm, while the thickness of the ZnO NW film is ~1 µm including the seed layer which supports the results obtained from surface profilometer analysis. The retained structure of 1D ZnO NW networks has been verified by the magnified cross-sectional image of the photoanode as shown in image (D).

5.3.3 BET SURFACE AREA ANALYSIS

N_2 adsorption–desorption isotherms of ZnO microspheres (HMSPs) measured are shown in figure **5.3.5**. The typical type IV isotherm and H3 hysteresis loops confirms the characteristic mesoporous nature of as-synthesized ZnO microspheres, which is a promising candidate for solar cell applications.

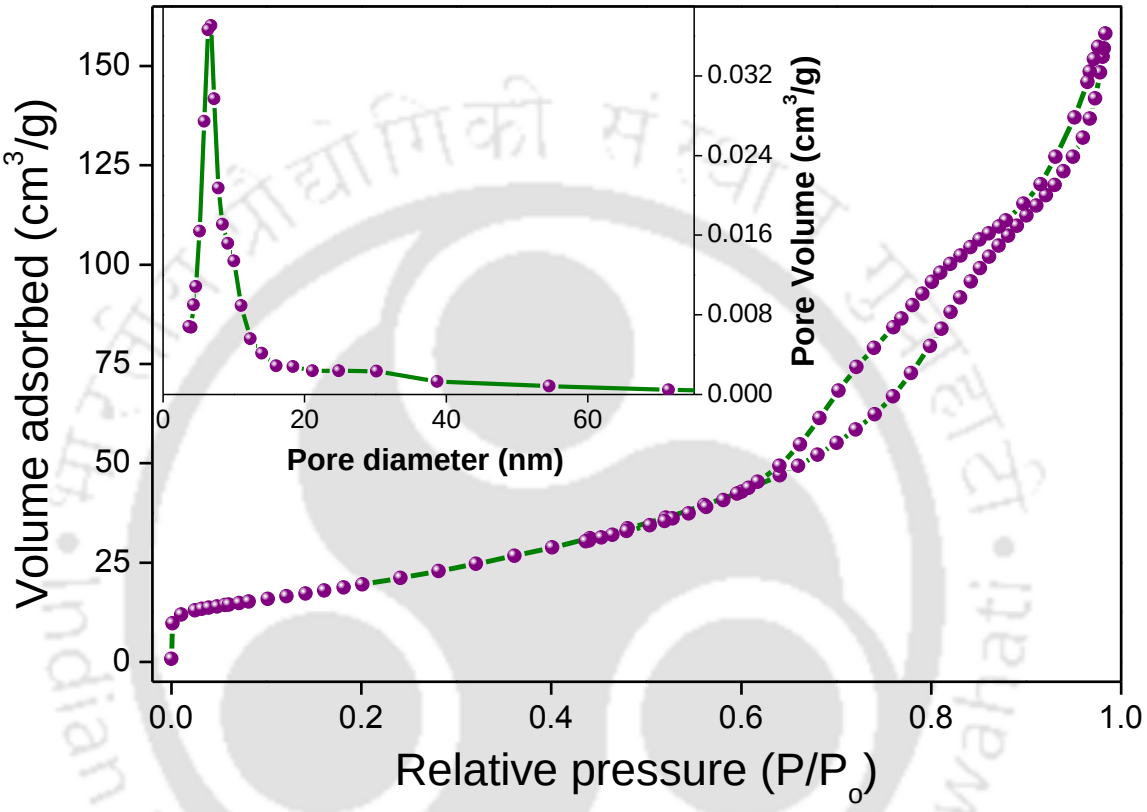

Figure 5.3.5 Nitrogen adsorption–desorption isotherms and Barrett−Joyner−Halenda (BJH) pore size distribution plot (inset) for as prepared ZnO HMSP microspheres

The observed BET surface area of as synthesized ZnO HMSP is 70.3 m^2/g. The Barrett–Joyner–Halenda (BJH) pore size distribution curve indicates high degree of uniformity of pores in the range of ~10 nm, which is in agreement to the FESEM analysis. Due to the mesoporous nature and high surface area of ZnO microspheres it provide more adsorption sites for CdS QD sensitization and electrolyte can readily penetrate through the holes for better functioning.

5.3.4 DIFFUSE REFLECTANCE UV–VISIBLE ABSORPTION SPECTRA

UV–visible (UV-vis) absorption spectra of the samples ZnO NW, ZnO NW–CdS, ZnO HMSP, ZnO HMSP–CdS, ZnO NW–ZnO HMSP–CdS and pure CdS NPs are recorded and compiled in figure **5.3.6**.

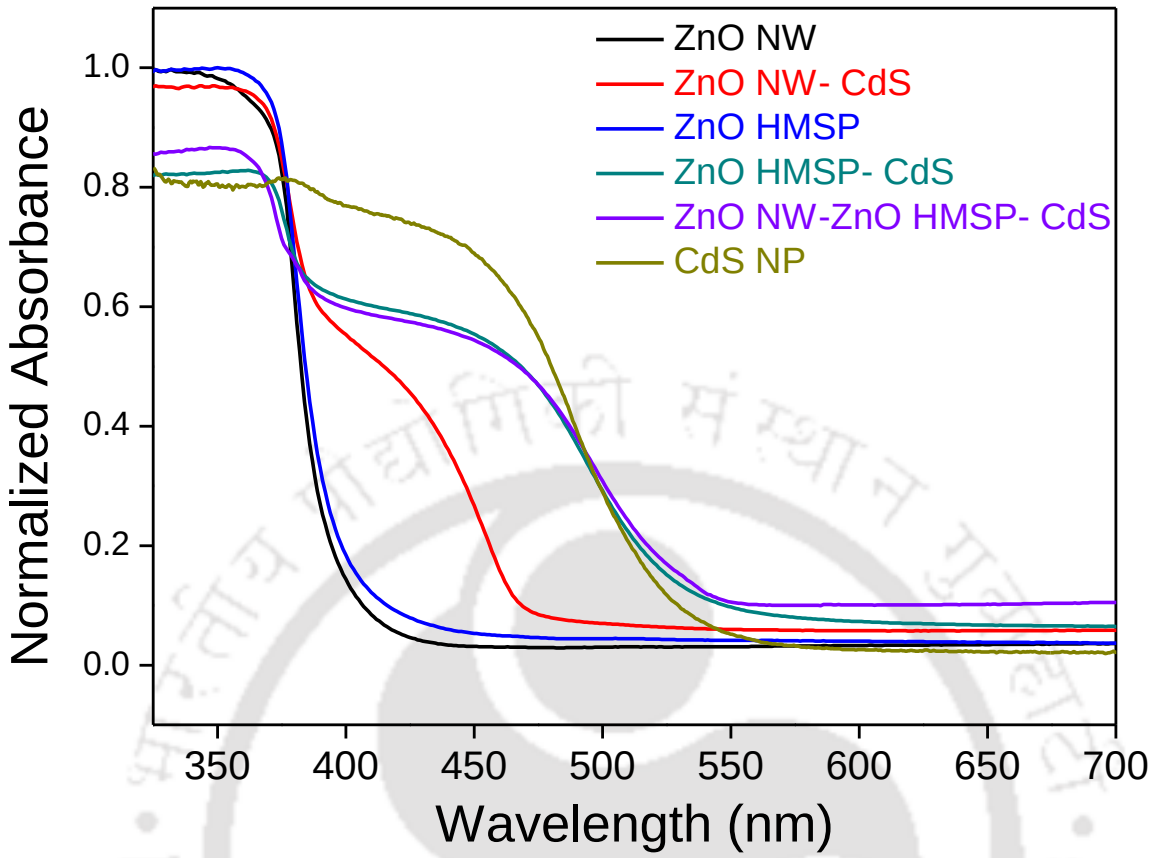

Figure 5.3.6 Diffuse reflectance UV–vis absorption spectra for ZnO NW (black line), ZnO NW–CdS (red line), ZnO HMSP (blue line), ZnO HMSP–CdS (dark cyan line), ZnO NW–ZnO HMSP–CdS (violet line) and bare CdS nanoparticles (dark yellow line) films on glass slides.

Nanocrystalline CdS QDs absorb photon energy in the visible region (380–520 nm) as shown in figure **5.3.6** (dark yellow line) and are widely used as sensitizers for QDSSC devices. We have observed almost similar absorption profiles in the visible region for both the photoactive layers, namely, ZnO NW–ZnO HMSP–CdS (violet line) and ZnO HMSP–CdS (dark cyan line). This confirms that the adsorption of CdS QDs are confined primarily on the surface of ZnO microspheres in the photoanode. However, very less amount of CdS QD adsorption on to 1D ZnO NWs (across ZnO HMSP layer) cannot be nullified. Increased absorbance and red shift observed for the samples ZnO HMSP–CdS and ZnO NW–ZnO HMSP–CdS as compared to the ZnO NW–CdS (red line) are because of increased adsorption amount of CdS QDs and subsequent growth of CdS QDs.[35] It further indicates that ZnO microspheres provide high surface area for better adsorption of sensitizer QDs. It should be noted that slight higher absorption has been observed in the UV region for ZnO NW–ZnO HMSP–CdS as compared to that of ZnO HMSP–CdS, indicating the role of ZnO NWs.

We have estimated the optical band gap values of CdS QDs deposited on all photoanodes from the Tauc plots where $(\alpha h\nu)^2$ is plotted as a function of photon energy ($h\nu$) as shown in figure **5.3.7**. The estimated band gap energy of CdS for the photoanode ZnO NW–CdS is found to be ~2.7 eV, while for the photoanodes ZnO HMSP–CdS and ZnO NW–ZnO HMSP–CdS are ~2.35 eV and ~2.39 eV respectively indicating smaller size of CdS QD deposition in ZnO NW–CdS. We have tabulated all the band gap values estimated for the photoanodic materials from the Tauc plots in Table **5.3.1.**

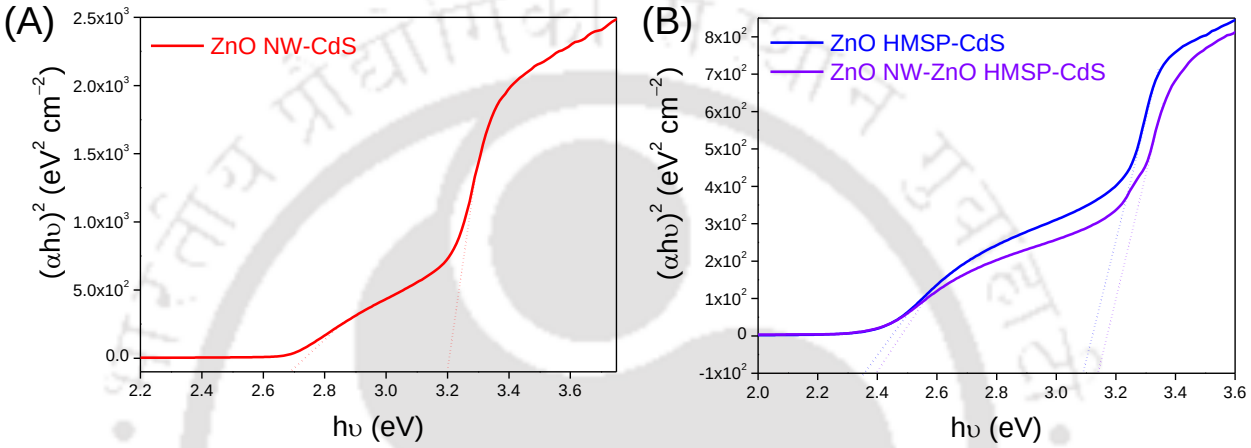

Figure 5.3.7 Tauc plots for (A) ZnO NW-CdS and (B) for ZnO HMSP-CdS and ZnO NW-ZnO HMSP-CdS photoanodes.

Table 5.3.1 Optical band gap values of ZnO and CdS estimated from the Tauc plots of all the photoanodes.

Photoanode	Photoanode Thickness (μm)	Band Gap of ZnO (eV)	Band Gap of CdS QDs (eV)
ZnO NW-CdS	~1	3.2	2.69
ZnO HMSP-CdS	~14	3.09	2.35
ZnO NW-ZnO HMSP-CdS	~1+14	3.14	2.39

Further, reflectance measurements are carried out to investigate the light scattering effect of ZnO NW, ZnO HMSP and ZnO NW–ZnO HMSP films. Figure **5.3.8** shows diffuse reflectance spectra of the respective samples. The films having ZnO HMSP layer exhibit much higher reflectance in the wavelength range 420–800 nm than that of pristine ZnO NW film. This confirms our claim on efficient light scattering by ZnO HMSP layer in the photoanodes acting as light shields.[36]

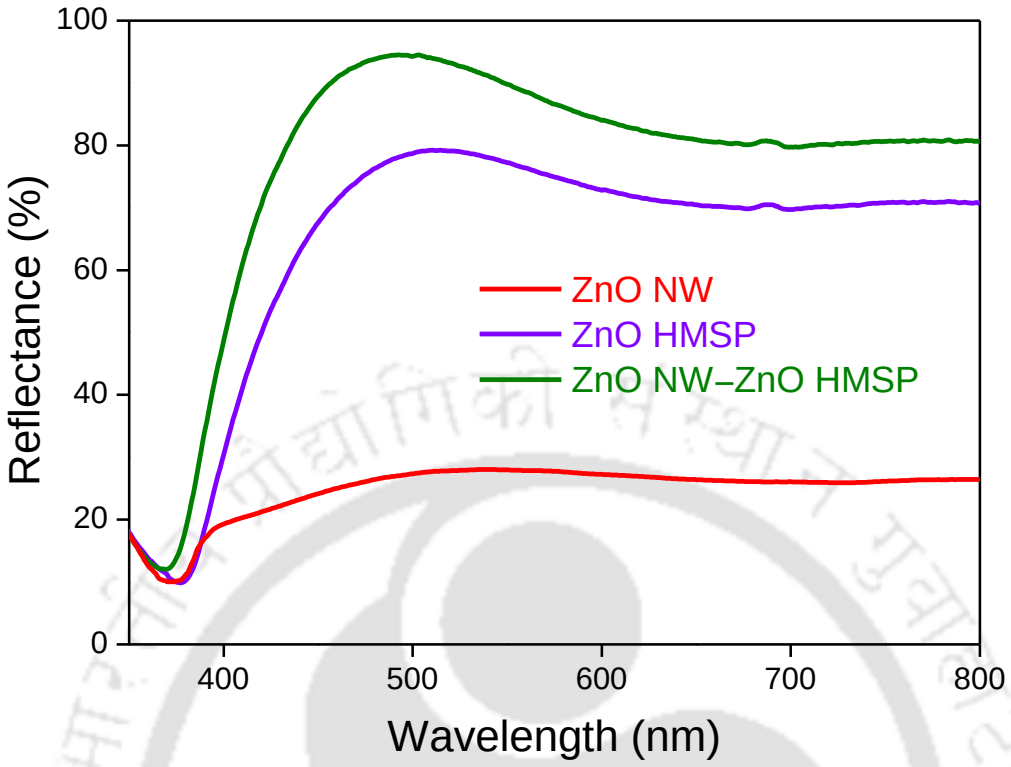

Figure. 5.3.8 Diffused reflectance spectra of the ZnO NW (red line) ZnO HMSP (violet line), ZnO HMSP and ZnO NW (olive line) films on glass substrates.

5.3.5 PHOTOLUMINESCENCE ANALYSES OF THE MATERIALS

Excited state electronic interactions between ZnO HMSP–CdS and ZnO NW layers in the hybrid photoanode are investigated by performing steady state and dynamic photoluminescence (PL) measurement of the samples ZnO HMSP–CdS, ZnO NW–CdS and ZnO NW–ZnO HMSP–CdS. Previously, Kamat *et al.* have reported that the injection of photoinduced electrons from QD sensitizer particles (e.g. CdSe, CdTe etc.) to the conduction band (CB) level of wide band gap semiconductor particles (e.g. TiO_2) leads to decrease in PL intensity as well as exciton lifetime of QDs.[37–39] Decreased photoluminescence intensity and exciton lifetime indicates the excited state electronic interaction between the QDs and semiconductor oxide and charge separation/delocalization in the system. Figure **5.3.9** (A) shows steady state PL spectra for all the photoanodes, i.e., ZnO HMSP–CdS (black line), ZnO NW–CdS (blue line) and ZnO NW–ZnO HMSP–CdS (olive line) recorded at an excitation wavelength 410 nm.

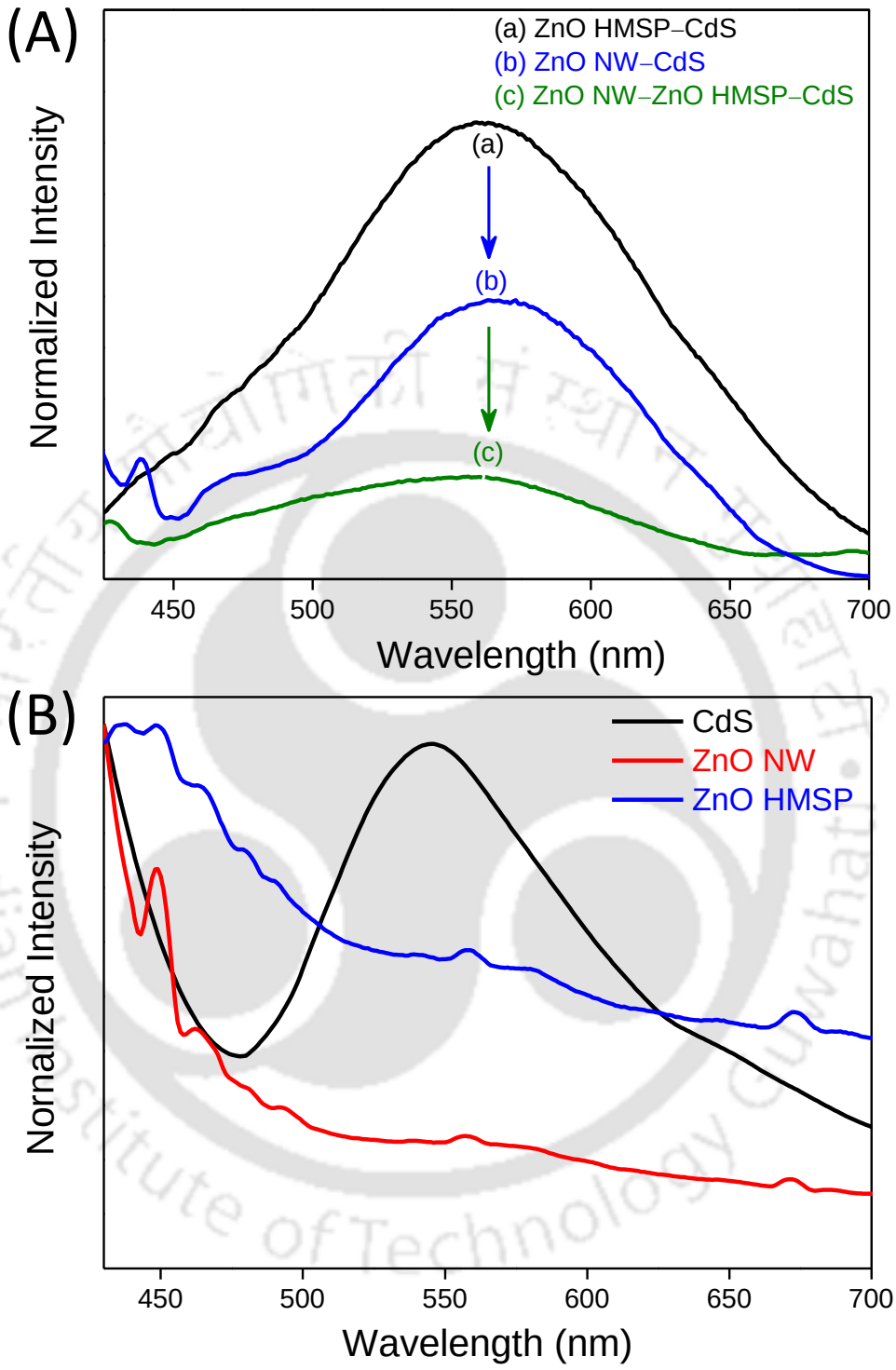

Figure 5.3.9 (A) Steady-state PL spectra for the photoanodic materials ZnO HMSP–CdS (black line), ZnO NW–CdS (blue line) and ZnO NW–ZnO HMSP–CdS (olive line) composite on glass slides. (B) Steady-state PL spectra of pure CdS NPs, ZnO NWs and ZnO HMSPs. All the spectra are recorded at an excitation wavelength of 410 nm.

From the figure **5.3.9** (A), we have observed a significant quenching in the PL intensity for ZnO NW–ZnO HMSP–CdS [trace (c)] as compared to ZnO HMSP–CdS [trace (a)] and ZnO NW–CdS

[trace (b)], indicating the inhibited recombination of photoinduced electron and hole and a possible excited state electronic interaction between ZnO HMSP–CdS layer and ZnO NWs in the photoanode. A possible reason for the inhibited recombination of photoinduced electron and hole in the photoanode could be attributed to an efficient charge migration to 1D ZnO NWs from ZnO HMSP–CdS layer. Efficient charge migration or separation effect is also explicit in the photoanode ZnO NW–CdS [trace (b)] because of a faster photogenerated electron migration along the 1D single crystalline ZnO NWs which is not in case of ZnO HMSP–CdS photoanode [trace (a)]. Please note that, although we have performed the PL experiments in order to excite only the CdS QDs (rather than ZnO) at an excitation wavelength of 410 nm, the effect of defect mediated visible light emission by ZnO cannot be ruled out completely. In the fluorescence spectrum of ZnO NW–CdS [trace (b); figure **5.3.9** (A)] the origin of the peak below 450 nm (i.e., blue emission) could be from transitions involving Zn interstitial defect states (Zn_i, Shallow donor) to the valance band levels while the shoulder in the range 450–500 nm (green emission) observed is may be due to transition from the conduction band to deep trap levels of ZnO (created by oxygen vacancies).[40] For better understanding we have carried out PL analysis of pure CdS, ZnO NW and ZnO HMSP excited at a wavelength of 410 nm as shown in figure **5.3.9** (B). From figure (B) it is clear that the emission peaks for all the photoanodes in the range spanning from 500-650 nm are originated from CdS QDs deposited on the photoanodes and not from ZnO. ZnO NWs (red line) and ZnO HMSPs (blue line) exhibit a defect mediated emission peaks at a wavelength ~448 nm with satellite peaks in the range of 455 nm to 480 nm.

Further, we have deconvoluted the PL emission spectra of the hybrid photoanode, i.e., trace (c) in figure **5.3.9** (A), as it is very broad with a clear indication of the overlap of two or more peaks. Figure 5.3.10 represents the deconvoluted steady-state PL spectra of the photoanode ZnO NW-ZnO HMSP-CdS. The strong PL emission at ~550 nm exhibits the band gap emission of CdS QDs arising from radiative excitonic recombination. Another broad emission band occurs at 605 nm, which is most likely due to the recombination of trapped carriers generated by defect states.[41]

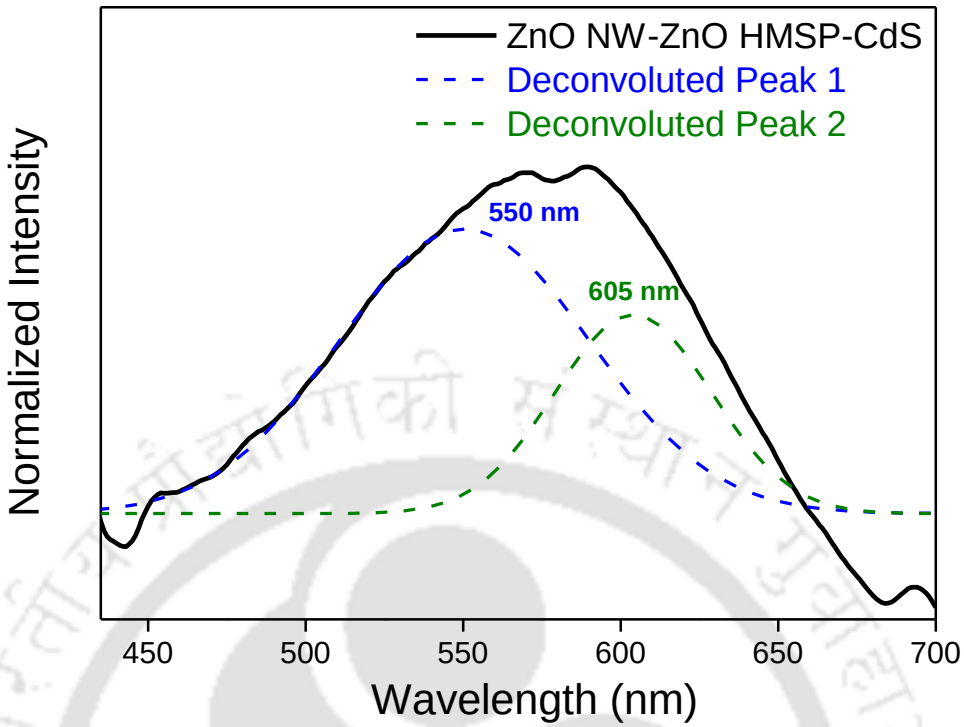

Figure 5.3.10 Deconvoluted Steady-state photoluminescence spectra of the photoanode ZnO NW-ZnO HMSP-CdS.

Dynamic PL spectra for all the samples excited at a wavelength 405 nm are recorded to confirm the enhanced charge separation in the photoanode ZnO NW–ZnO HMSP–CdS as shown in the figure **5.3.11**. The PL decay traces of all the samples are fitted with a bi-exponential function to calculate the exciton lifetime. The exciton lifetimes (τ_1 and τ_2) as well as average lifetime ($<\tau>$) for the samples are tabulated in the table **5.3.2**. The average lifetime values are calculated by using the expression in equation (1).[39]

$$< \tau >= \frac{\alpha_1 \tau_1^2 + \alpha_1 \tau_2^2}{\alpha_1 \tau_1 + \alpha_1 \tau_2} \qquad (1)$$

It is well known that photoexcited CdS QDs exhibit electron (e^-)–hole (h^+) pair separation followed by charge carrier recombination via radiative or non-radiative processes.[42] When CdS QDs are anchored to ZnO surface the photoexcited CdS QDs, which are capable of injecting electrons into the conduction band level of ZnO via the delocalization of electron wave function because of the lower conduction band offset of ZnO, yields a substantial decrease in exciton lifetime of the system.

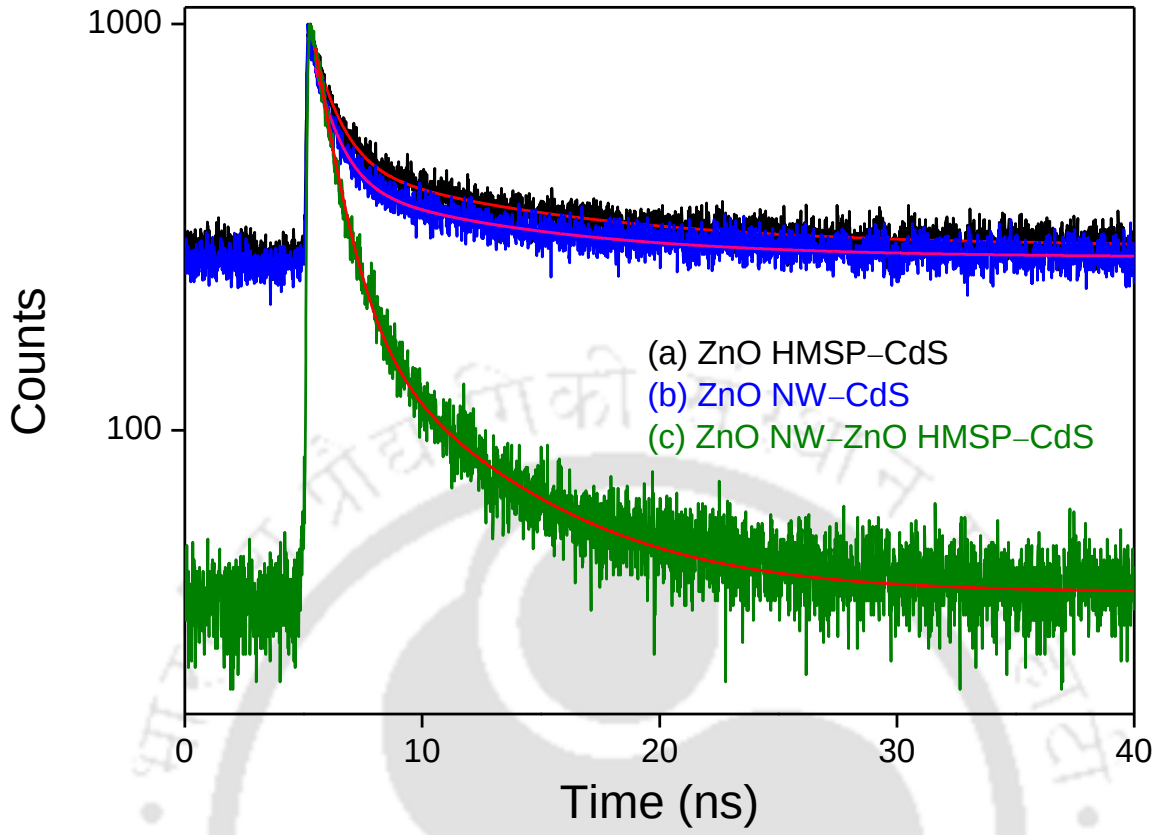

Figure 5.3.11 Time resolved PL spectra of (a) ZnO HMSP–CdS (black line), (b) ZnO NW-CdS (blue line) and (c) ZnO NW–ZnO HMSP–CdS (olive line) recorded at an excitation wavelength of 405 nm.

Table 5.3.2 values of fitting parameter (χ^2), exciton lifetimes (τ_1, τ_2), pre-exponential factors (α_1, α_2) and average exciton lifetimes ($<\tau>$).

Sample	χ^2	τ_1 (ns)	τ_2 (ns)	α_1	α_2	$<\tau>$ (ns)
(a) ZnO HMSP–CdS	1.03	1.03	9.1	19.5	80.5	8.88
(b) ZnO NW-CdS	1.05	0.96	8.02	24.8	75.2	7.75
(c) ZnO NW–ZnO HMSP–CdS	1.04	0.99	5.54	44.0	55.9	4.97

From the table **5.3.2**, faster exciton average lifetime for ZnO NW–CdS (7.75 nm) than ZnO HMSP–CdS (8.88 ns) indicates a stronger electronic interaction between ZnO NWs and CdS QDs and a favorable photogenerated charge migration along the 1D ZnO NWs.[43] A significant decrease in average exciton lifetime for ZnO NW–ZnO HMSP–CdS (4.97 ns) has been observed as compared to ZnO HMSP–CdS (8.88 ns). The static quenching in PL lifetime confirms the favorable excited state electronic interaction between ZnO NWs and ZnO HMSP–CdS layer and participation of ZnO NWs in efficient and spontaneous collection of photogenerated electrons from the ZnO HMSP–CdS layer.

5.3.6 PHOTOVOLTAIC CHARACTERISTICS OF THE SOLAR CELLS

Figure **5.3.12 (A)** shows the current density–voltage (*J*–*V*) characteristics for solar cells, constructed using the combination of 1D ZnO NWs, 3D ZnO HMSPs and CdS (**device 1**), 3D ZnO HMSPs and CdS (**device 2**) and the pristine 1D ZnO NWs and CdS (**device 3**) under AM 1.5G simulated sunlight with a light intensity of 100 mW cm^{-2}. **Figure (B)** shows the incident photon-to-current conversion efficiency (IPCE) as a function of wavelength for the fabricated QDSSCs.

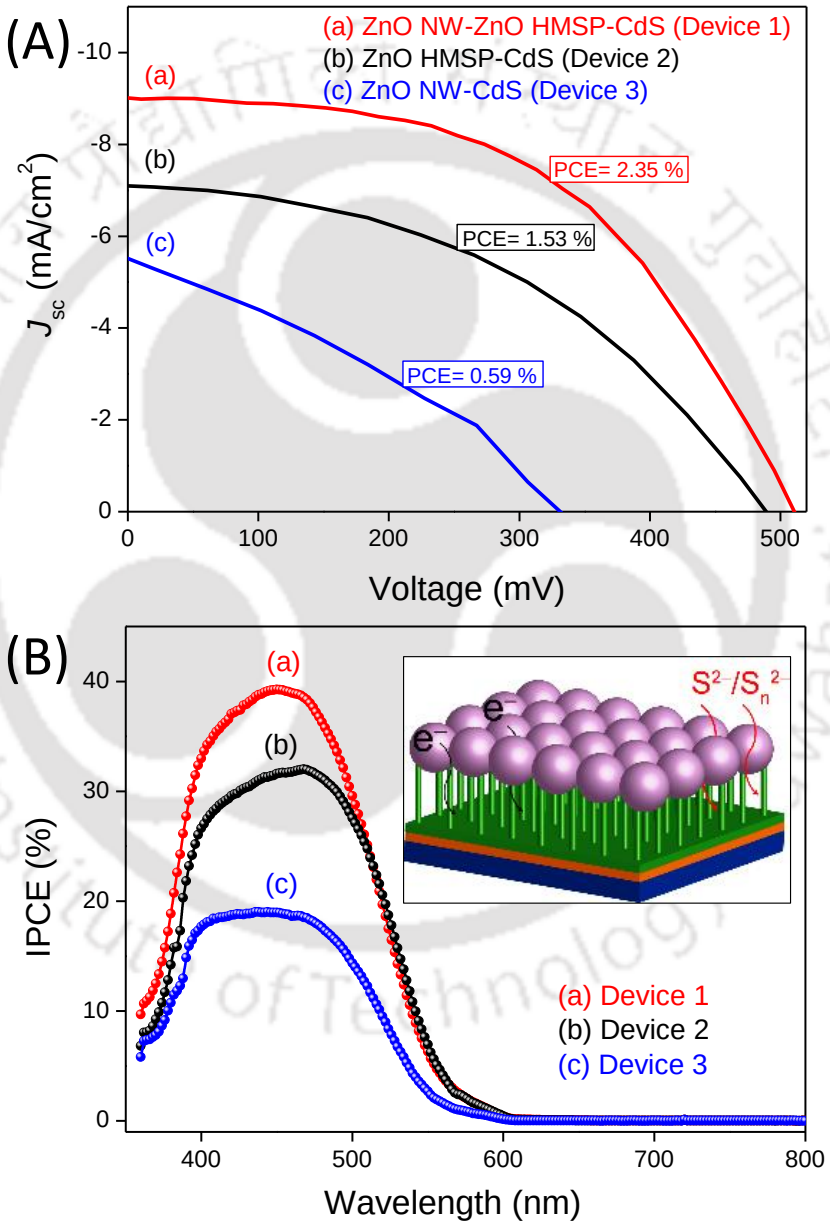

Figure 5.3.12 (A) Current density–voltage (*J*–*V*) curve for the photovoltaic devices under AM 1.5 G solar illumination showing an enhanced J_{sc} for the devices fabricated with ZnO HMSP. **(B)** IPCE plots for the respective devices employing (S^{2-}/S_n^{2-}) as redox couple. Inset to it shows the schematic of electron transfer from ZnO HMSP to ZnO NWs and the electrolyte diffusion within the hybrid photoanode.

The measured and calculated values of photovoltaic parameters such as short circuit current density (J_{sc}), open circuit voltage (V_{oc}), fill factor (FF) and the overall power conversion efficiency (PCE, η) for all the devices from respective (*J*–*V*) curves are summarized in table **5.3.3**.

Table 5.3.3 Short-circuit current density (J_{sc}), open-circuit voltage (V_{oc}), fill factor (FF), and power conversion efficiency (η) for the fabricated solar cells having different photoanodes.

Device	Thickness (μm)	J_{sc} (mA/cm^2)	V_{oc} (mV)	FF (%)	PCE (η, %)
(1) ZnO NW-ZnO HMSP-CdS	~1+14	9.01 (±0.4)	511 (±17)	51 (±1.1)	2.35 (±0.2)
(2) ZnO HMSP-CdS	~14	7.11 (±0.3)	490 (±36)	44 (±2.1)	1.53(±0.18)
(3) ZnO NW-CdS	~1	5.52 (±0.6)	330 (±13)	32 (±1.5)	0.59 (±0.1)

Form table **5.3.3**, the increase in J_{sc} from 5.52 mA/cm^2 (device 3) to 7.11 mA/cm^2 (device 2) is attributed to the enhanced photon absorption associated with sufficient loading of CdS QDs onto the surface of mesoporous ZnO microspheres (ZnO HMSPs) and excellent light scattering property of ZnO HMSP film. As a result, more number of photo-generated electrons will be injected by CdS QDs into 3D ZnO HMSPs in device 2 and as well as in device 1, which is not in the case of device 3. It should be noted that increment of J_{sc} value from 7.11 mA/cm^2 to 9.01 mA/cm^2 for the device 1 as compared to the device 2 is indicative of a better photogenerated charge separation in the former case due to an efficient charge collection and migration through the 1D ZnO NWs to the external circuit which is in accordance with our claim made from the photoluminescence studies. The significant increase in FF from 32% (device 3) to 44% (device 2) and to 51% (device 1) attributed to a lower recombination leading to a better charge separation, facilitated by an enhanced diffusion of electrolyte to regenerate the oxidized species.[23, 44] The enhancement in V_{oc} for the devices 1 and 2 over device 3 can be explained by the equation (2)[45]

$$V_{oc} = \left[\frac{kT}{q}\right] \ln \left[\frac{J_{inj}}{n_{cb} k_r [S_2^{2-}]}\right] \qquad (2)$$

Where, *k* is the Boltzmann constant, T is the absolute temperature, *q* is the electronic elementary charge, J_{inj} is the flux of electron injection from CdS QDs to ZnO, n_{cb} is the concentration of electrons on ZnO surface in dark equilibrium, k_r is the rate constant for the recombination reaction taking place at the ZnO/electrolyte interface, and [S_2^{2-}] is the concentration of S_2^{2-} in the electrolyte. From the equation (2) it is clear that V_{oc} is directly proportional to J_{inj} and indirectly to k_r. The combination of 3D ZnO HMSP to 1D ZnO NW in device 1 and presence of pristine ZnO HMSPs in device 2 enhances the surface area of ZnO film for higher loading of CdS QDs as

compared to that for bare ZnO NWs (device 3), which clearly reveals the higher J_{inj} value for both the devices 1 and 2. Moreover, CdS QDs adsorbed on the surface ZnO inhibits the direct electrolyte contact to ZnO surface thereby reducing the recombination rate (k_r). Combined effects of increase in J_{sc} and V_{oc} values are reflected in the increment of overall PCE performance for device 1.

Figure **5.3.12** (B) shows the IPCE as a function of wavelength for the fabricated QDSSC devices. In principle, IPCE of a solar cell is dependent on (i) light harvesting efficiency (ii) quantum yield of electron injection and (iii) efficiency of collecting injected electrons.[46] From figure 5.3.12 (B), it is clear that IPCE values for the hybrid photoanode based device (device 1, ~40 %) and pristine ZnO HMSP photoanode based device (device 2, ~32 %) are much higher than the device based on ZnO NWs only (device 3, ~19 %) in the measured wavelength range from 370 nm to 550 nm and exhibited a red shift of about 50 nm. These results indicate that the photoanodes having ZnO HMSP–CdS layer have better light harvesting and scattering ability than the device with only ZnO NWs. Better light harvesting ability is attributed to efficient sensitization of mesoporous ZnO film with CdS QDs and enhanced light confinement in the photoanodes of device 1 and 2 because of hollow architecture of ZnO microspheres. These factors are leading to a better absorption of solar irradiation and increase in quantum yield of electron injection in the respective devices. Further, efficient regeneration of oxidized CdS QDs by the redox couple (S^{2-}/S_n^{2-}) due to facile diffusion of electrolyte in the photoanodes of device 1 and 2 is reducing the recombination rate, increasing the photogenerated charge collection and improving the IPCE values as compared to device 3. Similar trend in the improved IPCE value for device 1 as compared to device 2 is observed due to the effective charge separation. In essence, the photoanode architecture that provides higher surface area, facile diffusion of electrolyte for oxidation reactions, excellent charge separation and light scattering allow us to design a photovoltaic with enhanced performance.

5.4 CONCLUSIONS

In conclusion, a new hybrid photoanode utilizing 3D mesoporous ZnO microspheres (ZnO HMSP) in combination with 1D ZnO NWs for CdS quantum dot sensitized solar cells is designed and successfully fabricated. Enhanced charge separation and excited state electronic interactions between ZnO HMSP–CdS and ZnO NWs in the photoanode have been proved by performing steady state and time decay photoluminescence measurements. We have obtained a PCE value as high as ~2.35 % for the hybrid photoanode solar cell, while the bare ZnO HMSP and conventional ZnO NW based solar cells have afforded PCE of 1.53 % and 0.6 % respectively. Hence a significant enhancement in the power conversion efficiency (PCE, η) is achieved for the proposed architecture of the solar cell, i.e. ~35 % and ~74% when compared to the pristine ZnO HMSP and conventional ZnO NW based photovoltaic devices respectively. Improved IPCE value for the hybrid photoanode based solar cell (~40 %) compared to pristine ZnO HMSP (~32 %) and ZnO NW (~19 %) based solar cells confirm better light harvesting ability of the device. Additionally, the presented work shows a way to use 3D mesoporous materials in combination with 1D structures for making efficient QDSSCs.

5.5 REFERENCES

(1) Anta, J. A.; Guillen, E.; Tena-Zaera, R. *J. Phys. Chem. C*, **2012**, *116*, 11413.

(2) Zhang, Q.; Cao, G. *Nano Today*, **2011**, *6*, 91.

(3) Zhang, Q.; Dandeneau, C. S.; Zhou, X.; Cao, G. *Adv. Mater.*, **2009**, *21*, 4087.

(4) Li, L.; Zhai, T.; Bando, Y.; Golberg, D. *Nano Energy*, **2012**, *1*, 91.

(5) Chen, H.-Y.; Kuang, D.-B.; Su, C.-Y. *J. Mater. Chem.*, **2012**, *22*, 15475.

(6) Law, M.; Greene, L. E.; Johnson, J. C.; Saykally, R; Yang, P. *Nat. Mater.*, **2005**, *4*, 455.

(7) Concina, I.; Vomiero, A. *Small*, **2015**, *11*, 1743.

(8) Tian, J.; Cao, G. *J. Phys. Chem. Lett.*, **2015**, *6*, 1859.

(9) Martinson, A. B. F.; Hamann, T. W.; Pellin, M. J.; Hupp, J. T. *Chem. Eur. J.* **2008**, *14*, 4458.

(10) Xu, C.; Wu, J.; Desai, U. V.; Gao D. *J. Am. Chem. Soc.*, **2011**, *133*, 8122.

(11) Zhu, Z.; Qiu, J.; Yan, K.; Yang, S. *ACS Appl. Mater. Interfaces*, **2013**, *5*, 4000.

(12) Kamat, P. V. *J. Phys. Chem. Lett.*, **2013**, *4*, 908.

(13) Kamat, P. V. *J. Phys. Chem. C*, **2008**, *112*, 18737.

(14) Kamat, P. V.; Tvrdy, K.; Baker, D. R.; Radich, J. G.; *Chem. Rev.*, **2010**, *110*, 6664.

(15) Shockley, W.; Queisser, J. H. *J. Appl. Phys.* **1961**, *32*, 510.

(16) Mora-Sero, I.; Bisquert, J. *J. Phys. Chem. Lett.*, **2010**, *1*, 3046.

(17) Hodes, G. *J. Phys. Chem. C* **2008**, *112*, 17778.

(18) Sun, W.-T.; Yu, Y.; Pan, H.-Y.; Gao, X.-F.; Chen, Q.; Peng, L.-M. *J. Am. Chem. Soc.*, **2008**, *130*, 1124.

(19) Li, L.; Yang, X.; Gao, J.; Tian, H.; Zhao, J.; Hagfeldt, A.; Sun, L. *J. Am. Chem. Soc.*, **2011**, *133*, 8458.

(20) Wang, H.; Bai, Y.; Zhang, H.; Zhang, Z.; Li, J.; Guo, L. *J. Phys. Chem. C*, **2010**, *114*, 16451.

(21) Robel, I.; Subramanian, V.; Kuno, M.; Kamat, P. V.; *J. Am. Chem. Soc.*, **2006**, *128*, 2385.

(22) Lee, H. J.; Yum, J.-H.; Leventis, H. C.; Zakeeruddin, S. M.; Haque, S. A.; Chen, P.; Seok, S. II.; Grätzel, M.; Nazeeruddin, M. K. *J. Phys. Chem. C*, **2008**, *112*, 11600.

(23) Plass, R.; Pelet, S.; Krueger, J.; Gratzel, M.; Bach, U. *J. Phys. Chem. B*, **2002**, *106*, 7578.

(24) Chang, J.-Y.; Lin, J.-M.; Su, L.-F.; Chang, C.-F. *ACS Appl. Mater. Interfaces*, **2013**, *5*, 8740.

(25) Choi, Y. C.; Lee, D. U.; Noh, J. H.; Kim, E. K.; Seok, S. I. *Adv. Funct. Mater.*, **2014**, *24*, 3587.

(26) Yin, X.; Battaglia, C.; Lin, Y.; Chen, K.; Hettick, M.; Zheng, M.; Chen, C. Y.; Kiriya, D.; Javey, A. *ACS Photonics*, **2014**, *1*, 1245.

(27) Yu, W. W.; Qu, L.; Guo, W.; Peng, X. *Chem. Mater.*, **2003**, *15*, 2854.

(28) Leatherdale, C. A.; Woo, W.-K.; Mikulec, F. V.; Bawendi, M. G. *J. Phys. Chem. B*, **2002**, *106*, 7619.

(29) Kan, S.; Mokari, T.; Rothenberg, E.; Banin, U. *Nat. Mater.*, **2003**, *2*, 155.

(30) Smestad, G.; Bignozzi, C.; Argazzi, R. *Sol. Energy Mater. Sol. Cells*, **1994**, *32*, 259.

(31) Han, L.; Fukui, A.; Chiba, Y.; Islam, A.; Komiya, R.; Fuke, N.; Koide, N.; Yamanaka, R.; Shimizu, M. *Appl. Phys. Lett.*, **2009**, *94*, 013305.

(32) Rao, J.; Yu, A.; Shao, C.; Zhou, X. *ACS Appl. Mater. Interfaces*, **2012**, *4*, 5346

(33) Park, H.; Chang, S.; Jean, J.; Cheng, J. J.; Araujo, P. T.; Wang, M.; Bawendi, M. G.; Dresselhaus, M. S.; Bulovic, V.; Kong, J.; Gradečak, S. *Nano Lett.*, **2013**, *13*, 233.

(34) Vayssieres, L. *Adv. Mater.*, **2003**, *15*, 464.

(35) Lin, S. C.; Lee, Y. L.; Chang, C. H.; Shen, Y. J.; Yang, Y. M. *Appl. Phys. Lett.*, **2007**, *90*, 143517.

(36) Shang, G.; Wu, J.; Tang, S.; Huang, M.; Lan, Z.; Li, Y.; Zhao, J.; Zhang, X.; *J. Mater. Chem.*, **2012**, *22*, 25335.

(37) Robel, I.; Kuno, M.; Kamat, P. V. *J. Am. Chem. Soc.*, **2007**, *129*, 4136.

(38) Bang, J. H.; Kamat, P. V. *ACS Nano*, **2009**, *3*, 1467.

(39) Kongkanand, A.; Tvrdy, K.; Takechi, K.; Kuno, M.; Kamat, P.V. *J. Am. Chem. Soc.*, **2008**, *130*, 4007.

(40) Zeng, H.; Duan, G.; Li, Y.; Yang, S.; Xu X.; Cai, W. *Adv. Funct. Mater.*, **2010**, *20*, 561.

(41) Kontos, A. G.; Likodimos, V.; Vassalou, E.; Kapogianni, I.; Raptis, Y. S.; Raptis, C.; Falaras, P.; *Nanoscale Res. Lett.*, **2011**, *6*, 266.

(42) Yang, Z.; Chen, C.-Y.; Roy, P.; Chang, H.-T. *Chem. Commun.*, **2011**, *47*, 9561.

(43) Cheng, H.-M.; Huang, K.-Y.; Lee, K.-M.; Yu, P.; Lin, S.-C.; Huang, J.-H.; Wu, C.-G.; Tang, J. *Phys. Chem. Chem. Phys.*, **2012**, *14*, 13539.

(44) Li, C.; Yang, L.; Xiao, J.; Wu, Y.-C.; Søndergaard, M.; Luo, Y.; Li, D.; Meng, Q.; Iversen, B. B. *Phys. Chem. Chem. Phys.*, **2013**, *15*, 8710.

(45) Zhang, Q.; Chen, G.; Yang, Y.; Shen, X.; Zhang, Y.; Li, C.; Yu, R.; Luo, Y.; Li, D.; Meng, Q. *Phys. Chem. Chem. Phys.*, **2012**, *14*, 6479

(46) Barpuzary, D.; Qureshi, M. *ACS Appl. Mater. Interfaces*, **2013**, *5*, 11673.

CHAPTER 6

Binary Hybrid Composite of g-C_3N_4 and ZnO as a Photoanodic Material: A Synergistic Approach for Enhanced Charge Separation and Injection

This chapter demonstrates a practical strategy to boost light harnessing ability of ZnO based QDSSC devices by introducing a low cost and environmentally benign organic semiconductor, graphitic carbon nitride (g-C_3N_4) in the photoanodic segment. ~70% improvement in power conversion efficiency (PCE, η) is observed for the devices fabricated with a binary hybrid composite (g-C_3N_4–ZnO) as compared to pristine ZnO based devices. It is concluded that g-C_3N_4 boosts light harvesting ability of the photovoltaic devices; primarily by impeding photo-induced electron interception to the redox couple and injecting population to the conduction band of ZnO.

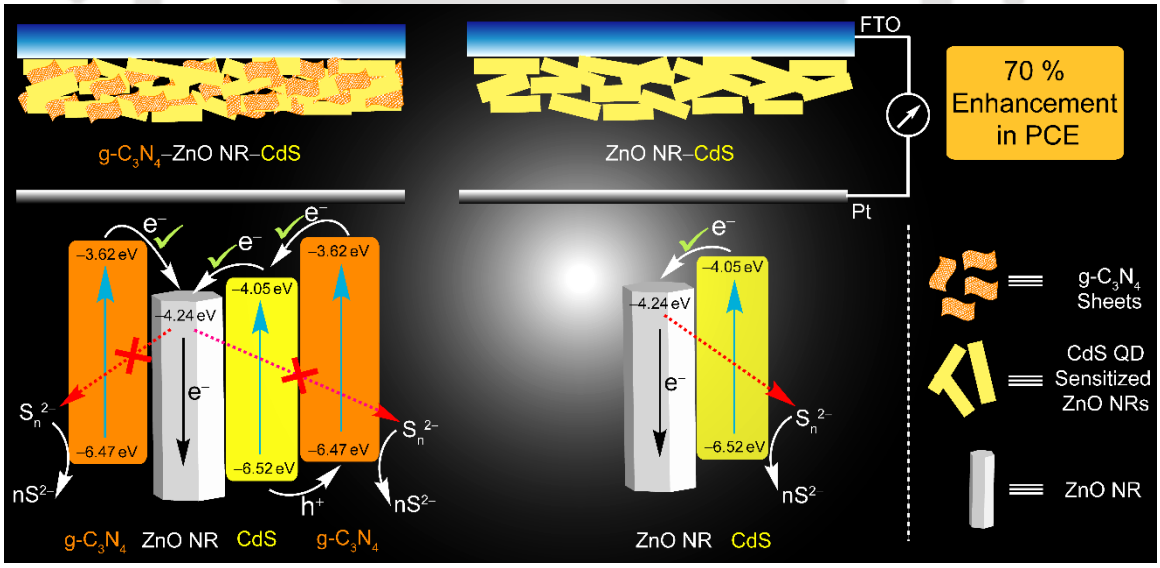

ROYAL SOCIETY OF CHEMISTRY Journal of Materials Chemistry A **T. R. Chetia**, M. S. Ansari, M. Qureshi **2016**, *DOI: 10.1039/C6TA00761A*.

6.1 INTRODUCTION

Exploration of non-toxic, low cost, environmental benign semiconductor materials with high solar energy conversion ability is a fascinating subject of research amongst the scientific community due to their potential applicability toward resolving the overuse of fossil fuels as well as fulfilling the clean energy demand.[1–3] To date, a number of UV or visible light responsive materials are introduced for harvesting most abundant renewable energy source "solar energy" to electrical energy or chemical fuels, such as hydrogen in large scale.[4–7] Recently, Wang et al. introduced a low cost, photoactive polymeric organic semiconductor, graphitic carbon nitride (g-C_3N_4) as a solar energy harvester with high efficacy showing a promise towards its practical use in hydrogen production using photocatalytic and photo-electrochemical ways.[8–10] g-C_3N_4 is an analog of graphite having tectonic structure with tri-s-triazine repeating units. It has an optical band gap (~2.77 eV) along with unique stability, including the heat endurance (as high as 600 °C) and chemical resistance.[11–13] However, the radiative recombination rate of photogenerated electrons (e^-) and holes (h^+) in pure g-C_3N_4 is very high resulting in high fluorescence yields, limiting its beneficial effects in photovoltaic device performance.[14,15] One of the practical approach to reduce the recombination rate of photogenerated (e^-–h^+) pairs or the excitons is the coupling of g-C_3N_4 with semiconductor materials like: ZnO, TiO_2, WO_3, $SrTiO_3$, CdS, etc with well-matched band edge alignments as shown in scheme **6.1.1**.[16–20]

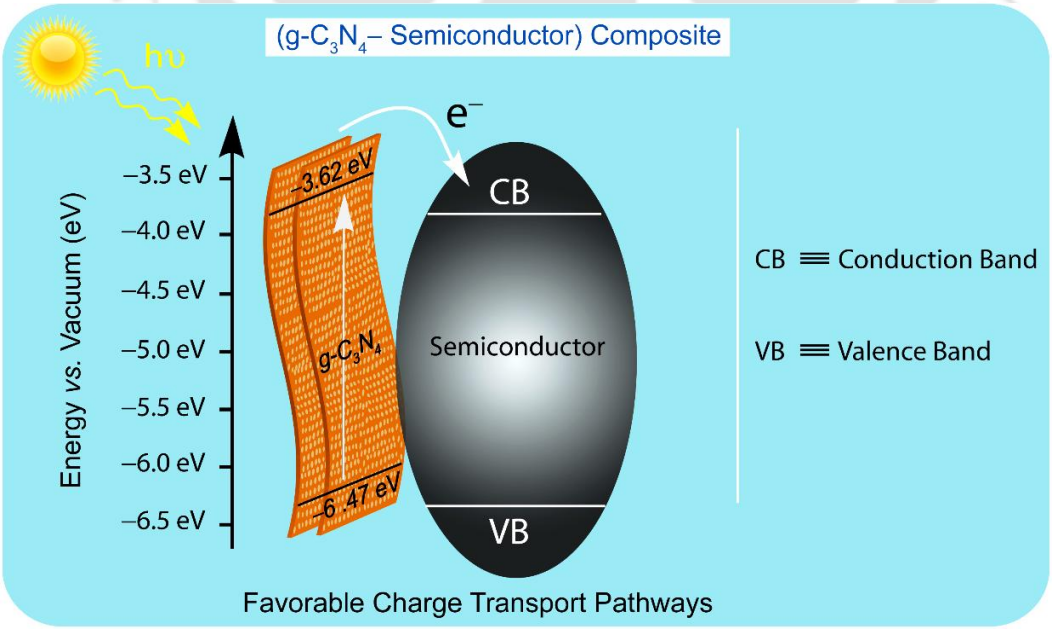

Scheme 6.1.1 Favorable Band alignment of (g-C_3N_4-semiconductor) composite for enhanced charge separation.

Low-lying conduction band (CB) edge of these semiconductors as compared to g-C_3N_4, facilitates a favorable excited state electron transfer process from g-C_3N_4 to the semiconductor; leading to a reduction in radiative annihilation of photogenerated excitons. In particular, tunable optical and charge transport properties of ZnO established it as a suitable material to design composite with g-C_3N_4 for solar energy harvesting. Optical and charge transport properties of ZnO can be tuned by tailoring it into various architectures of different dimensions such as nanoparticles (NPs), nanorods (NRs), nanodisks, nanosheets, microspheres, cages etc.[21–26] For example, ZnO NRs endowed with a minimum density of grain boundaries and charge trapping sites relative to its counterpart ZnO NPs, wherein photo-generated electrons have to interact repeatedly with the grain boundary induced trap sites.[27,28] Diverse morphologies of ZnO having unique electrical and optical properties can be achieved by varying the synthetic procedure which open up its potential application in wide spectrum of areas such as photocatalysis, gas sensing, optical devices, dye sensitized or quantum dot sensitized solar cells (DSSC/QDSSC).[29–33] Various research groups have reported an enhanced photocatalytic performance by (g-C_3N_4–ZnO) composites with different ZnO morphologies which demonstrates a facile electronic interaction among the composite.[34, 35] However, a systematic investigation on the effect of g-C_3N_4 in photovoltaic device performance is still scarce and needs to be explored.[36] In view of appropriate band edge alignments of g-C_3N_4 and ZnO, as well as high stability of g-C_3N_4, a composite (g-C_3N_4–ZnO) is utilized as a photoanodic material in QDSSC devices for the first time in this work. Previously, our group has also reported various methodologies for utilization of coupled semiconductor composites and materials with different dimensions in QDSSC devices to enhance the light harvesting ability.[37–40]

In this chapter, we have performed a systematic study on the effects of g-C_3N_4 in photovoltaic performance parameters of ZnO NR based CdS QD sensitized solar cell devices by introducing a binary hybrid composite of g-C_3N_4 and ZnO, i.e., (g-C_3N_4–ZnO NR) in the photoanodic segment. Addition of g-C_3N_4 sheets to the photoanodes are found to be reducing the reverse tunneling probability of photo-induced electrons to the redox couple, leads to a better light harvesting ability. Moreover, injection of photoexcited electrons from g-C_3N_4 sheets to ZnO upsurges the charge collection at the external load. A comparative study of (g-C_3N_4–ZnO) devices based on various morphologies (i.e., NR and NP) shows that the performance parameters of ZnO NR based devices are superior, suggesting a better/ smoother electron pathway.

6.2 EXPERIMENTAL METHODS

6.2.1 SYNTHESIS OF g-C_3N_4

The polymeric g-C_3N_4 sheets are synthesized by thermal polycondensation of urea followed by the decomposition.[41] In a typical synthesis process, 2 g of urea is taken in a mortar pestle and ground it for about 10 min. Grounded urea is then put into an alumina crucible with a cover and placed in a muffle furnace for heat treatment. The furnace temperature is raised upto 500 °C at a heating ramp of 5 °C min^{-1} and maintained at this temperature in air for 2 h. After cooling to room temperature in normal condition, the product is taken out and again ground into fine powers in the agate mortar.

6.2.2 SYNTHESIS OF ZnO NANORODS

For synthesis of ZnO NRs, 10 mmol of zinc nitrate hexahydrate (2.97 g) is dissolved in 50 mL of Milli-Q water with constant stirring. Equimolar amount of hexamine (0.7 g) is added into the reaction mixture and the solution is heated at a temperature of 90 °C for 4 h with constant stirring. After cooling down to the room temperature, the resultant precipitate is centrifuged and purified by washing with water and ethanol several times. As obtained product is dried in a hot air oven at 70 °C for 6 h and then calcined it at 450 °C for 1 h to get final product. Scheme 6.2.1 shows the pictorial presentation of ZnO NR synthetic protocol.

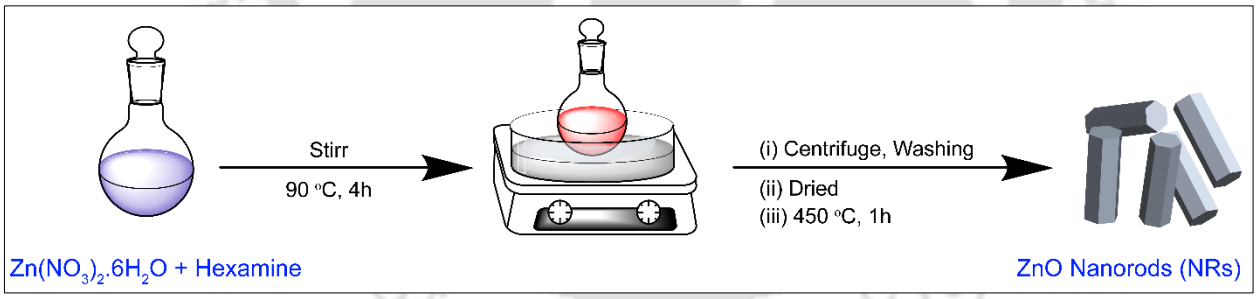

Scheme 6.2.1 Pictorial representation of step-by-step synthetic protocol for ZnO Nanorods (NRs).

6.2.3 SYNTHESIS OF ZnO NANOPARTICLES

ZnO nanoparticles (NPs) are synthesized by adopting a previously reported procedure.[42] In this synthetic procedure, 40 mmol of $ZnCl_2$ (1.1 g) is dissolved in Milli-Q water (40.0 mL) and heated upto a temperature of 90 °C with constant stirring. An aqueous solution of NaOH (5 M, 3.2 mL) is added slowly into the reaction mixture with constant stirring at the same temperature for another 30 min. The reaction mixture is allowed to cool down to room temperature normally and the precipitate is separated out by discarding the supernatant liquid. For purification, this

precipitate is washed with distilled water several times and dispersed in iso-propanol in an ultrasonic bath for 10 min at room temperature. The solution is centrifuged and dried in a hot air oven at 70 °C for 6 h. Finally, ZnO nanoparticles are obtained via calcination at 450 °C for 1 h in a muffle furnace. Detail synthetic protocol is presented schematically in scheme **6.2.2**.

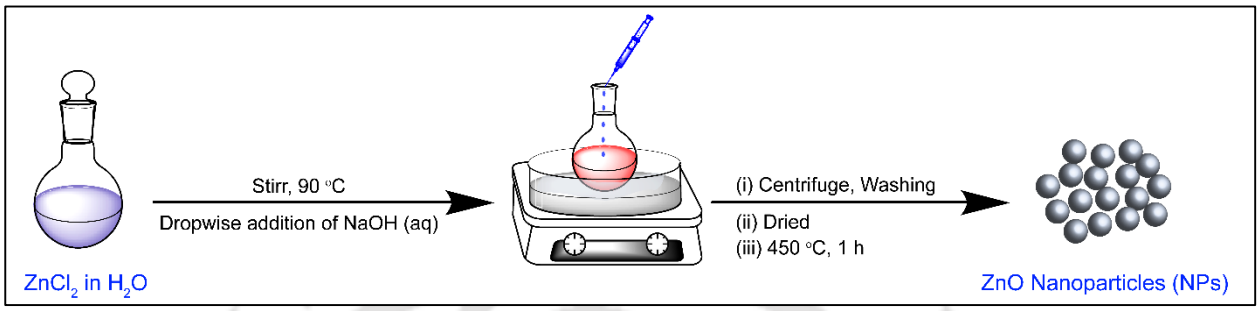

Scheme 6.2.2 Schematic representation of step-by-step synthetic protocol for ZnO Nanoparticles (NPs).

6.2.4 PREPARATION OF (g-C_3N_4–ZnO NR) AND (g-C_3N_4–ZnO NP) COMPOSITES

The g-C_3N_4 composites of ZnO NR and ZnO NP are prepared by ultra-sonication treatment of g-C_3N_4 sheets and ZnO heterostructures (i.e., NR and NPs). In detail, an appropriate amount of as synthesized g-C_3N_4 is dispersed in ethanol under ultrasonic treatment for 30 min. As synthesized ZnO NRs or ZnO NPs are added into solution and continued the ultrasonic treatment for another 1 h. Finally, the solutions is placed inside a hot air oven for evaporation of the solvent to obtain the composite product and named as (g-C_3N_4–ZnO NR) or (g-C_3N_4–ZnO NP). A series of (g-C_3N_4–ZnO NR) composites are prepared by following the same methodology with different weight ratios of g-C_3N_4 to ZnO NR.

6.2.5 FABRICATION OF PHOTOANODES AND DEVICES

The photoanodes with (g-C_3N_4–ZnO NR) composites are fabricated by preparing a homogeneous paste of the composite powders. For preparation of the paste appropriate amounts of terpineol and the triblock copolymer, "PEG-PPG-PEG" are added to the powders as binder materials and mixed well in an agate mortar. This homogenous paste is applied on a pre-cleaned conductive glass substrate i.e. FTO via doctor blade technique and dried in a hot air oven at 90 °C for 3 h. After cooling down to room temperature normally, all the films are calcined at 450 °C for 30 min to remove the binder. The thickness of the photoanodic films are measured by surface profilometer and they are found to be in the range of 10-12 µm. The photoanodes are sensitized with the CdS QDs via successive ionic layer adsorption and reaction (SILAR) technique. In

sensitization process, the electrodes are first dipped into an ethanolic solution of $Cd(NO_3)_2.6H_2O$ (0.5 M) for 5 min, rinsed with ethanol, and dried using a hot air drier. Again they are dipped into a Na_2S (0.5 M) solution in methanol for 5 min, rinsed with methanol and dried under a hot air blower. The amount of CdS grown onto the Photoanodes is controlled by the number of repeated SILAR cycles. A pictorial presentation of step by step composite preparation and photoanode fabrication processes along with expected energy transfer processes in the device is showing in the scheme **6.2.3**.

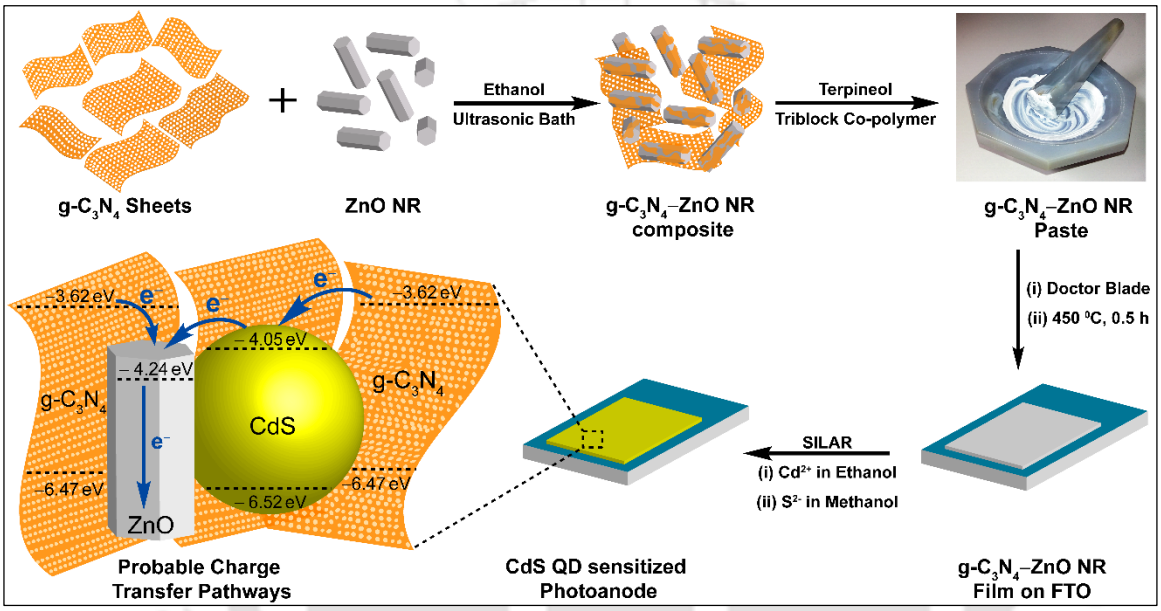

Scheme 6.2.3 Step by step fabrication process of g-C_3N_4–ZnO NR composite photoanode, CdS QD sensitization and their favorable band alignments for efficient charge transport

Similarly, (g-C_3N_4–ZnO NP) composite based photoanodes are fabricated by following the same procedure used for (g-C_3N_4–ZnO NR) composites. The Pt counter electrodes are prepared by spin coating a solution of chloroplatinic acid (5 mM in isopropanol) on a pre-cleaned FTO substrate followed by the calcination at 450 °C for (heating ramp of 5 °C /min) 30 min in a muffle furnace and cooled down to room temperature naturally. The photovoltaic devices are fabricated by sandwiching the photoanodes and counter electrodes. Electrolyte solution of sulfide/polysulfide (S^{2-}/S_n^{2-}) is added after sealing the device by using low-temperature thermoplastic sealant, (thickness ~50 µm). Sulfide/polysulfide (S^{2-}/S_n^{2-}) electrolyte is prepared by dissolving 1M Sulfur powder, 1M Na_2S and 0.2 KCl in Milli-Q water. The active area for all fabricated devices are fixed and it is found to be 0.5 cm^2. Before the photovoltaic measurements the fabricated devices are kept under dark condition for 24 h.

6.3 RESULTS AND DISCUSSIONS

6.3.1 POWDER X-RAY DIFFRACTION ANALYSIS

Figure **6.3.1** depicts powder X-ray diffraction (PXRD) patterns for as synthesized ZnO NRs, g-C_3N_4 and their composites. Trace (a) represents PXRD pattern of ZnO NRs which is defined to be hexagonal wurtzite phase with $(10\bar{1}0)$, (0002), $(10\bar{1}1)$, $(10\bar{1}2)$, $(11\bar{2}0)$, $(10\bar{1}3)$, $(20\bar{2}0)$, $(11\bar{2}2)$ and $(20\bar{2}1)$ crystal planes. The space group symmetry for ZnO NRs is $P6_3mc$ and Zn atoms are in tetrahedral sites according to the JCPDS Card No. 36-1451. Traces (b), (c), (d), (e), and (f) are PXRD patterns for the g-C_3N_4–ZnO NR composites with varying g-C_3N_4 to ZnO NR ratio while the trace (g) signifies the PXRD pattern for pure g-C_3N_4. No impurity peaks are detected in the PXRD patterns which implies products are pure and have no crystalline impurities.

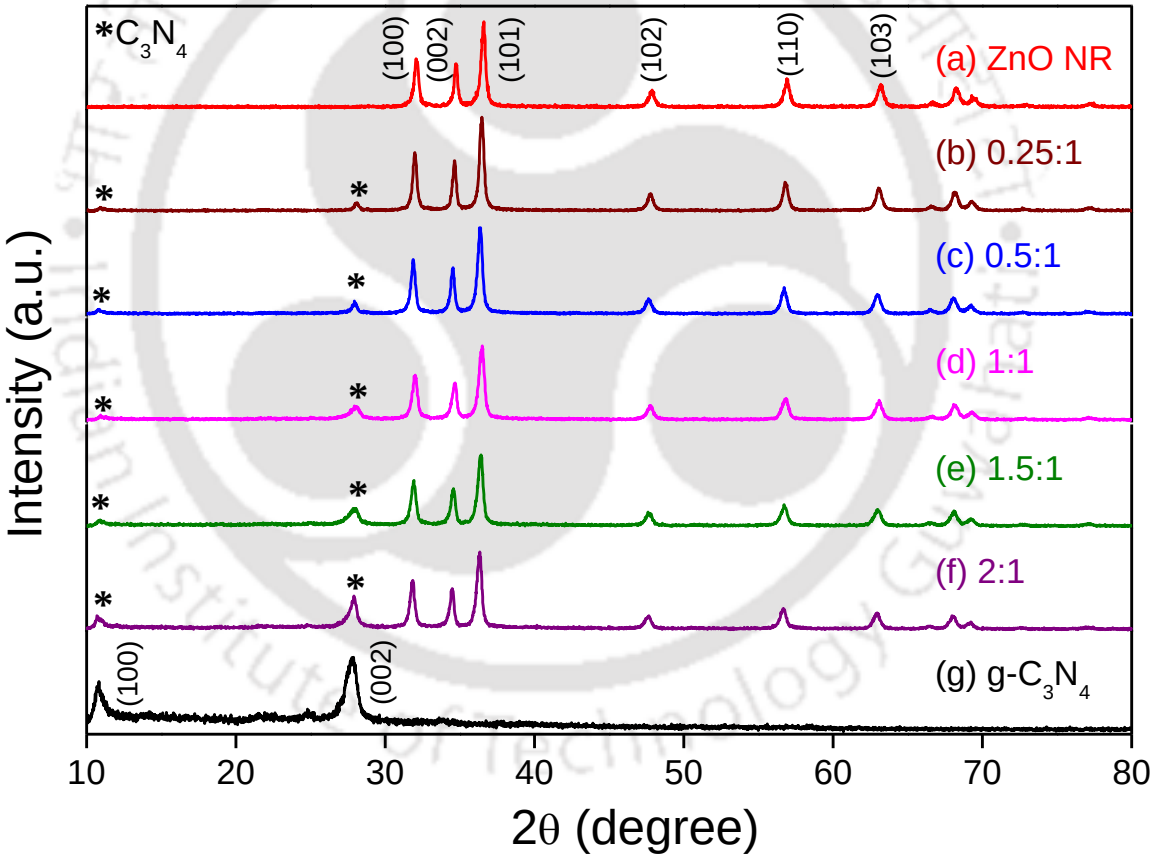

Figure 6.3.1 Powder X-ray diffraction (PXRD) patterns of all the synthesized products; (a) pristine ZnO NRs, (g-C_3N_4–ZnO NR) composite with weight ratios (b) 0.25:1, (c) 0.5:1, (d) 1:1, (e) 1.5:1, and (f) 2:1. Trace (g) represents the PXRD pattern for pristine g-C_3N_4.

From the PXRD pattern of pure g-C_3N_4 [trace (g)], two broad diffraction peaks at $2\theta \approx 11.2°$ and 27.5° with *d*-spacing values of 0.714 nm and 0.316 nm respectively are observed, which are

indexed to be as (001) and (002) crystal plane reflections for amorphous graphitic material. The diffraction peak at lower 2θ value corresponds to the characteristic in-plane repeating pattern of tri-s-triazine or melem units while the peak at higher 2θ value indicates interplanar staking of conjugated aromatic segments, as in graphite.[8, 41] Structural information obtained from the analysis of PXRD pattern of g-C_3N_4 is presented in scheme **6.3.1**.

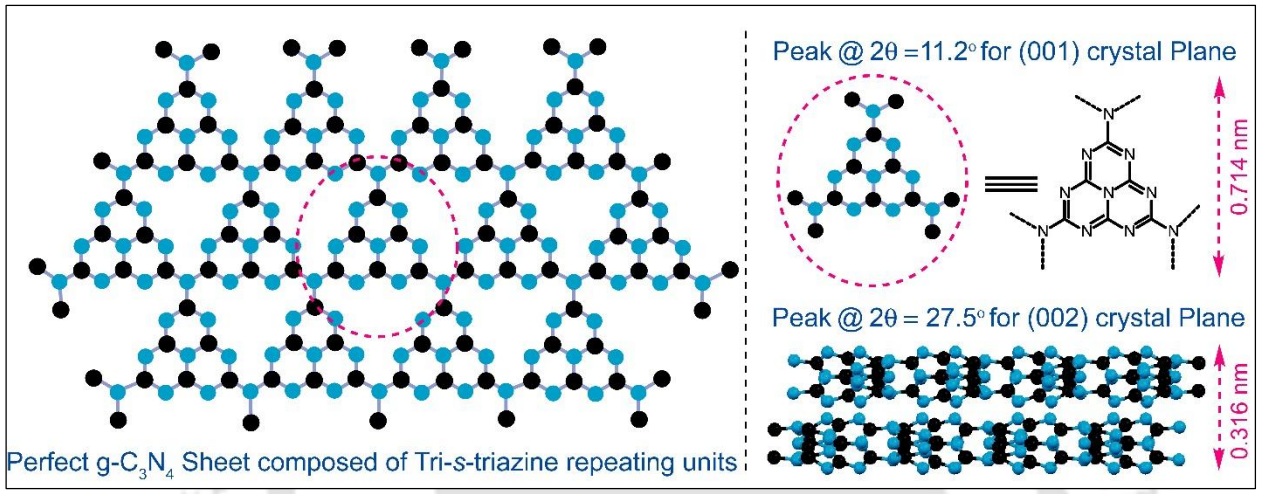

Scheme 6.3.1 Schematic presentation of g-C_3N_4 structure and *d*-spacing values for the (001) and (002) crystal planes obtained from PXRD analysis.

It should be noted that, as the weight ratio of g-C_3N_4 to ZnO NR increases from (0.25:1) to (2:1), the intensity of g-C_3N_4 diffraction peaks increases simultaneously as we have seen from figure **6.3.1**. This observation is symptomatic of retention of crystal structures of both the components namely g-C_3N_4 and ZnO NR in all the composite ratios, even after the composite preparation process.

6.3.2 MATERIAL MORPHOLOGY

Morphological and microstructural analysis of as synthesized g-C_3N_4 is carried out by performing FESEM and TEM studies as shown in the figure **6.3.2**. Lower and higher magnification FESEM images of g-C_3N_4 are shown in figure (A) and (B) respectively. FESEM analysis demonstrates porous, flake-like layered structure of g-C_3N_4, as similar to graphitic materials. From figure (B), we have seen that, size distribution of most of the g-C_3N_4 flakes are appear to be in submicron range (i.e., 0.5-1 μm). Furthermore, TEM analysis is performed to confirm the layered structure of g-C_3N_4. Figure (C) and (D) are TEM image of g-C_3N_4 and corresponding selected area diffraction (SAED) pattern respectively. Note that, as synthesized g-C_3N_4 powder was dispersed in ethanol by ultrasonic treatment for 30 minute, prior to the TEM sample preparation process.

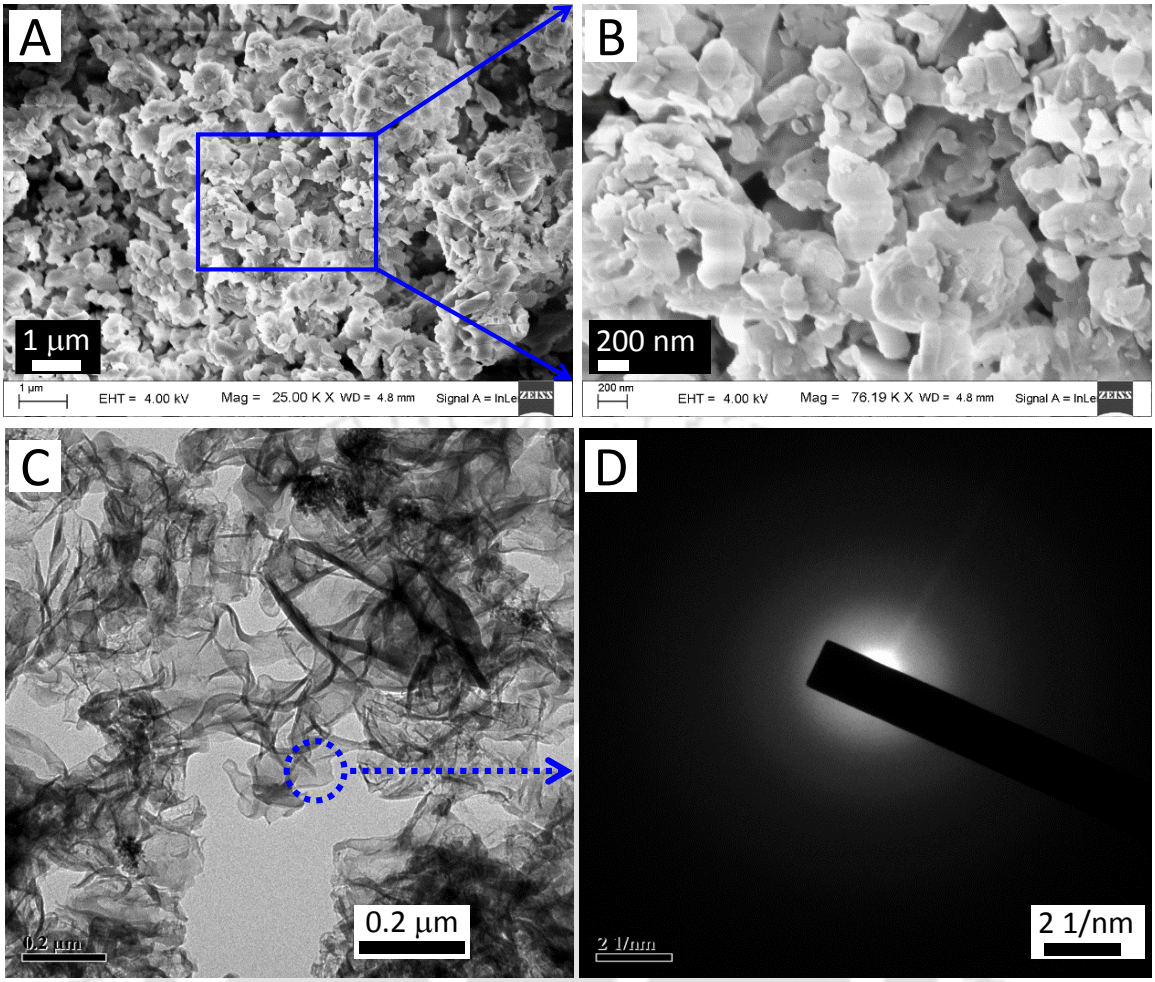

Figure 6.3.2 (A) & (B) are FESEM Images showing flake like features of g-C_3N_4 at different magnifications. Trace (C) shows TEM image of g-C_3N_4 sheet formation and trace (D) corresponding to the selected area electron diffraction (SAED) pattern showing a diffused ring pattern confirming the nano-sized sheet structures

Layered structure of g-C_3N_4 sheets is divulged through the TEM image (C) in figure **6.3.2**. g-C_3N_4 sheets in the TEM image are observed to be bigger in size than they appear in FESEM images. Probable reason for this observation could be the unfolding and exfoliation of the g-C_3N_4 flakes during the ultrasonic treatment. SAED pattern [trace (C)] for the indicated part (marked in blue circle) of TEM image showing a diffused diffraction ring which implies amorphous characteristic of the material, consistent with the PXRD analyses.

Morphological characteristics of as synthesized ZnO NRs are investigated by performing FESEM analysis as shown in the figure **6.3.3 (A)** and **(B)**.

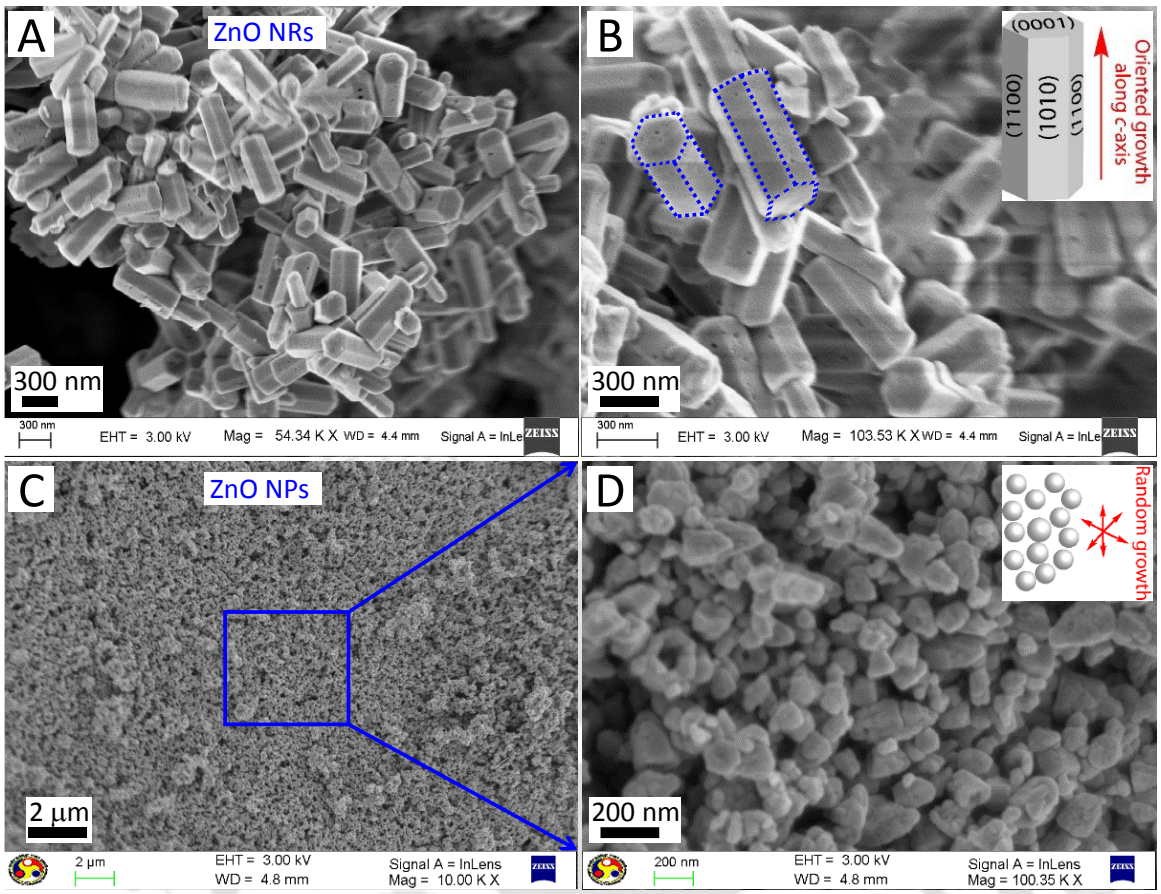

Figure 6.3.3 FESEM images (A) and (B) shows as synthesized hexagonal ZnO nanorods (NRs) while traces (C) and (D) represent ZnO nanoparticles (NPs) at low and high magnifications respectively.

Hexagon shaped morphology of ZnO NRs is evident from the FESEM images and the size distribution is observed to be ~500 nm. It should be mentioned that, we have synthesized ZnO NPs to evaluate and understand the morphology dependent photovoltaic characteristics of ZnO. Panels (C) and (D) are showing FESEM features of as synthesized ZnO NPs at low and high magnifications respectively. From image (C), homogeneous size distribution of ZnO NPs is observed, while size range is confirmed to be ~50–100 nm from the image (D).

Formation of two distinct morphologies of ZnO in two different reaction conditions can be explained from anisotropic growth behaviour of crystal planes.[39] It is well known that, wurtzite ZnO is a polar crystal phase with alternatively stacked O^{2-} and Zn^{2+} ions along *c-axis*, which results O-terminated $(000\bar{1})$ and Zn-terminated (0001) crystallographic planes with high surface energy.[43] In general, ZnO nuclei tend to grow faster along these polar crystal planes relative to the non-polar crystal planes such as $\pm(10\bar{1}0)$, $(1\bar{1}00)$, $(01\bar{1}0)$ etc., having lower surface energy which are composed of equivalent number of O^{2-} and Zn^{2+} ions. Faster growth rate of ZnO nuclei along *c*-

axis, results hexagon shaped ZnO NRs. In the present hydrothermal reaction condition for synthesis of ZnO NRs, we have used hexamethylenetetramine (HMTA) as a base, which readily undergo hydrolysis in water and gradually produces ammonia (NH_3) as well as formaldehyde (HCHO) molecules (step 1, scheme **6.3.2**). NH_3 molecules produce a basic environment in the reaction for the formation of ZnO growth units such as $[Zn(OH)_4]^{2-}$ and $[Zn(NH_3)_4]^{2+}$ (step 2, 3, 4, and 5). These growth units preferentially adsorb onto the O-terminated $(000\bar{1})$ and Zn-terminated (0001) polar surfaces of newly formed ZnO nuclei, leading to a faster growth along ±(0001) directions and consequently ZnO NR are formed (step 6).[44]

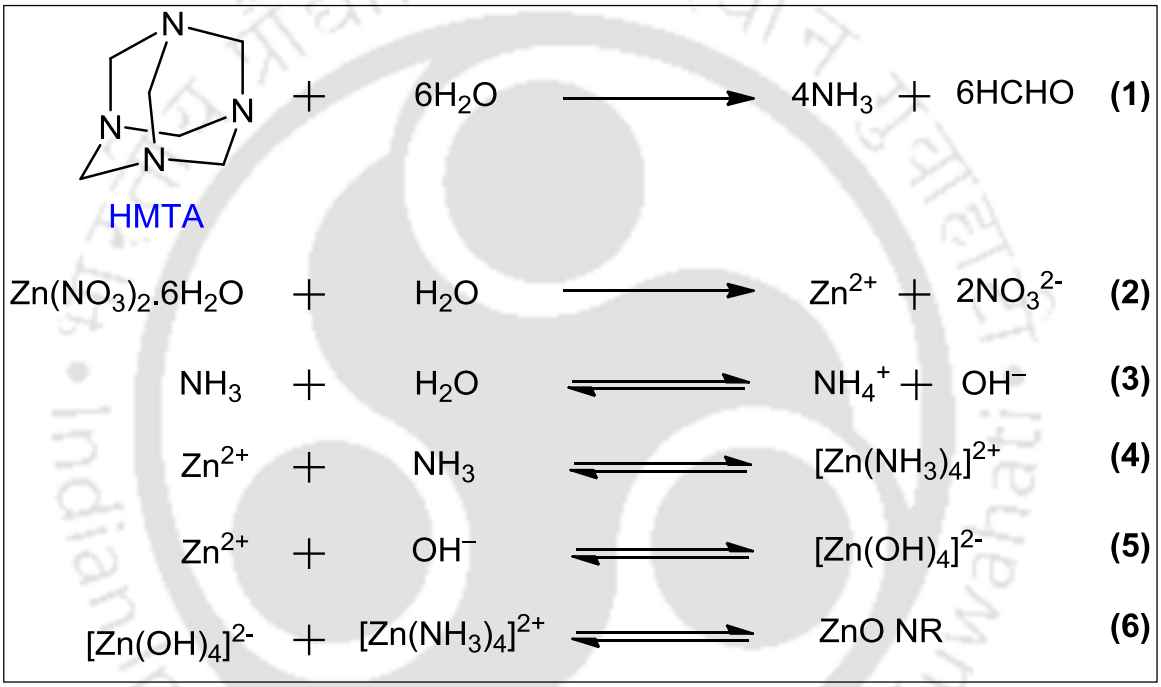

Scheme 6.3.2 Schematic presentation of plausible formation mechanism of ZnO nanorods.

In addition, nonionic HMTA molecules can act as a bidentate Lewis base that coordinate two Zn^{2+} ions.[45] As the reaction progresses, non-hydrolyzed HMTA molecules in the reaction mixture favorably bind to the Zn^{2+} ions in non-polar crystal facets of ZnO nuclei, which facilitates oriented anisotropic growth along ±(0001) directions and encourage the formation of ZnO NRs.[46] Previously, it was reported that rate of HMTA hydrolysis (step 1) decreases with increasing pH and vice versa.[44] Therefore, it is expected that concentration of non-hydrolyzed HMTA molecules increases in the reaction mixture as the reaction progresses.

However, in alkaline medium (i.e., aqueous NaOH) a large amount of OH^- ions are released in the reaction mixture within a short period of time. Consequently, due to high pH

environment, Zn^{2+} ions in the solution would precipitate out quickly as water insoluble $Zn(OH)_2$ and prohibit the oriented growth of ZnO crystal planes.[47] As the temperature of the reaction increases, $Zn(OH)_2$ dehydrates to form numerous ZnO nanoparticles, as we have confirmed from FESEM images (C) and (D) in figure **6.3.3**.

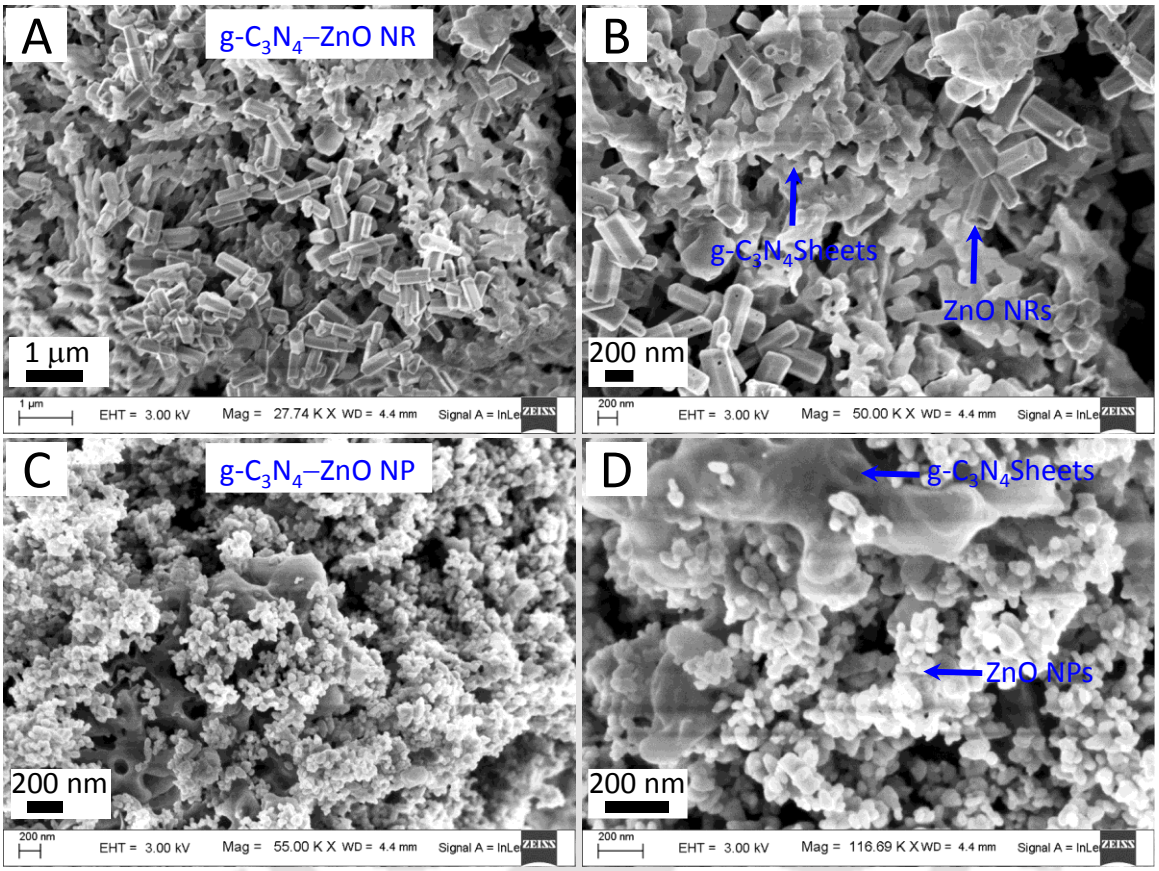

Figure 6.3.4 FESEM features of as prepared (g-C_3N_4–ZnO NR) composite (panels A and B) and (g-C_3N_4–ZnO NP) composite (panels C and D) at different magnifications.

Traces (A) & (B) of figure **6.3.4** are depicting FESEM images of as prepared (g-C_3N_4–ZnO NR) composites while traces (C) & (D) are representing (g-C_3N_4–ZnO NP) composites at different magnifications. From FESEM images of the composites it is clear that the ZnO NRs and ZnO NP are well embedded in the g-C_3N_4 sheets. This may be due to unfolding and exfoliation of g-C_3N_4 sheets during ultrasonic treatment. Additionally, probable preference between polar wurtzite ZnO crystals and delocalized π-electrons as well as non-bonding electrons in the g-C_3N_4 sheets might have facilitated the embedding process. From the FESEM images (B) and (D), we have seen a number of bare ZnO NRs and ZnO NPs in the composites, which is beneficial for optimum loading of CdS QDs onto the ZnO heterostructures for efficient photoexcited electron injection. Note that,

photoexcited electron injection from CdS QDs to g-C_3N_4 sheets is not energetically favorable according to their conduction band (CB) edge alignments whereas charge transfer from CB of g-C_3N_4 sheets to CdS QDs and ZnO are favorable processes. For confirmation of connection between the two materials (i.e., g-C_3N_4 and ZnO NR) in the composite, we have performed TEM analysis as depicted in the figure **6.3.5**.

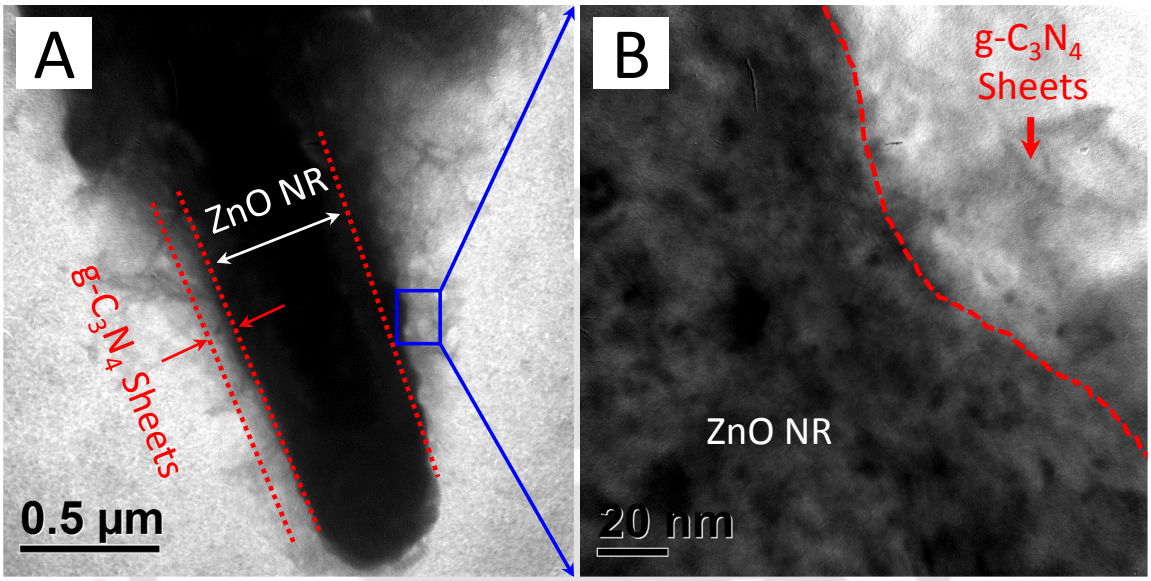

Figure 6.3.5 TEM images of as prepared (g-C_3N_4–ZnO NR) composite at lower magnification (Image A) and higher magnification (Image B) respectively

Figure **6.3.5** shows TEM images of the hybrid composite (g-C_3N_4–ZnO NR) at different magnifications. From the low magnification image (A), it is clear that, g-C_3N_4 sheets are wrapped around the ZnO NR. The high magnification image (B) further confirms connection between g-C_3N_4 sheets and ZnO NRs in composite. The connection between the two materials in the composite is favorable for electronic interactions and play a significant role in better performance of the device.

Further, to elucidate elemental distribution and composition in (g-C_3N_4–ZnO NR) composite, selected area elemental mapping is performed by energy dispersive X-ray (EDX) spectroscopic technique and depicted in the figure **6.3.6** (A), (B), (C) and (D). Homogeneous distribution of all the elements [i.e., Carbon (C), Nitrogen (N), Zinc (Zn) and Oxygen (O)] throughout the whole composite is observed from the EDX maps. This observation confirms successful incorporation of g-C_3N_4 sheets with the ZnO NRs and hence preparation of the composite. Figure 6.3.6 (E) represents corresponding EDX pattern which further validates the existence of all the elements namely, C, N, Zn and O in the composite and confirms purity of the

sample. Please note that, the peak for aluminum (Al) is observed due to the background aluminum foil used for deposition of the sample. Inset to the EDX pattern shows elemental compositions (wt %) contained in the composite which is in well agreement with the g-C_3N_4 to ZnO NR weight ratio of the sample [i.e., (0.5:1)].

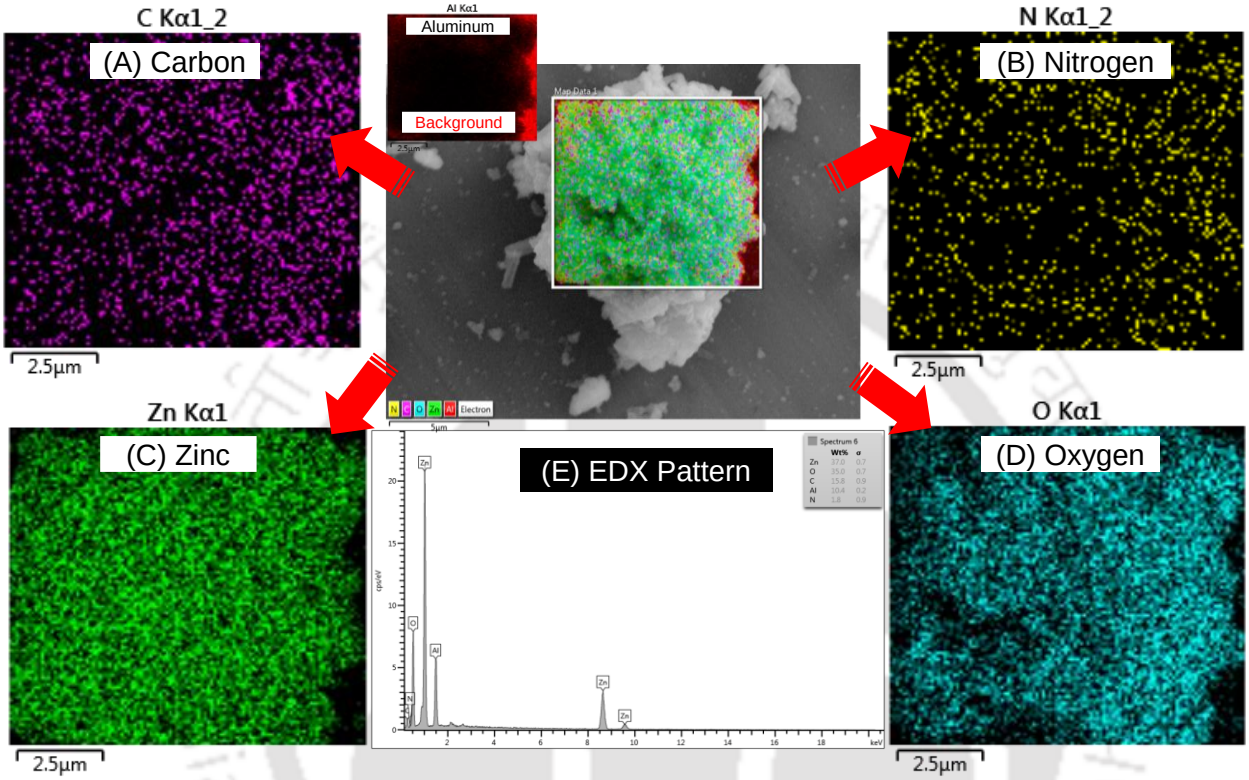

Figure 6.3.6 Energy-dispersive X-ray spectroscopy (EDX) maps (A, B, C & D) and corresponding EDX pattern (E) of the hybrid composite (g-C_3N_4–ZnO NR) with optimum weight ratio [i.e., (0.5:1)].

6.3.3 DIFFUSE REFLECTANCE UV-VISIBLE ABSORPTION SPECTRA ANALYSES

Diffuse reflectance UV-visible (UV-vis) absorption spectra of as prepared (g-C_3N_4–ZnO NR) composites with varied g-C_3N_4 to ZnO NR ratios along with pristine materials, i.e., g-C_3N_4 and ZnO NRs are compiled in figure **6.3.7 (A)**. Figure **6.3.7 (B)** represents a plot of optical band gap values estimated from corresponding Tauc plots vs pristine materials and composites. Inset to it shows the Tauc plot derived from absorption profiles of all the materials.

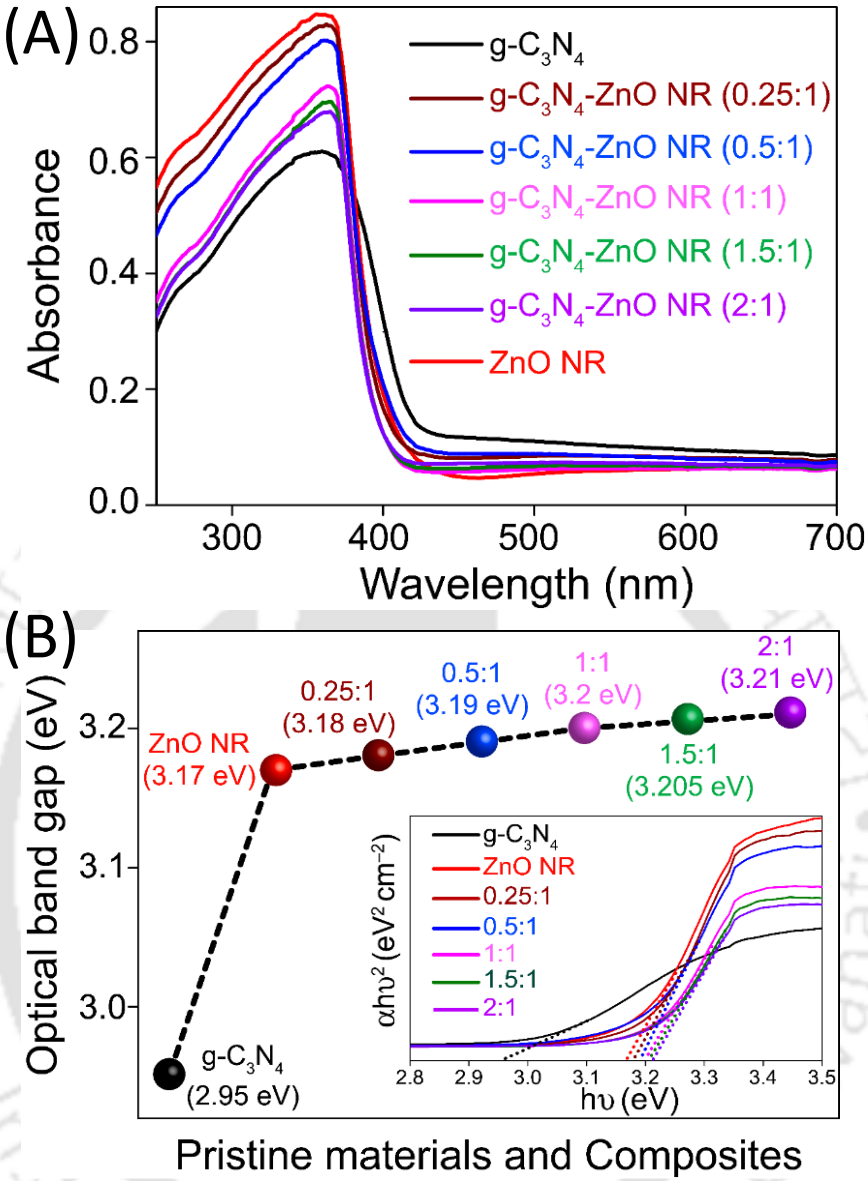

Figure 6.3.7 (A) Diffuse reflectance UV-visible (UV-vis) absorption profiles for all the synthesized products and composites namely; pristine g-C_3N_4 (black line), g-C_3N_4–ZnO NR composites with weight ratios 0.25:1 (wine red line), 0.5:1 (blue line), 1:1 (magenta line), 1.5:1 (olive line), and 2:1 (violet line). The red line represents UV-vis absorption profile for pure ZnO NRs. **(B)** Variation of optical band gap values for the composites as compared to the pristine materials which are estimated from the Tauc plots showing in the inset to it.

From figure (A), absorption edges of as synthesized pure g-C_3N_4 sheets and ZnO NR are observed to be at ~430 nm and ~398 nm respectively, corresponding to the band gap of 2.89 eV and 3.1 eV, which are also consistent with the approximate values obtained from Tauc plots (2.95 eV and 3.17 eV) as well as band gap values reported previously.[41] Moreover, we have observed a distinct blue shift of adsorption edges for all (g-C_3N_4–ZnO NR) composites as compared to the pristine materials. This blue shift is also reflected in the increment sequence of optical band gap

values for the composites as shown in figure (B). The observed sequence is: pure ZnO NR (3.17 eV) <0.25:1 (3.18 eV) <0.5:1 (3.19 eV) <1:1 (3.20 eV) <1.5:1 (3.205 eV) <2:1 (3.21 eV). The band gap values are increasing steadily as the weight ratio of g-C_3N_4 to ZnO increases from (0.25:1) to (2:1). This observation suggests a possible electronic interaction between g-C_3N_4 sheets and ZnO NRs.[48] In the absorption spectra, there appears to be a distinct progressive blue shift for the composites consisting of g-C_3N_4 and ZnO, indicative of a strong electronic coupling due to the migration of population from g-C_3N_4 to ZnO.

6.3.4 STEADY STATE AND TIME RESOLVED PHOTOLUMINESCENCE ANALYSES

Excited state charge transfers and recombination process in the photoactive electrode materials are monitored by steady-state and dynamic photo-luminescent studies. Figure **6.3.8 (A)** shows the steady state PL spectra for pure g-C_3N_4 (black line) and its composites with ZnO NR varying g-C_3N_4 to ZnO NR weight ratios, namely; 0.25:1 (wine red line), 0.5:1 (blue line), 1:1 (magenta line), 1.5:1 (olive line), and 2:1 (violet line), recorded at an excitation wavelength of 350 nm corresponding to g-C_3N_4. As-synthesized pure g-C_3N_4 sheets exhibits a strong PL emission peak at around 432 nm due to radiative annihilation of excitons or photogenerated (e^-–h^+) pairs.[14] A normalized PL spectra shows a gradual static quenching of PL intensity for the composites with decrease in g-C_3N_4 to ZnO NR weight ratio signifies an inhibited recombination of (e^-–h^+) pairs possibly due to photogenerated charge transfer at the heterojunctions of g-C_3N_4 sheets and ZnO NRs.[34, 35, 49] This observation is evocative of photogenerated charge injection from the CB edge of g-C_3N_4 sheets (–3.62 eV) to the more positive CB offset of ZnO NRs (–4.24 eV) as shown in the inset to figure (A). Consequently, photogenerated charges would be primarily localized at the ZnO NRs in composites during excitation process which is divulged through the monotonous blue shift of emission peaks (~20 nm) observed for all the composites. However, normalized PL intensity for the composite ratio (2:1) is observed to be comparable with pure g-C_3N_4, which is due to the presence of excess amount of g-C_3N_4 relative to the ZnO NRs.

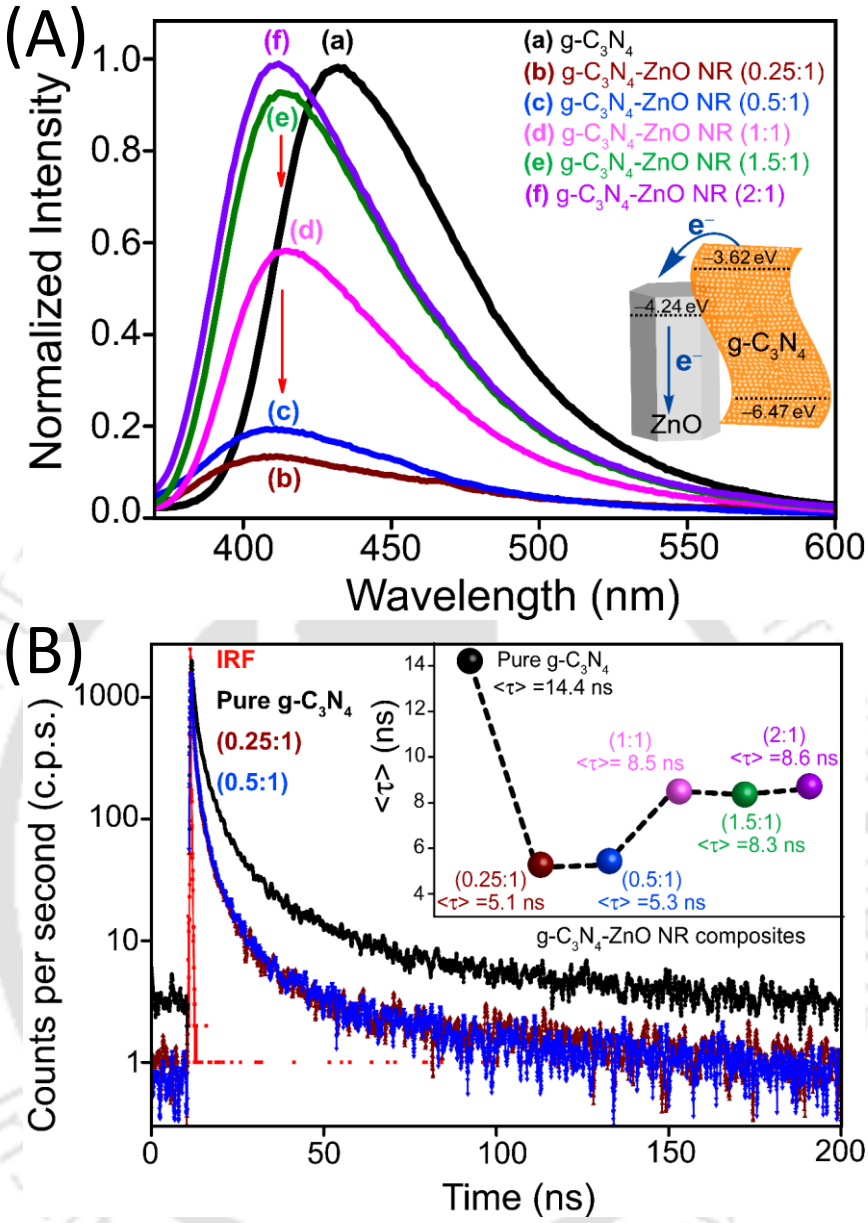

Figure 6.3.8 (A) Steady state photoluminescence (PL) spectra of pure g-C_3N_4 and its composites of ZnO NR with varying g-C_3N_4 to ZnO NR weight ratios. **(B)** Dynamic PL spectra for pure g-C_3N_4 (black spectrum), (g-C_3N_4–ZnO NR) composites with weight ratios 0.25:1 (wine red spectrum) and 0.5:1 (blue spectrum). Inset to it shows variation of average life time (<τ>) for all the (g-C_3N_4–ZnO NR) composites.

To further gain insights into the synergistic effects between g-C_3N_4 and ZnO NRs and charge transport kinetics in the composites, we have performed dynamic PL spectroscopy for the pristine materials and their composites as shown in figure **6.3.8 (B)**, measured at the emission peak with an excitation wavelength of 350 nm. PL decay traces are fitted with a tri-exponential function using fast software provided by Edinburgh instruments to calculate the exciton lifetime values. Observed multi-exponential decay patterns for all the materials infer multiple processes involved

during decay of emissive excitons or the radiative transitions. The values of fitting parameter (χ^2) and detailed spectroscopic results such as, exciton lifetimes (τ_1, τ_2, τ_3), pre-exponential factors (α_1, α_2, α_3), average exciton lifetimes (<τ>) etc. are summarized in the table **6.3.1**.

Table 6.3.1 Calculated parameters such as fitting parameter (χ^2), exciton lifetimes (τ_1, τ_2, τ_3), pre-exponential factors (α_1, α_2, α_3), average exciton lifetimes (<τ>) are summarized in the following table.

Sample	χ^2	τ_1 (ns)	τ_2 (ns)	τ_3 (ns)	α_1	α_2	α_3	<τ> (ns)
g-C_3N_4	1.055	0.831	3.6	19.094	36.50	41.01	22.49	14.41
(0.25:1)	0.935	0.210	1.324	6.855	32.22	44.98	22.80	5.17
(0.5:1)	0.941	0.831	1.275	6.766	31.13	43.86	25.01	5.27
(1:1)	0.968	0.351	2.091	11.497	35.32	44.35	20.32	8.51
(1.5:1)	0.972	0.358	2.066	11.285	36.18	43.44	43.44	8.37
(2:1)	0.974	0.318	1.995	1.995	35.27	44.69	20.04	8.60

The average lifetime values are derived from equation (1).[50]

$$< \tau >= \frac{\alpha_1 \tau_1^2 + \alpha_1 \tau_2^2 + \alpha_1 \tau_3^2}{\alpha_1 \tau_1 + \alpha_1 \tau_2 + \alpha_1 \tau_3} \qquad (1)$$

Inset to figure **6.3.8 (B)** shows the variation of average exciton life time (<τ>) for all the (g-C_3N_4–ZnO NR) composites. Exciton lifetimes are observed to be faster in all the composites as compared to pure g-C_3N_4 which confirms the role of ZnO NRs in decay process of excitons. However, a substantial decrease in exciton lifetimes for the composites namely; 0.25:1 (wine red spectrum) and 0.5:1 (blue spectrum) are noted, as evident from figure **6.3.8** (B). Calculated <τ> values are found to be ~5.1 ns (for 0.25:1) and ~5.3 ns (for 0.5:1) which are significantly lower than the average lifetimes estimated for its counterparts 8.5 ns (for 1:1), 8.3 ns (for 1.5:1), and 8.6 ns (for 2:1) as well as for pure g-C_3N_4 (<τ> ≈14.4 ns). This observation confirms a strong excited state electronic interactions between g-C_3N_4 sheets and ZnO NRs in the both the composites. Faster exciton life times observed for the composites are also symptomatic of photogenerated electron injection of from g-C_3N_4 to lower CB offset of ZnO NR. Considering photoexcited electron transfer is the only pathway for deactivation of excited g-C_3N_4, the rate constants of electron injection (k_{ei}) from g-C_3N_4 to ZnO NRs is calculated from equation (2) and listed in table 1:[50]

$$k_{ei} = \frac{1}{< \tau >_{composite}} - \frac{1}{< \tau >_{g-C_3N_4}} \qquad (2)$$

Table 6.3.2 Calculated values of rate constants of electron injection (k_{ei}) for all the composites

Materials and composites	<τ> (ns)	k_{ei} (s^{-1})
g-C_3N_4	14.4	————
g-C_3N_4–ZnO NR (0.25:1)	5.1	1.26×10^8
g-C_3N_4–ZnO NR (0.5:1)	5.3	1.18×10^8
g-C_3N_4–ZnO NR (1:1)	8.5	0.48×10^8
g-C_3N_4–ZnO NR (1.5:1)	8.3	0.5×10^8
g-C_3N_4–ZnO NR (2:1)	8.6	0.46×10^8

From table **6.3.2**, the k_{ei} values for the composites (0.25:1) and (0.5:1) are found to be (1.26×10^8) s^{-1} and (1.18×10^8) s^{-1}, which are significantly higher than the other composites. Faster charge injection dynamics in both the composites confirm an efficient charge transfer and optimum g-C_3N_4 to ZnO NR ratio. As the g-C_3N_4 to ZnO NR weight ratio increases from (1:1) to (2:1), amount of bare or unbound g-C_3N_4 sheets in the composites increases which are incapable of photogenerated charge transfer to the ZnO NRs. Consequently, number of excitons undergoing radiative decay are higher in the composites namely, (1:1), (1.5:1), and (2:1); which are reflected in slower charge injection dynamics from g-C_3N_4 to ZnO NR. Therefore, photogenerated charge transfer is believed to be facilitated by probable attraction forces between polar wurtzite ZnO NRs[40] and delocalized π-electrons as well as non-bonding electrons in the g-C_3N_4 sheets.

In addition, it is found that electronic interaction between g-C_3N_4 and ZnO NR is stronger in the composites than its counterpart ZnO NP. A comparative PL analyses for both the g-C_3N_4 composites of ZnO [weight ratio (0.5:1)] is performed as shown on figure **6.3.9**.

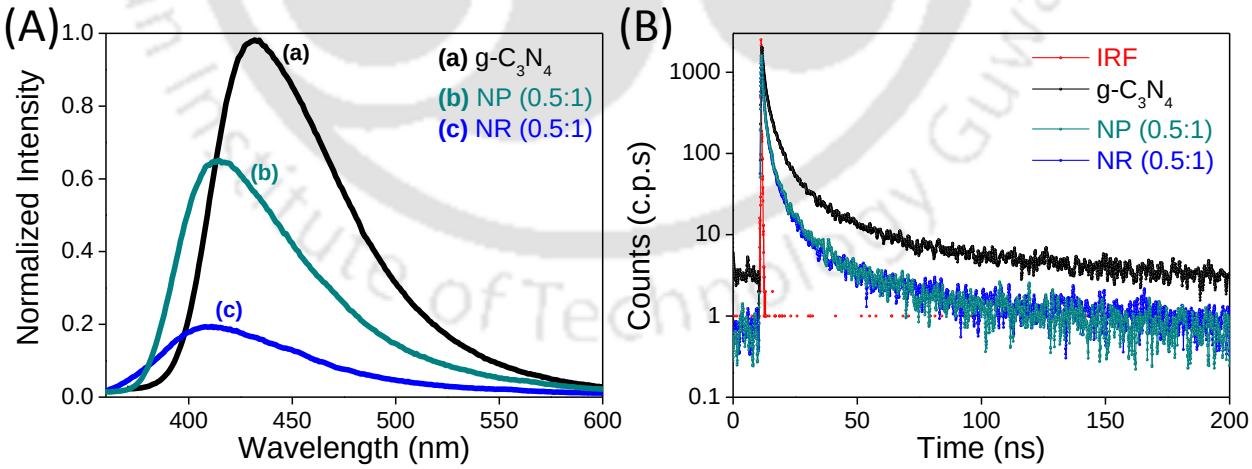

Figure 6.3.9 (A) Steady state photoluminescence (PL) spectra of (a) pure g-C_3N_4 and its composites of ZnO NP; (b) NP (0.5:1), and ZnO NR; (c) NR (0.5:1) respectively. (B) Corresponding dynamic PL spectra for the samples

Figure **6.3.9 (A)** shows steady state PL spectra for pure g-C_3N_4 (black line) and its composites of ZnO NP and ZnO NR with a weight ratio, (0.5:1); namely NP (0.5:1), [dark cyan

line] and NR (0.5:1), [blue line] respectively, recorded at an excitation wavelength of 350 nm. The intensity of characteristic PL emission peak at around 432 nm for g-C_3N_4 sheets is observed to be quenched more in case of the ZnO NR (0.5:1) composite [NR (0.5:1), trace (c)] as compared to the ZnO NP, [NP (0.5:1), trace (b)]; possibly due to better synergistic effects between ZnO NR and g-C_3N_4. Blue shift of the emission peak (~20 nm) is also observed for the g-C_3N_4 composite of ZnO NP, as we have seen in case of (g-C_3N_4–ZnO NR) composites.

Synergistic effects in the composites are further analyzed by dynamic PL spectroscopy technique. Figure **6.3.9 (B)** shows dynamic PL spectra for all the samples. Table **6.3.3** summarizes the values of fitting parameter (χ^2) and detailed spectroscopic results such as, exciton lifetimes (τ_1, τ_2, τ_3), pre-exponential factors (α_1, α_2, α_3), average exciton lifetimes ($<\tau>$) and calculated rate constants of electron injection (k_{ei}).

Table 6.3.3 Calculated values of parameters such as fitting parameter (χ^2), exciton lifetimes (τ_1, τ_2, τ_3), pre-exponential factors (α_1, α_2, α_3), average exciton lifetimes ($<\tau>$), the rate constants of electron injection (k_{ei}).

Sample	χ^2	τ_1 (ns)	τ_2 (ns)	τ_3 (ns)	α_1	α_2	α_3	$<\tau>$ (ns)	k_{ei} (s^{-1})
g-C_3N_4	1.055	0.831	3.600	19.094	36.50	41.01	22.49	14.41	----------
NR (0.5:1)	0.958	0.440	1.954	9.103	58.65	28.07	13.29	5.30	1.18×10^8
NP (0.5:1)	0.941	0.831	1.275	6.766	31.13	43.86	25.01	6.05	0.96×10^8

From table **6.3.3**, it is clear that the average life time ($<\tau>$) values are decreased substantially for both the composites namely, NR (0.5:1) and NP (0.5:1) as compared to g-C_3N_4, which confirms favorable photoexcited charge transfer from g-C_3N_4 sheets to ZnO. Faster and efficient charge transfer in the ZnO NR based composite than in ZnO NP composite is divulged trough the minimum ($<\tau>$) value estimated for ZnO NR composite. To authenticate our claim of faster charge migration from g-C_3N_4 sheets to ZnO NR, we have calculated the rate constants of electron injection (k_{ei}) for both the composites considering photoexcited electron transfer is the only pathway for deactivation of excited g-C_3N_4 sheets. The k_{ei} value for the ZnO NR based composite is found to be higher (~1.18×10^8) s^{-1} than the ZnO NP composite (~0.96×10^8) s^{-1} which confirms faster photogenerated charge transfer from g-C_3N_4 sheets to ZnO NR. From all aforementioned discussions it is implicit that excited state electronic interaction between g-C_3N_4 sheets and ZnO NRs is stronger compared to ZnO NPs

6.3.5 FOURIER TRANSFORM-INFRARED (FT-IR) ANALYSES

For further confirmation of electronic interaction between ZnO NRs and g-C_3N_4 sheets we have performed Fourier Transform Infrared (FT-IR) analyses for the composites. Figure **6.3.10** shows FT-IR spectra for (a) pristine g-C_3N_4 (black line); (g-C_3N_4–ZnO NR) composite weight ratios namely, (b) 0.25:1 (magenta line), (c) 0.5:1 (olive line) and (d) 1:1 (navy blue line) as well as for (e) pristine ZnO nanorods (NR) (red line).

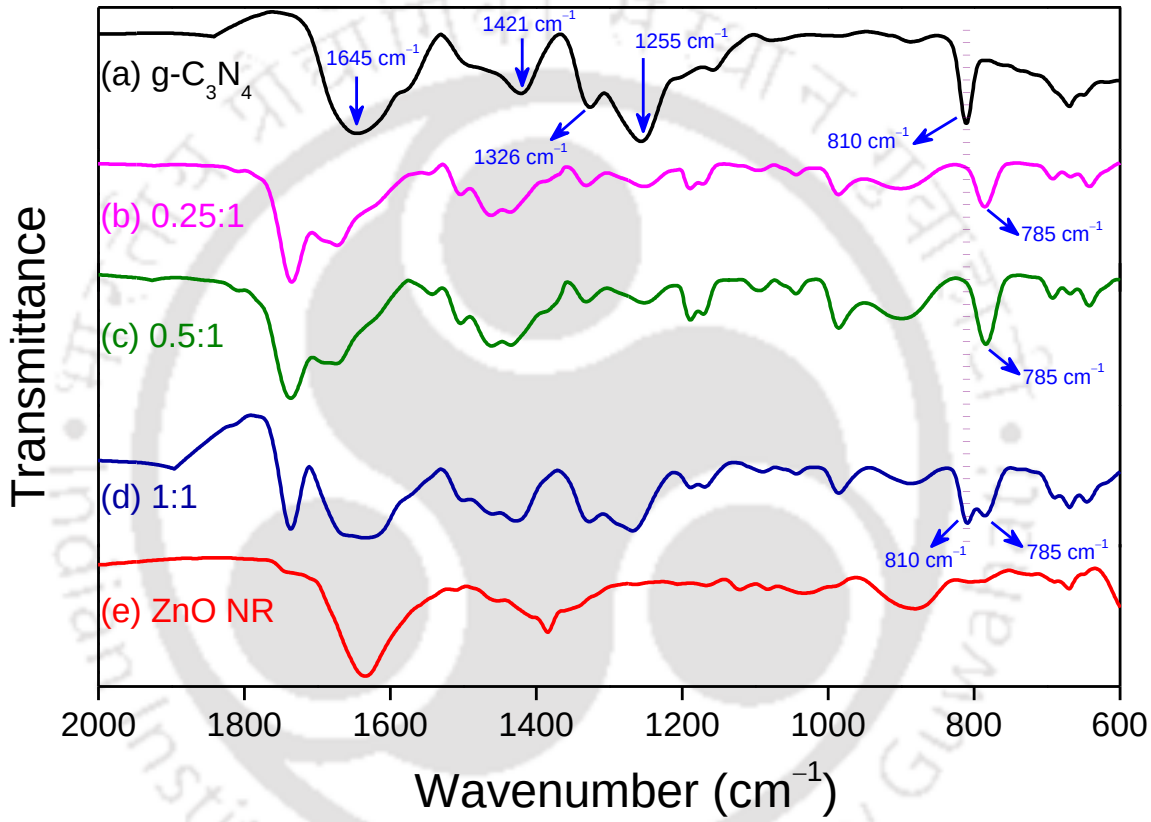

Figure 6.3.10 FT-IR spectra of (a) pristine g-C_3N_4, (g-C_3N_4–ZnO NR) composite weight ratios namely, (b) 0.25:1, (c) 0.5:1 (d) 1:1 and for (e) pristine ZnO nanorods (NR).

In the FT-IR spectrum of pristine g-C_3N_4, trace (a), dominating peaks centered at 1255 cm^{-1}, 1326 cm^{-1} and 1421 cm^{-1} are corresponding to C–N stretching vibration modes while the broad peak centered at ~1645 cm^{-1} is attributed to C═N stretching vibrations.[51] In addition, the peak observed at 810 cm^{-1} is due to the characteristic out-of-plane bending modes of *s*-triazine repeating unis of g-C_3N_4 sheets.[52] All the characteristic peaks of g-C_3N_4 and ZnO NR can be seen clearly in the spectra of (g-C_3N_4–ZnO NR) hybrid composites. It is observed that, the peaks of g-C_3N_4 are suppressed and broadened in the (g-C_3N_4–ZnO NR) hybrid composites. Moreover, the peak of *s*-

triazine unit is shifted towards the lower wavenumber for the composite ratios (0.25:1) and (0.5:1) which is indicative of an electronic interaction between ZnO and the s-triazine units.[36] This electronic interaction may be of great significance to transfer charge carriers and induce a synergetic effect between g-C_3N_4 sheets and ZnO NRs in the hybrid material. It should be noted that, in case of composite ratio (1:1), the characteristic peak of *s*-triazine unit is appeared as a doublet and the peaks for C–N as well as C═N are observed to be prominent than the other two composite ratios namely, (0.5:1) and (0.25:1). This observation suggests that a significant number of g-C_3N_4 sheets are remain unbound to the ZnO NRs in the composite ratio (1:1) due to high content of g-C_3N_4. Hence, FT-IR analyses demonstrates that an electronic conjugation is built between g-C_3N_4 and ZnO NR in the hybrid composite which in accordance with the inferences carried out from dynamic PL studies.

6.3.6 DIFFUSE REFLECTANCE UV–VISIBLE ABSORPTION SPECTRA OF THE PHOTOANODES

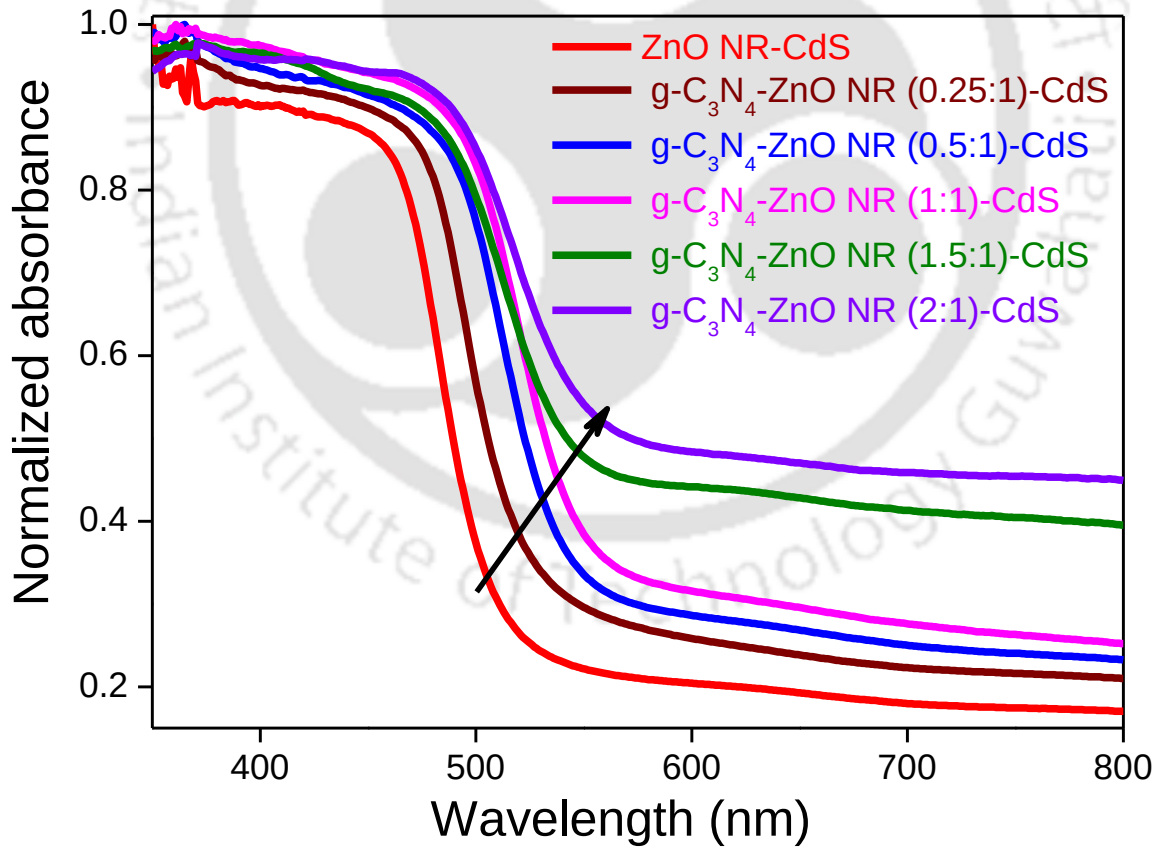

Figure 6.3.11 Diffuse reflectance UV-vis absorption spectra for all photoanodes fabricated with (g-C_3N_4–ZnO NR) composites and sensitized with CdS QDs.

Figure **6.3.11** shows normalized UV-vis absorption profiles for all the CdS QD sensitized photoanodes fabricated with pristine ZnO NR (red line) and (g-C_3N_4–ZnO NR) composites namely; 0.25:1 (wine red line), 0.5:1 (blue line), 1:1 (magenta line), 1.5:1 (olive line) and 2:1 (violet line). The absorption profiles are recorded against blank FTO as a reference and the scan range is 200–800 nm for all the samples. Absorption range for all the photoanodes are observed to be in the visible region (380–520 nm), which infer to a successful anchoring of CdS QDs onto the pristine ZnO NR as well as (g-C_3N_4-ZnO NR) composite scaffolds. Moreover, with increase in g-C_3N_4 to ZnO NR weight ratio in the photoanodes, we have noted a gradual red shift of absorption onsets (indicated with a black arrow) in the absorption profiles. The observed red shift is due to subsequent growth of CdS QDs in photoanodes with increased deposition cycles.[51] Note that we have carried out five SILAR cycles for sensitization of all the photoanodes with CdS QDs in order to have a match with the fabrication process. A steady increase in absorbance for the photoanodes with composite ratios, (0.25:1), (0.5:1), and (1:1) as compared to the pristine ZnO NR photoanode is attributed to the increased deposition amount of CdS QDs in presence of g-C_3N_4 sheets. However, absorbance of the photoanode with composite ratio (1.5:1) is comparable to the photoanode (0.5:1), but less than the photoanode (1:1), possibly due to the inhibited deposition caused by higher content of sheet-like g-C_3N_4 in the (1.5:1) photoanode. Presence of excess g-C_3N_4 sheets in the photoanode offer more adsorption sites for loading of CdS QDs onto their surfaces and with repeated deposition cycles the QDs tend to form bigger agglomerates which is not in case of other aforementioned photoanodes. These bigger CdS agglomerates might have clogged the pores in the photoanodic film to inhibit further penetration of precursor ions (i.e., Cd^{2+} and S^{2-}) which impede smooth and uniform deposition of CdS QDs. This conclusion is in accordance with comparable absorbance observed for the photoanodes (2:1) and (1:1). Hence, effective surface area for CdS QD deposition in the photoanodes is increased only upto an optimum weight ratio of (1:1); i.e., g-C_3N_4 relative to ZnO NRs.

6.3.7 PHOTOVOLTAIC CHARACTERISTICS OF THE SOLAR CELLS

To understand the effects of g-C_3N_4 in light harvesting ability of as prepared (g-C_3N_4–ZnO NR) composites, photovoltaic devices sensitized with CdS QDs are fabricated and systematically analyzed the performance parameters. Figure **6.3.12 (A)** demonstrates current density–voltage (*J*–

V) curves for all the CdS QD sensitized (g-C_3N_4–ZnO NR) composite and pristine ZnO NR devices.

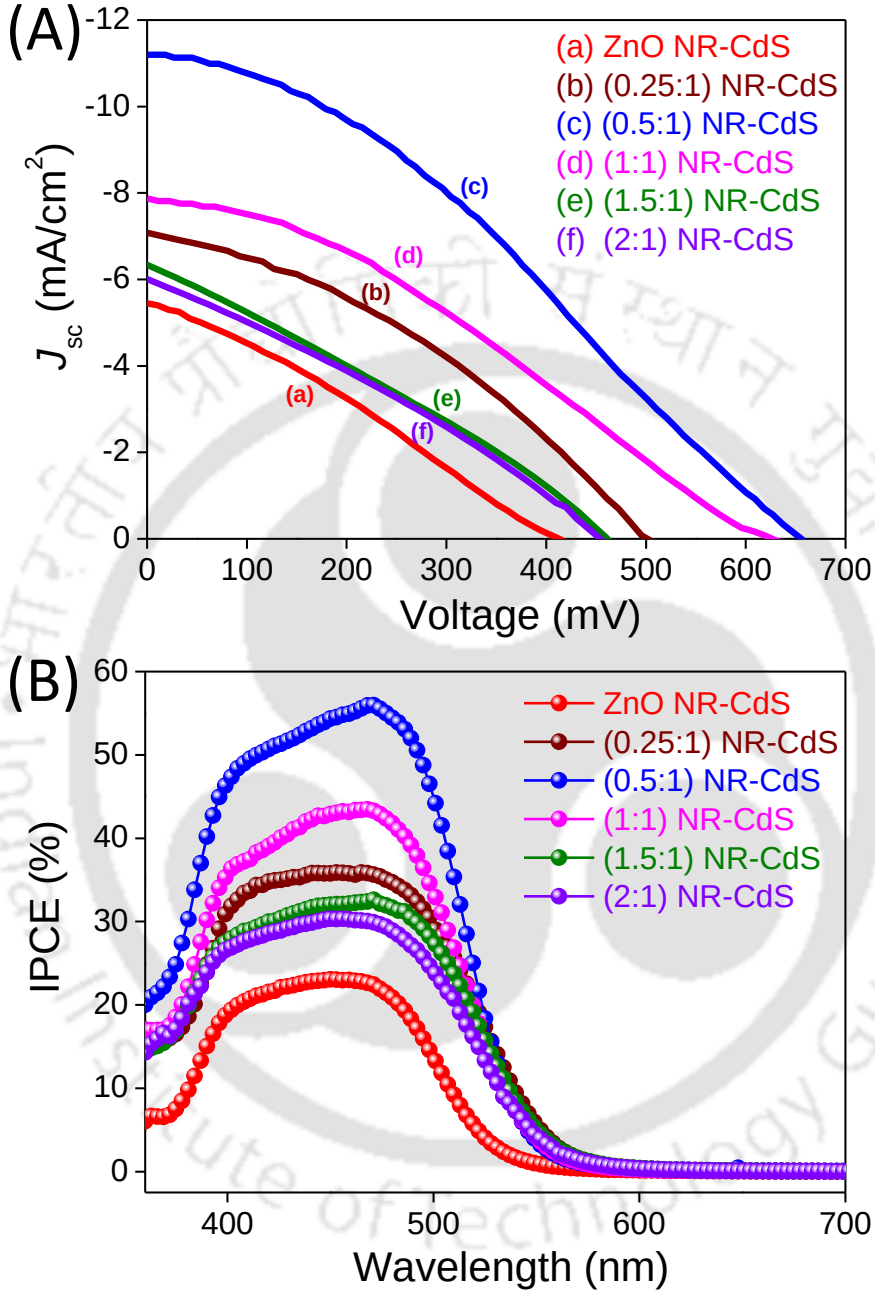

Figure 6.3.12 (A) Current density–Voltage (*J*–*V*) curves for the photovoltaic devices with pristine ZnO NR [device (a)] and (g-C_3N_4–ZnO NR) composites namely: (b) (0.25:1) NR-CdS, (c) (0.5:1) NR-CdS, (d) (1:1) NR-CdS, (e) (1.5:1) NR-CdS, and (f) (2:1) NR-CdS. **(B)** Corresponding IPCE plots for the respective devices employing S^{2-}/S_n^{2-} as the redox couple.

All measured and calculated values of the performance parameters for all the photovoltaic devices such as, short circuit current density (J_{sc}), open circuit voltage (V_{oc}), fill factor (*FF*) and the overall power conversion efficiency (PCE, η) are summarized in table **6.3.4**.

Table 6.3.4 Values of Short-circuit current density (J_{sc}), open-circuit voltage (V_{oc}), fill factor (*FF*), and power conversion efficiency (η) for the fabricated solar cells incorporating different photoanodes.

Devices	J_{sc} (mAcm^{-2})	V_{oc} (mV)	FF (%)	PCE (η %)
(a) ZnO NR-CdS	5.4 (± 0.2)	410 (± 3)	29 (± 2)	0.65
(b) g-C_3N_4–ZnO NR (0.25:1)-CdS	7.1 (± 0.3)	500 (± 3)	36 (± 1)	1.27
(c) g-C_3N_4–ZnO NR (0.5:1)-CdS	11.1 (± 0.2)	650 (± 1)	34 (± 2)	2.43
(d) g-C_3N_4–ZnO NR (1:1)-CdS	7.8 (± 0.2)	625 (± 4)	31 (± 1)	1.51
(e) g-C_3N_4–ZnO NR (1.5:1)-CdS	6.3 (± 0.1)	461 (± 1)	29 (± 2)	0.84
(f) g-C_3N_4–ZnO NR (2:1)-CdS	6.0 (± 0.1)	452 (± 2)	30 (±1)	0.81

From table **6.3.4**, it is clear that PCE values for all the (g-C_3N_4–ZnO NR) composite devices are superior to that of the pristine ZnO NR [device (a), η ≈0.65 %], which confirms the beneficial role of g-C_3N_4 sheets in enhancing the light harvesting ability of the devices. The photovoltaic parameters, i.e., J_{sc}, V_{oc} and *FF* values are found to be ~5.4 mAcm^{-2}, ~410 mV and ~29 % respectively for the device (a). Upon introduction of g-C_3N_4, as we have seen in case of device (b) with (0.25:1) composite ratio the performance parameters are increased to J_{sc} ≈7.1 mAcm^{-2}, V_{oc} ≈500 mV, and FF ≈36 %. Increase in J_{sc} is might be due to the higher loading of sensitizer particles (CdS QDs) in the (0.25:1) photoanode as compared to the pristine ZnO NR photoanode. Improved V_{oc} and *FF* are symptomatic of minimum recombination of photogenerated charge and faster regeneration kinetics of oxidized CdS QDs respectively.[52] Faster regeneration kinetics of the sensitizer particles imply a better functioning of redox couple facilitated by maximum pores availability in the photoanodic film. Minimum content of g-C_3N_4 sheets in the photoanodic film of device (c) is the most probable reason for maximum available pores after sensitization. As the g-C_3N_4 content increases in the photoanodes, CdS QDs tend to agglomerate and clog the available pores in the mesoscopic films during sensitization process as we have discussed in the diffuse reflectance UV-vis analyses. Deprived estimated values of FF for the devices with higher content of g-C_3N_4, i.e., ~34 % [for device (c)], ~31 % [for device (d)], 29 % [for device (e)] and ~30 [for device (f)] are also in accordance with our explanation. Nevertheless, optimum PCE (η ≈2.43 %) is exhibited by the device (c) with composite ratio (0.5:1), which is due to higher J_{sc} ≈11.1 mAcm^{-2}, and V_{oc} ≈650 mV recorded for the device. Enhanced J_{sc} value is in agreement with the higher loading of CdS QDs in the photoanode as well as better electronic

interaction between g-C_3N_4 sheets and ZnO NR in the (0.5:1) composite which might have increased the flux of photoinduced electron injection. However, further increase in CdS QD loading in the photoanodes of devices (d), (e), and (f), is not observed to be beneficial in the improvement of photovoltaic parameters. Current density values of device (d) with a composition of (1:1) of g-C_3N_4 to ZnO, exhibited low values ~7.8 $mAcm^{-2}$ [for (d)] and the trend continued for the devices (e) J_{sc} ≈6.3 $mAcm^{-2}$ and (f) J_{sc} ≈6.0 $mAcm^{-2}$, which infers higher recombination rate of photoinduced electrons due to agglomeration of sensitizer particles, i.e., CdS in the photoanodes. Moreover, decrease in V_{oc} values observed for the respective devices as ~625 mV [for (d)], ~461 mV [for (e)], and ~452 mV [for (f)] is also supporting our claim of higher recombination rate in the devices. It is noteworthy that V_{oc} of the highest performed device [i.e., device (c) with (0.5:1) composite ratio] is increased significantly upto ~650 mV which is about 60 % improvement over the pristine ZnO NR device (V_{oc} ≈410 mV). This is a clear indication of inhibited photoinduced electron interception to the redox couple (S^{2-}/S_n^{2-}) in presence of g-C_3N_4 sheets.[53] To probe minimum reverse tunneling probability of photoinduced electrons in the devices with (g-C_3N_4–ZnO NR) composites we have performed electrochemical impedance spectroscopic analyses and discussed in later. In the present work, low FF values observed for the devices may be due to the slower intrinsic hole recovery rate of sulfide/polysulfide (S^{2-}/S_n^{2-}) redox couple and poor diffusion of electrolyte in the photoanode.[54, 55] This inference is also in accordance with the increase in FF values observed for the devices having porous g-C_3N_4 sheets, i.e., device (b) with g-C_3N_4 to ZnO weight ratio (0.25:1) [FF ~36%] and device (c) with weight ratio (0.5:1) [FF ~34%] in contrast to the pristine ZnO NR device [FF ~29%]. This observation is primarily due to the porous g-C_3N_4 assisted acceleration of electrolyte diffusion in the photoanodes. However, the choice of polysulfide electrolyte is justified, as it is reported to be more suitable for stabilization of the CdS QDs.[56]

Figure **6.3.12 (B)** illustrates corresponding incident photon-to-current conversion efficiency (IPCE) plots for all the as fabricated photovoltaic devices. Better light harvesting ability of the device with (0.5:1) composite ratio [i.e., device (c)], is attributed to the optimum loading of g-C_3N_4 sheets and CdS QDs, which resulted in reduced recombination rate of photoinduced electrons. In figure (B) the composition of (0.5:1) exhibits IPCE of ~55 % in the wavelength range of 380 nm to 520 nm. The IPCE plots are observed to follow the similar increasing trend of J_{sc} values as in case of (*J*–*V*) curves for the devices [i.e., (a)< (f)< (e)< (b)< (d)< (c)]. Minimum IPCE

(~22%) for device (a) with pristine ZnO NR is pragmatic of higher recombination rate in the device apart from lower CdS QD loading as compared to the (g-C_3N_4–ZnO NR) composite devices. Hence, photovoltaic boosting ability of g-C_3N_4 is confirmed from enhanced light harvesting by the (g-C_3N_4–ZnO NR) composite devices in contrast to the pristine ZnO NR device.

To monitor electron transport and charge recombination kinetics in the photovoltaic devices we have performed electrochemical impedance spectroscopy (EIS) analyses as shown in **figure 6.3.13**.

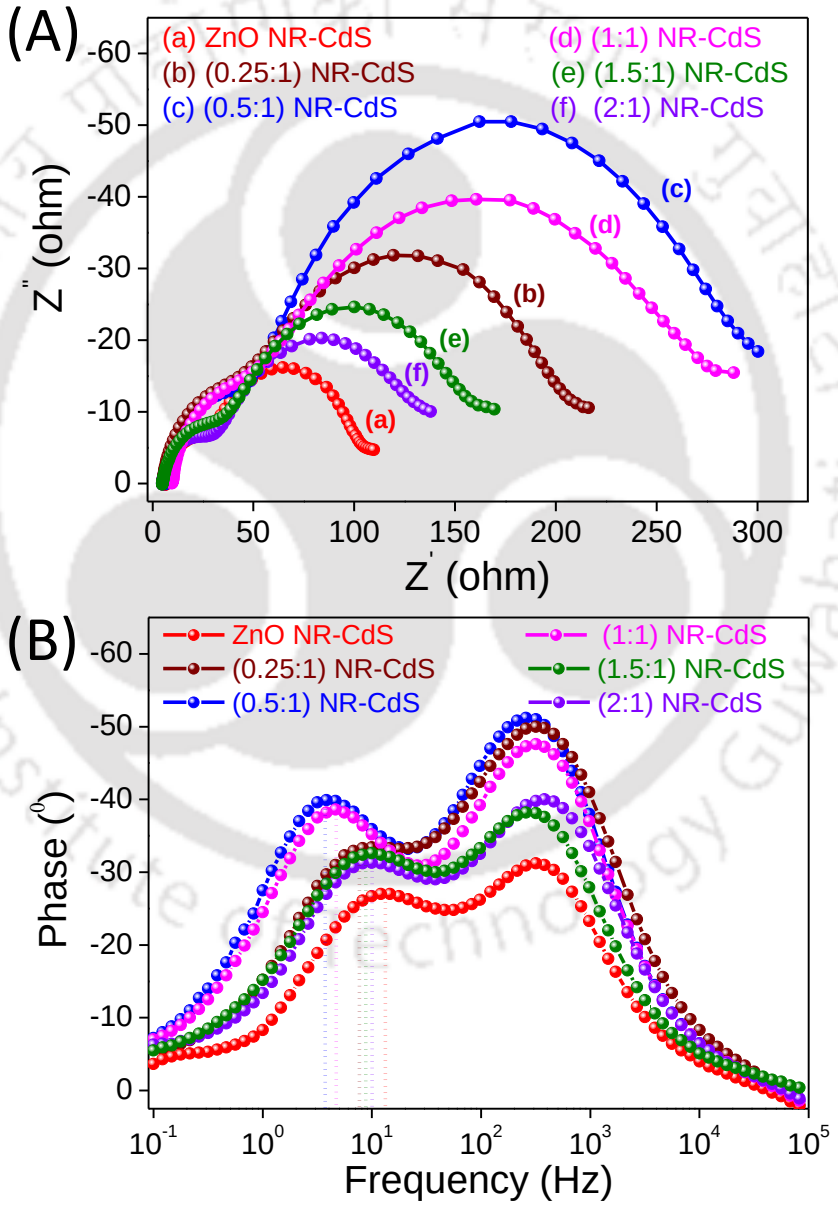

Figure 6.3.13 (A) Nyquist plots for all the photovoltaic devices with pristine ZnO NR and (g-C_3N_4–ZnO NR) composites in dark at open-circuit voltage and in a frequency range from 0.1 Hz to 100 kHz. **(B)** Bode phase plots for all the respective devices.

Figure (A) shows the Nyquist plots recorded under dark condition in a frequency range from 0.1 Hz to 100 kHz at the applied bias equivalent to the open-circuit voltages. All the Nyquist plots are comprises of two semicircles, one in the medium frequency region while another one in the higher frequency region. The semicircle in the medium frequency region encompasses the charge-transfer process at the working electrode/electrolyte interface, while the smaller semicircle in the higher frequency region is attributed to the counter electrode/electrolyte interfacial redox reactions.[57] The diameter of the right semicircle (R_k) primarily contributed from electron recombination resistance and is partly due to the transport resistance.[58] From figure (A), we have seen that R_k is significantly higher in case of best performed device (c) [i.e., with (0.5:1) composite ratio (blue line)] in contrast to the pristine ZnO NR device (a). This observation confirms our claim of retarded backward redox reactions or inhibited recombination at the ZnO NR/electrolyte or ZnO NR/CdS/electrolyte interfaces in the device (c) with optimum loading of g-C_3N_4. The increasing trend of R_k for the devices is: (a) < (f) < (e) < (b) < (d) < (c) which is the similar order observed for the increment of V_{oc} values. Therefore it can be concluded that enhanced V_{oc} values in the devices with (g-C_3N_4–ZnO NR) composites are mainly due to the minimized reverse tunneling probability of photoinduced electrons in presence of g-C_3N_4 sheets.

Corresponding Bode phase plots for all the fabricated devices are presented in figure **6.3.13 (B)**. The characteristic peak frequencies in the medium frequency region (f_{max}), calculated photoinduced electron lifetimes (τ_e) in the photoanodes are listed in table **6.3.5**. We have estimated the values of τ_e in the photoanodes using the equation (3):[59]

$$\tau_e = \frac{1}{2\pi f_{max}} \qquad (3)$$

Table 6.3.5 Characteristic peak frequencies in the medium frequency region (f_{max}) and calculated values of photoinduced electron lifetimes (τ_e) in all the devices.

Devices	f_{max} (Hz)	τ_e (ms)
(a) ZnO NR-CdS	13.3	12
(b) g-C_3N_4–ZnO NR (0.25:1)-CdS	7.6	21
(c) g-C_3N_4–ZnO NR (0.5:1)-CdS	3.7	43
(d) g-C_3N_4–ZnO NR (1:1)-CdS	4.7	34
(e) g-C_3N_4–ZnO NR (1.5:1)-CdS	8.9	18
(f) g-C_3N_4–ZnO NR (2:1)-CdS	10.1	16

Higher (τ_e) values furnished by the devices with (g-C_3N_4–ZnO NR) composites are authenticating inhibited electron interception to the redox shuttle (S^{2-}/S_n^{2-}) at the working electrode/electrolyte

interfaces, i.e., ZnO/electrolyte and ZnO/CdS/electrolyte interfaces. Appropriate band edge alignments of g-C_3N_4 to that of CdS QDs and ZnO NRs for favorable charge transfer process is the most probable reason for minimum recombination rate in the (g-C_3N_4–ZnO NR) composite devices. Energy level alignments of CdS QD sensitized (g-C_3N_4–ZnO NR) composite devices showing charge transfer pathways are depicted in the scheme **6.3.3**.

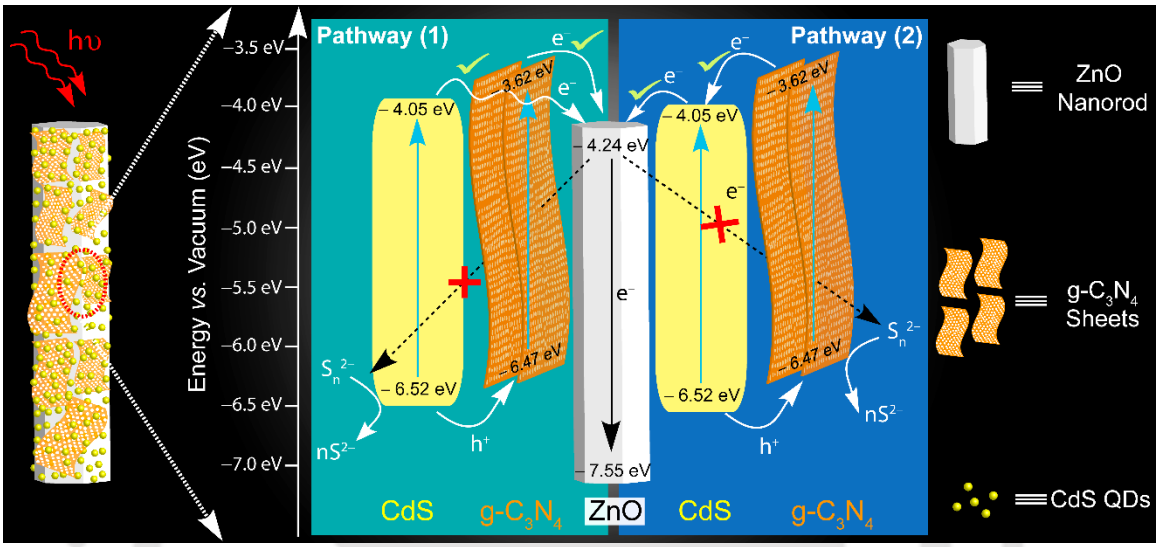

Scheme 6.3.3 Energy level alignments of CdS QD sensitized (g-C_3N_4–ZnO NR) composite devices showing charge transfer pathways and inhibited electron interception at the ZnO NR/electrolyte as well as ZnO NR/CdS/electrolyte interfaces.

From scheme **6.3.3**, we have seen that CB position of g-C_3N_4 (–3.62 eV) is more negative to that of CdS (–4.05 eV) and ZnO NR (–4.24 eV). Hence, back transfer of photoinduced electrons from ZnO NR to the CdS QDs and g-C_3N_4 is an energetically unlikely process. Moreover, due to the higher band gap of g-C_3N_4 sheets as compared to CdS QDs, they are acting as a barrier for electron interception at the ZnO/electrolyte and ZnO/CdS/electrolyte interfaces which is not in the case of pristine ZnO NR based device (a). We have shown the impeded electron recombination pathways with red crossed black dotted lines in scheme **6.3.3**. It is noteworthy that, sensitization of CdS QDs in the photoanodes leads to the probability of deposition on both the scaffolds, i.e., g-C_3N_4 sheets and ZnO NRs; therefore, two pathways of charge transfer processes are possible in the devices. The charge transfer **pathway (1)** represents the condition when adsorption of CdS QDs primarily on the g-C_3N_4 sheets while **pathway (2)** signifies preferential adsorption of CdS QDs on the exposed surface of ZnO NRs. As the g-C_3N_4 to ZnO weight ratio increases in the composite, the CdS QDs are adsorbed mainly on the g-C_3N_4 sheets due to the lack of exposed ZnO

surface. Consequently, probability of charge transfer according to pathway (1) is increased in this situation wherein electron injection from CdS to ZnO is hindered by the g-C_3N_4 sheets resulting a decrease in photoinduced electron density in the photoanode. Lower values of (τ_e) as well as PCE (η) for the (g-C_3N_4–ZnO NR) composites with high content of g-C_3N_4, i.e., [(1:1), device (d)], [(1.5:1), device (e)] and [(2:1), device (f)] are reflecting impeded photoinduced electron injection from CdS QDs to ZnO. However, tunneling possibility of far less photoinduced electrons from CdS QDs to ZnO across the g-C_3N_4 barrier cannot be nullified; as the CB level of CdS QDs is energetically well above the CB offset of ZnO. It is believed that, at optimum g-C_3N_4 to ZnO weight ratio, i.e., [(0.5:1), device (c)], the charge transfer pathway (2) surpasses its counterpart pathway (1) and hence increases the photoinduced electron density in the photoanode. Maximum electron lifetime (~43 ms) observed for the device (c) is indicative of increased photoinduced electron density which eventually leads to higher values of $V_{oc} \approx 650$ mV, $J_{sc} \approx 11.1$ mAcm^{-2} and $\eta \approx 2.43$ %.

6.3.8 MORPHOLOGY DEPENDENT PHOTOVOLTAIC CHARACTERISTICS

Morphology dependent photovoltaic properties of ZnO are evaluated by performing a comparative photovoltaic study between highest performed (g-C_3N_4–ZnO NR) composite device and similar device fabricated with g-C_3N_4 composite of ZnO NP. For better clarity, we have also compared the performance parameters of pristine ZnO NR and ZnO NP devices. Figure **6.3.14 (A)** illustrates characteristic (*J*–*V*) curves for optimized (g-C_3N_4–ZnO NR) composite device [device (a)], similar device fabricated for (g-C_3N_4–ZnO NP) composite [device (b)], along with pristine ZnO NR [device (c)] and ZnO NP [device (d)]. Figure **6.3.14 (B)** shows IPCE plots for the respective devices. From figure (A) and (B), we have observed better light harvesting ability of ZnO NR based devices over the ZnO NP. Table **6.3.6** summarizes all the recorded and calculated performance parameters for the compared devices in figure **6.3.14**.

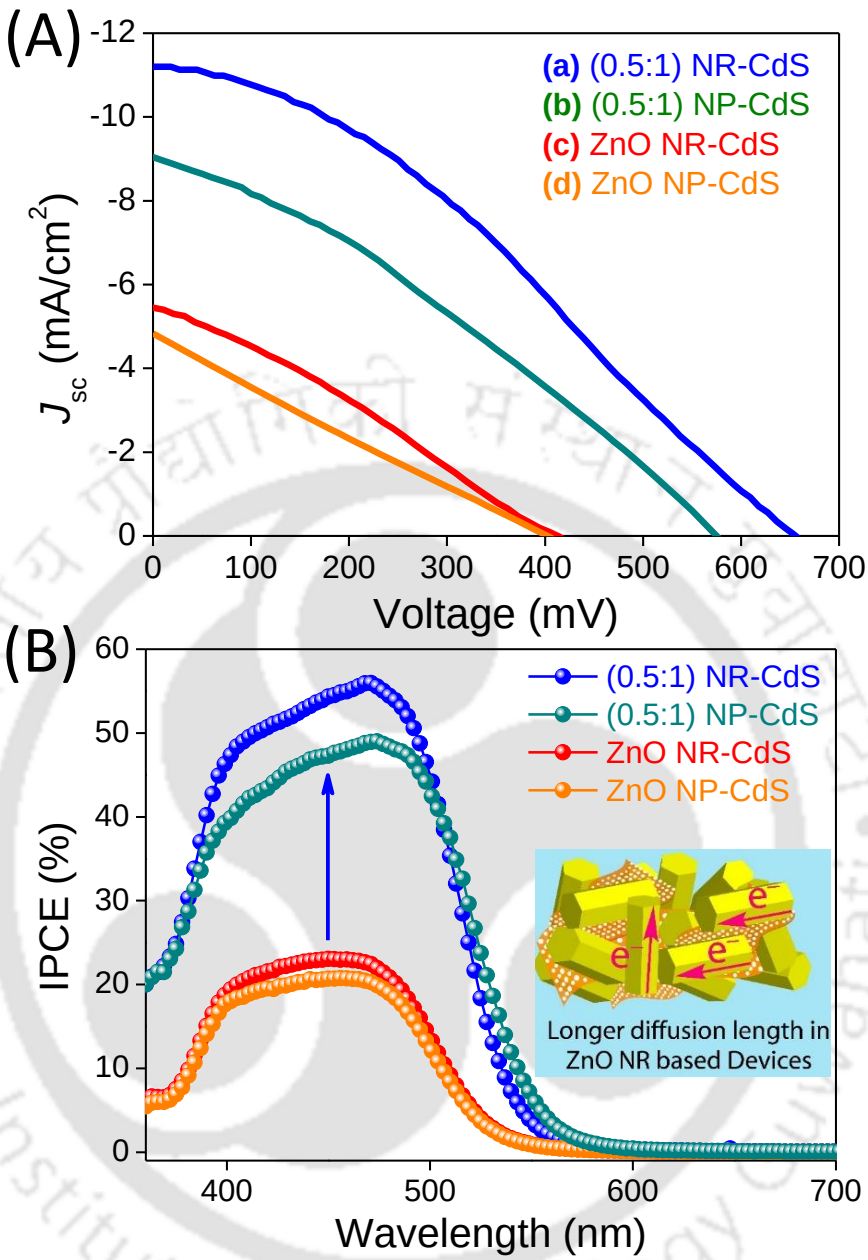

Fig. 6.3.14 (A) Current density–Voltage (*J–V*) curves for the CdS QD sensitized photovoltaic devices with g-C_3N_4 composites; (a) (0.5:1) NR-CdS [blue line], (b) (0.5:1) NP-CdS [dark cyan line], and pristine (c) ZnO NR [red line], (d) ZnO NP [orange line] **(B)** IPCE plots for the respective devices employing S^{2-}/S_n^{2-} as the redox couple.

Table 6.3.6 Short-circuit current density (J_{sc}), open-circuit voltage (V_{oc}), fill factor (FF), and power conversion efficiency (η) for the fabricated solar cells incorporating different photoanodes.

Devices	J_{sc} (mAcm^{-2})	V_{oc} (mV)	FF (%)	PCE (η %)
(a) g-C_3N_4(0.5:1) NR-CdS	11.1 (± 0.2)	650 (± 1)	34 (± 2)	2.43
(b) g-C_3N_4(0.5:1) NP-CdS	9.02 (± 0.1)	575 (± 3)	33 (± 1)	1.85
(c) ZnO NR-CdS	5.4 (± 0.2)	410 (± 3)	29 (± 2)	0.65
(c) ZnO NP-CdS	4.8 (± 0.3)	400 (± 2)	22 (± 3)	0.41

From table **6.3.6**, we have seen that J_{sc} (~9.02 mA cm^{-2}) and V_{oc} (~575 mV) values for the device (b) with (g-C_3N_4–ZnO NP) composite are lower than the optimized device (a); (J_{sc} ≈11.1 mA cm^{-2} and V_{oc} ≈650 mV). Interestingly, similar inferior performance is also observed in case of pristine ZnO NP based device (J_{sc} ≈4.83 mA cm^{-2} and V_{oc} ≈400 mV) as compared to the pristine ZnO NR device (J_{sc} ≈5.44 mA cm^{-2} and V_{oc} ≈410 mV). Higher J_{sc} values recorded for ZnO NR based devices are may be due stronger synergistic effects between g-C_3N_4 and ZnO NR, minimum population of grain boundary induced trap sites and longer diffusion length of photoinduced electrons as depicted in the inset to figure **6.3.14 (B)**. Minimum distribution of grain boundaries is expected in ZnO NR based photoanodes due to the larger size of as synthesized single crystalline ZnO NRs (~500 nm) than the ZnO NP [~70 nm]. It is well known that grain boundaries minimize the diffusion length of photoinduced electrons in QDSSCs and facilitate recombination processes. To compare sensitizer particle loading in the photoanodes, we have performed diffuse reflectance UV-vis analysis for all the CdS QD sensitized ZnO NP and ZnO NR based photoanodes as shown in figure **6.3.15**.

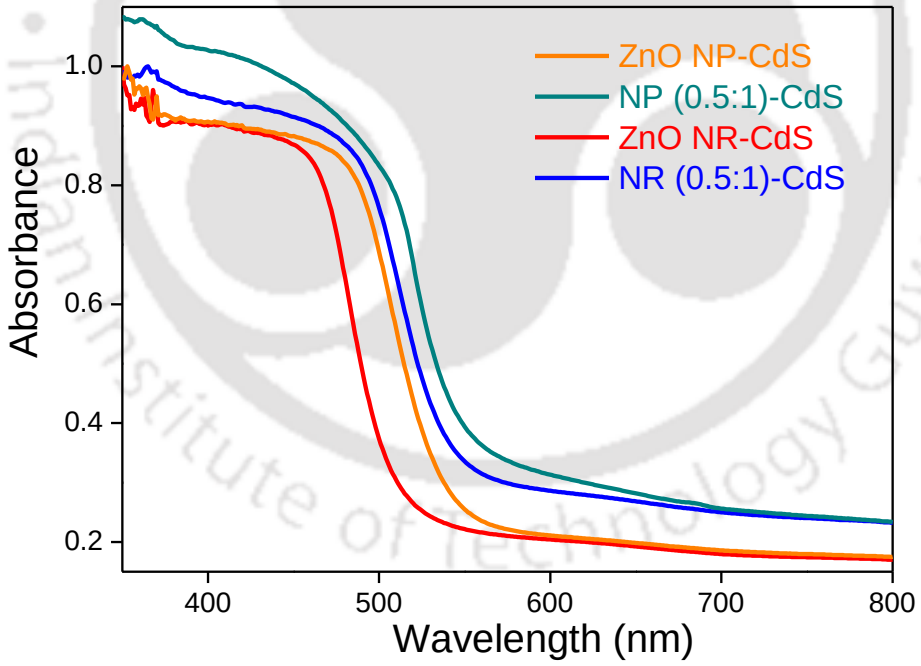

Figure 6.3.15. Diffuse reflectance UV-vis spectra of CdS sensitized ZnO NP and ZnO NR based photoanodes.

From figure **6.3.15**, it is clear that, quantitatively CdS QDs are loaded higher in ZnO NP based photoanodes than in the ZnO NR based photoanodes. This is due to higher specific surface area provided by the ZnO NP based photoanodic films than the ZnO NR based films as evident from

the N_2 adsorption-desorption isotherms recorded for the materials. Figure **6.3.16 (A)** depicts N_2 adsorption and desorption isotherms for pristine g-C_3N_4 [black line], ZnO NP [orange line], ZnO NR [red line], and for the composites namely NP (0.5:1) [dark cyan line], and NR (0.5:1) (Blue line). Figure **(B)** shows corresponding Barrett–Joyner–Halenda (BJH) pore size distribution plots.

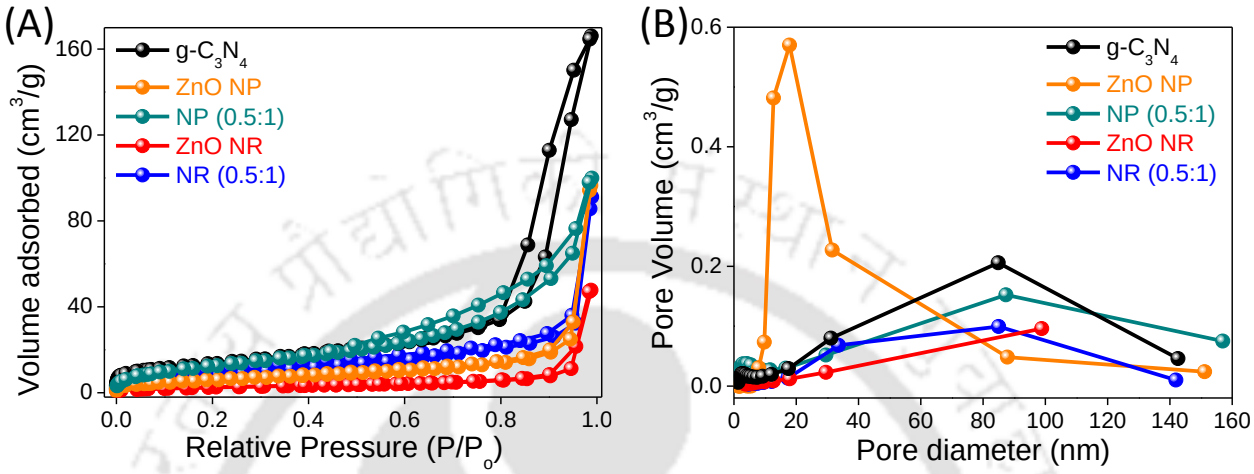

Figure 6.3.16. (A) Nitrogen adsorption–desorption isotherms and **(B)** Barrett–Joyner–Halenda (BJH) pore size distribution plots for as synthesized pristine g-C_3N_4 (Black line), ZnO NP (Orange line), ZnO NR (Red line) and composites namely, NP(0.5:1) [dark cyan line], and NR(0.5:1) (Blue line)

Type IV isotherms with H3 hysteresis loops are observed for as synthesized g-C_3N_4, ZnO NPs and also for both the composites which confirm mesoporous characteristic of the materials. The observed BET surface area values for all the as-synthesized materials are: 78 m^2g^{-1} for g-C_3N_4, 36 m^2g^{-1} for ZnO NP, 48 m^2g^{-1} for composite NP (0.5:1), 16 m^2g^{-1} for ZnO NR, and 30 m^2g^{-1} for composite NR (0.5:1). Hence, the BET surface area for ZnO NP and its g-C_3N_4 composite [i.e., NP (0.5:1)] are found to be higher than their counterparts; ZnO NR and NR (0.5:1) respectively. This observation is in accordance with the diffuse reflectance UV-vis analyses for CdS QD sensitized photoanodes; wherein, a higher loading of CdS QDs is noted in the ZnO NP based photoanodes. Therefore, the flux of electron injection by the CdS QDs is more in case of ZnO NP based devices. Despite, lower values of J_{sc}, V_{oc}, as well as IPCE observed for ZnO NP based devices is supporting our claim of maximum recombination in the respective devices. From table 6.3.6, it is noteworthy that the FF values for ZnO NP based devices namely device (b) and (d) are lower than the ZnO NR based devices [i.e., (a) and (c)]. This observation is suggesting a slower regeneration kinetics of CdS QDs in the devices (b) and (d). Higher loading of CdS QDs in the ZnO NP photoanodes might have clogged the pores and obstructed the diffusion of electrolyte causing an inefficient regeneration of sensitizer particles.

Recombination processes and charge transfer kinetics in the ZnO NP based devices are further monitored in EIS analyses. Figure **6.3.17 (A)** and **(B)** shows the Nyquist and Bode phase plots for the devices namely: (a) optimized (g-C_3N_4–ZnO NR) composite device, (b) similar device fabricated with (g-C_3N_4–ZnO NP) composite, pristine (c) ZnO NR and (d) ZnO NP devices.

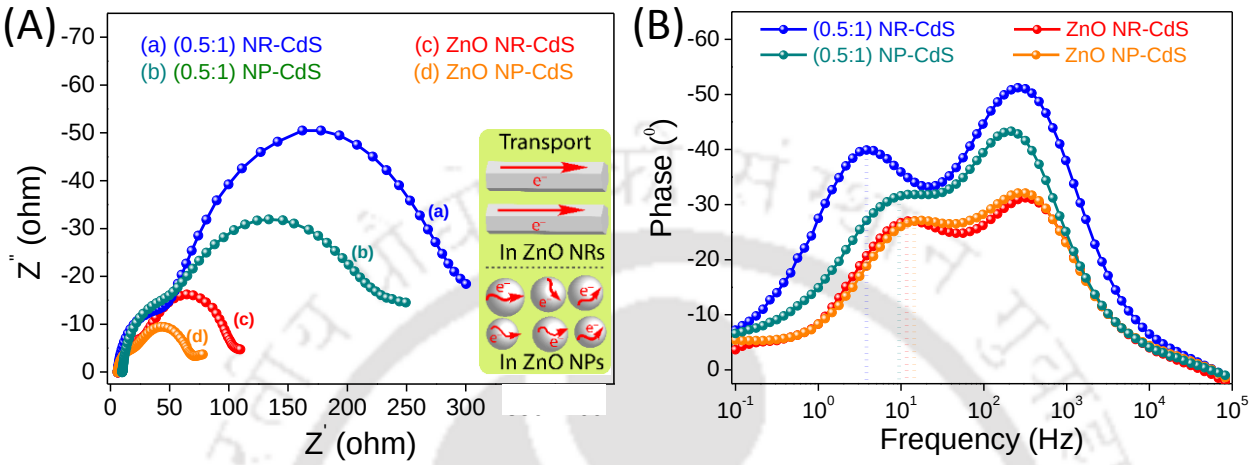

Fig. 6.3.17 (A) Nyquist plots for the photovoltaic devices with g-C_3N_4 composites; (a) (0.5:1) NR-CdS [blue line], (b) (0.5:1) NP-CdS [dark cyan line], and pristine (c) ZnO NR [red line], (d) ZnO NP [orange line] in dark at open-circuit voltage and in a frequency range from 0.1 Hz to 100 kHz. **(B)** Bode phase plots for all the respective devices.

From figure (A), we have observed smaller semicircles with lesser R_k in the medium frequency region for the ZnO NP based devices (b) and (d) in contrast to ZnO NR devices (a) and (c). Higher electron interception to the redox shuttle (i.e., S^{2-}/S_n^{2-}) in case of the ZnO NP based devices is confirmed from this observation as we have discussed in the performance parameter analyses part. Further, our claim is validated by the larger f_{max} values exhibited by the devices (b) [9.5 Hz] and (d) [14.4 Hz] which in turn yield lower values of τ_e relative to the devices (a) and (c). The corresponding τ_e values for the device (b) is found to be 16.8 ms while for device (d) it is 11.1 ms. The smaller τ_e values for ZnO NP based devices infer minimum photoinduced electron density due to shorter diffusion length of electrons which are reflected in the poor values of performance parameters, i.e., V_{oc}, J_{sc}, and overall power conversion efficiencies. In essence, stronger electronic interaction between g-C_3N_4 and ZnO NR, longer diffusion length, and minimum recombination rate of electrons in ZnO NRs have contributed to the higher light harvesting ability of the devices.

6.4 CONCLUSIONS

In summary, a facile approach for an enhanced charge injection and separation in ZnO based CdS QD sensitized solar cell devices is demonstrated by introducing a low cost and easily available organic semiconductor g-C_3N_4. It is found that g-C_3N_4 sheets act as a barrier for reverse tunneling of photoinduced electrons at the interface of working electrode/electrolyte and boosts the photovoltaic efficacy. Synergistic effects between g-C_3N_4 sheets and ZnO NR in the composites with varied g-C_3N_4 to ZnO NR weight ratios [i.e., (0.25:1), (0.5:1), (1:1), (1.5:1) and (2:1)] are investigated. Stronger excited state electronic interactions are noted in case of optimized weight ratios; (0.25:1) and (0.5:1), which have confirmed photoinduced electron injection from the CB edge of g-C_3N_4 to the low-lying CB offset of ZnO NR. Photovoltaic characterizations of the materials have revealed that light harnessing capability of the device with composite ratio (0.5:1) is optimum in contrast to all other devices. Reduced probability of photoinduced electron interception, optimum loading of sensitizer particles as well as g-C_3N_4, and stronger electronic interactions between g-C_3N_4 sheets and ZnO NR are the key factors for enhancement of photovoltaic parameters in the (0.5:1) composite device. In addition, similar devices fabricated with ZnO NPs have exhibited lower light harvesting ability. Higher rate of electron interception at the working electrode/electrolyte interfaces owing to shorter diffusion length of electrons in ZnO NPs and weaker excited state electronic interactions between g-C_3N_4 and ZnO NP are concluded as primary reasons for the lower performance in contrast to ZnO NR devices.

6.5 REFERENCES

(1) Fujishima, A.; Honda, K. *Nature*, **1972**, *238*, 37.

(2) O'Regan, B.; Grätzel, M. *Nature*, **1991**, *353*, 737.

(3) Kamat, P. V.; Tvrdy, K.; Baker, D. R.; Radich, J. G. *Chem. Rev.*, **2010**, *110*, 6664.

(4) Hagfeldt, A.; Boschloo, G.; Sun, L.; Kloo L.; Pettersson, H. *Chem. Rev.*, **2010**, *110*, 6595.

(5) Xu, X.; Randorn, C.; Efstathiou P.; Irvine, J. T. S. *Nat. Mater.*, **2012**, *11*, 595.

(6) Wu, D.; Shi, X.; Dong, H.; Zhu, F.; Jiang, K.; Xu, D.; Ai, X.; Zhang, J. *J. Mater. Chem. A*, **2014**, *2*, 16276.

(7) Wu, D.; He, J.; Zhang, S.; Cao, K.; Gao, Z.; Xu, F.; Jiang, K. *J. Power Sources*, **2015**, *282*, 202.

(8) Wang, X.; Maeda, K.; Thomas, A.; Takanabe, K.; Xin, G.; Carlsson, J. M.; Domen, K.; Antonietti, M. *Nat. Mater.*, **2009**, *8*, 76.

(9) Wang, X.; Maeda, K.; Chen, X.; Takanabe, K.; Domen, K.; Hou, Y.; Fu, X.; Antonietti, M. *J. Am. Chem. Soc.*, **2009**, *131*, 1680.

(10) Zhang, Y.; Mori, T.; Ye, J. *Sci. Adv. Mater.*, **2012**, *4*, 282.

(11) Wang, Y.; Wang, X.; Antonietti, M. *Angew. Chem. Int.*, **2012**, *51*, 68.

(12) Zhu, J.; Xiao, P.; Li, H.; Carabineiro, S. A. C. *ACS Appl. Mater. Interfaces*, **2014**, *6*, 16449.

(13) Cao, S.; Yu, J. *J. Phys. Chem. Lett.*, **2014**, *5*, 2101.

(14) Zhang, Y.; Pan, Q.; Chai, G.; Liang, M.; Dong, G.; Zhang, Q.; Qiu, J. *Sci. Rep.*, **2013**, *3*, 1943.

(15) Byers, J. C.; Billon, F.; Debiemme-Chouvy, C.; Deslouis, C.; Pailleret, A.; Semenikhin, O. A. *ACS Appl. Mater. Interfaces*, **2012**, *4*, 4579.

(16) Zhou, J.; Zhang, M.; Zhu, Y. *Phys. Chem. Chem. Phys.*, **2014**, *16*, 17627.

(17) Zhou, S.; Liu, Y.; Li, J.; Wang, Y.; Jiang, G.; Zhao, Z.; Wang, D.; Duan, A.; Liu, J.; Wei, Y. *Appl. Catal. B*, **2014**, *158–159*, 20.

(18) Huang, L.; Xu, H.; Li, Y.; Li, H.; Cheng, X.; Xia, J.; Xu, Y.; Cai, G. *Dalton Trans.*, **2013**, *42*, 8606.

(19) Kumar, S.; Tonda, S.; Baruah, A.; Kumar, B.; Shanker, V. *Dalton Trans.*, **2014**, *43*, 16105.

(20) Cao, S. W.; Yuan, Y. P.; Fang, J.; Shahjamali, M. M.; Boey, F. Y. C.; Barber, J.; Loo, S. C. J.; Xue, C. *Int. J. Hydrogen Energy*, **2013**, *38*, 1258.

(21) Zeng, H.; Duan, G.; Li, Y.; Yang, S.; Xu, X.; Cai, W. *Adv. Funct. Mater.*, **2010**, *20*, 561.

(22) Chen, Y. W.; Liu, Y. C.; Lu, S. X.; Xu, C. S.; Shao, C. L.; Wang, C.; Zhang, J. Y.; Lu, Y. M.; Shen, D. Z.; Fan, X. W. *J. Chem. Phys.*, **2005**, *123*, 134701.

(23) Li, F.; Ding, Y.; Gao, P.; Xin, X.; Wang, L. Z. *Angew. Chem.*, **2004**, *116*, 5350.

(24) Chen, S.; Liu, Y.; Shao, C.; Mu, R.; Lu, Y.; Zhang, J.; Shen, D.; Fan, X.; *Adv. Mater.*, **2005**, *17*, 586.

(25) Liu, B.; Zeng, H. C. *Chem. Mater.*, **2007**, *19*, 5824.

(26) Wang, A.-J.; Liao, Q.-C.; Feng, J.-J.; Zhang, P.-P.; Li, A.-Q.; Wang, J.-J. *CrystEngComm*, **2012**, *14*, 256.

(27) Concina, I.; Vomiero, A. *Small*, **2015**, *11*, 1744.

(28) Guillen, E.; Peter, L. M.; Anta, J. A. *J. Phys. Chem. C*, **2011**, *115*, 22622.

(29) Liu, Y.; Goebl, J.; Yin, Y. *Chem. Soc. Rev.*, **2013**, *42*, 2610.

(30) Mclaren, A.; Valdes-Solis, T.; Li, G.; Tsang, S. C. *J. Am. Chem. Soc.*, **2009**, *131*, 12540.

(31) Hu, P.; Han, N.; Zhang, X.; Yao, M.; Cao, Y.; Zuo, A.; Yang, G.; Yuan, F. *J. Mater. Chem.*, **2011**, *21*, 14277.

(32) Xu F.; Sun, L. *Energy Environ. Sci.*, **2011**, *4*, 818.

(33) Xu, J.; Chen, Z.; Zapien, J. A.; Lee, C.-S.; Zhang, W. *Adv. Mater.*, **2014**, *26*, 5337.

(34) Zhu, Y.-P.; Li, M.; Liu, Y.-L.; Ren, T.-Z.; Yuan, Z.-Y. *J. Phys. Chem. C*, **2014**, *118*, 10963.

(35) Fageria, P.; Nazir, R.; Gangopadhyay, S.; Barshilia, H. C.; Pandea, S. *RSC Adv.*, **2015**, *5*, 80397.

(36) Wu, D.; Cao, K.; Wang, F.; Wang, H.; Gao, Z.; Xu, F.; Guo, Y.; Jiang, K. *Chem. Eng. J.*, **2015**, *280*, 441.

(37) Barpuzary, D.; Qureshi, M. *ACS Appl. Mater. Interfaces*, **2013**, *5*, 11673.

(38) Chetia, T. R.; Barpuzary, D.; Qureshi, M. *Phys. Chem. Chem. Phys.*, **2014**, *16*, 9625.

(39) Chetia, T. R.; Ansari, M. S.; Qureshi, M. *ACS Appl. Mater. Interfaces*, **2015**, *7*, 13266.

(40) Barpuzary, D.; Banik, A.; Gogoi, G.; Qureshi, M. *J. Mater. Chem. A*, **2015**, *3*, 14378.

(41) Dong, F.; Wu, L.; Sun, Y.; Fu, M.; Wu, Z.; Lee, S. C. *J. Mater. Chem.*, **2011**, *21*, 15171.

(42) Becheri, A.; Dűrr, M.; Nostro, P. L.; Baglioni, P. *J. Nanopart. Res.*, **2008**, *10*, 679.

(43) Han, X. G.; He, H. Z.; Kuang, Q.; Zhou, X.; Zhang, X. H.; Xu, T.; Xie, Z. X.; Zheng, L. S. *J. Phys. Chem. C*, **2009**, *113*, 584.

(44) Govender, K.; Boyle, D. S.; Kenway, P. B.; O'Brien, P. *J. Mater. Chem.*, **2004**, *14*, 2575.

(45) Ahuja, I. S.; Yadav, C. L.; Singh, R. *J. Mol. Struct.*, **1982**, *81*, 229.

(46) Baruah, S.; Dutta, J. *Sci. Technol. Adv. Mat.*, **2009**, *10*, 013001.

(47) Ashfold, M. N. R.; Doherty, R. P.; Ndifor-Angwafor, N. G.; Riley, D. J.; Sun, Y. *Thin Solid Films*, **2007**, *515*, 8679.

(48) Jiang, F.; Yan, T.; Chen, H.; Sun, A.; Xu, C.; Wang, X. *Appl. Surf. Sci.*, **2014**, *295*, 164.

(49) Tonda, S.; Kumar, S.; Kandula, S.; Shanker, V. *J. Mater. Chem. A*, **2014**, *2*, 6772.

(50) Kongkanand, A.; Tvrdy, K.; Takechi, K.; Kuno, M.; Kamat, P. V. *J. Am. Chem. Soc.*, **2008**, *130*, 4007.

(51) Kumar, S.; Baruah, A.; Tonda, S.; Kumar, B.; Shanker, V.; Sreedhar, B. *Nanoscale*, **2014**, *6*, 4830.

(52) Wang, Y.J.; Shi, R.; Lin, J.; Zhu, Y.F. *Energy Environ. Sci.*, **2011**, *4*, 2922.

(53) Lin, S.-C.; Lee, Y.-L.; Chang, C.-H.; Shen, Y.-J.; Yang, Y.-M. *Appl. Phys. Lett.*, **2007**, *90*, 143517.

(54) Li, C.; Yang, L.; Xiao, J.; Wu, Y.-C.; Søndergaard, M.; Luo, Y.; Li, D.; Meng, Q.; Iversen, B. B. *Phys. Chem. Chem. Phys.*, **2013**, *15*, 8710.

(55) Qureshi, M.; Chetia, T. R.; Ansari, M. S.; Soni, S. S. *J. Mater. Chem. A*, **2015**, *3*, 4291.

(56) Lee, Y.-L.; Chang, C.-H. *J. Power Sources*, **2008**, *185*, 584.

(57) Chen, H.; Li, W.; Liu, H.; Zhu, L. *Electrochem. Commun.*, **2011**, *13*, 331.

(58) Mora-Seró, I.; Giménez, S.; Fabregat-Santiago, F.; Gómez, R.; Shen, Q.; Toyoda, T.; Bisquert, J. *Acc. Chem. Res.*, **2009**, *42*, 1848.

(59) Phadke, S.; Pasquier, A. D.; Birnie, D. P. *J. Phys. Chem. C*, **2011**, *115*, 18342.

(60) Tian, J.; Uchaker, E.; Zhang, Q.; Cao, G. *ACS Appl. Mater. Interfaces*, **2014**, *6*, 4466.

(61) Kern, R.; Sastrawan, R.; Ferber, J.; Stangl, R.; Luther, J. *J. Electrochim. Acta*, **2002**, *47*, 4213.

APPENDIX

Boosting Photovoltaic Performance of SnO_2 Based Dye Sensitized Solar Cells by Utilizing 2D MgO Nanosheets

This chapter presents an idea to enhance the power conversion efficiency (PCE) of SnO_2 based DSSCs, introducing an electron barrier layer in the form of porous hierarchical 2D MgO nanosheets by a simple ultra-sonication route followed by mixing process. A metal free Donor-π linker-Acceptor type dye, namely 2-cyano-3-(4-(2-(9-p-tolyl-9H-fluoren-6-yl)vinyl)phenyl) acrylic acid (i.e. SK1 dye) is used as the sensitizer in the devices.

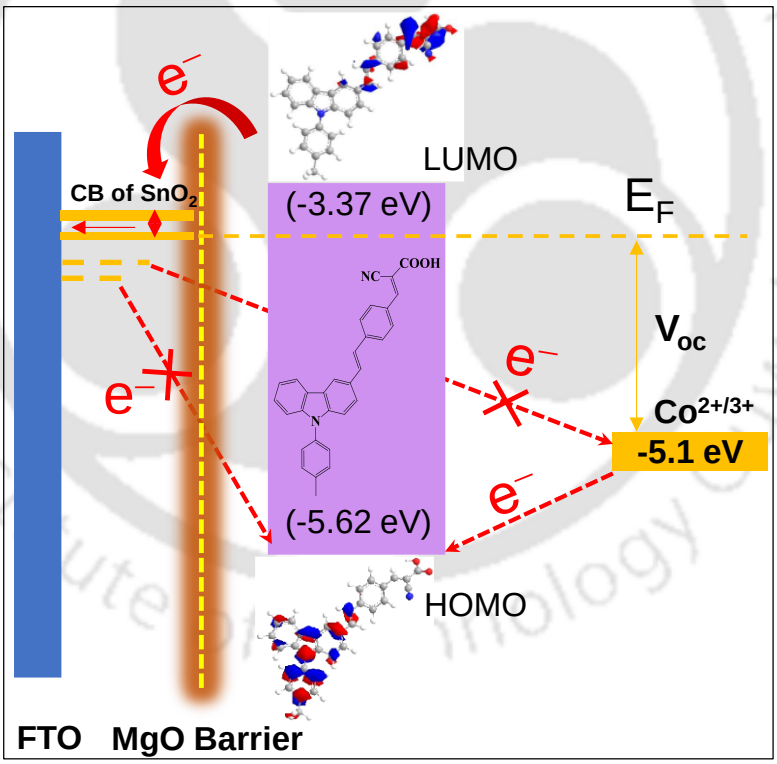

Journal of Materials Chemistry A M. Qureshi, **T. R. Chetia**, M. S. Ansari, **2015**, *3*, 4291.

7.1 INTRODUCTION

Low cost fabrication techniques for the photovoltaic devices have drawn significant attention amongst the scientific community since the first report on the dye-sensitized solar cell (DSSC) in 1991 by O'Regan and Grätzel.[1,2] The DSSC's working principle is based on efficient visible light absorption by dye molecules onto the surface of a wide band gap metal oxide semiconductor and generation of photoexcited electrons followed by injection into the conduction band (CB) of metal oxide. Meanwhile, a suitable redox couple completes the transport cycle in DSSCs by regenerating the oxidized dye molecules.[3–5] Numerous wide band gap semiconductors, such as ZnO,[6] Nb_2O_5,[7] SnO_2,[8–10] $SrTiO_3$,[11] etc., have been explored as an alternative to TiO_2 in DSSCs. Among these semiconductors, use of SnO_2 over TiO_2 has two main advantages: (i) SnO_2 has an electron mobility of (~100-200 $cm^2V^{-1}s^{-1}$),[12] much higher than that of anatase TiO_2 (0.1–1 $cm^2V^{-1}s^{-1}$)[13] or porous TiO_2 (~10^{-2} $cm^2V^{-1}s^{-1}$),[14] which leads to faster transport of photo-injected electrons to FTO (ii) Formation of fewer oxidative holes in the valence band under UV illumination due to its wider band gap (3.6 eV) than that of anatase TiO_2 (3.2 eV), thus minimizing the rate of dye degradation.[15] Inspite of these advantages, the DSSCs based on SnO_2 have lower energy conversion efficiency than those based on TiO_2 so far. Poor performance of SnO_2 based DSSCs is due to the faster electron recombination and back electron transfer to the redox shuttle due to reactive low energy trap states in SnO_2 and minimal dye adsorption because of its low isoelectric point (pH 4–5).[16,17] In order to overcome these drawbacks, engineering of the SnO_2 nanoparticle (NP) surface with barrier layers such as ZnO,[18,19] TiO_2, [20] MgO[21,22] etc. have been implemented to improve the power conversion efficiency. In principle, these barrier layers could passivate the reactive surface states in SnO_2 and slow down the electron interception process. A photoanode with thin MgO layer on SnO_2 nanoparticles is of particular interest, as it enhances the photovoltaic device performance of pristine SnO_2 from 1% to 7% in some cases.[15,21,22] Wide band gap metal oxide shells have an unfathomable impact on the solar cell performance parameters, as they can affect innumerable characteristics of a photoanode such as dye loading, charge recombination, photoinduced electron transfer, conduction band edge position etc.[23,24]

Another critical factor for better device output is the selection of the dye molecule to be used in sensitization. Dye molecules which absorb solar irradiation in a broad range of wavelength to get excited and efficiently inject electrons into the wide band gap semiconductor scaffold is considered to be an ideal candidate for utilization in DSSC devices.[25] Nowadays, metal-free

organic dye molecules with donor–π linker–acceptor (D–π–A) moieties are gaining much attention among the scientific community due to their low band gap, high molar extinction coefficients, facile molecular design with simple synthetic and purification routes.[25] Several metal free derivatives of carbazole, indoline, triarylamine, coumarin, *etc.*, have used in DSSC devices and achieved PCE upto ~10 %; challenging the light harvesting ability of metal complex based dyes such as N719, N3, Z907, porphyrins *etc*. Figure **7.1.1** shows some examples of (D–π–A) type dye molecules used in DSSC devices.[26–29]

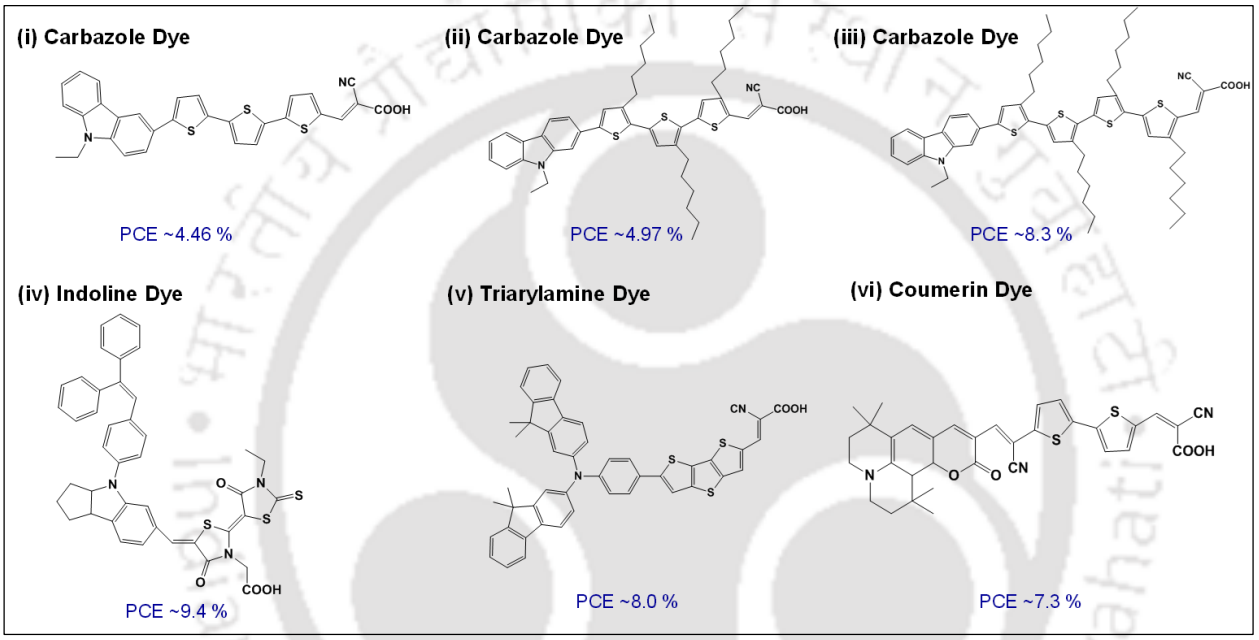

Scheme 7.1.1 Examples of some highly efficient metal-free organic dyes with (D-π-A) moieties used in DSSC devices.

Primary advantage of (D–π–A) type dye molecules is the tunability of absorption and electrical properties *via* suitable incorporation of chromophoric groups of different types. Moreover, modulation of π-conjugated linker groups can further improve the molar absorptivity and intramolecular charge transfer feasibility for a better light harvesting ability.[30,31]

In this chapter we have demonstrated the effect of porous hierarchical MgO composed of 2D nanosheets on the photovoltaic characteristics of SnO_2 based DSSCs by a simple sonication followed by mixing process and sensitized with a metal free carbazole dye, namely 2-cyano-3-(4-(2-(9-*p*-tolyl-9H-fluoren-6-yl)vinyl)phenyl)acrylic acid, (i.e., SK1 dye). We have optimized the amount of MgO to be added to SnO_2 for maximum performance of the photovoltaic devices and made a comparative study of the SnO_2-MgO with pristine SnO_2 devices by employing two redox couples (I^-/I_3^-) and $[Co(bpy)_3]^{2+/3+}$ to understand the effects of electrolyte as well.

7.2 EXPERIMENTAL SECTION

7.2.1 SYNTHESIS OF SK1 DYE

Synthesis of the dye molecule is carried out by following the steps presented in the scheme **7.2.1**. In a typical procedure, the aldehyde was reduced by reacting with sodium borohydride in the presence of in tetrahydrofuran at 5 °C, followed by stirring at room temperature for 6 h. After that the reaction mixture was poured into cold water and extracted using dichloromethane. The organic layer was dried using anhydrous sodium sulfate, and the solvent was removed under vacuum to yield the oil.

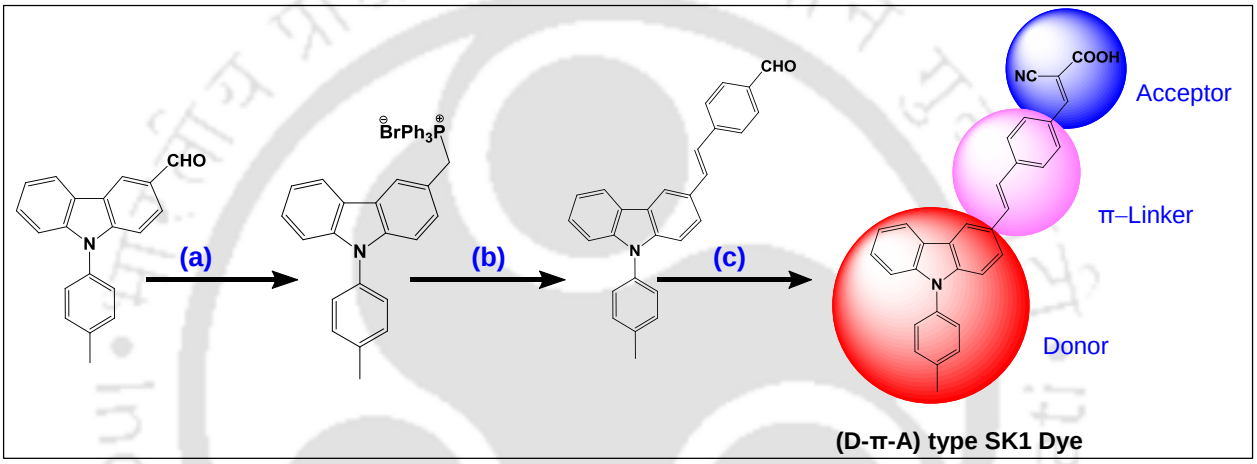

Scheme 7.2.1 Synthesis procedure for 2-Cyano-3-(4-(2-(9-*p*-tolyl-9H-fluoren-6-yl)vinyl)phenyl) acrylic acid or SK1 dye.
[Reagents and conditions: **(a)** 0.4 equivalent of $NaBH_4$ in THF followed by triphenylphosphine hydrobromide in dichloromethane, **(b)** terephthaldehyde, sodium ethoxide in ethanol at 5 °C, and **(c)** cyanoacetic acid and catalytic amount of piperidine in acetonitrile.]

The alcohol obtained in the previous step was then converted into Wittig salt by using triphenylphosphine hydrobromide in dichloromethane and separated out it as a white colored salt by adding of diethyl ether. Further it was condensed with terephthaldehyde in ethanol using sodium ethoxide as a base under cold conditions (5−10 °C) and the reaction mixture was stirred at room temperature for 2 h, poured into water followed by the neutralizing with dilute hydrochloric acid to obtain a yellow colored solid crude. As obtained yellow solid product was dissolved in tetrahydrofuran in the presence of a catalytic amount of iodine and refluxed for 4 h. Then the reaction mass was poured into dilute alkali solution to separate the solid product which is purified by column chromatography (EtOAc: n-hexane, 3:7, v/v). In the next step, purified aldehyde was dissolved in acetonitrile and cyanoacetic acid, and then added a catalytic amount of piperidine.

The reaction mass was allowed to reflux for 3 h, after which solvent was removed under vacuum. Finally the dried crude product was purified by column chromatography (EtOAc: n-hexane, 1:1, v/v) to obtain an orange solid product.

The ^{1}H NMR (in $CDCl_3$) and ^{13}C NMR (in DMSO-d6) spectra of SK1 dye are shown in figures **7.2.1** and **7.2.2** respectively.

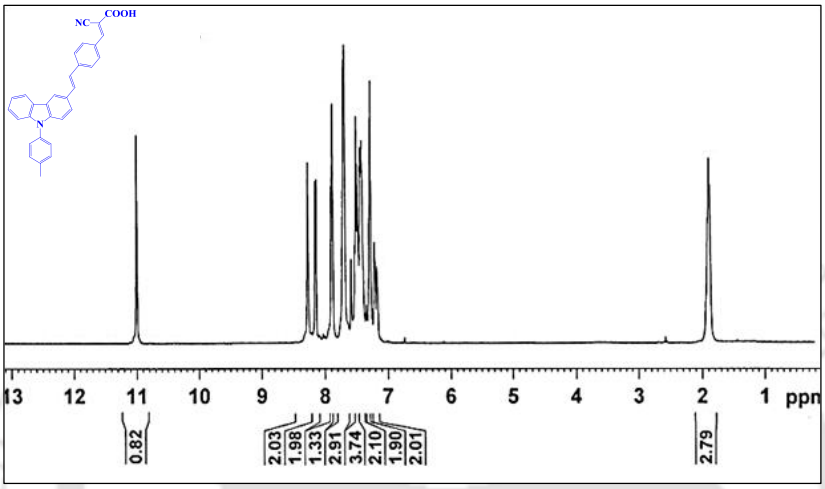

Figure 7.2.1 400 MHz ^{1}H NMR spectrum of metal-free carbazole SK1 dye recorded in $CDCl_3$ as the solvent.

^{1}H NMR ($CDCl_3$, 400 MHz) δ (ppm): 11.00 (s, 1H), 8.30 (s, 2H), 8.20 (s, 2H), 7.86 (s, 1H), 7.72 (s, 3H), 7.42 (d, 4H), 7.41 (d, 2H), 7.40 (d, 2H), 7.20 (d, 2H), 1.90 (s, 3H).

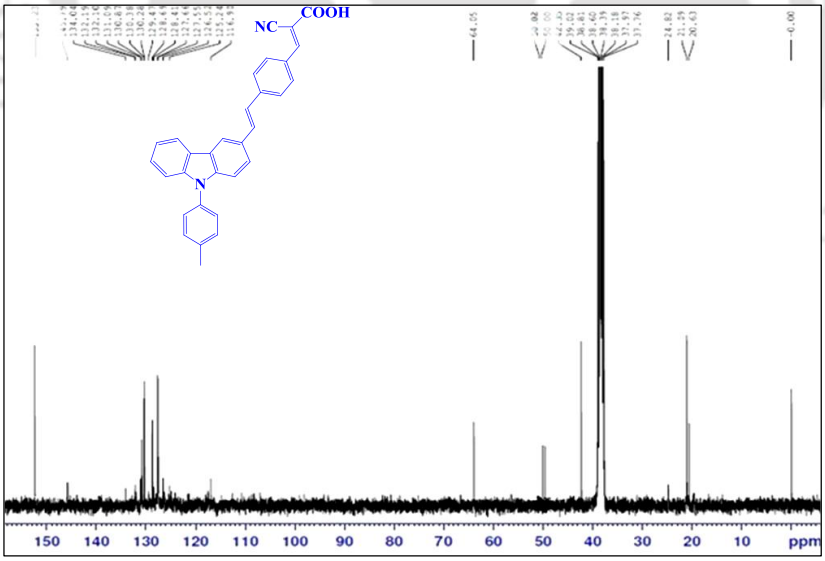

Figure 7.2.2 400 MHz ^{13}C NMR spectrum of metal-free carbazole SK1 dye recorded in $CDCl_3$ as the solvent.

^{13}C NMR (DMSO-d6, 400 MHz) δ (ppm): 21.09, 64.05, 116.90, 125.24, 126.52, 127.55, 127.66, 128.41, 128.69, 129.47, 130.28, 130.38, 130.87, 131.09, 132.10, 132.19, 134.04, 145.79, and 153.23.

The mass spectrum of SK1 dye is shown in Figure **7.2.3**. MS m/z: [M]+ for $C_{31}H_{22}N_2O_2$, calculated, 454.16; observed, 453.80. Elemental analysis for $C_{31}H_{22}N_2O_2$: calculated C, 81.83; H, 5.10; N, 6.16; O, 7.03. Observed: C, 81.70; H, 5.13; N, 6.10; O, 7.07.

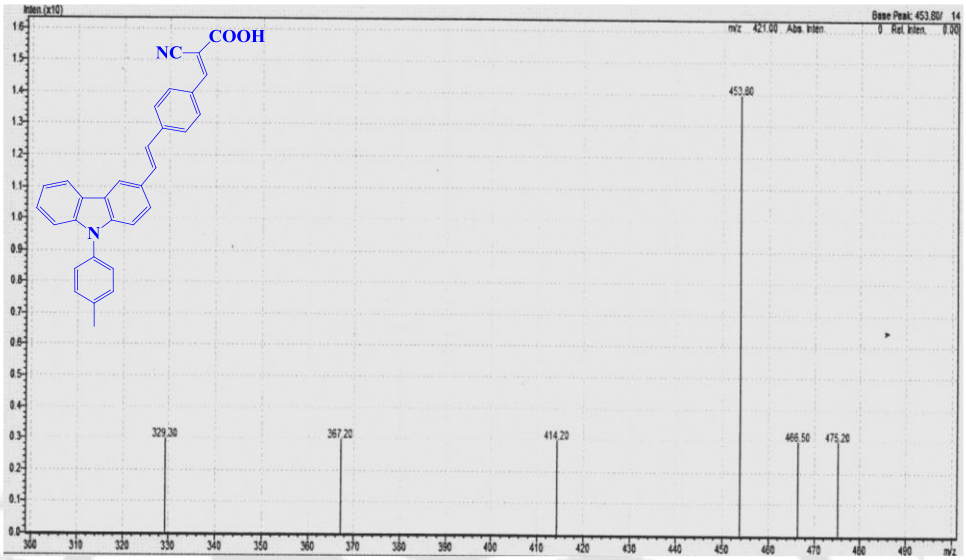

Figure 7.2.3 Mass spectrum of SK1 dye.

7.2.2 SYNTHESIS OF 3D HIERARCHICAL SnO_2 MICROSPHERES

3D hierarchical SnO_2 was synthesized by following a previously reported protocol.[32] To prepare 3D SnO_2 microspheres, 2.25 g tin dichloride dihydrate (10 mmol) and 5.6 g oxalic acid (44.4 mmol) were dissolved in Milli-Q water (20 mL) followed by the addition of 0.4 mL hydrochloric acid (35 wt %). Aqueous solution (80 wt %) of hydrazine monohydrate, 2.16 g (41.5 mmol) was added dropwise under magnetic stirring until the solution became clear. Finally the solution was transferred to a Teflon-lined stainless steel autoclave and maintained at 180 °C for 14h. After that the autoclave was naturally cooled to room temperature and the obtained product was centrifuged and rinsed thoroughly with distilled water and absolute ethanol several times, dried in hot air oven at 60 °C for 24 h and calcined at 500 °C for 2 h to obtain the final product.

7.2.3 SYNTHESIS OF POROUS 3D HIERARCHICAL MgO

In a typical procedure, the $MgCl_2.6H_2O$ (0.5mmol) was dissolved in 25 mL distilled water, followed by the addition of sodium bicarbonate (5 mmol) into the solution. This solution was slowly added into vigorously stirring ethanol (100 mL, in a 250 mL two-necked flask) at 80 °C. After 10 min, the stirring was stopped and the solution was maintained at 80 °C for 2 h. After cooling down to room temperature, the obtained precipitate was centrifuged and washed with

water and absolute ethanol several times followed by drying in a hot air oven at 60 °C for 12 h. Finally, the obtained precursor [$Mg_5(CO_3)_4(OH)_2.4H_2O$] was annealed in air at 400 °C for 4 h to obtain the porous hierarchical MgO.

7.2.4 FABRICATION OF PHOTOANODES AND DEVICES

Pristine SnO_2 and SnO_2-MgO based photoanodes were fabricated as follows. For the fabrication of bare SnO_2 based photoanode, synthesized hierarchical SnO_2 microsphere powder (0.5 g) was added to a mixture of 1.0 mL of terpineol and 0.2 g of PEG-PPG-PEG and ground well in an agate mortar until a homogeneous paste was obtained. This paste was coated on the conductive glass substrates by using doctor blade technique. These films were then dried in hot air oven at 70 °C and calcined at 450 °C for 30 min to remove the polymer. SnO_2-MgO photoanodes were fabricated by following the same procedure used for pristine SnO_2 based photoanode except that the ultra-sonication of the mixture of porous hierarchical MgO powder and SnO_2 microspheres with different weight ratios in ethanol (5 mL) for 1 h, prior to making the paste. Step-by-step fabrication process of the photoanodes is schematically shown in the scheme **7.2.2**.

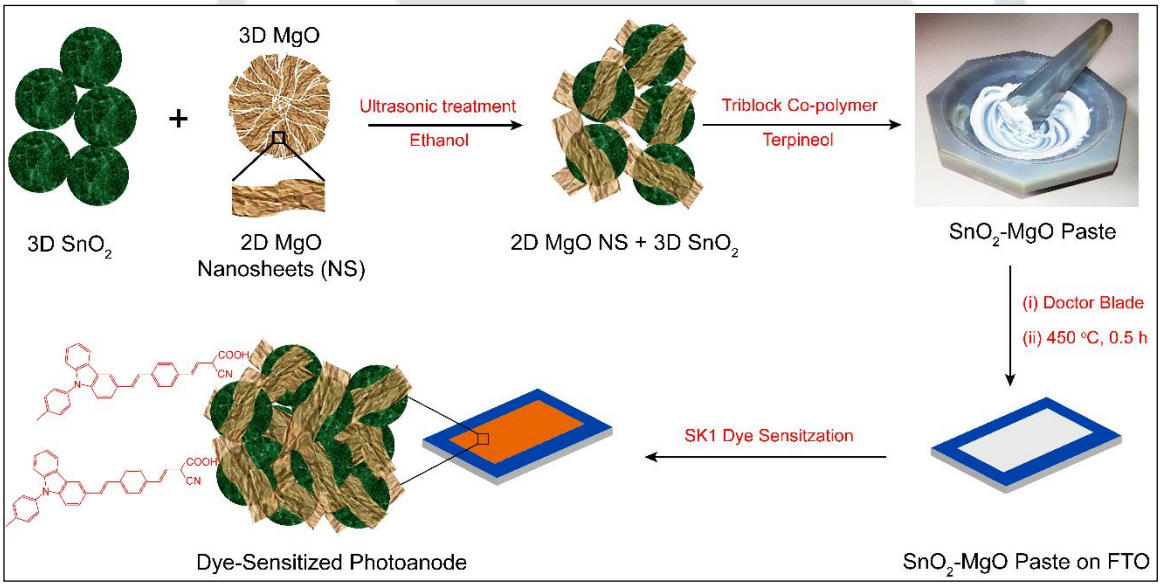

Scheme 7.2.2 Step-by-step fabrication process of SnO_2–MgO photoanode.

The paste was coated by using doctor blade technique over the precleaned FTO substrates. The substrates were dried in air and then calcined at 450 °C for 30 min to obtain SnO_2-MgO films. These substrates were then sensitized with SK1 dye solution in anhydrous ethanol: dichloromethane (1:1, v/v) mixed solvents for 6 h, washed with ethanol and dried under hot air blow. The thickness of all the photoanode films were found to be in the range of 12−15 μm by

using a surface profilometer. For the preparation of counter electrode, a 50 mM H_2PtCl_6 solution prepared in isopropanol was spin coated on pre-cleaned, ozonized FTO substrates, followed by calcination at 450 °C for 30 min. The photovoltaic devices were fabricated by sandwiching the photoanodes and counter electrodes and then electrolyte solution was injected after sealing (using low-temperature thermoplastic sealant, thickness ~50 μm) to complete the device. In this work, we also studied the effect of two electrolytes on the PCE of fabricated devices. To prepare I^-/I_3^- electrolyte solution, 0.5 M LiI, 0.05 M I_2, 0.1 M guanidium thiocyanate, and 0.5 M 4-tert-butylpyridine dissolved in a solvent mixture of acetonitrile: valeronitrile (9:1, v/v) and similarly Co(II/III) electrolyte solution was prepared by dissolving 0.2 M $[Co(bpy)_3](PF_6)_2$, 0.02 M $[Co(bpy)_3](PF_6)_3$, and 0.5 M 4-tert-butylpyridine in acetonitrile: valeronitrile (9:1, v/v) solvent mixture. Before the photovoltaic measurements, the fabricated devices were kept under dark condition for 24 h. It should be noted that an active surface area of ~0.25 cm^2 was fixed for all the devices.

7.3 RESULTS AND DISCUSSIONS

7.3.1 POWDER X-RAY DIFFRACTION ANALYSIS

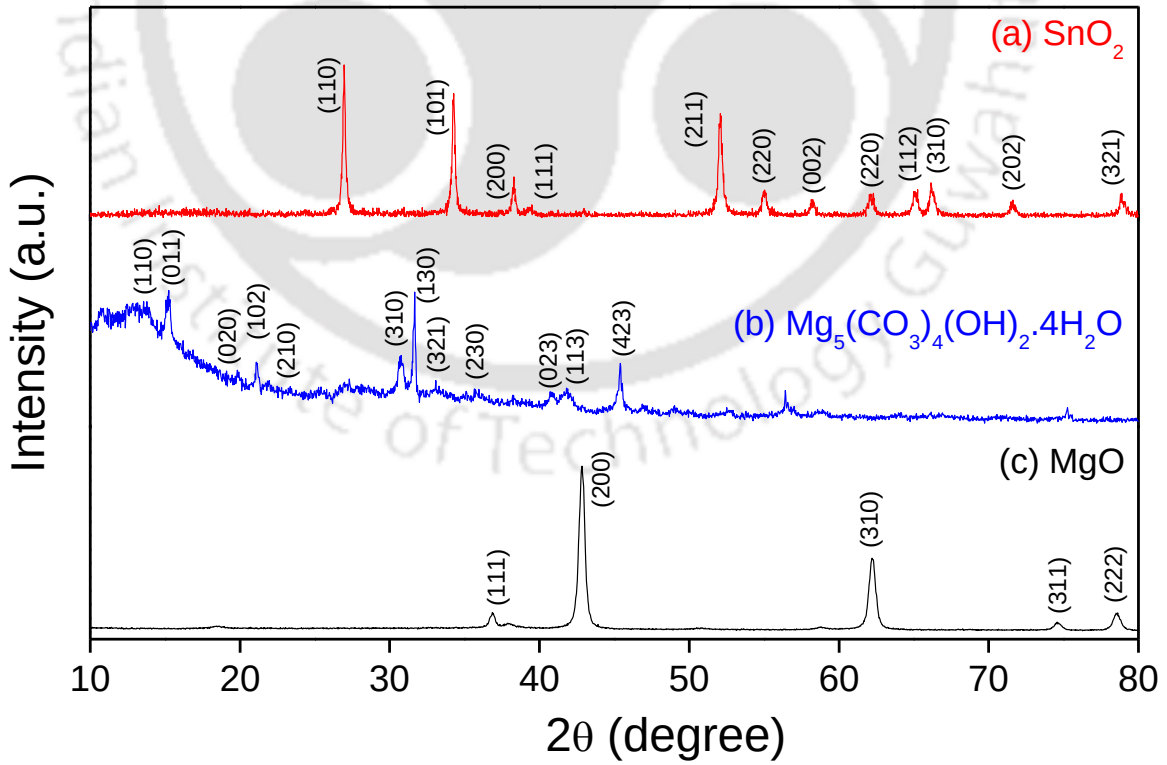

Figure 7.3.1 Powder X-ray diffraction pattern of as synthesized (a) SnO_2, the (b) carbonate precursor $Mg_5(CO_3)_4(OH)_2.4H_2O$ and (c) 3D porous MgO

Figure **7.3.1** shows the PXRD patterns of (a) 3D SnO_2 microspheres, (b) carbonate precursor of MgO, i.e., $Mg_5(CO_3)_4(OH)_2.4H_2O$ and (c) 3D porous MgO. The diffraction peaks of 3D SnO_2 microspheres [trace (a)] are observed from the lattice planes (110), (101), (200), (111), (211), (220), (002), (310), (112), (301), (202) and (321) of a rutile crystal structure of SnO_2 (JCPDS card no.# 41-1445). Trace (b) shows XRD diffraction pattern of carbonate precursor of MgO and confirm its structure $Mg_5(CO_3)_4(OH)_2.4H_2O$ from JCPDS card no.# 25-0513. The PXRD peaks trace (c), are matched well with the diffraction from the (111), (200), (220), (311) and (222) planes of cubic MgO (JCPDS card no. # 04-0829). No peaks for other phases are observed for all the three samples confirming that SnO_2 microspheres, the carbonate precursor $Mg_5(CO_3)_4(OH)_2.4H_2O$ of MgO and 3D porous MgO are highly pure. High crystallinity of as synthesized SnO_2 and MgO was confirmed from high intensity diffraction peaks observed for both of the compounds.

7.3.2 MATERIAL MORPHOLOGY

Figure **7.3.2** shows the FESEM and SEM features of as synthesized 3D SnO_2 and MgO microspheres at different magnifications. Images (A) and (B) are showing the SnO_2 microspheres having average size dimension of 1–3 μm. The magnified FESEM image (C) of a SnO_2 microsphere confirms its porous nature with numerous randomly arranged SnO_2 2D Nanoplates on the surface of it. Images (E), (F) and (G) represent SEM images of 3D porous MgO microspheres at different magnifications. From (E) and (F) it is clear that diameter of the MgO microspheres are in the range of 2–4 μm. Higher magnification SEM images (F and G) reveal that the microspheres are porous in nature and made up of numerous 2D nanosheets and which is further confirmed by transmission electron microscopy.

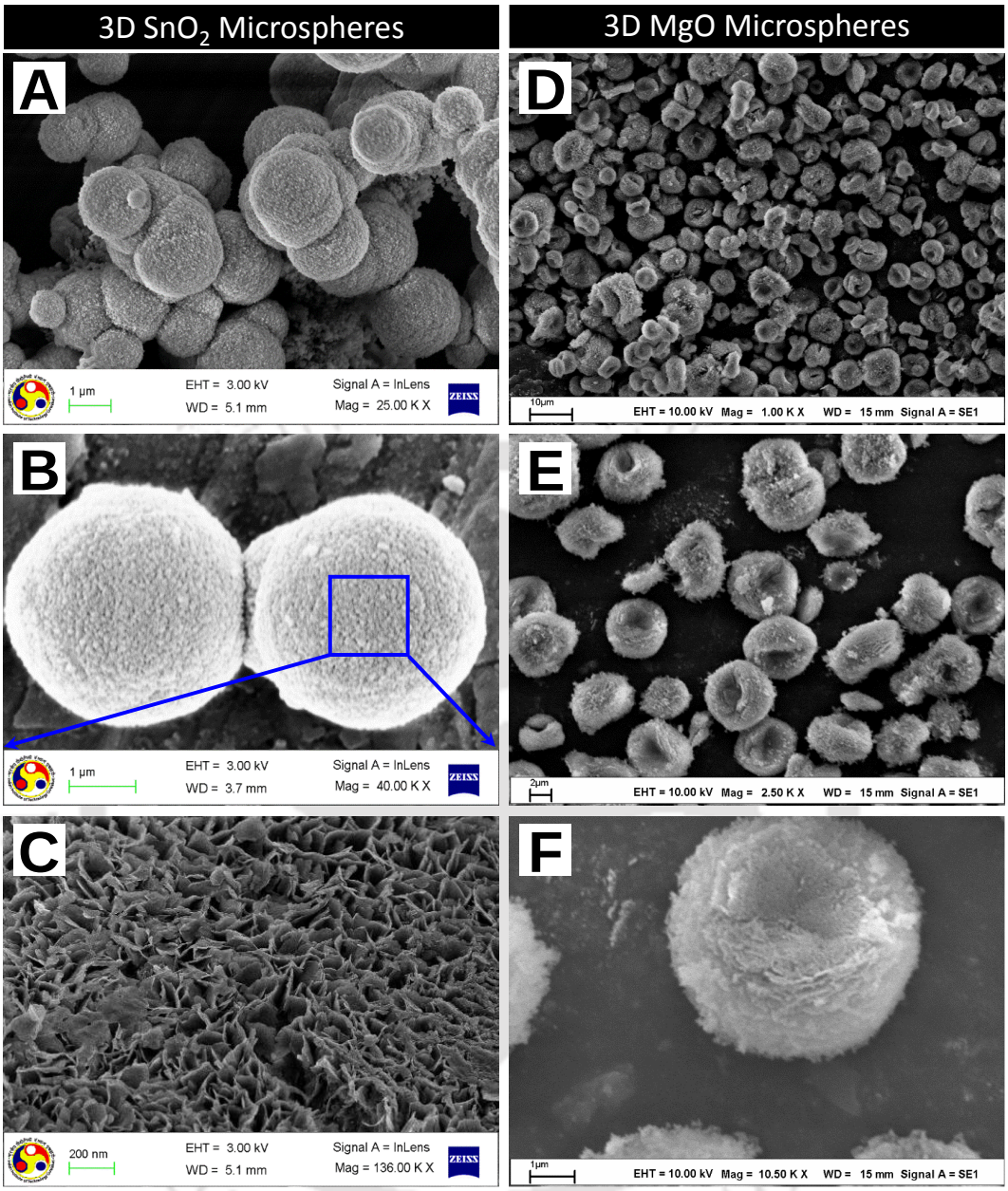

Figure 7.3.2 FESEM images of 3D porous SnO_2 microstructures (A and B) which are composed of randomly arranged 2D nanoplates as we see from high resolution image (C). SEM images of flowerlike 3D porous MgO at different magnifications (E, F and G).

Figure **7.3.3 (A)** represents TEM image of SnO_2 nanoplates obtained from SnO_2 microspheres after ultrasonication for 1h in ethanol. The ultrasonicated solution was allowed to settle down for 15 min and a drop of supernatant solution was drop-casted on the TEM grid. The size of SnO_2 nanoplates are in the range of 10-15 nm. High-resolution TEM (HRTEM) image [Figure 7.3.3 (B)] of a single SnO_2 nanoplate shows well resolved lattice pattern which indicates its crystalline nature and is beneficial for efficient photogenerated charge migration. Interplanar

distance of the lattice pattern was obtained from inverse fast Fourier transform (IFFT) of atomic planes (trace C) and was found to be ~0.33 nm which corresponds to the (110) lattice planes. Inset to trace C represents FFT obtained from the HRTEM image. Figure 7.3.3 (D) is showing an MgO microsphere from where 2D MgO nanosheets are coming out after ultrasonication for 1h in ethanol. Trace E of figure 7.3.3 represents TEM image of ultrathin MgO nanosheets. These nanosheets have number of pores resulting from thermal decomposition process of the carbonate precursor $Mg_5(CO_3)_4(OH)_2.4H_2O$, which causes generation of large amount of gases (e.g., CO_2 and H_2O).[33] Trace F represents selected area electron diffraction (SAED) pattern of 2D MgO nanosheets which is consistent with the PXRD pattern and confirms their crystalline nature. These porous 2D MgO nanosheets can enhance the surface area of the photoanode for higher adsorption of dye molecules and also facilitate the electrolyte diffusion process for faster regeneration of the oxidized dye molecules.

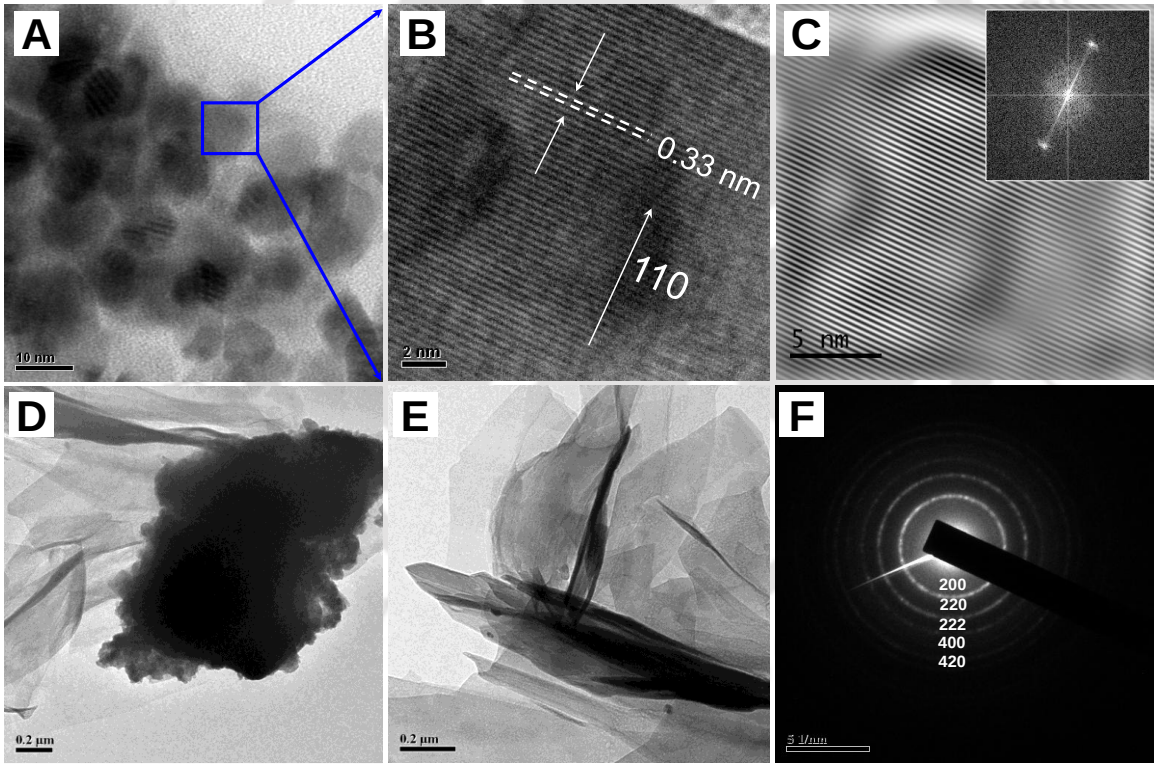

Figure 7.3.3 (A) TEM image of SnO_2 nanoplates obtained from SnO_2 microspheres after ultrasonication for 1h in ethanol. Trace (B) represents high resolution-TEM (HR-TEM) image of a SnO_2 2D nanosheet showing the growth along (110) lattice plane and interplanar *d*-spacing using IFFT of the HR-TEM image (Trace C). Inset to trace C represents FFT obtained from the HRTEM image. Image (D) is showing an MgO microsphere from where 2D MgO nanosheets are coming out after ultrasonication for 1h in ethanol. Traces E and F are representing TEM image of 2D MgO nanosheets and corresponding selected area electron diffraction pattern respectively.

7.3.3 BET SURFACE AREA ANALYSIS

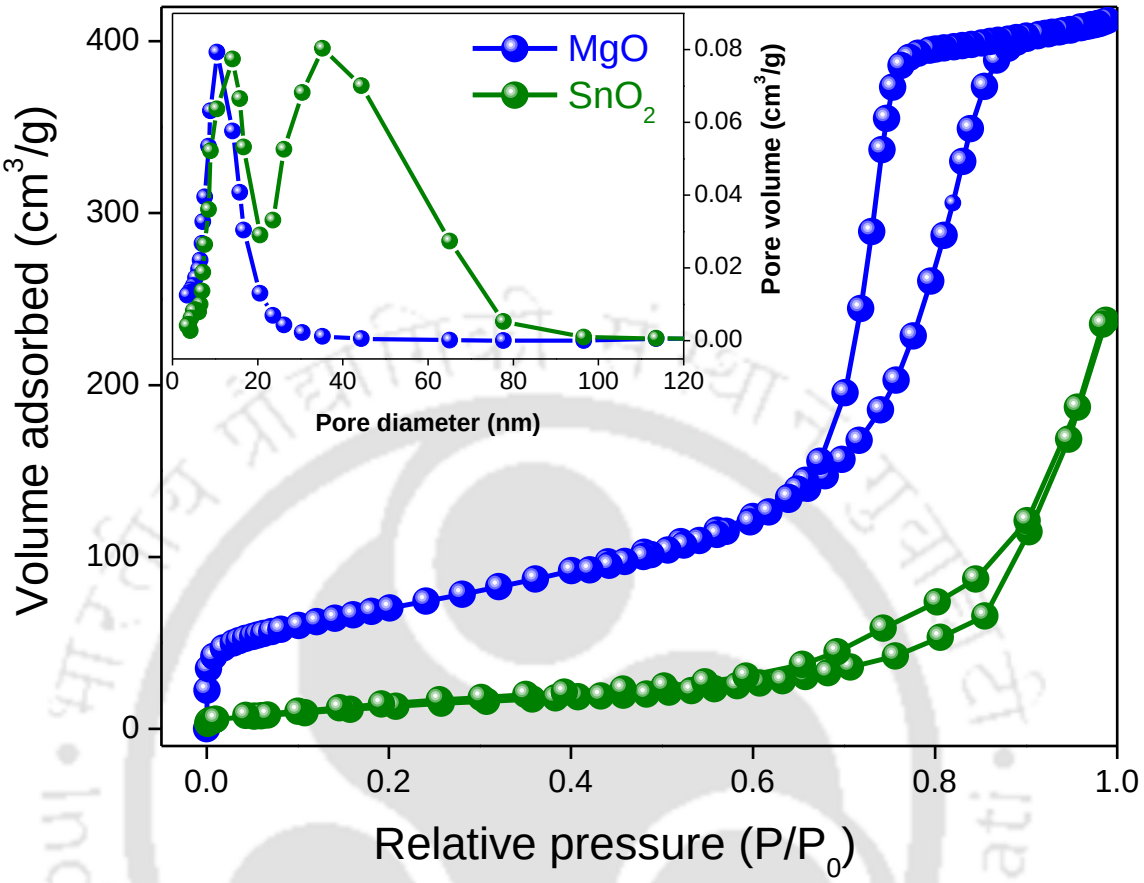

Figure 7.3.4 Nitrogen adsorption–desorption isotherms and Barrett–Joyner–Halenda (BJH) pore size distribution plots (inset) for as prepared SnO_2 and MgO microspheres.

BET surface area analysis of as prepared SnO_2 and MgO microspheres is shown in the figure **7.3.4**. To achieve better photovoltaic performance of a solar cell the electron transporting materials (i.e. Photoanodic materials) should have high surface area. Both the samples, SnO_2 and MgO, exhibit type IV isotherm patterns with H3 hysteresis loops confirming characteristic mesoporous nature. The observed BET surface area of the as-synthesized SnO_2 microspheres was found to be 123 m^2g^{-1}, whereas for MgO it was found to be 219 m^2g^{-1}. The Barrett–Joyner–Halenda (BJH) pore size distribution curve for SnO_2 indicates two type of pores are present in the material, one in the range of ~10-20 nm and other in the range of ~30-60 nm. The pore size distribution in MgO is in the range of ~10-15 nm. Due to the mesoporous nature and high surface area of the SnO_2 and MgO microspheres, they provide more adsorption sites for dye sensitization as well as better penetration of electrolyte to regenerate the oxidized dye molecules.

7.3.4 DIFFUSE REFLECTANCE UV–VISIBLE ABSORPTION SPECTRA

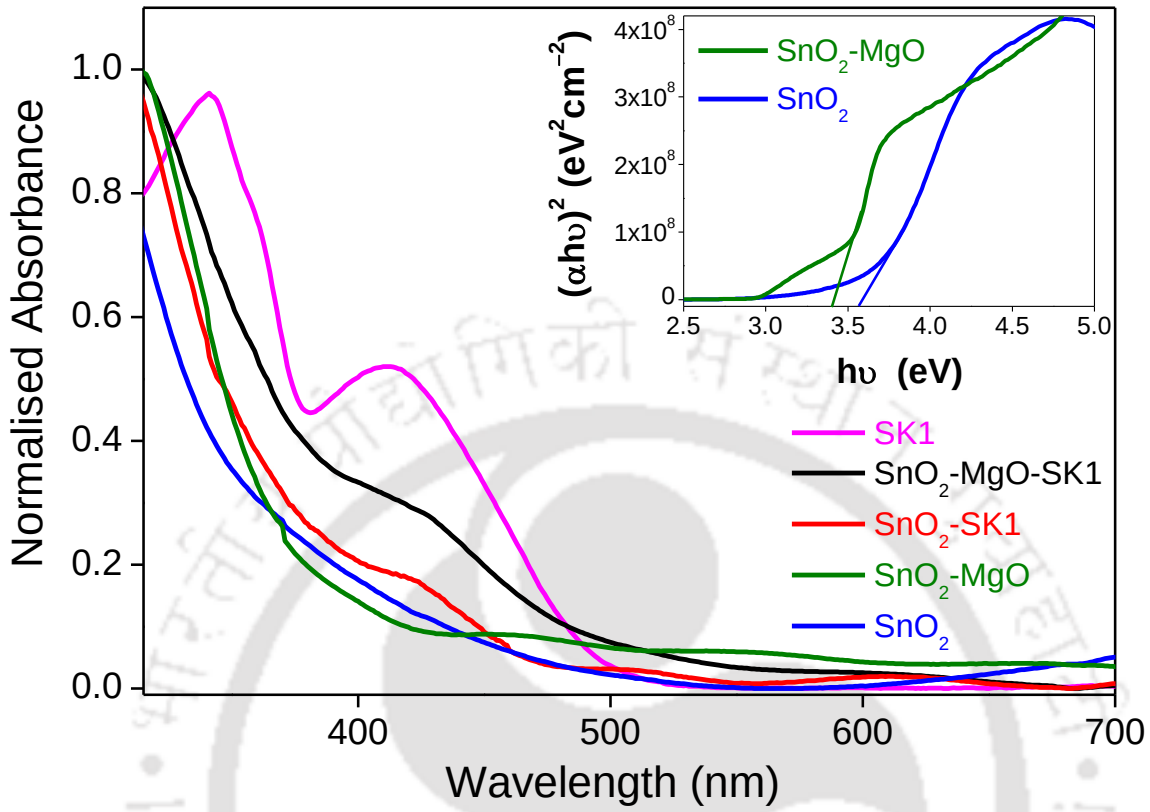

Figure 7.3.5 UV-vis diffuse reflectance spectra of SK1 dye thin-film spin-coated on FTO substrate, SK1 dye sensitized SnO_2-MgO, SnO_2 films and unsensitized bare SnO_2 and SnO_2-MgO films. Inset shows the Tauc's plots to estimate the band gap values of SnO_2 and SnO_2-MgO films on FTO.

Figure **7.3.5** represents the normalized diffuse reflectance UV–vis spectra (DRS) of spin-coated thin-film of SK1 dye on FTO (SK1, magenta line), unsensitized bare SnO_2 (blue line) and SnO_2–MgO films (olive line), SK1-sensitized pristine 3D SnO_2 microsphere (SnO_2-SK1, red line) and SK1- sensitized SnO_2–MgO film (SnO_2–MgO-SK1, black line) on FTO substrates. The scan range was 200–800 nm for all the samples and recorded against blank FTO as a reference. The characteristic absorption spectrum of SnO_2 (blue line) shows a steep absorption edge at ~340 nm, while SnO_2–MgO film displays at ~360 nm. From the Tauc's plot (inset to figure 7.3.5) the band gap of 3D SnO_2 and SnO_2–MgO films are found to be ~3.57 eV and ~3.42 eV respectively where $(\alpha h\nu)^2$ is plotted against the photon energy ($h\nu$) and α is the absorption coefficient. The absorption spectrum of SK1 dye thin-film (magenta line) shows its absorbance in the range of 350–550 nm with a high molar extinction coefficient (ε) of 3.42×10^4 $M^{-1}cm^{-1}$. The absorption spectrum of SK1-sensitized 3D SnO_2 microsphere (red line) film shows the characteristic absorption edges for both the components SnO_2 and SK1, indicating adsorption of the dye on the surface of the SnO_2.

Interestingly, the absorption onset of SK1 dye in the SnO_2-MgO (black line) is higher than the pristine SnO_2 film, indicating higher loading of dye molecules. This is mainly due to low isoelectric point (IEP) of SnO_2 (i.e. at pH 4-5) which indicates acidic surface of SnO_2, causing minimum adsorption of SK1 dye having carboxylic acid (–COOH) as anchoring group. After addition of MgO (IEP at pH 12) the dye molecules are anchoring on both the surfaces, i.e., on MgO as well as SnO_2, resulting higher loading of dye molecules on the photoanode.[18]

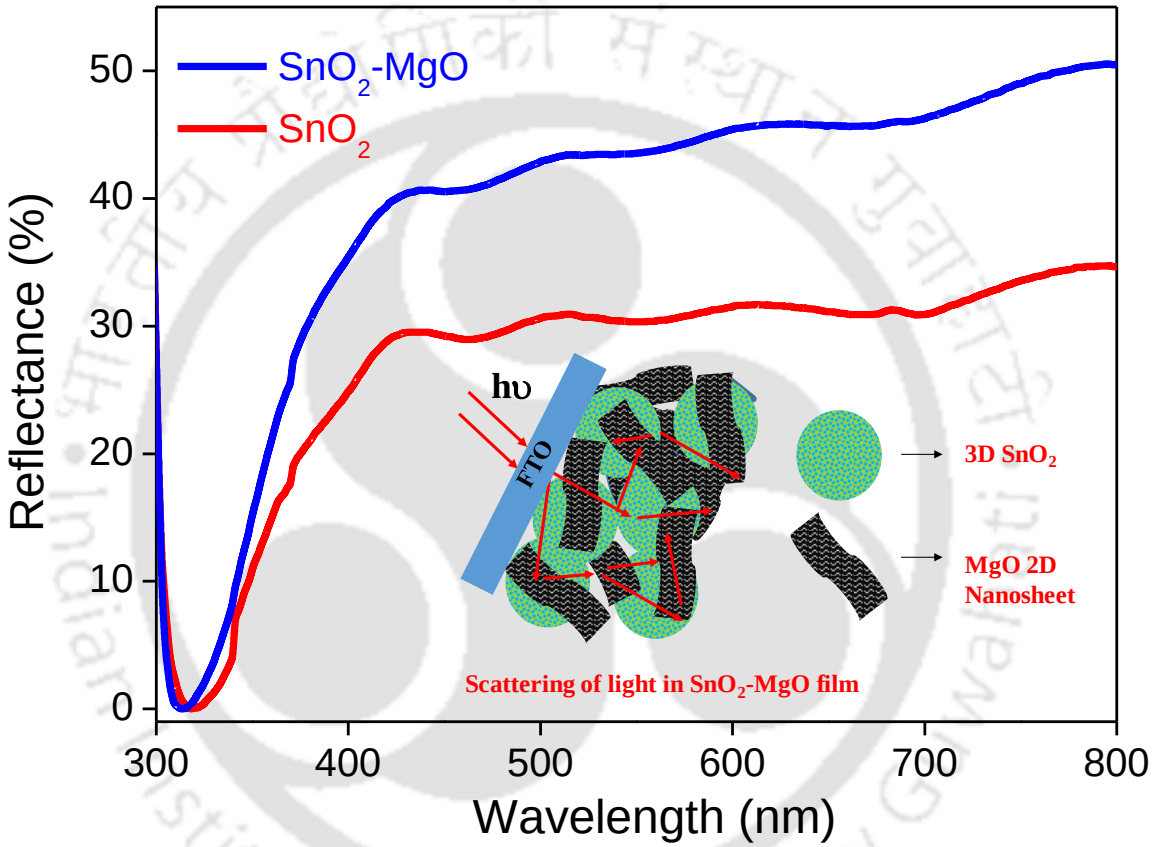

Figure 7.3.6 Diffuse reflectance spectra of the SnO_2-MgO and pristine SnO_2 films of similar thickness on FTO substrates. Inset shows confinement of light in SnO_2-MgO Photoanode.

Figure **7.3.6** shows the diffused reflectance spectra of pristine SnO_2 microsphere and SnO_2-MgO films. Diffuse reflectance measurements were carried out to investigate the light scattering properties of both the films. The SnO_2-MgO film exhibit much higher reflectance in the wavelength range 420–800 nm than that of the pristine SnO_2 film. This confirms better light scattering effect after addition of 2D nanosheets of MgO in the photoanode.[34]

7.3.5 DENSITY FUNCTIONAL THEORY (DFT) STUDY OF SK1 DYE

In order to obtain information regarding various parameters of frontier molecular orbitals of the SK1 dye such as geometric configuration, electronic density distribution and minimal energy, density functional theory (DFT) calculations were carried out by using Accelrys Materials Studio 4.0. From the DFT calculations, we can easily predict the theoretical behavior of molecular orbitals of SK1 dye. The optimization of molecular geometries of SK1 was carried out in DMol3 program package using generalized gradient approximation (GGA) with BLYP as the basis set. These simulations were carried out in a vacuum for the single molecule. Figure **7.3.7** shows the optimized geometry of the molecule along with electron density map for HOMO and LUMO energy levels.

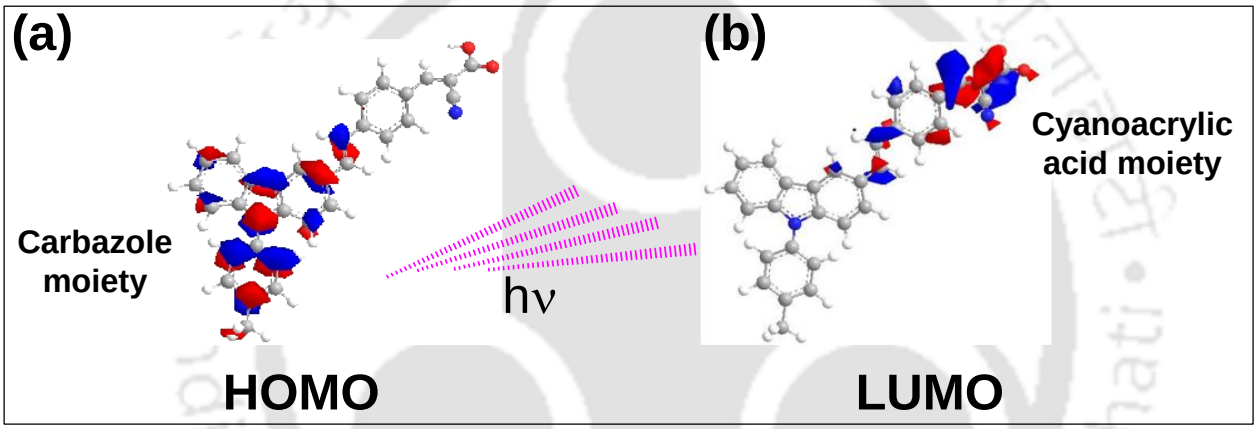

Figure 7.3.7 HOMO and LUMO frontier molecular orbitals of SK1 dye as calculated from the density functional theory (DFT) at a B3LYP/6-31+G(d) level showing the electronic distributions in its ground and excited states.

Figure **7.3.7 (a)** represents the electronic density at the HOMO energy level of SK1 is consistently distributed over the donor and π-conjugated units i.e. carbazole and oligo-phenylenevinylene respectively. On the other hand, the LUMO energy level of SK1 represents the photoinduced electronic excitation of the molecule resulting in the intramolecular charge transfer leading to an electron migration from the donor unit to the cyanoacrylic acceptor unit. This clearly represents the transfer of excited state electronic cloud from carboxylic group attached to the carbon atom bonded with cyano group to the CB of SnO_2. Moreover, the energy levels of HOMO and LUMO are separated remarkably which allow a long-lived excited state. Due to more life time of excited electrons, facilitate the charge transfer process which enhances performance parameters of photovoltaic devices.

7.3.6 ELECTROCHEMICAL ANALYSIS OF SK1 DYE

Electrochemical analysis of metal-free carbazole dye (SK1) was carried out by performing cyclic voltammetry (CV) and shown in the figure **7.3.8**.

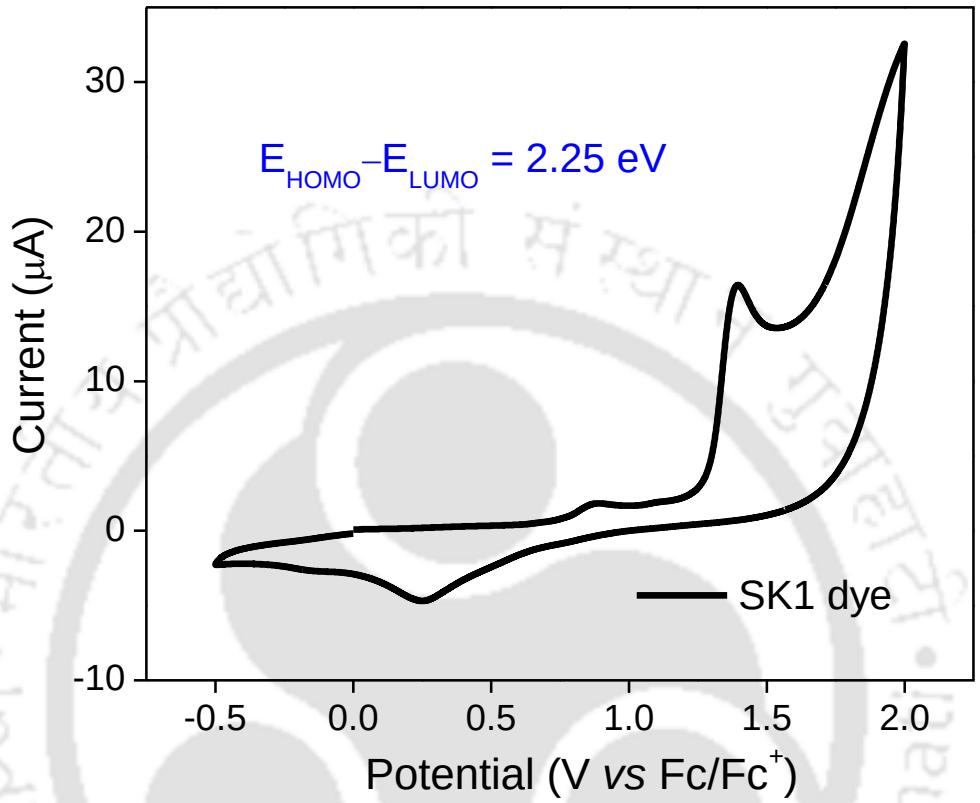

Figure 7.3.8 Cyclic-Voltagram of SK1 dye recorded at a scan rate of 50 mVs^{-1} acetonitrile solvent by using TBAP as an electrolyte

Highest-occupied molecular orbital (HOMO) level of SK1 dye was estimated in the anhydrous acetonitrile by using 0.1M Tetra-n-butyl ammoniumhexafluorophosphate (TBAP) electrolyte. The oxidation half-potential for SK1 is found to be +1.37 V (*vs* NHE). HOMO energy level of SK1 dye can be calculated by using following expression $E_{HOMO} = -[E_{onset\ (Fc/Fc+)} + 4.8]$ eV, and it is found to be at −5.62 eV (vs Fc/Fc^+), which is more positive than the redox potentials of I^-/I_3^- (−4.8 eV) and $Co^{3+/2+}$ (−5.1 eV) electrolyte. From the optical energy band gap (E_g) value and HOMO level of SK1 dye, lowest unoccupied molecular orbital (LUMO) energy level was calculated by using the following expression i.e. $E_g = E_{HOMO} - E_{LUMO}$. The value of E_g for SK1 is found to be 2.25 eV from absorption onset (Figure 7.3.5). The LUMO energy level for SK1 is estimated at −3.37 eV (vs Fc/Fc^+), which is higher than the CB energy level of SnO_2 (−4.53 eV). Electron transfer from the LUMO of the dye to the CB of SnO_2 is favorable due to fine matching of their band positions.

7.3.7 PHOTOVOLTAIC CHARACTERISTICS OF THE SOLAR CELLS

Figure **7.3.9 (A)** shows the current density–voltage (*J*–*V*) characteristics of the SK1 dye sensitized solar cells constructed using the combination of 3D SnO_2 and optimized weight percentage of 3D porous MgO, also for pristine 3D SnO_2 microspheres under AM 1.5G simulated sunlight with a light intensity of 100 mW cm^{-2}. Figure **(B)** shows corresponding incident photon to current conversion efficiency (IPCE) plots recorded for the respective solar cell devices.

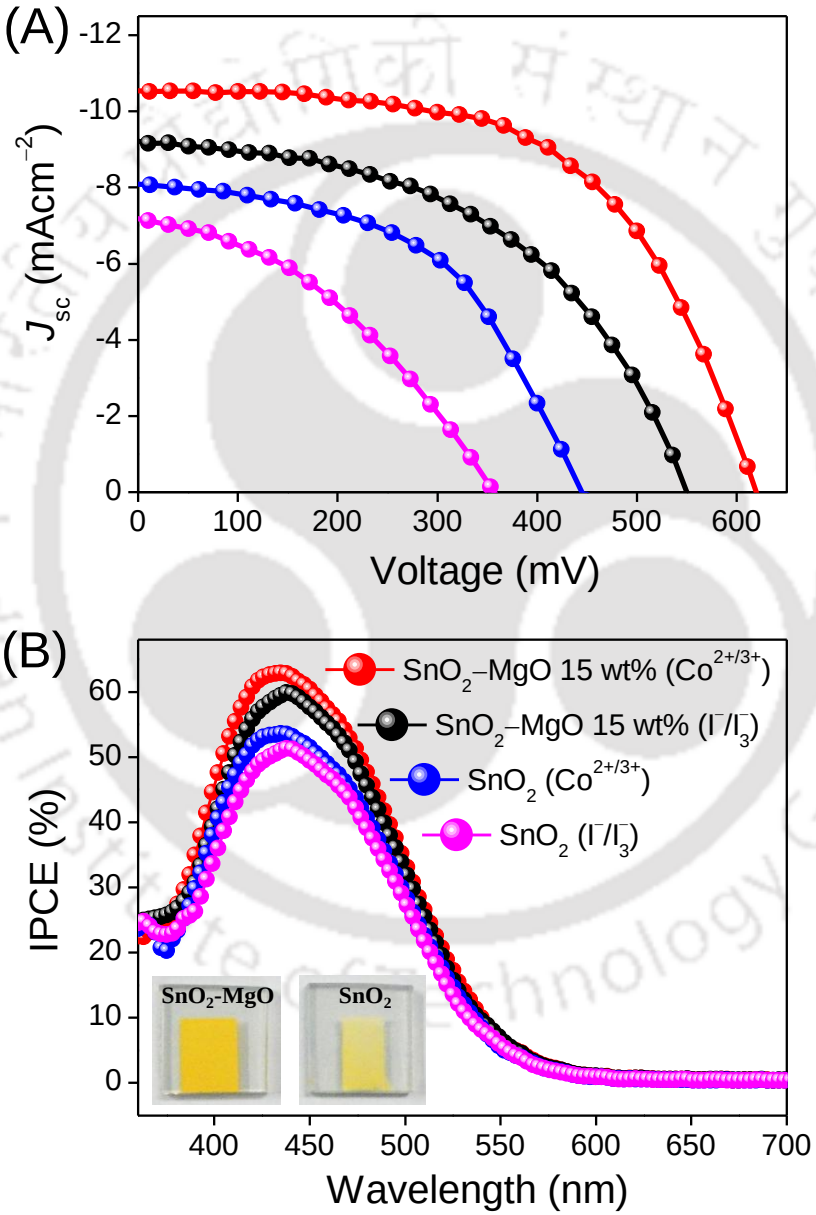

Figure 7.3.9 (A) Current density–voltage (*J*–*V*) curves for the photovoltaic devices (a) SnO_2–MgO (15 wt %) ($Co^{2+/3+}$) and (b) SnO_2–MgO (15 wt %) (I^-/I_3^-) and (c) SnO_2 ($Co^{2+/3+}$) and (d) SnO_2 (I^-/I_3^-) under AM 1.5 G solar illumination **(B)** IPCE plots for the respective devices employing $[Co(bpy)_3]^{2+/3+}$ and (I^-/I_3^-) as the redox couples. Inset shows digital photographs of the fabricated photoanodes.

Table **7.3.1** summarizes the measured and calculated values obtained from each (*J–V*) curve, the average values and standard deviations for each device configuration.

Table 7.3.1 Short circuit current density (J_{sc}), open circuit voltage (V_{oc}), fill factor (*FF*) and power conversion efficiency (η) for the fabricated devices incorporating different photoanodes and redox shuttles.

Devices	J_{sc} (mA/cm^2)	V_{oc} (mV)	*FF* (%)	PCE (η %)	Redox couple
SnO_2-MgO (15 wt %)	10.53 (±0.5)	619 (± 25)	57 (± 1.4)	3.71 (± 0.27)	$[Co(bpy)_3]^{2+/3+}$
SnO_2-MgO (15 wt %)	9.21 (± 0.6)	550 (± 26)	49 (± 1.5)	2.48 (± 0.23)	I^-/I_3^-
SnO_2	8.04 (± 0.4)	445 (± 25)	51 (± 1.3)	1.82 (± 0.25)	$[Co(bpy)_3]^{2+/3+}$
SnO_2	7.2 (± 0.6)	357 (± 33)	38 (± 1.8)	0.98 (± 0.24)	I^-/I_3^-

From table **7.3.1**, we have observed a dramatic enhancement of V_{oc}, fill factor (*FF*) and η in the SnO_2-MgO system with an increase in J_{sc} values as well. The lower V_{oc} values of pristine SnO_2 devices (357 mV and 445 mV respectively for I^-/I_3^- and $[Co(bpy)_3]^{2+/3+}$ redox couples) may be due to faster back electron transfer from CB of SnO_2 to the redox shuttle (roughly 3 fold faster than TiO_2), resulting from the reactive low-energy trap states of SnO_2.[16,35,36] The V_{oc} values for SnO_2-MgO devices are observed to be considerably higher (i.e. 550 mV, 619 mV respectively for I^-/I_3^- and $[Co(bpy)_3]^{2+/3+}$ redox couples) indicating significant drop of reverse tunneling probability in presence of MgO. Thus, the MgO barrier is minimizing the recombination rate of the photoinduced electrons with the I_3^- at the electrolyte/SnO_2 interface. In addition, the conduction band-edge of the SnO_2 may be shifted by MgO resulting in a higher quasi-Fermi level and higher V_{oc}.[8,24,37] To probe this, we have performed CV measurements for both the electrodes (i.e. pristine SnO_2 and SnO_2-MgO) and presented in figure **7.3.10**.

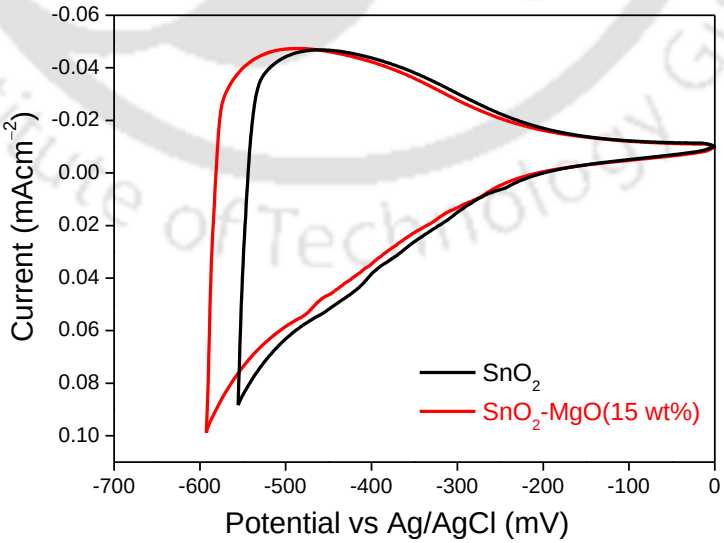

Figure 7.3.10 Cyclic-Voltagram of pristine SnO_2 electrode (black line) and SnO_2-MgO electrode (red line) in 0.1 M $NaClO_4$ in dry acetonitrile.

Figure **7.3.10** indicates shift in the conduction band edge by ~30 mV in case of SnO_2-MgO electrode as compared to the pristine SnO_2 electrode. In principle, V_{oc} of a DSSC is defined as the potential difference between the Fermi level of the semiconductor (i.e. SnO_2) and the redox potential of the redox couple. Therefore, the observed positive shift of the conduction band edge of SnO_2 after addition of MgO is also contributed toward significant increment in V_{oc} (i.e. from ~445 mV to ~ 619 mV, employing $[Co(bpy)_3]^{2+/3+}$ as redox shuttle and from ~357 mV to ~ 550 mV, employing I^-/I_3^- as redox shuttle) as we have illustrated in scheme **7.3.1**.

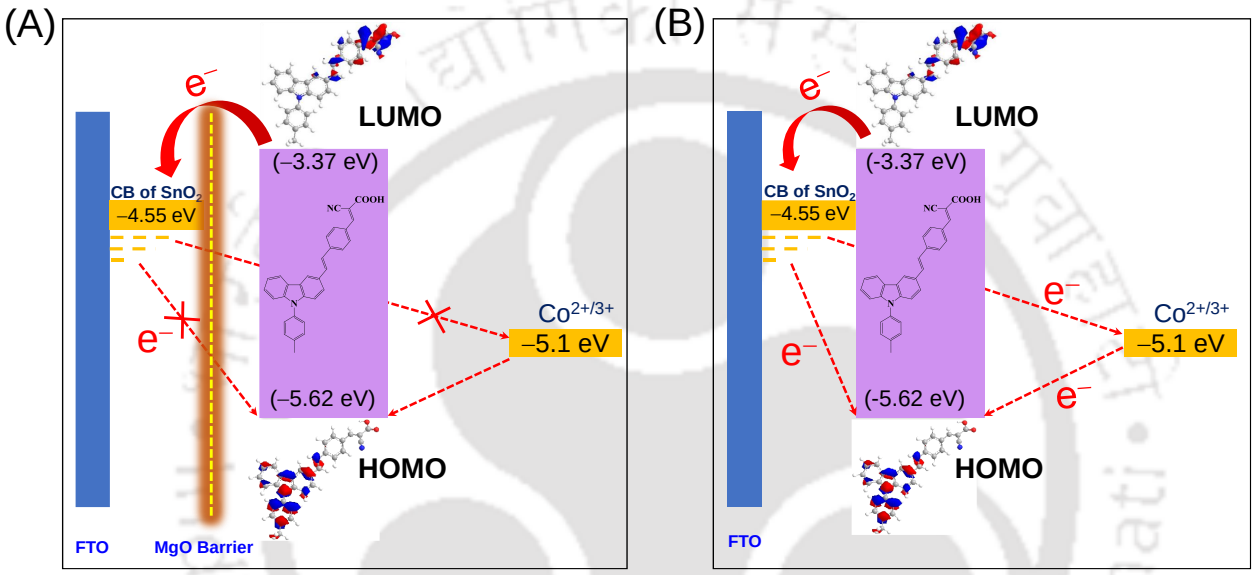

Scheme 7.3.1 Schematic representations of the energy levels of pristine SnO_2 **(A)** and SnO_2-MgO **(B)** devices showing shifting of conduction band edge of SnO_2 and inhibited electron interception at the SnO_2/electrolyte interface in presence of 2D MgO nanosheets.

It should be noted that the SK1 dye molecules are energetically capable of injecting photoinduced electrons across the MgO barrier as the excited level of the dye (LUMO) is located well above the CB of SnO_2. Further increase in V_{oc} for the redox couple $[Co(bpy)_3]^{2+/3+}$ is due to minimization of the mismatch between the redox potential and the sensitizer HOMO level to 550 mV whereas for I^-/I_3^- redox couple the mismatch is 770 mV. This is contributed in higher V_{oc} and PCE of the devices with $[Co(bpy)_3]^{2+/3+}$ redox couple as compared to the I^-/I_3^- redox couple. Higher fill factor and short circuit current density values achieved for the devices with $[Co(bpy)_3]^{2+/3+}$ redox couple (FF ≈57 % , J_{sc} ≈10.53 mA/cm^2 and ≈51%, ≈8.04 mA/cm^2 for SnO_2-MgO and pristine SnO_2 respectively) compared to I^-/I_3^- redox couple (≈49%, ≈9.21 mA/cm^2 and ≈38.2%, ≈7.20 mA/cm^2 respectively for SnO_2-MgO and pristine SnO_2) describe minimum recombination and faster regeneration kinetics. It is well known that the energy disbursement for

the effective regeneration of the oxidized dye molecules by I^-/I_3^- redox couple is larger due to the complex regeneration kinetics involved in the formation of intermediates, i.e. the $I_2^{-\cdot}$ radical, which slows down the process.[3,4,37]

Increase in J_{sc} values due to minimum photoinduced electron interception, higher loading of dye molecules and faster regeneration kinetics of $[Co(bpy)_3]^{2+/3+}$ redox couple are also explicit in the IPCE plot of SnO_2-MgO device, figure **7.3.9 (B)**, exhibiting the highest value ~60-63% in the measured wavelength range from 400 nm to 530 nm. From figure 7.3.9 (B), it is clear that the IPCE values for the device SnO_2-MgO, (I^-/I_3^-) as redox couple is ~55-60% while for pristine SnO_2 devices employing $[Co(bpy)_3]^{2+/3+}$ and (I^-/I_3^-) as redox couple are ~50-54% and ~47-51% respectively indicating a better light harvesting ability of SnO_2–MgO photoanode and superiority of $[Co(bpy)_3]^{2+/3+}$ as redox couple in the device.

To further gain insight into the effect of MgO in the electron transport and recombination kinetics of the DSSCs, electrochemical impedance spectroscopy (EIS) was employed. Figure **7.3.11 (A)** represents the electrochemical impedance (EIS) spectra of all the devices obtained under dark condition in a frequency range from 0.1 Hz to 100 kHz at the applied bias equivalent to the open-circuit voltage. As can be seen from Figure **7.3.11** (A), all Nyquist plots are composed of two semicircles. The right semicircle in the medium-frequency region is due to the charge-transfer process at the working electrode/electrolyte interface, and the left semicircle in the high-frequency region is ascribed to the redox reaction at the counter electrode/electrolyte interface.[38] It is observed that the diameter (R_k) of the right semicircles in the medium-frequency region are decreased considerably for the SnO_2-MgO devices indicating that the charge transfer resistance at SnO_2-MgO/SK1/electrolyte interfaces is lower compared to SnO_2/SK1/electrolyte interfaces.[39] Hence introduction of MgO into the devices is providing a faster charge transfer process at the working electrode-electrolyte interfaces in case of SnO_2-MgO than in pristine SnO_2 devices. This may be due to inhibited photo-induced electron recombination at the SnO_2/electrolyte interface in presence of MgO, faster dye regeneration kinetics of $[Co(bpy)_3]^{2+/3+}$ redox couple and charge transfer through the highly crystalline 2D nanoplates in the SnO_2 microspheres. The smaller diameter of the semicircle observed for the devices with Co(II/III) electrolyte in contrast to iodide/tri-iodide electrolyte, in the high frequency region, indicates a faster regeneration of $[Co(bpy)_3]^{2+/3+}$ redox shuttle at the Pt/electrolyte interface, [as shown in the inset to the figure **7.3.11 (A)**].

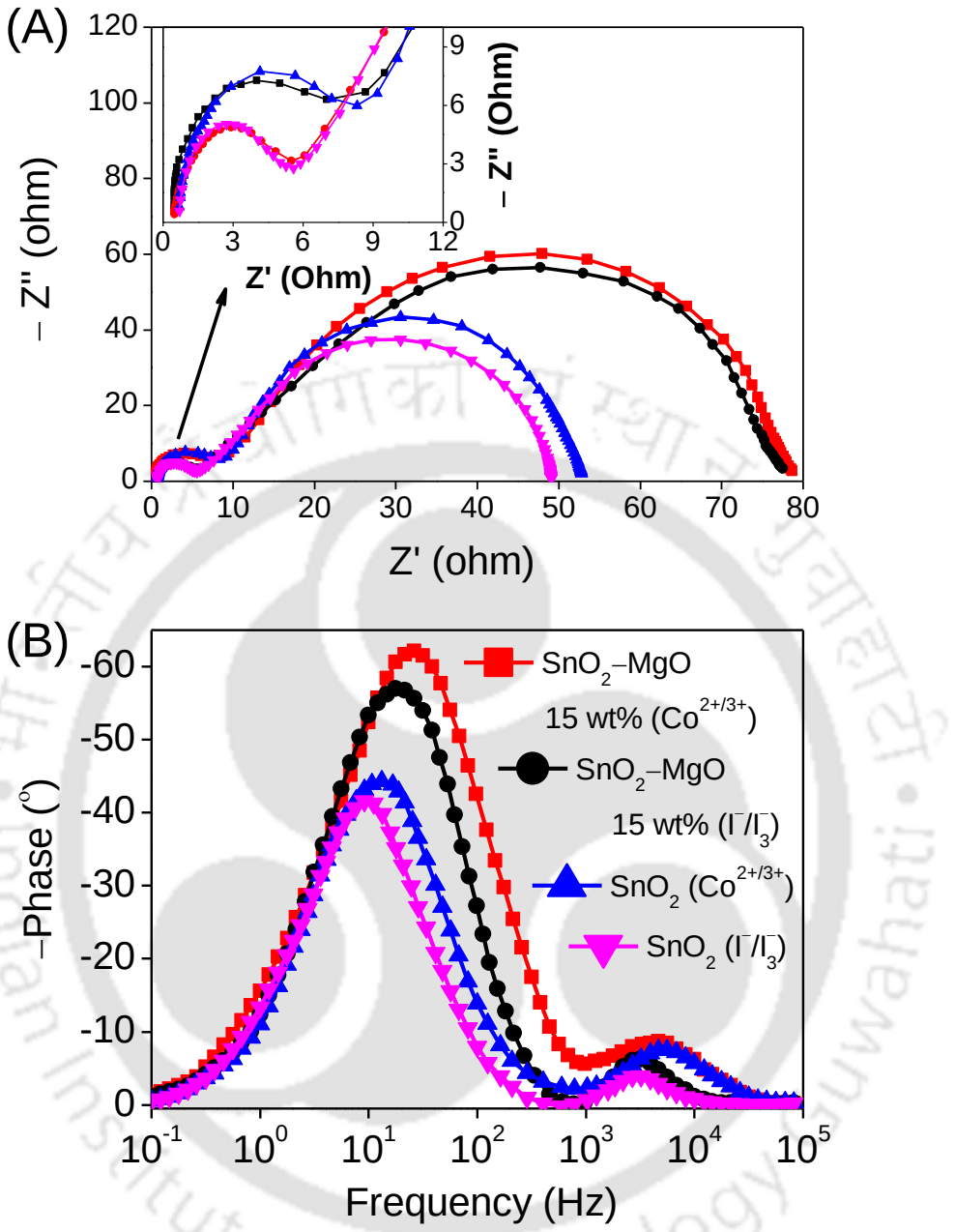

Figure 7.3.11 (A) Nyquist plots for the fabricated DSSCs in dark at open-circuit voltage and in a frequency range from 0.1 Hz to 100 kHz. Inset shows the semicircle in high frequency region of the plot. **(B)** Bode phase plots for the respective devices.

The Bode phase plots for all the fabricated devices are shown in the figure **7.3.11 (B)**. The characteristic peak frequencies in the medium frequency region (f_{max}) for the pristine SnO_2 devices are located at ~26.1 Hz and ~21.54 Hz respectively by employing I^-/I_3^- and $[Co(bpy)_3]^{2+/3+}$ as redox couples. We have calculated the photo-induced electron lifetimes in the CB of SnO_2 (τ_e) by using the formula ($\tau_e = 1/2\pi f_{max}$)[40] and are found to be 6.1 ms and 7.3 ms. The increase in electron

life time further confirms minimum photo-induced electron interception to the $[Co(bpy)_3]^{2+/3+}$ redox shuttle compared to the I^-/I_3^-. Similar trend is observed for the SnO_2-MgO devices with I^-/I_3^- and $[Co(bpy)_3]^{2+/3+}$ redox shuttles, for which f_{max} values are located at around 13.3 Hz and 10.07 Hz, yielding electron life time 11.9 ms and 15.8 ms respectively. As we have seen that there is a considerable increase in photoinduced electron lifetime in the SnO_2–MgO devices than the pristine SnO_2 devices, suggesting effective suppression of electron recombination in the devices in presence of MgO. As a result, photoinduced electron density in the CB level of SnO_2 increases, leading to the higher value of open circuit voltage (V_{oc}). This result also confirms the increased trend of power conversion efficiency of the device.

7.4 CONCLUSIONS

In conclusion, we have successfully fabricated a mesoporous SnO_2 based photoanode, utilizing the benefits of 3D hierarchical MgO composed of 2D nanosheets, by a simple sonication followed by mixing process resulting improved photovoltaic performances. Comparative study of the devices with two different redox couples i.e. (i) (I^-/I_3^-) and (ii) $[Co(bpy)_3]^{2+/3+}$ is also carried out and found that $[Co(bpy)_3]^{2+/3+}$ furnish superior photovoltaic performance as compared to I^-/I_3^- redox couple. An increment of ~74 % in PCE, i.e., from ~1 % (pristine SnO_2 device, redox mediator I^-/I_3^-) to ~3.71 % (SnO_2-MgO device, redox mediator $[Co(bpy)_3]^{2+/3+}$) has been achieved by employing 15 wt% of hierarchical MgO with porous SnO_2 microspheres. Further, from EIS measurements we have explained the charge transfer dynamics across the interfaces in the photovoltaic devices and life time of the photoinduced electrons in CB of SnO_2. It is also implicit that high BET surface area provided by the SnO_2 microspheres as well as MgO nanosheets, boost adsorption of dye molecules which upsurges the flux of photoinduced electron injection for an esteemed value of short circuit current density.

7.5 REFERENCES

(1) O'Regan, B.; Gratzel, M. *Nature*, **1991**, *353*, 737.

(2) Kay, A.; Gratzel, M. *Sol. Energy Mater. Sol. Cells*, **1996**, *44*, 99.

(3) Yum, J.-H.; Baranoff, E.; Kessler, F.; Thomas, M.; Ahmad, S.; Bessho, T.; Marchioro, A.; Ghadiri, E.; Moser, J.-E.; Yi, C.; Nazeeruddin, Md. K.; Grätzel, M. *Nat. Commun.*, **2012**, *3*, 631.

(4) Feldt, S. M.; Gibson, E. A.; Gabrielsson, E.; Sun, L.; Boschloo, G.; Hagfeldt, A. *J. Am. Chem. Soc.*, **2010**, *132*, 16714.

(5) Zhang, Z.; Chen, P.; Murakami, T. N.; Zakeeruddin, S. M.; Grätzel, M. *Adv. Funct. Mater.*, **2008**, *18*, 341.

(6) Rensmo, H.; Keis, K.; Lindström, H.; Södergren, S.; Solbrand, A.; Hagfeldt, A.; Lindquist, S.-E.; Wang, L. N.; Muhammed, M. *J. Phys. Chem. B*, **1997**, *101*, 2598.

(7) Sayama, K.; Sugihara, H.; Arakawa, H. *Chem. Mater.*, **1998**, *10*, 3825.

(8) Snaith, H. J.; Ducati, C. *Nano Lett.* **2010**, *10*, 1259.

(9) Kamat, P. V.; Bedja, I.; Hotchandani, S.; Patterson, L. K. *J. Phys. Chem.*, **1996**, *100*, 4900.

(10) Ferrere, S.; Zaban, A.; Gregg, B. A. *J. Phys. Chem. B*, **1997**, *101*, 4490.

(11) Burnside, S.; Moser, J.-E.; Brooks, K.; Gratzel, M.; Cahen, D. *J. Phys. Chem. B*, **1999**, *103*, 9328.

(12) Arnold, M. S.; Avouris, P.; Pan Z. W.; Wang, Z. L. *J. Phys. Chem. B*, **2003**, *107*, 659.

(13) Tang, H.; Prasad, K.; Sanjines, R.; Schmid P. E.; Levy, F. *J. Appl. Phys.*, **1994**, *75*, 2042.

(14) Hendry, E.; Koeberg, M.; O'Regan, B.; Bonn, M. *Nano Lett.*, **2006**, *6*, 755.

(15) Senevirathna, M. K. I.; Pitigala, P. K. D. D. P.; Premalal, E. V. A.; Tennakone, K.; Kumara, G. R. A.; Konno, A. *Sol. Energy Mater. Sol. Cells*, **2007**, *91*, 544.

(16) Green, A. N. M.; Palomares, E.; Haque, S. A.; Kroon, J. M.; Durrant, J. R. *J. Phys. Chem. B*, **2005**, *109*, 12525.

(17) Parks, G. A. *Chem. Rev.*, **1965**, *65*, 177.

(18) Ito, S.; Makari, Y.; Kitamura, T.; Wada, Y.; Yanagida, S. *J.Mater.Chem.*, **2004**, *14*, 385.

(19) Tennakone, K.; Kumara, G. R. R. A.; Kottegoda, I. R. M.; Perera, V. P. S. *Chem. Commun.*, **1999**, 15.

(20) Chappel, S.; Chen, S.-G.; Zaban, A. *Langmuir*, **2002**, *18*, 3336.

(21) Kay, A.; Gratzel, M. *Chem. Mater.*, **2002**, *14*, 2930.

(22) Tennakone, K.; Bandara, J.; Bandaranayake, P. K. M.; Kumara G. R. A.; Konno, A. *Jpn. J. Appl. Phys.*, **2001**, *40*, L732.

(23) Docampo, P.; Tiwana, P.; Sakai, N.; Miura, H.; Herz, L.; Murakami, T.; Snaith, H. J. *J. Phys. Chem. C*, **2012**, *116*, 22840.

(24) Ramasamy, E.; Lee, J. *J. Phys. Chem. C*, **2010**, *114*, 22032.

(25) Hagfeldt, A.; Boschloo, G.; Sun, L.; Kloo, L.; Pettersson, H. *Chem. Rev.*, **2010**, *110*, 6595.

(26) Wang, Z. S.; Koumura, N.; Cui, Y.; Takahashi, M.; Sekiguchi, H.; Mori, A.; Kubo, T.; Furube, A.; Hara, K. *Chem. Mater.*, **2008**, *20*, 3993.

(27) Ito, S.; Miura, H.; Uchida, S.; Takata, M.; Sumioka, K.; Liska, P.; Comte, P.; Pechy, P.; Grätzel, M. *Chem. Commun.*, **2008**, 5194.

(28) Qin, H.; Wenger, S.; Xu, M.; Gao, F.; Jing, X.; Wang, P.; Zakeeruddin, S. M.; Grätzel, M. *J. Am. Chem. Soc.*, **2008**, *130*, 9202.

(29) Wang, Z. S.; Cui, Y.; Dan-Oh, Y.; Kasada, C.; Shinpo, A.; Hara, K. *J. Phys. Chem. C*, **2008**, *112*, 17011.

(30) Hwang, S.; Lee, J. H.; Park, C.; Lee, H.; Kim, C.; Park, C.; Lee, M. H.; Lee, W.; Park, J.; Kim, K.; Park, N. G.; Kim, C. *Chem. Commun.* **2007**, 4887.

(31) Li, S.-G.; Jiang, K.-J.; Huang, J.-H.; Yang, L.-M.; Song, Y.-L. *Chem. Commun.*, **2014**, *50*, 4309.

(32) Kim, H.-R.; Choi, K.-II; Lee, J.-H.; Akbar, S. A. *Sens. Actuators, B*, **2009**, *136*, 138.

(33) Tian, P.; Han, X.-Y.; Ning, G.-L.; Fang, H.-X.; Ye, J.-W.; Gong, W.-T.; Lin, Y. *ACS Appl. Mater. Interfaces*, **2013**, *5*, 12411.

(34) Chetia, T. R.; Barpuzary, D.; Qureshi, M. *Phys. Chem. Chem. Phys.*, **2014**, *16*, 9625.

(35) Bisquert, J.; Cahen, D.; Hodes, G.; Rühle S.; Zaban, A. *J. Phys. Chem. B*, **2004**, *108*, 8106.

(36) Yella, A.; Humphry-Baker, R.; Curchod, B. F. E.; Astani, N. A.; Teuscher, J.; Polander, L. E.; Mathew, S.; Moser, J.-E.; Tavernelli, I.; Rothlisberger, U.; Grätzel, M.; Nazeeruddin M. K.; Frey, J. *Chem. Mater.*, **2013**, *25*, 2733.

(37) Prasittichai, C.; Hupp, J. T. *J. Phys. Chem. Lett.*, **2010**, *1*, 1611.

(38) Wu, M.; Lin, X.; Hagfeldt, A.; Ma, T. *Chem. Commun.*, **2011**, *47*, 4535.

(39) Phadke, S.; Pasquier, A. D.; Birnie, D. P. *J. Phys. Chem. C*, **2011**, *115*, 18342.

(40) Papageorgiou, N.; Maier, W. F.; Grätzel, M. *J. Electrochem. Soc.*, **1997**, *144*, 876.

THESIS
OVERVIEW

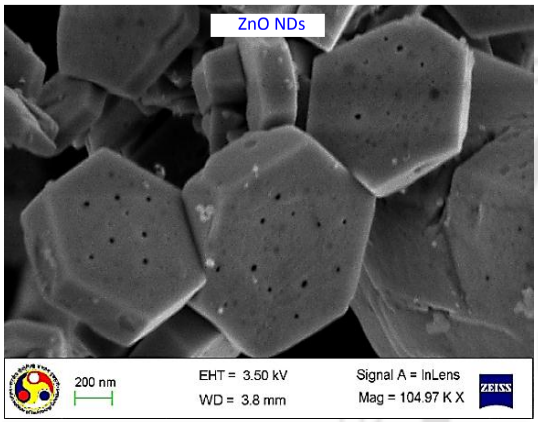

Chapter 3: PCE ≈ 4.86 %

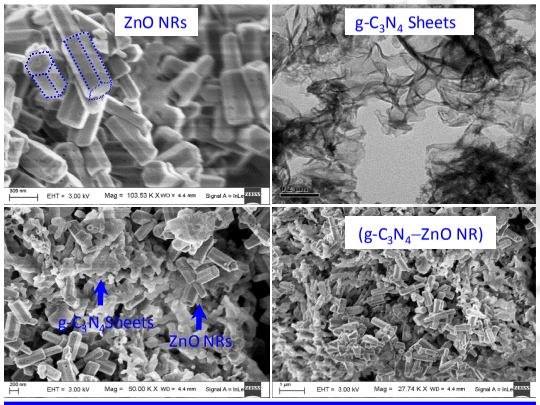

Chapter 6: PCE ≈ 2.43 %

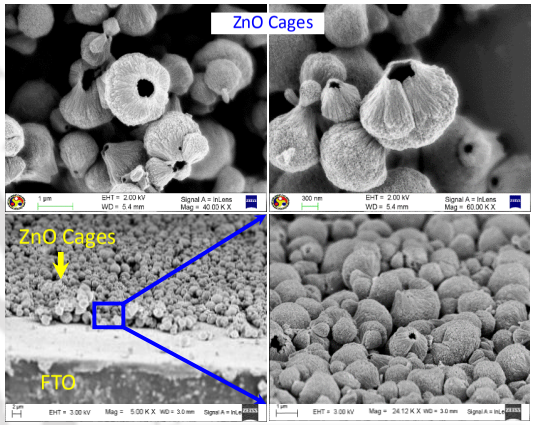

Chapter 4: PCE ≈ 4.26 %

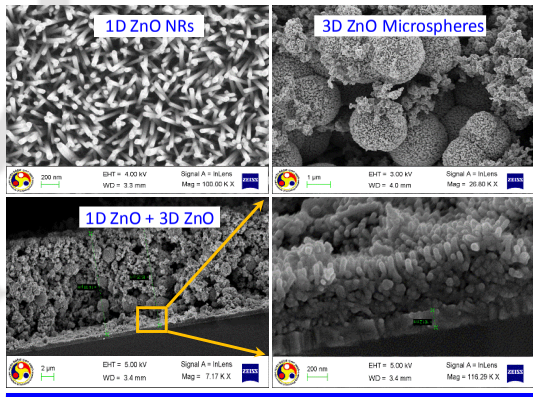

Chapter 5: PCE ≈ 2.35 %

LIST OF PUBLICATIONS AND CONFERENCES ATTENDED

Journal Articles:

Included in Thesis:

1. **T. R. Chetia**, M. S. Ansari, M. Qureshi; *Graphitic Carbon Nitride as a Photovoltaic Booster in Quantum Dot Sensitized Solar Cells: A Synergistic Approach for Enhanced Charge Separation and Injection.*
   J. Mater. Chem. A, 2016, *4*, 5528–5541. (*DOI: 10.1039/C6TA00761A*)

2. **T. R. Chetia**, M. S. Ansari, M. Qureshi; *Rational Design of Hierarchical ZnO Superstructures for Efficient Charge Transfer: Mechanistic and Photovoltaic Studies of Hollow, Mesoporous, Cage-Like Nanostructures with Compacted 1D Building Blocks.*
   Phys. Chem. Chem. Phys., 2016, *18*, 5344–5357. (*DOI: 10.1039/C5CP07687K*)

3. **T. R. Chetia**, M. S. Ansari, M. Qureshi; *Ethyl Cellulose and Cetrimonium Bromide Assisted Synthesis of Mesoporous, Hexagon Shaped ZnO Nanodisks with Exposed ±{0001} Polar Facets for Enhanced Photovoltaic Performance in Quantum Dot Sensitized Solar Cells.*
   ACS Applied Mater. Interfaces, 2015, *7*, 13266–13279. (*DOI: 10.1021/acsami.5b01039*)

4. M. Qureshi, **T. R. Chetia**, M. S. Ansari, S. S. Soni; *Enhanced Photovoltaic Performance of Mesoporous SnO_2 Based Solar Cells Utilizing 2D MgO Nanosheets Sensitized By a Metal-free Carbazole Derivative.*
   J. Mater. Chem. A, 2015, *3*, 4291-4300. (*DOI: 10.1039/C4TA05877A*)

5. **T. R. Chetia**, D. Barpuzary, M. Qureshi; *Enhanced Photovoltaic Performance Utilizing Effective Charge Transfers and Light Scattering Effects by the Combination of Mesoporous, Hollow 3D-ZnO along with 1D-ZnO in CdS Quantum Dot Sensitized Solar Cells.*
   Phys. Chem. Chem. Phys., 2014, *16*, 9625–9633. (*DOI: 10.1039/C3CP55276D*)

Not Included in Thesis:

1. Z. Khan, **T. R. Chetia**, M. Qureshi; *Rational Design of Hyperbranched 3D Heteroarrays of SrS/CdS: Synthesis, Characterization and Evaluation of Photocatalytic Properties for Efficient Hydrogen Generation and Organic Dye Degradation.*
   Nanoscale, 2012, *4*, 3543–3550. (*DOI: 10.1039/C2NR30666B*)
2. Z. Khan, **T. R. Chetia**, A. K. Vardhaman, D. Barpuzary, C. V. Sastri, M. Qureshi; *Visible Light Assisted Photocatalytic Hydrogen Generation and Organic Dye Degradation by CdS–Metal Oxide Hybrids in Presence of Graphene Oxide.*
   RSC Adv., 2012, *2*, 12122–12128. (*DOI: 10.1039/C2RA21596A*)

Conferences Attended

Oral Presentations:

1. *Hexagon Shaped ZnO Nanodisks with Exposed ±{0001} Polar Facets for Enhanced Photovoltaic Performance in Quantum Dot Sensitized Solar Cells.* **4th International Conference on Advanced Nanomaterials and Nanotechnology (ICANN)** at Indian Institute of Technology Guwahati, Guwahati, Assam, India **(2015)**.
2. *Fabrication of Bilayer ZnO Based Hybrid Photoanode for Enhanced Photovoltaic Performance in CdS Quantum dot Sensitized Solar Cells.* **Frontiers in Chemical Sciences (FICS)** at Indian Institute of Technology Guwahati, Guwahati, Assam, India **(2014)**

Poster Presentation:

1. *Enhanced Photovoltaic Performance by the Combination of Mesoporous Hollow 3-D ZnO Microspheres and 1-D ZnO Nanowires in CdS Quantum Dot Sensitized Solar cells.* **International Symposium on Advances in Spectroscopy and Ultrafast Dynamics (ASUD)** at Indian Association for the Cultivation of Science, Kolkata, India **(2014)**.